Dissertation

Functional Layers for Enhanced Photon Extraction in ITO-free OLEDs

Lorenz Bießmann

28. Juni 2019

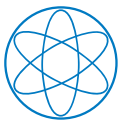


Technische Universität München

Physik-Department
Lehrstuhl für Funktionelle Materialien

TECHNISCHE UNIVERSITÄT MÜNCHEN

Physik-Department
Lehrstuhl für Funktionelle Materialien

Functional Layers for Enhanced Photon Extraction in ITO-free OLEDs

Lorenz Bießmann, M. Sc.

Vollständiger Abdruck der von der Fakultät für Physik der Technischen Universität München zur Erlangung des akademischen Grades eines

Doktors der Naturwissenschaften (Dr. rer. nat.)

genehmigten Dissertation.

Vorsitzender:		Prof. Dr. Martin Zacharias
Prüfer der Dissertation:	1.	Prof. Dr. Peter Müller-Buschbaum
	2.	Prof. Jonathan J. Finley, Ph. D.

Die Dissertation wurde am 16.05.2019 bei der Technischen Universität München eingereicht und durch die Fakultät für Physik am 18.06.2019 angenommen.

Abstract

The present work tackles the question how the device efficiency of organic light emitting diodes (OLEDs) can be enhanced. For this purpose, zinc oxide (ZnO) scattering layers were tailored to improve the light extraction from such devices. In order to enhance the photon outcoupling required for this purpose, hierarchically structured layers were cast from solution via spray deposition and were evaluated regarding their diffuse scattering ability. Furthermore, ZnO/PEDOT:PSS bilayers were fabricated, which combine the ability of increased light outcoupling through enhanced scattering with the advantages of polymeric materials used as an electrode. To identify mechanisms which eventually lead to device failures, PEDOT:PSS electrodes were further investigated regarding their water sensitivity by employing in situ ToF-NR measurements in humid atmosphere. The electrical conductivity and water sensitivity is found to be linked to the morphological structure and the excess PSS content in the thin films. Thus, weak and strong acid post-treatments of PEDOT:PSS thin films were examined regarding their PSS extraction yield and the associated morphological changes. Finally, the obtained high conducting polymeric electrodes were evaluated regarding their device performance in ITO-free OLEDs.

Zusammenfassung

Die vorliegende Arbeit beschäftigt sich mit der Frage, wie die Effizienz organischer Leuchtdioden (OLEDs) erhöht werden kann. Zu diesem Zweck wurden aus Zinkoxid (ZnO) bestehende Streuschichten entwickelt, um die Lichtextraktion aus solchen Geräten zu verbessern. Um die hierfür notwendige Photonenauskopplung zu steigern, wurden hierarchisch strukturierte Schichten mittels Sprühbeschichtung aus einer Lösung hergestellt und bezüglich ihrer diffusen Streueigenschaften untersucht. Zusätzlich wurden ZnO/PEDOT:PSS Doppelschichten hergestellt, welche die Fähigkeiten der Streuschicht mit denen einer leitfähigen Polymerelektrode vereinen. Um Mechanismen zu identifizieren, die zu Geräteausfällen führen könnten, wurden die PEDOT:PSS Elektroden weiter mittels in situ ToF-NR Messungen hinsichtlich ihrer Wasserempfindlichkeit untersucht. Die elektrische Leitfähigkeit und die Wasserempfindlichkeit sind abhängig von der morphologischen Struktur und dem überschüssigen PSS Gehalt in den dünnen Filmen. Hierfür wurden Säurenachbehandlungen von dünnen PEDOT:PSS Filmen mit starken und schwachen Säuren hinsichtlich ihrer PSS Extraktionsausbeute und der damit verbundenen morphologischen Veränderungen untersucht. Schließlich wurden die erhaltenen hochleitfähigen Polymerelektroden bezüglich ihrer Leistungsfähigkeit in ITO-freien OLEDs bewertet.

Contents

List of Abbreviations

AC . . . . . alternating current

AFM . . . . . atomic force microscopy

ASH . . . . . average step height

BCC . . . . . body-centered cubic

BZ . . . . . Brillouin zone

DA . . . . . decoupling approximation

DC . . . . . direct current

DMF . . . . . N,N-dimethylformamid

DMSO . . . . . dimethyl sulfoxide

DOS . . . . . density of states

DWBA . . . . . distorted-wave Born approximation

EBL . . . . . electron blocking layer

EDX . . . . . energy-dispersive X-ray spectroscopy

EG . . . . . ethylene glycol

EGMT . . . . . ethylene glycol-modified titanate

EIA . . . . . effective interface approximation

EIL . . . . . electron injection layer

EL . . . . . emissive layer

EQE . . . . . external quantum efficiency

ETL . . . . . electron transport layer

FFT . . . . . fast Fourier transform

FoM . . . . . figure of merit

FTO . . . . . flurine-doped tin oxide

FWHM . . . . . full width at half maximum

GISANS . . . . . grazing-incidence small-angle neutron scattering

GISAS . . . . . grazing-incidence small-angle scattering

GISAXS . . . . . grazing-incidence small-angle X-ray scattering

GIWAXS . . . . . grazing-incidence wide-angle X-ray scattering

GIXS . . . . . grazing-incidence X-ray scattering

HBL . . . . . hole blocking layer

HCl . . . . . hydrochloric acid

HCOOH . . . . . formic acid

HIL . . . . . hole injection layer

HNO_3 . . . . . nitric acid

HOMO . . . . . highest occupied molecular orbital

H_2SO_4 . . . . . sulfuric acid

HTL . . . . . hole transport layer

IC . . . . . integrated circuit

IPA . . . . . isopropyl alcohol

IQE . . . . . internal quantum efficiency

IR . . . . . infrared light

ITO . . . . . indium-doped tin oxide

LCAO . . . . . linear combination of atomic orbitals

LED . . . . . light emitting diode

LMA . . . . . local monodisperse approximation

LUMO . . . . . lowest unoccupied molecular orbital

MLZ . . . . . Heinz Maier-Leibnitz Zentrum

NMR . . . . . nuclear magnetic resonance

NR . . . . . neutron reflectometry

ODT . . . . . order-disorder transition

OFET . . . . . organic field-effect transistor

OLED . . . . . organic light emitting diode

OPV . . . . . organic photovoltaic

PDI . . . . . polydispersity index

PDY-132 . . . . . Super Yellow®

PEDOT . . . . . poly(3,4-ethylene dioxythiophene)

PEDOT:PSS . . . . poly(3,4-ethylene dioxythiophene):poly(styrene sulfonate)

PEIS . . . . . potentiostatic electrochemical impedance spectroscopy

PEO . . . . . poly(ethylene oxide)

PPV . . . . . poly(*p*-phenylen-vinylen)

PS . . . . . polystyrene

PS-*b*-PEO . . . . . polystyrene-*block*-poly(ethylene oxide)

PSS . . . . . poly(styrene sulfonate)

PTFE . . . . . polytetrafluoroethylene

PVC . . . . . polyvinyl chloride

PVDF . . . . . polyvinylidenfluorid

PWM . . . . . pulse-width modulation

QP . . . . . quasiparticle

rms . . . . . root mean square

RPSD . . . . . radial power spectral density

SAXS . . . . . small-angle X-ray scattering

SDD . . . . . sample-to-detector distance

SEM . . . . . scanning electron microscopy

SLD . . . . . scattering length density

SLD_N . . . . . neutron scattering length density

SLD_x . . . . . X-ray scattering length density

SSH . . . . . Su-Schrieffer-Heeger

SSL . . . . . strong segregation limit

TCO . . . . . transparent conductive oxide

TiO_2 . . . . . titanium dioxide

ToF . . . . . time of flight

ToF-NR . . . . . time of flight neutron reflectometry

US-B . . . . . ultrasonic bath

UV . . . . . ultraviolet light

WLI . . . . . white light interferometry

WSL . . . . . weak segregation limit

XPS . . . . . X-ray photoelectron spectroscopy

XRD . . . . . X-ray diffraction

XRR . . . . . X-ray reflectometry

ZAD . . . . . zinc acetate dihydrate

ZnO . . . . . zinc oxide

CHAPTER 1

Introduction

In the last century, the development of semiconductor based transistors and light emitting diodes (LEDs) changed the field of application for electronics significantly. The realization of the first point-contact transistor in 1947 in the Bell Laboratories[1] marked the starting point of a still ongoing miniaturization process of integrated circuits that led to modern world technologies. Consequently, it was awarded with the Nobel prize for Bardeen, Brattain and Shockley in the year 1956. In the following decades, the field of semiconductor electronics was dominated by inorganic materials such as Si or GaAs. The discovery of conductivity in polyacetylene by Heeger, Shirakawa and McDiarmid in 1977[2] – awarded with the Nobel prize in chemistry in the year 2000 – extended the field of semiconducting materials by polymers. In combination with the research on electroluminescence in organic materials in the 1960s,[3,4] this led to the development of first thin film organic light emitting diode (OLED) devices in the 1980s.[5]

Since then, the field of organic electronics presents fascinating opportunities and possesses new possibilities for electronics. Within the last decades, a trend towards mechanically flexible and light weight electronic devices can be observed. The inherent flexibility of conducting polymers in combination with deposition from solution permits industrial fabrication processes such as roll-to-roll printing and thus enables large scale production. One key aspect in this field is the use of polymer electrodes. Consequently, conducting polymers have been heavily investigated for their potential use as polymeric electrodes[6–10] in devices such as organic solar cells,[11–13] OLEDs,[14–17] sensor applications,[18,19] and most recently for organic thermoelectric devices.[20–23]

Among the various applications of organic electronics, OLED devices are by far the longest investigated ones and posses numerous advantages in comparison to inorganic LED technology. As polymer science facilitates nearly infinite possible combinations of polymers comprising of different functional groups, the materials can be tailored to their specific needs. From this, a large amount of different emitters arise to cover a broad color spectrum in the visible range of light. Furthermore, the Gaussian distribution of energetic states in conducting polymers results in a broad emission spectrum that leads to a more natural appearance of colors and white light. In combination with their inherent flexibility, this enables the fabrication of (flexible) high quality OLED displays that found nowadays widely application in smartphones and further consumer electronics. However, the overall efficiency and especially the brightness of OLEDs are still behind the one of inorganic devices, which is one reason why the application of such devices in room lighting is yet at its beginning. Nevertheless, the thin film technology and adjustable color temperature of (white) OLEDs allow the fabrication of extended surface emitting devices that facilitates a new field of application in room lighting. In order to enhance the device's efficiency, mainly three factors have to be taken into account:

I. Low electrical power losses by charge carrier transport from the electrodes to the emitting layer.

II. High conversion efficiency with high photon yield in the emitting layer.

III. Large extraction yield of the generated photons.

By the introduction of additional functional layers into the device stack, the transport of the injected charge carriers to the emissive layer is enhanced. Via this so-called band alignment, a low operating voltage is achieved that is – in the ideal case – given by the band gap of the emissive layer itself.[5] One example for such a transport layer is the widely used poly(3,4-ethylene dioxythiophene):poly(styrene sulfonate) (PEDOT:PSS). Hence, in the best case, ohmic contacts are achieved that fulfill the first requirement (I). Furthermore, research was focused on the conversion efficiency of the emitting layer, sandwiched between the transport and blocking layers. The development of triplet emitting materials that facilitate the relaxation of triplet excitons via light emission, led to a jump in the internal quantum efficiency of OLED devices from ~25 % to nearly 100 %.[24] Thus, the second requirement (II) is accomplished and the devices reached almost full energy conversion via photon generation. As a consequence, the extraction of the generated photons (III) stays a limiting factor in the device's efficiency. In standard devices, roughly 80% of the generated photons are trapped in the device and are eventually absorbed by the organic layers. Hence, research is focused on possibilities to extract the generated photons in order to enhance the overall device efficiency.

In the recent years, some approaches have been developed that mainly have in common to reduce the total internal reflection via scattering and redirection of the generated photons towards the emission direction of the device. Typical approaches are, for instance, based on the implementation of a thick polymer layer with embedded

inorganic, high refractive index particles, such as TiO_2 nanoparticles, with a diameter in the range of the visible light.[25] Another approach is realized via scattering layers on the substrate in the form of micro-lenses[26,27] or patterned Bragg lattices.[28] While such approaches work very well for point emitters such as inorganic LEDs, they are inconvenient for large scaled surface emitters such as white OLEDs. In addition, the mentioned approaches reveal further issues, such as additional degradation effects of the polymer layer or strong wavelength dependent scattering at the Bragg lattice. Therefore, the present work focuses on the question how the efficiency of (white) OLEDs might be enhanced by the implementation of such an additional scattering layer, whereas the issues arising from its introduction are minimized. For this purpose, it is required to insert the scattering layer in between the substrate and the typically used indium-doped tin oxide (ITO) electrode. As a consequence, the brittle and costly ITO electrode is replaced by the earlier mentioned PEDOT:PSS, which enables the fabrication of a conducting ZnO/PEDOT:PSS scattering bilayer.

Hence, the most important theoretical background for the loss mechanisms arising in OLED devices, together with the basic concepts of charge transport in organic semiconductors and of the employed characterization techniques, are provided in Chapter 2 of the present thesis. This chapter is followed by a specific description of the sample preparation routines used to fabricate the mentioned scattering layers, which is shown together with the explanation of the fabrication and treatment of PEDOT:PSS polymeric electrodes in Chapter 3. The spectroscopic, electrical, and structural characterization techniques required to investigate the obtained thin films are described in detail in Chapter 4. Additionally, the construction of a spectrometric measurement setup is shown, which allows recording of the angular and wavelength dependent transmission of scattering layers and emission of OLED devices, respectively. Furthermore, it is capable to determine the device's efficiency.

In the following, a brief motivation of the presented work is provided, including a graphical overview of the three main chapters in Figure 1.1. As mentioned earlier, the external quantum efficiency (EQE) of OLED devices is limited by the outcoupling efficiency of generated photons. The photon extraction is strongly reduced by organic and substrate modes, originated in the different refractive indices of the used materials, which results for instance in total reflection at the substrate-air interface. In order to suppress such modes, a ZnO scattering layer is examined regarding its angular scattering behavior and its color stability in Chapter 5 with the aim to reduce total internal reflection via enhanced scattering of the generated photons. ZnO thin films are fabricated via spray deposition from solution, applying a structure directing diblock copolymer route based on sol-gel chemistry. Additionally, PS microspheres are introduced in order to serve as template for further scattering centers in the range of visible light. Hence, a hierarchically structured, porous film is obtained. As the deposition of ITO on such a film might harm the scattering layer and increases production costs, a polymeric PEDOT:PSS electrode is employed to serve as transparent

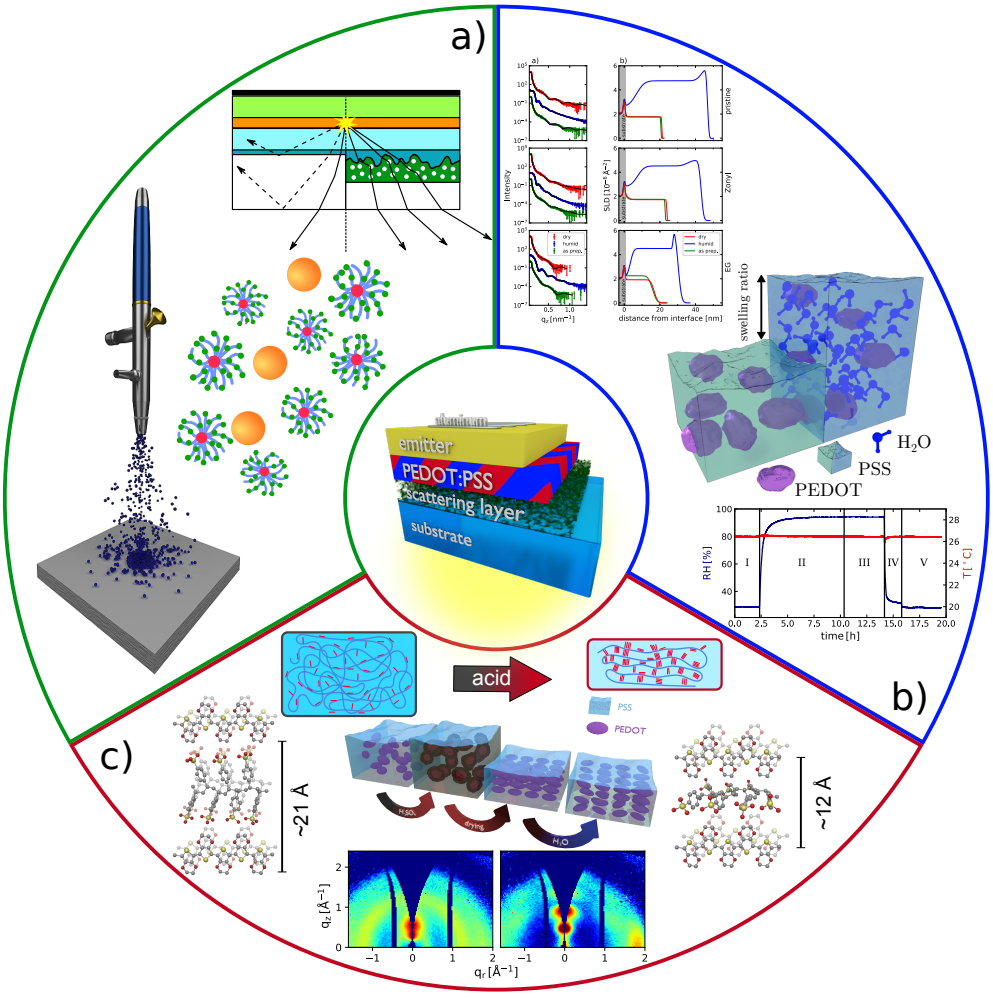

Figure 1.1
Graphical overview of the research topics addressed in the present thesis. a) Hierarchically structured ZnO scattering layers (green) providing enhanced diffuse scattering, obtained via spray deposition. Conducting ZnO/PEDOT:PSS bilayers have been successfully fabricated. b) In situ ToF-NR investigation on PEDOT:PSS electrodes under high humidity conditions (blue). Swelling and water incorporation is monitored, revealing a strong influence on the PSS content in the film. Reproduced with permission.[29] c) Compositional and morphological investigations on highly conducting PEDOT:PSS electrodes by means of XPS and GIWAXS (red). PSS extraction via acid post-treatment is examined and linked to the acid's strength, revealing compact lamellar stacking of alternating PEDOT and PSS molecules which facilitates enhanced conductivity. Reproduced with permission.[30]

electrode in final devices. Therefore, fabricated ZnO/PEDOT:PSS bilayers are further investigated regarding their performance as translucent conductor.

The presence of further organic layers might potentially promote degradation processes in final devices. For instance, PEDOT:PSS is known to have reduced conductivity in the presence of water. In addition, the PSS amount in such layers is expected to adsorb water which might be detrimental for adjacent organic layers. As a result, expected film swelling might create stress on the adjacent functional layers which could increase the probability of device failure. Therefore, the influence of high humidity on differently treated PEDOT:PSS electrodes is tested in Chapter 6. For this purpose, the films are exposed to a water saturated atmosphere and their response regarding water sorption and film swelling is examined in situ via ToF-NR.

In order to be able to replace the costly and brittle ITO or FTO metal oxides as transparent electrode in organic electronics, the conductivity of PEDOT:PSS has to be further enhanced. Its conducting behavior is strongly related to the thin film's morphology and its PSS content. Hence, in Chapter 7, post-treatments via weak and strong acids are investigated upon their morphological change on the final thin films and the PSS extraction yield. Reducing the PSS content is expected to enhance the electrode performance and – as a side effect – reduces its sensitivity against water. Thus, the resilience of the electrodes versus an extensive water treatment is additionally examined. ITO-free OLED devices are fabricated with the best performing polymeric electrodes in order to test their influence on the efficiency of final devices. Furthermore, not only the DC conductivity is of interest for organic electronics. Since OLEDs might be powered via a pulse-width modulation (PWM) mode to enhance lifetime and reduce the energy consumption, the response on an alternating current (AC) is of high importance. This behavior is especially relevant if such materials find application in organic field-effect transistors (OFETs), as those require typically frequencies of several kHz to MHz.

The above posted questions are tackled in the corresponding chapters of this work. All findings obtained in the framework of the conducted thesis are put together in Chapter 8, answering the raised questions. Based on the obtained results, an outlook for future projects is provided in order to incite and inspire future researchers to work in the field of organic electronics.

CHAPTER 2

Theoretical Aspects

The following chapter provides the most relevant concepts for the work conducted in the frame of the present thesis. In the beginning, the underlying principles of structure formation of block copolymers and the resulting templating effect for ZnO scattering layers is explained in Section 2.1. Closely related, Section 2.2 provides information about the Flory-Huggins theory, which is employed in a swelling model that describes the response of polymer layers in a saturated solvent atmosphere. As the main part of this thesis examines polymeric electrodes, some theoretical background about charge transport in organic semiconductors is provided in Section 2.3. The thin films prepared from these are used in OLEDs for which Section 2.4 covers the basic working principle and typical loss mechanisms. Finally, the main techniques of characterization in this work rely on scattering methods. Therefore, the underlying principles together with aspects of data analysis of the used scattering techniques are provided in Section 2.5.

2.1 Diblock Copolymer Assisted Sol-Gel Synthesis

The upcoming section covers the basics of diblock copolymer assisted sol-gel synthesis, which is used for ZnO sample preparation for Chapter 5. In the following, some basic aspects about the micro-phase separation of diblock copolymers is given in Subsection 2.1.1. The high degree of order caused by phase separation in such a system can be combined with common sol-gel synthesis, which yields a nanoparticle network consisting of metal oxides (Subsection 2.1.2). By combining both approaches, as described in Subsection 2.1.3, a highly ordered metal oxide network can be obtained for which structural length scales can be tailored to fit the desired morphology.

2.1.1 Diblock Copolymers

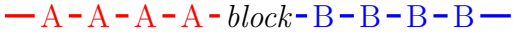

Figure 2.1
Diblock copolymer PA-*b*-PB.

Copolymers describe a group of special designed polymers, consisting of different kinds of monomers A and B. The order and sequence of the linked monomers has a large impact on the final behavior of the copolymer. In the case of a diblock copolymer, the two monomers form different homopolymers which are covalently linked together in order to build a linear chain, as depicted in Figure 2.1. The resulting copolymer is named accordingly as polyA-*block*-polyB or short PA-*b*-PB. The block ratio f_A of such a copolymer depends on the different degree of polymerization N_A and N_B of each block and is calculated according to

$$f_A = \frac{N_A}{N_A + N_B} \tag{2.1}$$

$$f_B = \frac{N_B}{N_A + N_B} = 1 - f_A, \tag{2.2}$$

with the total degree of polymerization $N = N_A + N_B$. In general, different polymers are not miscible and consequently phase separate in order to minimize their interfacial area. The chains of the respective homopolymers agglomerate and specific domains are formed. For a blend of homopolymers, pure separate phases occur, which becomes apparent on a macroscopic scale with domain sizes in the order of several micrometer.[31] In contrast, in the case of covalently bound copolymers, the domain size is restricted to typically less than a micrometer, depending on the degree of polymerization of the respective homopolymers. Their block lengths on the other hand govern the domain structure. This process is referred to as micro-phase separation.

In addition to the total degree of polymerization N and the fraction of both blocks f, the interaction parameter χ is necessary to describe the phase separation in detail. According to the Flory-Huggins theory, the interaction parameter describes the miscibility of two materials and therefore can be used in order to describe the interaction between the two blocks of such a copolymer.[32,33] The mentioned interaction parameter calculates as

$$\chi = \chi_S + \frac{\chi_H}{k_B T} \tag{2.3}$$

with the Boltzmann constant k_B, the temperature T, and the entropic and enthalpic part of the Flory-Huggins parameter χ_S and χ_H, respectively. The entropic component χ_S considers contributions from the chain ends and the chain conformations. For diblock copolymers, the contribution from the entropic part is more significant as the end-to-end distance of the copolymer is longer compared to the single homopolymer chains. Hence, the Flory-Huggins interaction parameter for a diblock copolymer χ_{A-b-B} is always equal or greater than for a blend of the corresponding homopolymers,

χ_{A+B}. In general, a small value of χ correlates to higher miscibility of the two materials, and therefore allow a mixed phase. Thus, with increasing χ the polymers start to repel each other and tend to minimize their surface energy by phase separation. This is in accordance to the typically enhanced solubility of most polymers with increasing temperature, as the enthalpic part χ_H in Equation 2.3 is reduced for elevated temperatures.

For very short chain lengths or weak interaction of the monomers, the diblock copolymer becomes a homogeneous melt without any ordered structure. This becomes apparent in the exemplary phase diagram for diblock copolymers, depicted in Figure 2.2, where the relation between the domain structures and the block lengths is visualized. Here, the parameter χN decides the degree of phase separation of a diblock copolymer. The green line represents the order-disorder transition (ODT) between the mixed phase and ordered structure. According to mean-field calculations performed by Leibler[34] and Bates et al.,[35] the diblock copolymer is present in a disordered mixed phase for $\chi N \ll 10.5$. They showed for a symmetric copolymer with $f_A = 0.5$ the occurrence of a critical point at $\chi N = 10.495$ (Figure 2.2, pink dot). At this so-called weak segregation limit (WSL), a phase transition from a disordered state to an ordered lamellar structure happens with increasing χN. With further increase, the separation becomes more distinct and the order of the structure is enhanced in the so-called strong segregation limit (SSL) for $\chi N \gg 10.5$.[31,34,35] Around the mean-field critical point, small changes in either the polymer environment (χN) or the fraction of chain lengths (f_A) results in different structures. Therefore, various morphologies ranging from BCC ordered spheres, over hexagonal ordered cylinders to gyroids and lamellar structures are available around the WSL, as depicted in Figure 2.2a-g.

In reality, the chemical difference of the monomers A and B results in asymmetric phase diagrams. In addition, conformationally different polymer blocks, crystallization effects or geometric limitations (confinement), e.g., going from bulk to thin films, further influences the phase separation that intensifies the asymmetry of the phase diagrams.

2.1.2 Basic Principles of Sol-Gel Synthesis

Sol-gel synthesis describes a wet chemical solution-based synthesis route, which has been initially developed for the synthesis of inorganic metal oxides such as silica networks and carbon based materials in a solution medium.[37] In the last years, this technique has been adapted for the development of nanostructures based on inorganic metal oxide semiconducting materials such as TiO_2 and ZnO.[38,39] The sol-gel process itself is classified as bottom-up approach where a structured network consisting of the given material is established from initially small molecules, that are typically the precursors for the desired material. Generally, the desired material is functionalized with an organic group R, obtaining metal alkoxides as precursors. The resulting precursors

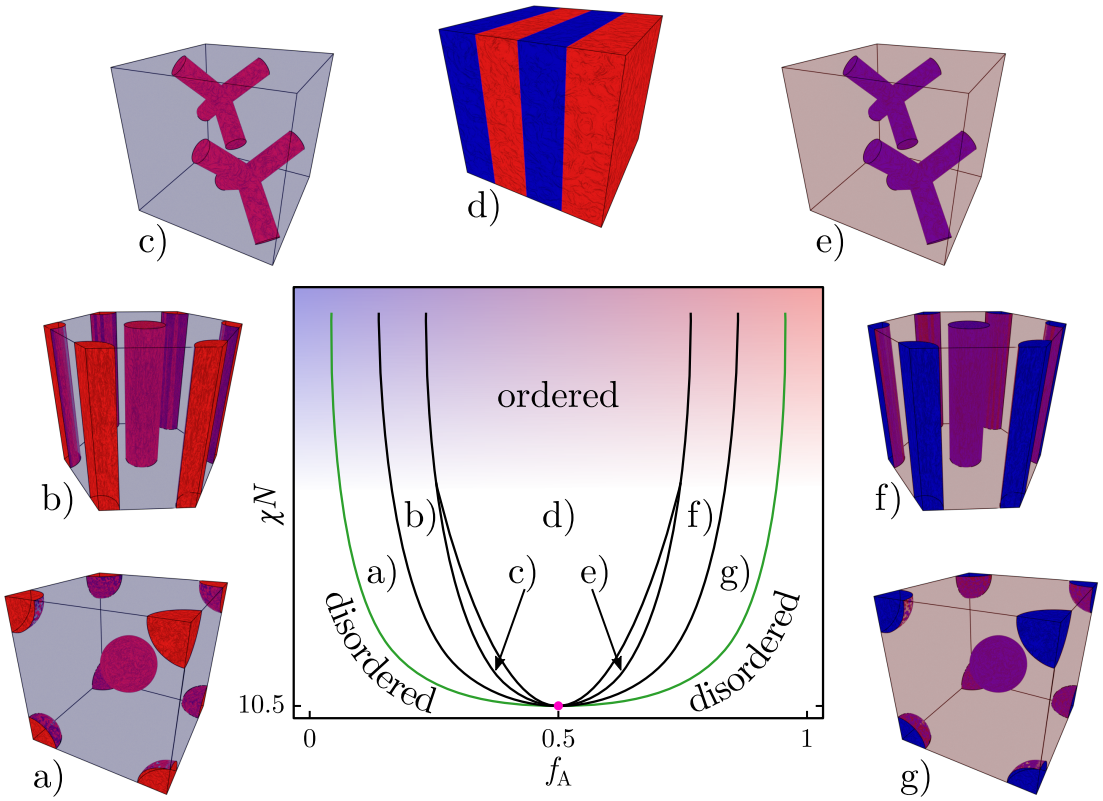

Figure 2.2
Exemplary phase diagram of a conformationally symmetric diblock copolymer melt of the form PA-*b*-PB. Depending on the ratio of both blocks, the phase separation leads to different structures according to mean-field calculations.[34–36] With increasing block ratio f_A of block A, the structure of the A-domains inside the matrix of block B is changing from (a) spheres (BCC) via (b) hexagonally packed cylinders to (c) an ordered bicontinuous gyroid network. For an approximately equal fraction of the two blocks, (d) a lamellar structure is formed. With further increase of f_A, the morphology inverts to structures of the B-block embedded in a matrix of A, changing again from (e) an ordered bicontinuous gyroid network via (f) hexagonally packed cylinders to (g) spheres (BCC). The green line marks the order-disorder transition (ODT) below which the polymeric system is present in a mixed phase. The pink dot at $\chi N = 10.495$ and $f_A = 0.5$ represents the mean-field critical point.

interact with the solvent and subsequently undergo hydrolysis, as exemplary given in Equation 2.4 for a ZnO precursor

$$(\mathrm{RCOO})\mathrm{Zn}{-}\mathrm{OOCR} + \mathrm{H_2O} \overset{\text{hydrol.}}{\rightleftharpoons} (\mathrm{RCOO})\mathrm{Zn}{-}\mathrm{OH} + \mathrm{RCOOH}. \tag{2.4}$$

In the present case of ZnO, an acetate containing precursor is used, namely ZAD, which is described later on page 50. A big advantage of the sol-gel approach is the large variety of available materials that allow the fabrication of different metal oxide layers such as TiO_2.[40,41] The nanoparticles generated by the hydrolysis reaction with the precursor form a so-called *sol* in the provided solution. The obtained nanoparticles then induce secondary reactions, more precisely water and alcohol condensation (acid for acetate group containing precursors such as ZAD), as exemplary given for the ZnO system in Equation 2.5 and 2.6, respectively.

$$(\mathrm{RCOO})\mathrm{Zn}{-}\mathrm{OH} + \mathrm{HO}{-}\mathrm{Zn}(\mathrm{OOCR}) \overset{\text{cond. 1}}{\rightleftharpoons} (\mathrm{RCOO})\mathrm{Zn}{-}\mathrm{O}{-}\mathrm{Zn}(\mathrm{OOCR}) + \mathrm{H_2O} \tag{2.5}$$

$$(\mathrm{RCOO})\mathrm{Zn}{-}\mathrm{OH} + (\mathrm{RCOO}){-}\mathrm{Zn}(\mathrm{OOCR}) \overset{\text{cond. 2}}{\rightleftharpoons} (\mathrm{RCOO})\mathrm{Zn}{-}\mathrm{O}{-}\mathrm{Zn}(\mathrm{OOCR}) + \mathrm{RCOOH} \tag{2.6}$$

These reactions result in a cross-linking of the hydrolyzed nanoparticles, obtaining a 3D network in the solution. As the network is formed in solution, the remaining solvent gets trapped in the created pores and consequently forms a *gel*. It is noteworthy to mention that the described hydrolysis and condensation reactions 1 and 2 take place at equilibrium conditions in the sol-gel solution. The pore size of such a network highly depends on the reaction environment and is tunable in the sub-micrometer range via adjusting the reaction parameters. Literature has shown that the adjustment of reaction temperature, concentration, pH-value, or humidity influences the reaction kinetics resulting in the formation of varied length scales in the nanostructured network.[42] Furthermore, the reaction rate is strongly related to the size of the precursor molecules. Larger molecules have distinctly slower reaction kinetics compared to smaller ones, as shown by Rivallin et al.[43] However, the length scales available by the sol-gel approach via adjusting the processing parameters is limited. Additionally, the obtained nanostructures are typically ill-defined, which raise the need for additional templating of the bottom-up approach. The sol-gel solution containing the synthesized nanoparticles allow the use of solution processable deposition techniques such as spin coating, spray coating or roll-to-roll printing.

Typical available precursors result in an amorphous network in the final films. Therefore, a high temperature treatment is required in order to impart crystallization of the nanoparticles and remove the residual solvent. In the case of ZnO, typically a calcination temperature of 400 °C is used. However, ongoing research proofed the realization of low temperature routes, based on specially designed precursors such as ethylene glycol-modified titanate (EGMT) for TiO_2 films that provide already crystallized nanoparticles after deposition.[44] Further information about the sol-gel process in general can be found in literature.[45,46]

2.1.3 Introducing Copolymer Templates

In order to overcome the length scale limitations of sol-gel chemistry approaches and to enhance the order of the obtained network, an additional structure directing template can be applied. In the present thesis, diblock copolymers are introduced into the sol-gel solution to serve as a template. Thus, their high degree of order is combined with the sol-gel process, providing a tunable enhanced structure of the final films.

Typically used diblock copolymers are amphiphilic in nature and consist of a hydrophobic and a hydrophilic block, covalently linked at one end to a linear chain. By selecting an appropriate precursor/copolymer combination, selective accretion of the sol-gel on one of the blocks is provided, which allows tailoring of the nanoparticle network. In the present thesis, PS-*b*-PEO in combination with the precursor ZAD is used, as it provides the required selectivity for the hydrophilic block (PEO). As described in Subsection 2.1.1, such copolymers undergo a phase transition from disordered to ordered state for $\chi N > 10.5$. The induced micro-phase separation makes differently ordered morphologies accessible, such as spherical, cylindrical, gyroid, or lamellar structures.

To benefit from the high order of the copolymer and obtain the mentioned structures in solution, the interaction parameter χ can be adjusted by introducing a suitable pair of solvents. Due to the amphiphilic behavior of the different blocks, one of the solvents has to be selected in order to provide good solubility of both blocks. In such a commonly called *good* solvent, both blocks are equally well dissolved and are present in a relaxed, extended state. The other solvent needs to be a selective solvent, commonly phrased as *bad* solvent, which is only miscible with one of the blocks. The addition of the selective solvent leads to a series of complex thermodynamic processes, in which one of the blocks tend to minimize its surface area to the *bad* solvent, which leads to an agglomeration of the respective blocks of the copolymer. As a result, micelles are formed in solution, in which the non-dissolved blocks form the micellar core. The well-dissolved blocks remain in a stretched state and form the extended shell, screening the other blocks from the selective solvent environment. In the present thesis, a polar selective solvent is used in order to serve as *bad* solvent for the non-polar PS block, whereas the hydrophilic PEO block remains dissolved. Therefore, the hydrophobic PS

block forms the inner core, whereas the hydrophilic PEO block builds up the micellar shell, as exemplarily depicted in Figure 2.3.

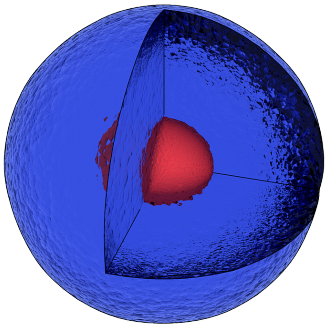

Figure 2.3
Graphical representation of a PS-*b*-PEO micelle.

The obtained micelles provide a phase separation on the nanoscale, which is used in the present study for nanostructuring of metal oxides. Depending on the different weight fractions of the solvent system, micelles of different sizes are obtained, that can further interact with each other and undergo fusion and separation with one another. Here, the selectivity of the diblock copolymer towards the precursor is of importance. In the present study, the hydrophilic block preferentially hosts the precursor nanoparticles via hydrogen bonds in combination with electrostatic and van-der-Waals interactions. The incorporation of the precursor nanoparticles in one of the polymer blocks in turn, results in its selective swelling. Additionally to the micelle formation of the diblock copolymer, the sol-gel process happens in the same time as described in Subsection 2.1.2. This leads to a formation of metal oxide colloids which further cross-link to different micelles. Thus, an expanded ordered network of nanoparticles directed by the skeletal structure of the diblock copolymer is obtained. Furthermore, various metastable structures can be formed in solution, caused by different equilibrium conditions in the system.[47] By adjusting the block length of the used copolymers as well as the weight fractions of the solvents and the precursor, a high degree of control of the accessible length scales is achieved. Additionally, the reaction environment that can be adjusted via parameters such as the pH-value or the temperature, provide enhanced flexibility to manipulate the length scales derived from the system, and therefore the final structure of the films.

As mentioned earlier, the chemical and physical environment of the copolymer/sol-gel mixture has a strong impact on the reactions occurring in the solution and therefore the final structure. Thus, it is reasonable that different kind of deposition of the solution on the substrates may result in structural variations in the final film morphology. This is caused by the different equilibration of the rearrangement processes on the film after deposition with respect to the drying time provided by a particular method. The polymer/sol-gel composite solution shows mainly two opposing processes modifying the final film morphology. Namely, the cross-linking tendency among the colloidal nanoparticles created by the sol-gel process and the interaction among the copolymer molecules forcing a micro-phase separation. In case the former process dominates, the obtained structure is less ordered and resembles common morphologies obtained by a pure sol-gel process. On the contrary, for the latter case, a more ordered morphology is obtained if the rearrangement of the polymer chains dominates. The structure directing influence of the polymeric matrix also depends on the size and distribution of the provided nanoparticles. On one hand, low nanoparticle concentrations result

in a high mobility, yielding the formation of large aggregates in the final films. Very high concentrations on the other hand, lead to a more homogeneous distribution of the nanoparticles along the polymer matrix, which results in a connected metal oxide network.[40] Additional treatment of the deposited composite film such as solvent vapor annealing may further influence the final film morphology.

As mentioned in Subsection 2.1.2, typically a high temperature treatment in ambient atmosphere is required to obtain crystallized structures. Calcination of the composite film has the additional effect of combusting the polymer scaffold, leaving behind the pure metal oxide network. However, low temperature routes, such as the use of EGMT as precursor for TiO_2, allow for less energy demanding polymer extraction methods, such as decomposition of the copolymer by UV light or removal by solvent extraction.[48,49] It is noteworthy to mention that any of these methods for removal of the template from the system might lead to modification of the surface properties of the films. Furthermore, the removal of the polymer matrix might cause a collapse of the established metal oxide network, which would result in a shrinkage of the deposited material.[50]

Overall, the diblock copolymer assisted sol-gel approach provides a high degree of control over the obtainable length scales and morphologies of metal oxide thin films. The large variety of available copolymers and metal oxide precursors allow a high degree of freedom in designing and structuring functional layers for a manifold of applications. Furthermore, by choosing different polymer block lengths and precursor concentrations as well as adjusting the processing parameters, the functional layer morphology can be further optimized, e.g., for exciton separation in OPV applications.[47] Being a solution based approach, further flexibility is provided by the large number of available deposition techniques such as spin coating or spray deposition. In addition, the solution processibility in combination with a suitable deposition technique allows an easy upscalability in order to fabricate such metal oxide layers for commercial applications on large scale. Moreover, the synthesis can be extended with further templating methods in order to achieve hierarchical structuring, as investigated in the present study.

2.2 Swelling of Polymer Thin Films

The following section covers some of the theoretical aspects required for the examination of the swelling behavior of polymer thin films in Chapter 6. Swelling of a thin film can be described by the absorption of a solvent, which is well miscible with a part or component of the film. The miscibility can be described according to the Flory-Huggins theory[32,33] with an interaction parameter χ. In general, the incorporation of solvent molecules into a material leads to a volume increase. As for thin films the volume expansion is preferred into the direction of the surface normal, film swelling can be observed. The increase in the relative thickness $d(t)/d_0$ can be observed via several methods such as WLI, XRR, or NR, as long as the time resolution is capable

to follow the thickness changes. In the present thesis, ToF-NR is selected in order to follow the swelling kinetics, as it allows for monitoring the thickness change and the SLD_N change independently from each other. By selecting an appropriate solvent, such as D_2O, with a high SLD_N difference to the film, the material composition can be determined, which translates to the amount of absorbed solvent by

$$\Phi_{solv}(t) = \frac{SLD(t) - SLD_{init}}{SLD_{solv} - SLD_{init}}, \tag{2.7}$$

with the SLDs of the swollen film ($SLD(t)$), of the pure solvent (SLD_{solv}), and of the initially dry film (SLD_{init}). The solvent incorporation together with the film thickness holds information about the swelling kinetics and the dynamic processes in the thin film. The used solvents in the present study are H_2O and D_2O and therefore are denoted in the following as water.

The water content and relative thickness increase for thin films obtained from ToF-NR measurements are described according to a humidity sensitive model introduced by Magerl et al.[51] The swelling model takes into account an intrinsic swelling process, which describes a swelling driven by diffusion of the evaporated solvent molecules into the film. The diffusion driven swelling can be described by an exponential function[52]

$$\frac{d(t)}{d_0} = \frac{d_\infty}{d_0} - \left(\frac{d_\infty}{d_0} - 1\right) B \exp\left(-\frac{t}{\tau}\right). \tag{2.8}$$

Here, d_∞/d_0 describes the maximum swelling ratio the film is able to reach for a given relative humidity. d_0 is the initial film thickness and $d(t)$ is the measured film thickness at a given time t. The specific time constant of the diffusion of the solvent molecules into the polymer film is denoted as τ. The parameter B takes into account the sample's geometry and reaches for thin films in the first order typical values of $B \approx 0.6$.[52] The swelling process is time dependent and reaches for an infinite time t asymptotically a saturation state, for which the concentration gradient of the solvent molecules equilibrates with the absorption of the solvent molecules in the film. The maximum swelling ratio can be derived from Equation 2.8 as

$$\frac{d_\infty}{d_0} = \frac{\frac{d(t)}{d_0} - B \exp\left(-\frac{t}{\tau}\right)}{1 - B \exp\left(-\frac{t}{\tau}\right)}. \tag{2.9}$$

The absorption of evaporated solvent molecules by a polymer can be regarded as a dissolution process similar to that in liquid solvents. Thus, the equilibrium sorption and therefore the maximum swelling at saturation of a polymer at a certain relative humidity p/p_{sat} of water vapor can be described by regular solution theory[53] as

$$\ln\left(\frac{p}{p_{sat}}\right) = \ln\left(1 - \frac{d_0}{d_\infty}\right) + \left(1 - \frac{V_{water}}{V_{polymer}}\right)\frac{d_0}{d_\infty} + \chi_{eff}\left(\frac{d_0}{d_\infty}\right)^2, \tag{2.10}$$

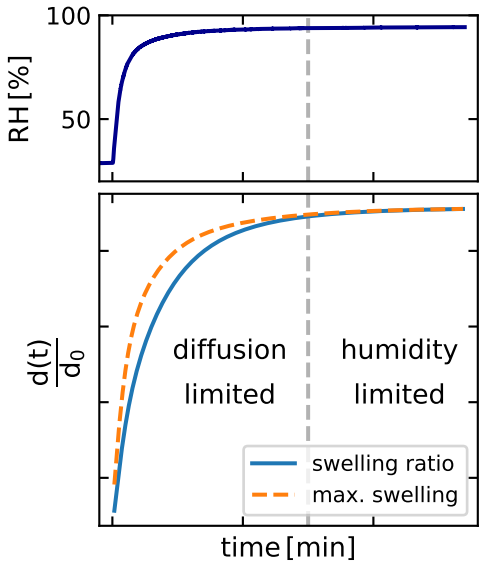

Figure 2.4
Exemplary plot of the applied swelling model (bottom) for a fast increasing relative humidity (top) saturating around ~95 % relative humidity. The difference of the maximum achievable swelling (dashed orange) to the measured swelling ratio (blue) is caused by the diffusion of the solvent molecules into the polymer thin film. Thus, for a rapid increasing relative humidity in the beginning, the swelling is limited by the diffusion of the solvent molecules into the polymer network. If the humidity increase slows down and the relative humidity approaches an equilibrium state, the swelling is mainly dominated by the small humidity changes.

where d_0 and d_∞ are the initial and the maximum film thickness at equilibrium conditions, respectively. V_{water} and V_{polymer} describe the molar volumes of water and the polymer. As polymers typically show a large molar volume compared to the solvent, the fraction becomes in practice ${}^{V_{\text{water}}}/_{V_{\text{polymer}}} \approx 0$ and therefore can be neglected. As further effects such as the interaction of the solvent with the substrate cannot be neglected and easily be separated, the interaction of the solvent with the polymer is denoted with the effective Flory-Huggins interaction parameter χ_{eff}. As seen in Subsection 2.1.1, a small interaction parameter translates to good miscibility of the components, in this case the polymer and water, and therefore is an indication of the polymer film's hydrophilicity.

In the case of swelling experiments, the relative humidity rises and no equilibrium conditions are present. Thus, the swelling is coactive driven by diffusion of the solvent molecules into the polymer film and the rising humidity, which increases the evaporated solvent concentration in the samples environment. Both contributions are considered by combining Equation 2.8 and 2.10 in an implicit function that can be solved numerically to obtain the fitting parameters τ, χ_{eff} and B. In practice, the required relative humidity ${}^{p}/_{p_{\text{sat}}}$ is simultaneously tracked and reproduced by a set of exponential functions in order to interpolate the measured humidity data to match the time evolution of the relative thickness and SLD_N measurements.

An exemplary solution of the swelling model along with the corresponding maximum swelling ratio and the related relative humidity changes are depicted in Figure 2.4. In the beginning of the swelling experiment, the relative humidity increases faster than the solvent molecules can diffuse into the thin film. Therefore, the swelling ratio is in the beginning limited by diffusion and follows predominantly Equation 2.8, which is responsible for the delayed film response. As soon as the relative humidity reaches an

equilibrium state, diffusion of the solvent molecules into the thin film happens on a faster time scale than the humidity changes in the atmosphere. Thus, at this stage, the swelling ratio is limited by the relative humidity and follows Equation 2.10.

Due to the adhesive forces of thin films to the substrates, the film swelling is mainly restricted into the direction of the surface normal, which becomes apparent in a thickness increase. Therefore, the swelling ratio of Equation 2.8 translates to the polymer volume fraction and is related to the water content $\Phi_{\text{water}}(t)$ in the thin film by[51]

$$\frac{d(t)}{d_0} = \frac{1}{1 - \Phi_{\text{water}}(t)}. \tag{2.11}$$

This relation enables the use of the above described swelling model on the measured water content derived from SLD_N values via Equation 2.7. Therefore, the effective Flory-Huggins interaction parameter and the diffusion time constant can be further verified.

2.3 Organic Semiconductors

In the last decades, polymers have been proven as very versatile to tailor materials with specific mechanical or thermodynamic properties, which is originated in the infinite possible combinations of organic molecules. In general, polymers are considered as electrically well insulating and chemically stable and therefore are often used for encapsulating or insulating electronic circuits. However, chemical composition of some polymers enables charge transport under certain conditions. Heeger, MacDiarmid and Shirakawa reported in 1977 about an increase in electrical conductivity in the simple polymer polyacetylene upon iodine vapor exposure. The chemical doping revealed a conductivity increase of seven orders of magnitude and leads to an metal-insulator transition in the conjugated polymer. These observings proved to be an important step for understanding the generation and transport of charge carriers in polymers. Hence, these processes are of utmost importance to understand the electrical conductivity in polymers. The simple chemical structure and high periodicity of polyacetylene makes it to an ideal case study for understanding the properties of such semiconducting polymers. The theoretical background regarding the band structure formation and charge carrier transport is given in the following section.

2.3.1 Band Structure in Polymers

An important factor for the conductivity in polymers is the hybridization of the carbon atoms of the polymer backbone. The four valence electrons of a carbon atom are unequally filled into the $2s$ and two of the $p_{x,y,z}$-orbitals. As it is energetically more favorable to distribute these electrons homogeneously, three equally filled sp^2 hybrid

orbitals are formed. Those hybrid orbitals are energetically equivalent and planar distributed, leaving behind a single p_z-orbital, each orbital filled with one electron. The hybrid orbitals then contribute to σ-bonds, while the single electron in the p_z-orbital enables more stable π-bonds. With increasing chain length, the number of π-bonds is increased, leading to a conjugated π-electron system along the polymer backbone, which is the origin for its semiconducting behavior. As a result of the long sequence of conjugated bonds, a 1D crystal is obtained in which each carbon atom contributes with one electron to the delocalized π-electron system.

In the ideal case of an infinite long linear chain, all bonds between the carbon atoms reveal an equivalent distance of a that leads to equally distributed electrons over the whole chain. These delocalized electrons behave nearly as free electrons and therefore form a parabola shaped dispersion relation $E_n(k) \propto k^2$, as depicted in Figure 2.5a. The periodic sequence of the carbon atoms (ions) with distance a reveals periodic fluctuations in the electron density. Thus, charge density waves are formed that allow collective transport of charge carriers along the chain. The interference of different wave functions at the intersection of higher order Brillouin zones (BZs) leads to the degeneration of the states. Therefore, the group velocity of these charge density waves becomes $v_{n,k} \propto \frac{\partial E_n(k)}{\partial k} = 0$ at the end of the BZ and nodes of standing waves are formed, which flattens the dispersion relation at the BZ's edge. As each carbon atom is contributing one electron to the π-electron system, the energy band in Figure 2.5a is half filled and charge transport is enabled.

However, according to the Peierl's instability theorem, such a 1D chain with equally spaced ions, contributing one electron each, is unstable. The formation of a binding (π) and anti-binding (π^*) molecule orbital is energetically favored in comparison to separated equitable atomic orbitals. Therefore, already a small distortion δ is sufficient to deflect one of the ions and form alternating spaced bonds with $a \pm \delta$. This so-called Peierl's transition or dimerization leads to a new periodicity with doubled lattice spacing $2a$, which in turn results in a bisected BZ, as depicted in Figure 2.5b. As the total number of available electrons is not changed, the newly created band is completely filled while all states in the 2nd order band are unoccupied, corresponding to the π- and π^*-orbitals, respectively. As the wave functions form again nodes at the newly created BZ's edge, the energy dispersion flattens and creates an energy gap in between. This bisection of the BZ results in small energy savings that favors this state in comparison to an equally spaced chain. The energy savings and therefore the size of the energy gap is limited by the elastic cost of the lattice/polymer chain which is required to rearrange the lattice. However, the Fermi level is now located in the newly created energy gap, which conforms the base of the semiconducting properties of the polymer and explains their generally insulating behavior

As analogous to classical inorganic semiconductors, the formation of the energy gap defines two energy bands. According to the theoretical approach of the linear combination of atomic orbitals (LCAO), the overlap of neighboring p_z atom orbitals results in

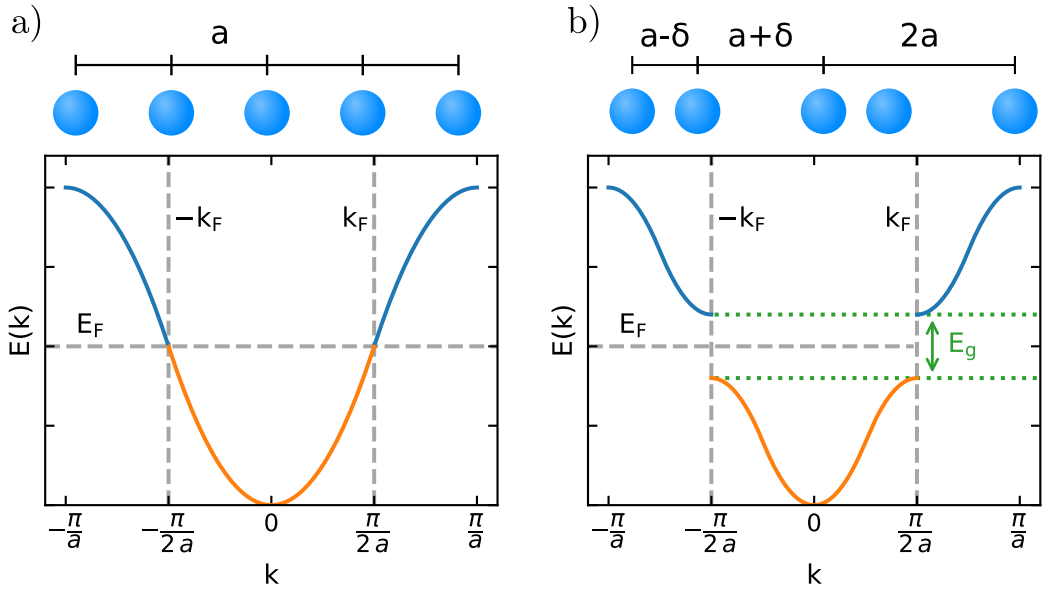

Figure 2.5
Schematic illustration of the band structure in polymers derived via the Peierl's instability theorem. a) Band structure of a one-dimensional equidistant metal chain. b) Dimerization leads to formation of a superstructure which cuts the BZ into half and creates an additional energy band gap E_g at $|k_\mathrm{F}| = \frac{\pi}{2a}$. Sketches of the corresponding 1D chain with lattice spacing a and $2a$ are depicted above.

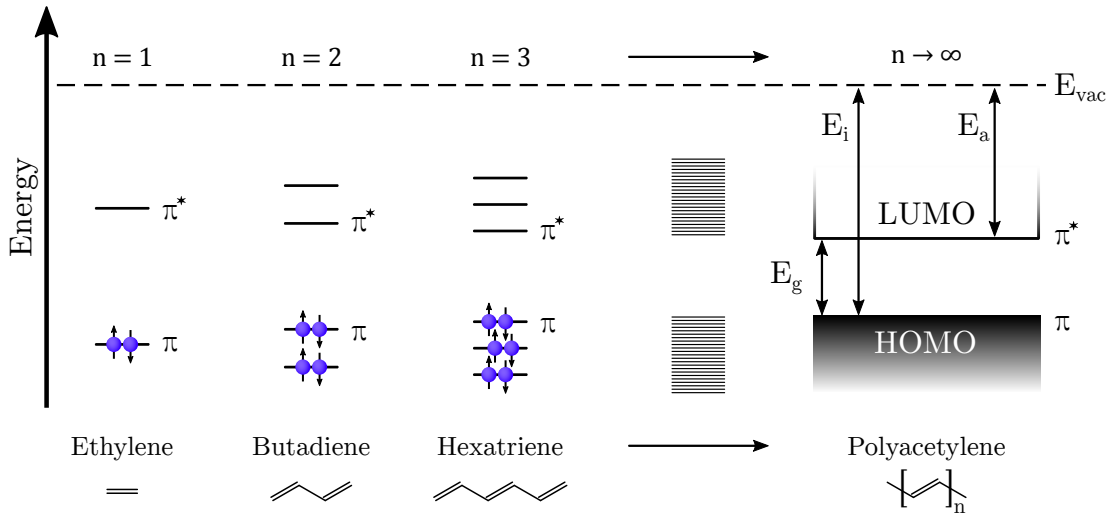

Figure 2.6
Formation of band structure derived from LCAO. For a large number of coupled units, HOMO and LUMO states forming energy bands separated by a band gap E_g, an ionization energy E_i and an electron affinity E_a with respect to the vacuum energy level E_vac (inspired from Schaffer[54]).

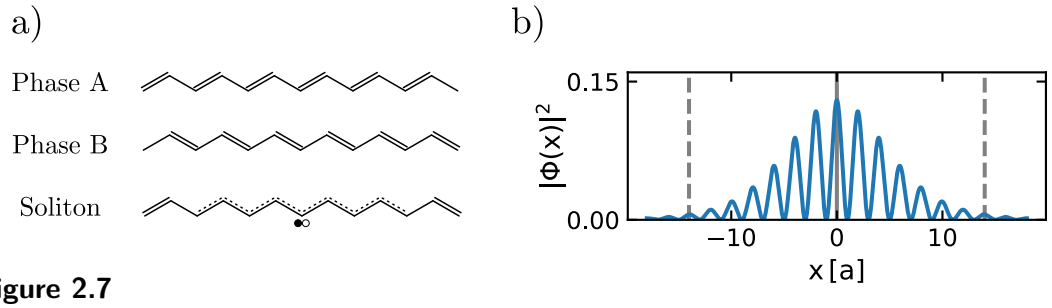

Figure 2.7
a) Both mesomeric ground states of polyacetylene leading to a soliton formation at the meeting point of phase A and B (exemplary sketch). b) The calculated probability distribution $|\Phi_0(x)|^2$ of the soliton extends over ~14 carbon atoms in each direction.[55]

two different solutions of the corresponding Schrödinger equation. The obtained wave functions describe the earlier mentioned binding (π) and anti-binding (π^*) molecule orbitals, that are located at lower and higher energy with respect to the single p_z-orbitals, respectively (n = 1 in Figure 2.6). With further polymerization, the number of carbon atoms and therefore the number of π- and π^*-orbitals is increased. As each carbon atom undergoes this process twice, one for each of its neighbors, the amount of states is doubled. With increasing chain length and degree of polymerization, the number of π/π^*-orbitals is consequently increased, while the corresponding binding and anti-binding states show a closer packing, separated by an energy gap. For an infinite long chain, the binding and anti-binding states merge, forming the so-called highest occupied molecular orbital (HOMO) and lowest unoccupied molecular orbital (LUMO), which are equivalent to the valence and the conduction band for inorganic semiconductors ($n \rightarrow \infty$ in Figure 2.6). Consequently, the HOMO and LUMO are separated by the energy band gap E_g.

2.3.2 Charge Transport in Polymers

Charge Carrier Generation

According to the Peierl's instability theorem and the LCAO approach in the previous section, the HOMO and LUMO bands of polymer chains are separated by an energy gap. As the Fermi level is located in between this energy gap, no charge transport is possible and the polymer is referred as insulating or semiconducting material. However, the natural appearance of charge carriers in polymers is mainly related to defects in the polymer structure created by bonding irregularities, kinks or chemical defects and so forth. The simple linear chain of polyacetylene makes it again a suitable case study for charge carrier creation in polymers.

Polyacetylene generates a conjugated π-electron system consisting of alternating single and double bonds. Thus, two degenerated ground state configurations are present, depicted in Figure 2.7a as phase A and B. The double and single bonds can swap and

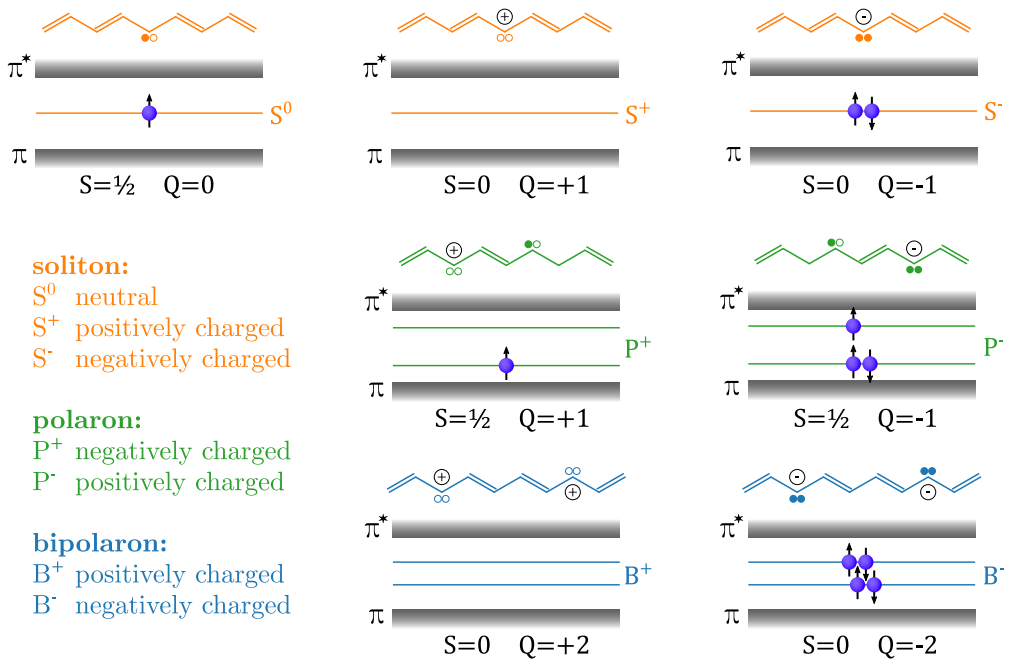

Figure 2.8
Overview of main charge carriers present in conducting polymers on the example of polyacetylene. Top row shows neutral, positive and negative charged solitons with their corresponding total spin S and charge Q. By combination of several solitons, further quasiparticles (QPs) are created as shown in the second (polarons) and third (bipolarons) row (adapted from Palumbiny[56]).

both phases can transform in each other one. The meeting point of the different phases reveals a defect in the polyacetylene chain, leaving behind a single unpaired electron, which forms a quasiparticle (QP) state. The negative charge of the generated radical and the positive charge of the corresponding carbon nucleus cancel out and the QP state is consequently named as neutral soliton (S^0). Therefore, the net charge of the neutral soliton is Q = 0, while the total spin is S = $^1/_2$. According to the Su-Schrieffer-Heeger (SSH) theory, named after Su, Schrieffer, and Heeger, the created QP state is located in between the energy gap of the HOMO and LUMO bands.[55] Thus, the unpaired electron provides an unoccupied QP state that enables electrical conductivity along the polymer chain. The soliton can be described as a charge density wave, that is able to travel along the chain, as mentioned in Subsection 2.3.1. According to the SSH theory it is expanded over ~14 carbon atoms,[55] as depicted in Figure 2.7b. Furthermore, the effective mass of a soliton is found to be ~6× the mass of a free electron m_e. Due to a small activation energy of ~2 meV $\ll k_B T$, solitons are widely present at room temperature and will eventually meet.

Removal of the unpaired electron from the chain by, e.g., an oxidizing agent, yields a positive net charge. Consequently, a positive charged soliton with a total spin of S = 0 is created. Similarly, by adding an electron to the neutral soliton, e.g., by a reducing

agent, a negatively charged soliton (S^-) is formed. Coupling of different solitons leads to the formation of further QPs, such as polarons ($P^{+/-}$) and bipolarons ($B^{+/-}$), or annihilation of the QP state. In contrast to solitons, only charged QPs of higher order are possible. In Figure 2.8, an overview of the most common charge carriers present in polyacetylene is provided. It is noteworthy to mention that polarons are typically the dominating kind of charge carriers present in conducting polymers. Even polyacetylene is an ideal candidate for showing the generation of QP charge carriers, due to the degenerated ground state, it is also the only polymer where the creation of solitons is possible.

The generation of charge carriers, and therefore the available states that contribute to electrical conductivity, can be increased by doping of the polymer. To do so, typically oxidizing agents are introduced in order to form positively charged polaronic and bipolaronic states along the polymer chain. Even the creation of negatively charged QPs is possible via application of reducing agents, it typically requires more complex systems which are further less chemically stable. Therefore, p-doped organic semiconductors are more popular. This process is commonly referred as *primary doping* of polymers and thus charge transport along the chain is favored. In the case of polyacetylene, the presence of iodine vapor led to an increase in electrical conductivity of seven orders of magnitude.[2] However, in contrast to inorganic semiconductors where only a small amount of dopants are necessary in order to enhance the conductivity significantly, for organic semiconductors much larger amounts are required. For example in the case of PEDOT:PSS, which is subject of investigation in the present thesis, the mixing ratio of PEDOT and the dopant PSS is close to 1.

Charge Transport Mechanisms

Charge carrier transport of QPs along a conjugated polymer backbone and ordered crystals is considered as highly efficient. This band-like transport is well described via the earlier mentioned SSH theory, in which highly delocalized QPs move freely along the polymer chain.[55] Similarly to inorganic semiconductors, this type of charge transport highly depends on the order of the system and therefore is limited by permanently or temporarily chain defects. This includes for example kinks and chain ends or phonons, respectively. The interaction of the QPs with lattice vibrations is responsible for the decrease in conductivity with rising temperature, as the coherent charge transport along the chain is altered.

The band-like transport depends on the size of the extended π-electron system, which is related to the order of the whole system. As (semi-)conducting polymers show typically a high amount of amorphous or semicrystalline regions, the band-like transport is limited to microscopic regions. The distribution of such crystalline regions in an amorphous polymer matrix results in an energy landscape with locally defined domains of band-like transport. The small variations in the energy landscape are

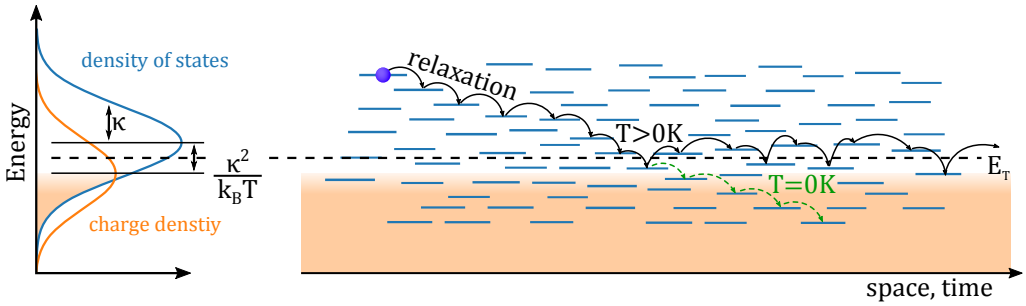

Figure 2.9
Graphical representation of the hopping transport in polymers. Hopping transport occurs between localized states with a Gaussian energy distribution and disorder parameter κ (blue). Density of states (DOS) is partially occupied and reveals so-called steady-state charge distribution with its center shifted by $\kappa/k_\mathrm{B}T$ (orange). Excited charge carriers undergo relaxation by downwards hopping to trap states (T = 0 K). Hopping upwards is thermally activated (T > 0 K) and leads to charge transport around the effective transport energy E_T (adapted from Deibel et al.[62]).

typically described via the Bässler model, in which the energy states are Gaussian distributed and charge carriers require a small amount of energy to tunnel from one site to another.[57,58] The probability for tunneling between adjacent sites was first described in terms of a hopping rate by Marcus,[59,60] while Miller and Abrahams followed a similar approach.[61]

$$v_{ij} = v_0 \exp\left(-2\,\gamma\,\Delta R_{ij}\right) \begin{cases} \exp\left(-\dfrac{\epsilon_j - \epsilon_i}{k_\mathrm{B}\,T}\right) & \text{for } \epsilon_j > \epsilon_i \\ 1 & \text{for } \epsilon_j \leq \epsilon_i \end{cases} \tag{2.12}$$

Hereby, v_0 is a model prefactor, γ the inverse localization radius, and R_{ij} the distance between two sites i and j, with their corresponding energy $\epsilon_{i,j}$. The first term in Equation 2.12 describes the tunneling probability, whereas the second part contributes with a temperature dependent hopping probability. Thereby, if the energy of the target site exceeds the one of the starting site ($\epsilon_j > \epsilon_i$), the probability of tunneling is enhanced for higher temperatures, while the tunneling is independent on the temperature in case the target site has lower energy ($\epsilon_j \leq \epsilon_i$) and relaxation occurs. This process is commonly referred to as *hopping transport* and is found to be a good approximation for describing the macroscopic charge carrier mobility in organic semiconductors.

However, both processes of band-like and hopping transport contribute to the macroscopic conductivity. Which mechanism dominates, is related to the morphology and crystallinity of the polymer. Thus, band-like transport is dominating in highly crystalline regions, while the charge transport in semicrystalline and amorphous polymers is typically defined by the hopping transport. For providing a framework of the combined hopping and band-like transport, the Gaussian disorder model has been introduced,[62] which is depicted in Figure 2.9. Hereby, it is assumed, that the energetic disorder of

the hopping sites is Gaussian distributed with a width of κ, which results in a Gaussian density of states (DOS). These sites are partially filled and resemble the Gaussian distributed charge carrier density. The center of the steady-state charge distribution is shifted to lower energies by $\kappa^2/k_\mathrm{B}T$. In between the energy gap, defined by the center of charge carrier density and the DOS, the so-called transport energy E_T is located. Charge carriers nearby the transport energy can potentially be thermalized and receive sufficient energy to overcome the energy barriers to adjacent sites, which becomes apparent in hopping/tunneling to neighboring sites. In the case of $T = 0\,\mathrm{K}$, no transport energy is provided, therefore no thermalization happens and charge carriers relax in trap states.

In order to achieve high conductivities in amorphous and semicrystalline polymers, the hopping transport has to be optimized. As described above, this is strongly related to the morphology and the arrangement of the highly conducting crystalline regions embedded into the amorphous polymer matrix. Therefore, the structure and the crystallinity of the polymer chains needs to be enhanced, which is commonly referred to as *secondary doping*. The interplay of band-like transport and hopping transport leads to a macroscopic mobility μ which defines a charge carrier drift velocity $\vec{v}$ for an applied electric field $\vec{E}$ by

$$\vec{v} = \mu \vec{E}. \tag{2.13}$$

Considering the contribution of the QP charge q and the corresponding charge carrier density n, the current density $\vec{j}$ can be determine as

$$\vec{j} = \sigma \vec{E} = n\, q\, \mu \vec{E}. \tag{2.14}$$

2.4 Organic Light Emitting Diodes

Due to their versatile capabilities, organic semiconductors gained increasing interest in the last decades. They conquered fields in research and industry which were formerly exclusively belonging to inorganic semiconductors. Due to the infinite possible combinations of polymers, organic semiconductors allow tailoring their characteristics to the required needs. Thus, they found application in organic field-effect transistors (OFETs),[63] organic lasers,[64] organic photo detectors,[65] or organic solar cells.[62,66] However, organic light emitting diodes (OLEDs) are by far the longest investigated devices. Beginning with the first observations of electroluminescence in anthracene single crystals in the 1960s,[3,4] the discovery of high conductivity in polyacetylene obtained by doping[2] paved the way for thin film devices in the 1980s.[5] With the development of such green emitting thin films, first commercial displays became already available in the 1990s. Improvements in the last decades, such as high internal quantum efficiencies (IQEs),[24] made them widely available in today's display technology. In the last years, white OLEDs reached efficiencies which made them also competitive

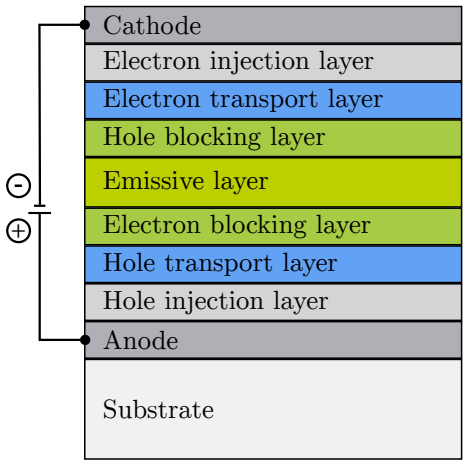

Figure 2.10
Schematic representation of a typical OLED device stack. The emissive layer (EL) is sandwiched between electron/hole blocking layers (EBL/HBL), hole/electron transport (HTL/ETL) and injection layers (HIL/EIL). A transparent anode and reflecting cathode is used to apply an external field and direct the generated photons into the substrate direction (adapted from Riedel[73]).

in room lighting applications.[67–69] The upcoming section covers some basic principles about OLED devices (Subsection 2.4.1) and draws attention to their different mechanisms that resemble the final device efficiency (Subsection 2.4.2). Subsection 2.4.3 covers typical optical loss mechanisms that occur in OLED devices which limits the total external quantum efficiency (EQE). Possible approaches to partly overcome the described loss mechanisms are subject of investigations in the present thesis and are especially tackled in Chapter 5.

2.4.1 Device Stack & Working Principle

The most simple OLED consists of a light emitting organic layer sandwiched between an anode and a cathode, where one of them has to be transparent for light extraction. Over time, the simple device stack has been optimized via additional injection, transport and blocking layers in order to enhance the device's efficiency.[70] Such an idealized OLED device stack is depicted in Figure 2.10. As the layer thicknesses varies between 10 nm – 100 nm, a mechanical stable and transparent substrate is required to support the thin film device. Furthermore, flexible devices can be fabricated by choosing appropriate electrode materials and substrates. Depending on the type of OLED, the different layers are deposited via evaporation (e.g. small molecules) or are processed from solution. While the first one typically provides higher control and device efficiency, the latter one is suitable for large scale applications. Typically, ITO and evaporated aluminum is used as anode and cathode, respectively. The depicted device stack (Figure 2.10) represents the typical composition of a single color OLED. For fabricating white OLED devices a more complicated stack is required. One option is combining several stacks in a so-called active matrix geometry, where each pixel is built up by three differently colored OLEDs. This kind of device is typically used in display applications. Another option is combining differently colored emitters in an alternating layer stack,[14,68,71] so-called tandem OLEDs, or mixing the different emitters with appropriate weight ratios in one single emitting layer.[72]

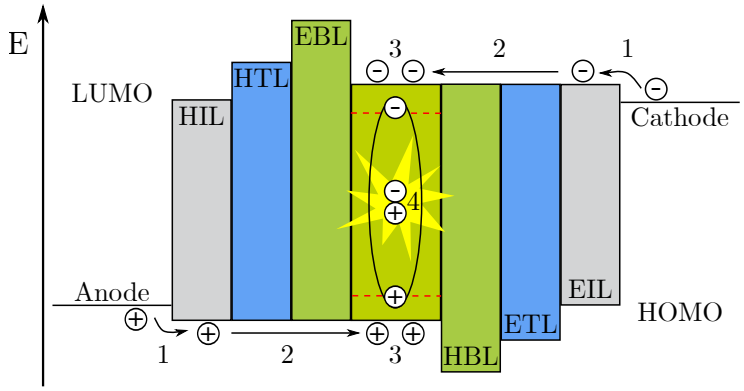

Figure 2.11
Schematic representation of the working principle of a typical OLED device. (1) Charge carriers are injected from the anode and cathode via the corresponding injection layers (HIL/EIL) into the HOMO and LUMO, respectively. (2) Positive charge carriers travel through the HTL and the EBL and accordingly negative charge carriers travel through the ETL and HBL towards the EL. (3) Due to the blocking layers, the charge carriers accumulate at the emitting layer. (4) Exciton generation eventually leads to recombination and photon emission (adapted from Riedel[73]).

All kind of them have the basic working principle in common, which is depicted in Figure 2.11 for an ideal device. Hereby, the materials for the different layers are carefully chosen in order to minimize energy barriers for charge carrier injection and transport. By applying an operating voltage, charge carriers are injected at the anode and cathode into the device. The obtained electrical field leads to a drift current through the transport layers and charge carrier accumulation at the blocking/emissive layer interface. There, excitons are formed which eventually decay via photon recombination. In order to reduce radiationless recombination and avoid short circuits between the contacts, the blocking layers are adjusted to provide a large energy barrier for the complement charge carriers. In the ideal case, the band alignment is set such that only ohmic contacts occur and the required operating voltage is mainly defined by the band gap of the emitting layer (EL).

Besides the band alignment, the layer thickness is an additional important parameter. Careful adjustment is required in order to optimize charge carrier transport and exciton generation. The latter highly depends on the thickness of the emission layer, as exciton generation requires Coulomb interaction between the positive and negative charged quasiparticles. Therefore, the accumulated charge carriers at the interfaces need a distance below the Coulomb radius of

$$r_\mathrm{c} = \frac{q^2}{4\,\pi\,\epsilon_0\,\epsilon_\mathrm{r}\,k_\mathrm{B}\,T}, \tag{2.15}$$

where q is the QP charge, k_B Boltzmann's constant, T the temperature, and ϵ_0 and ϵ_r the dielectric and relative permittivity of the material. Compared to inorganic

semiconductors, the relative permittivity for polymers is much smaller (PPV: $\epsilon_r \approx 3$, GaAs: $\epsilon_r \approx 13$), which results in larger Coulomb radii (PPV: $r_c \approx 20\,\text{nm}$, GaAs: $r_c \approx 4\,\text{nm}$).[74,75] Therefore, the Coulomb screening of the Frenkel excitons in organic semiconductors is not as pronounced as for inorganic materials, which results in a strong exciton binding energy and small exciton radii. The generated excitons may eventually decay by photon emission. In order to enhance the radiant recombination, the layer thickness of the EL is typically set to 10 nm – 20 nm. It is noteworthy to mention that the strong exciton binding lowers the energy of the optical band gap compared to the transport band gap, which is defined by the HOMO and LUMO level of the emitting layer. Therefore, the emitted photon has typically a slightly lower energy. Furthermore, the Gaussian disorder of the HOMO and LUMO levels, as discussed in Subsection 2.3.2, result in a band gap distribution, which becomes visible in a broad emission spectrum of the OLED.

2.4.2 Efficiency Aspects

The performance of an OLED can be described in terms of its luminous power, which is measured in lumen (lm) per consumed electrical power (W). As this value is normalized to the human's eye sensitivity, a more practicable measure is the luminous efficiency, which gives the brightness (luminance) of an OLED for a certain current input ($\text{cd}\,\text{A}^{-1}$). The latter one is equivalent to the external quantum efficiency (EQE) of a device. The main requirement for a high EQE is that the injected charge carriers are converted with a high yield to emitted photons. Therefore, the EQE of an OLED device is given as[75]

$$\text{EQE} = \underbrace{\gamma\,\eta_{s/t}\,\eta_L}_{\text{IQE}}\,\eta_{out}, \tag{2.16}$$

where γ is the charge carrier ratio in the emitting layer, $\eta_{s/t}$ is the amount of states in the system providing emissive recombination, η_L is the luminescence yield of the emitting chromophore, and η_{out} is the outcoupling efficiency. The charge carrier ratio γ can be adjusted by tailoring the injection and transport layers in order to fit the different charge carrier mobilities. By this procedure, a charged particle equilibrium can be reached in the emitting layer and leads in an ideal case to $\gamma = 1$.

$\eta_{s/t}$ gives the probability of exciton creation that leads to emissive recombination in the system. It can be estimated by the singlet-triplet ratio of the emitter. According to spin statistics, the probability for exciting a singlet and triplet exciton is 25 % and 75 %, respectively.[75] Therefore, for a singlet emitter, $\eta_{s/t}$ is limited to ~25 %. In the case of triplet emitters, heavy atoms such as iridium are introduced into the chromophore that enables an enhanced intersystem crossing probability, e.g., for the green emitter Ir(ppy)_3. Thus, the lifetime of triplet excitons is reduced, which results in a depopulation of the triplet levels. Thereby, the probability of exciton generation that can recombine via photon emission is close to $\eta_{s/t} \approx 100\,\%$.[24,76]

The luminescence yield η_L of the chromophore is a measure for the photon generation efficiency of the emitting material. It describes the ratio of generated photons to the number of excitons which are able to recombine via photon emission. Exciton annihilation, quenching and self absorption can reduce this efficiency. The above mentioned values together are often referred to as the IQE.

The last factor η_{out} in Equation 2.16 is a measure for the extracted photons that actually leave the device and contribute to the emitted light intensity. In the last years, research was mainly focused on enhancing the IQE via layer optimization of the the device stack, yielding the outcoupling efficiency to be the main limiting factor in OLED devices. Typical loss mechanisms occurring in such devices are discussed in the following section.

2.4.3 Loss Mechanisms in OLEDs

As seen in Subsection 2.4.2, the efficiency of an OLED device relies on many different factors, where each of them can limit the total device performance. By adjusting the energy levels via appropriate material selection and proper band alignment low operating voltages are achieved. Thus, introducing the above mentioned injection, transport, and blocking layers and matching them up with the properties of the emission layer, gives a good control on the IQE. Furthermore, by using so-called triplet emitter materials a high quantum yield is achieved, which results in an IQE of nearly 100 %.[24,77] Thus, each injected pair of charge carriers leads to an exciton creation and further generates a photon, which subsequently contributes to the emission. With an IQE $\approx$ 100 % and according to Equation 2.16, the outcoupling efficiency η_{out} becomes the limiting factor in the device efficiency. The following section discusses some of the occurring loss mechanisms that limit the photon extraction from OLED devices.

An OLED, schematically depicted in Figure 2.12, consists of different stacked materials with varying thicknesses and refractive indices. Due to the changes in the refractive index, especially at the organic/metal and organic/substrate interface, an OLED can be considered as an asymmetric 2D wave guide. The thickness and refractive index difference of the layers is comparable to the quantum mechanical problem of a particle in a potential well. Thus, organic modes are established in the layers, which cannot leave the device and are eventually absorbed by the organic. Together with surface plasmon polaritons, that are formed at the organic/metal electrode interface, around 40 % – 50 % of the generated photons are trapped in the device by such organic modes.[73]

The second essential limiting factor for photon extraction is the reflection at each layer interface, as depicted in Figure 2.13. Where the refractive index changes from high to low values, such as for the substrate/air interface, total reflection occurs. Thus, the reflected photons are either redirected into the organic layers and become absorbed or are trapped in substrate modes. In both cases they cannot contribute to the emission

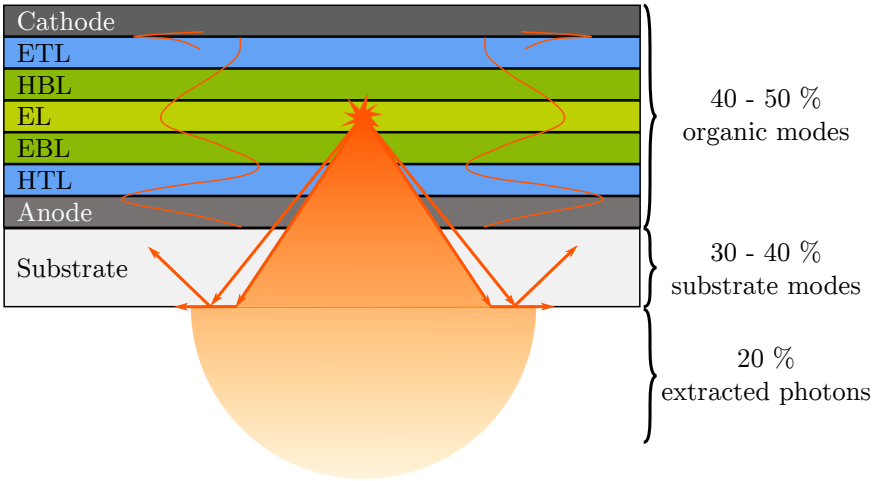

Figure 2.12
Graphical representation of loss mechanisms in OLEDs. ~50 % of the generated photons stay as guided modes or surface plasmon polariton modes in the organic layers and at the organic/metal interface (orange lines). These photons become eventually absorbed by the organic. ~30 % are redirected via total reflection at the substrate/air interface (orange arrows) to the organic layers or may eventually leave the device at its edges. Only ~20 % of the generated photons are able to leave the device to the emission direction (orange cone), which defines the outcoupling efficiency η_{out} and therefore limits the overall device efficiency (adapted from Riedel[73]).

and reduce the device efficiency. As the substrate is thick in comparison to the emitted wavelength ($d \gg \lambda$), the total reflection can be described with classical optics:

$$\sin(\theta_1) = \frac{n_2}{n_1} \sin(\theta_2). \tag{2.17}$$

According to Snell's law in Equation 2.17, total refection occurs for incident angles $\theta_1 > \theta_c$, which is the case for $\sin(\theta_2) = 1$ and $n_1 > n_2$. For a glass/air interface with $n_1 \approx 1.5$ and $n_2 \approx 1$, the critical angle becomes $\theta_c \approx 42°$ and therefore is crucial for surface-emitting light sources such as OLEDs. Hence, due to substrate modes, the amount of emitted photons is further reduced by ~30 %.

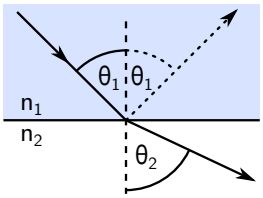

Figure 2.13
Graphical representation of Snell's law.

All together, the extracted photon yield for a common OLED is limited to roughly 20 %,[78,79] as depicted in Figure 2.12. The internal loss mechanisms trap a significant amount of generated photons in the device that become eventually absorbed and limit the overall EQE. Organic and substrate modes can be potentially suppressed by cancel the planar 2D wave guide geometry. This can be realized, for example, by introducing patterned low refractive index layers into the thin film device,[28] or patterning the substrate via micro-lens arrays.[26,27] However, patterning the device in such a way

typically results in scattering with a strong wavelength dependency that leads to a color shift of the redirected light. This is less significant for colored LEDs, as the pattern can be adjusted in order to match the emitted wavelength, but it becomes problematic for white light sources. Therefore, a more randomly structure can be achieved by self-organizing approaches such as embedding scattering centers into a polymer matrix.[25]

Another approach is the implementation of an additional scattering layer in order to redirect the generated photons and reduce the total reflection, as depicted in Figure 5.1. By adjusting the refractive indices of the materials, organic modes may further be suppressed which would further enhance the extracted photon yield. In Chapter 5, the application of a ZnO scattering layer with hierarchical structure with additionally implemented scattering centers in the size of the visible light wavelengths range is tested. In combination with highly conducting polymer electrodes, this potentially allows the fabrication of flexible devices with enhanced outcoupling efficiency.

2.5 Scattering

Structural investigations in the present thesis are performed by employing scattering techniques. In contrast to real space imaging techniques, scattering with X-rays or neutrons provide statistical information about a large sample volume with a certain penetration depth. In the present thesis, elastic scattering is performed, where the energy of the incident beam E_i of X-rays or neutrons is preserved and equals the energy of the final beam ($E_\mathrm{i} = E_\mathrm{f}$). In the upcoming section, some basic concepts and general definitions about scattering with X-rays and neutrons are provided in Subsection 2.5.1. In Subsection 2.5.2 the underlying principle of small angle scattering is discussed, including the applied model for data analysis. Subsection 2.5.3 covers the theoretical background on wide angle scattering, including required corrections to account for the measurement geometry. Lastly, in Subsection 2.5.4, the gravitational effect for neutron measurements and the special feature of ToF mode is described, which allows the simultaneous measurement of a neutron bunch with different wavelengths.

2.5.1 Basic Concepts

The underlying concept of scattering is based on the response of an incoming beam on the change in the refractive index $n(\vec{r}, \lambda)$ inside one material or at material inter-

faces. The modulus of the incoming beam is described with $k_\mathrm{i} = \left|\vec{k}_\mathrm{i}\right| = {}^{2\pi}/_{\lambda}$ and the wavelength λ. The refractive index of matter is then given as[80]

$$n(\vec{r},\lambda) = 1 - \delta(\vec{r},\lambda) + \mathrm{i}\beta(\vec{r},\lambda) \tag{2.18}$$

$$= 1 - \frac{\lambda^2}{2\pi}\,\Re(\mathrm{SLD}) + \frac{\lambda^2}{2\pi}\,\Im(\mathrm{SLD})$$

where $\delta(\vec{r},\lambda)$ and $\beta(\vec{r},\lambda)$ describe the dispersive and absorbing part of the material, respectively. The dispersion and absorption can be further expressed by the real and imaginary part of the scattering length density (SLD). In good approximation, the SLD can be computed in terms of the scattering length contribution of each atom per volume. For hard X-rays ($E \gtrsim 5\,\mathrm{keV}$) and neutrons, the dispersion is typically very small and almost no absorption is present ($1 \gg \delta > \beta$). Thus, the refractive index just slightly deviates from unity. If two materials can be distinguished by scattering, and therefore provide scattering contrast, depends on the difference of their refractive indices

$$\left|\Delta n\right|^2 = \Delta\delta^2 + \Delta\beta^2. \tag{2.19}$$

Therefore, a high difference in the refractive index, or the equivalent SLD, scales with the scattered intensity and provides a high signal to noise ratio. This can also be used for contrast matching, especially for neutron experiments, in order to enhance or reduce the contribution of a specific component.

X-ray Contrast

In the case of X-rays, the scattering contrast relies on the interaction of the photons, described as electromagnetic wave, with the electron cloud of the atoms in the material. As the refractive index is wavelength dependent and therefore varies with the incoming beam energy, it is highly meaningful to approximate it using atomic scattering factors, which were first published by Henke et al.[81] The atomic scattering factor f_j of an atom j is given by

$$f_j(\lambda) = f_j^0 + f_j'(\lambda) + \mathrm{i}f_j''(\lambda) \tag{2.20}$$

where i denotes the imaginary number that shows responsible to the wavelength dependent absorption of X-rays by a single atom. If the chemical composition is known, the complex $\mathrm{SLD_x}$ can then be calculated by[80,81]

$$\mathrm{SLD_x} = r_\mathrm{e}\,\rho_\mathrm{e} \sum_{j=1}^{N} \frac{f_j(\lambda)}{Z_j}, \qquad \text{with } r_\mathrm{e} = \frac{e^2}{4\,\pi\,\epsilon_0\,m_\mathrm{e}\,c^2} \tag{2.21}$$

$$= r_\mathrm{e}\,\rho\,N_\mathrm{A} \sum_{j=1}^{N} \frac{f_j(\lambda)}{M_j}, \qquad \text{with } \rho_\mathrm{e} = \rho\,N_\mathrm{A} \sum_{j=1}^{N} \frac{Z_j}{M_j} \tag{2.22}$$

where r_e is the classical Thomson electron radius, ρ_e the electron density, and Z_j the total number of electrons per atom j. As the electron density is often unknown, it can be approximated by the number of electrons per volume and therefore is computed by using the material's mass density ρ, Avogadro's constant N_A, and the molar mass M_j of each atom j, which results in Equation 2.22. In terms of grazing-incidence X-ray scattering (GIXS) experiments, the momentum transfer $\vec{q} = \vec{k}_f - \vec{k}_i$ is small. Therefore, the atomic scattering factors can be approximated by $f_j^0 \approx Z_j$ and $f_j' \ll f_j^0$. In the case of a homogeneous medium and far away from absorption edges, the refractive index in Equation 2.18 becomes then[80]

$$n = 1 - \frac{\lambda^2}{2\pi} r_e \rho_e + i\frac{\lambda}{4\pi}\mu(\lambda), \tag{2.23}$$

with the linear absorption coefficient for X-rays $\mu(\lambda)$ that defines the absorption length Λ_{abs} as

$$\mu(\lambda) = \frac{4\pi\beta(\lambda)}{\lambda} \quad \Rightarrow \quad \Lambda_{abs} = \frac{1}{\mu} = \frac{\lambda}{4\pi\beta(\lambda)}. \tag{2.24}$$

For hard X-rays, the dispersive and absorbing part of the refractive index are typically in the order of $\delta = \mathcal{O}(10^{-6})$ and $\beta = \mathcal{O}(10^{-7} \ldots 10^{-9})$. Thus, the scattering contrast for X-ray experiments relies on electron density fluctuations in a sample. This can either be related to different materials or to density variations, such as for enrichment layers of the same material.

It is noteworthy to mention that the above approximations do not hold for the case of soft X-rays, were the photon energy is in the range of electronic transitions in the material. In such a case, electrons are excited by the incident X-ray beam and high, wavelength dependent absorption occurs. This can be used for spectroscopic measurements or to enhance the scattering contrast for a specific compound by setting the photon energy close to its resonant frequency, which is the basic principle of resonant X-ray scattering.

Neutron Contrast

In contrast to X-rays, where the photons interact with the atomic shell, the scattering contrast for neutrons arises from the interaction with the atomic nuclei. Therefore, a different scattering length density occurs which results in a different scattering contrast. Nonetheless, in analogy to X-rays, the refractive index can be written in terms of a dispersive and absorbing part δ and β and results in Equation 2.18 with[82,83]

$$\delta(\vec{q}, \lambda) = \frac{\lambda^2}{2\pi} N b = \mathcal{O}(10^{-6}), \tag{2.25}$$

$$\beta(\lambda) = \frac{\lambda}{4\pi} N \alpha_a = \mathcal{O}(10^{-12}). \tag{2.26}$$

Here, N represents the number density of atoms, while b denotes the bound coherent scattering length and α_a the absorption cross section for neutrons. While the dispersion of neutrons is comparable to X-rays, the absorption is of several magnitudes lower. Hence, the absorption of neutrons can often be neglected.[82] In analogy to X-rays, the product of Nb is called the (coherent) $\mathrm{SLD_N}$[83] and is calculated by the sum of the coherent scattering length b_j^coh of each atom j per unit volume V_m. Thus, if the material composition is known, the $\mathrm{SLD_N}$ can be further expressed in terms of the material's mass density ρ and the atomic molar mass M_j

$$\mathrm{SLD_N} = N\,b = \frac{1}{V_\mathrm{m}} \sum_{j=1}^{N} b_j^\mathrm{coh} = \rho\, N_\mathrm{A} \sum_{j=1}^{N} \frac{b_j^\mathrm{coh}}{M_j}. \tag{2.27}$$

Since the $\mathrm{SLD_N}$ arises from the interaction with the atomic nuclei, neutron scattering measurements are highly sensitive to isotopes and allow distinguishing of chemically very similar materials. This is for example the case for the hydrogen atom H ($b_\mathrm{H}^\mathrm{coh} = -3.74$)[84] and deuterium D ($b_\mathrm{D}^\mathrm{coh} = 6.67$),[84] which is especially helpful in polymer science.[85] Due to the large difference in the resulting $\mathrm{SLD_N}$, deuteration of specific components in a polymer allows an increased contrast of specific groups, as performed in the first GISANS experiments.[86] In a similar case, so-called contrast matching can be performed by mixing $\mathrm{H_2O}$ and $\mathrm{D_2O}$ (or other deuterated solvents) in specific ratios in order to adjust the contrast of the surrounding solvent to one part of the polymer in the solution. Hence, by this procedure, the scattering signal of specific compounds can be suppressed and a selective measurement is obtained. Note: In contrast to X-rays, negative values of the $\mathrm{SLD_N}$ are possible, which represent a phase shift of 180° for neutrons relative to those that are scattered by nuclei with a positive $\mathrm{SLD_N}$.[87]

Scattering Geometry

The scattering vector $\vec{q}$ describes the momentum transfer from a sample to the scattered beam and therefore is defined as the difference of the final ($\vec{k}_\mathrm{f}$) and incident ($\vec{k}_\mathrm{i}$) beam:[31]

$$\vec{q} = \vec{k}_\mathrm{f} - \vec{k}_\mathrm{i}. \tag{2.28}$$

A schematic diagram of the scattering geometries, along with the basic definitions of the angles, is depicted in Figure 2.14. The incident beam with wave vector $\vec{k}_\mathrm{i}$ impinges the sample under the incident angle α_i with respect to the sample's surface. The final exiting beam is typically denoted as $\vec{k}_\mathrm{f}$. In the case of specular reflection geometry, such as XRR, the observed scattering occurs only in the xz-scattering plane. As in this case the exit angle equals the incident angle ($\alpha_\mathrm{f} = \alpha_\mathrm{i}$), only changes in $\hat{z}$-direction are detectable. Since only elastic scattering is considered here, the scattering vector only describes a change in the direction of the incident beam, while the modulus remains

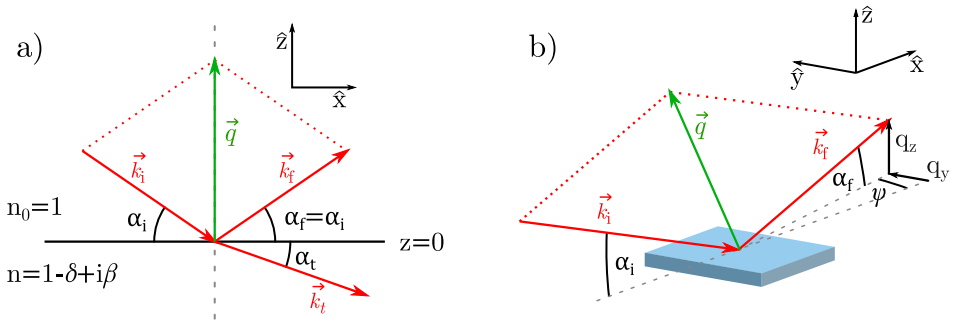

Figure 2.14
Scattering geometry and definitions for specular and diffuse scattering with $\vec{q} = \vec{k}_\mathrm{f} - \vec{k}_\mathrm{i}$. a) In specular reflection geometry the momentum change is only measured in $\hat{z}$-direction with being the x-component of the momentum unchanged and $q_y = 0$. b) In diffuse scattering the off-specular reflection is detected where the momentum change in $\hat{y}$-direction under the scattering angle ψ cannot be neglected.

constant. The modulus of the wave vector is given as $k = \frac{2\pi}{\lambda}$, with its corresponding wavelength λ.

In the case of diffuse scattering (Figure 2.14b), the off-specular reflection is recorded, which contains a momentum transfer in $\hat{y}$-direction. Therefore, an additional scattering angle ψ in the xy-scattering plane is introduced. Furthermore, the final angle deviates from the incident angle ($\alpha_\mathrm{f} \neq \alpha_\mathrm{i}$). According to Snell's law (Equation 2.17), which applies for X-rays and neutrons in the same way, a transmitted beam $\vec{k}_\mathrm{t}$ is observed under the refracted angle α_t. As the dispersion is always positive ($\delta > 0$)[80] and the absorption for hard X-rays and neutrons is small ($\beta < \delta$), the refractive index is typically slightly below but close to unity. Therefore, considering the incident beam hits the sample at an air interface ($n_\mathrm{air} = 1$), total external reflection occurs below a certain incident angle. The critical incident angle α_c, below which total reflection occurs, is calculated for $\alpha_\mathrm{t} = 0°$. In the small angle approximation, Equation 2.17 becomes then

$$\cos(\alpha_\mathrm{i}) = n\,\cos(\alpha_\mathrm{t}) \overset{\alpha_\mathrm{t}=0°}{=} n \tag{2.29}$$

$$\overset{\alpha_\mathrm{i}=\alpha_\mathrm{c}}{\Rightarrow} \; n = \cos(\alpha_\mathrm{c}) \approx 1 - \frac{\alpha_\mathrm{c}^2}{2} \tag{2.30}$$

$$\Rightarrow \; \alpha_\mathrm{c} = \sqrt{2 - 2n} = \sqrt{2\delta} = \lambda\sqrt{\frac{\Re(\mathrm{SLD})}{\pi}} \tag{2.31}$$

for both, X-rays and neutrons. However, Equation 2.31 is only valid for negligible absorption ($\beta \ll \delta$).

The critical angle is of particular interest for small angle scattering experiments performed in grazing-incidence geometry, such as GISAXS. The Fresnel transmission

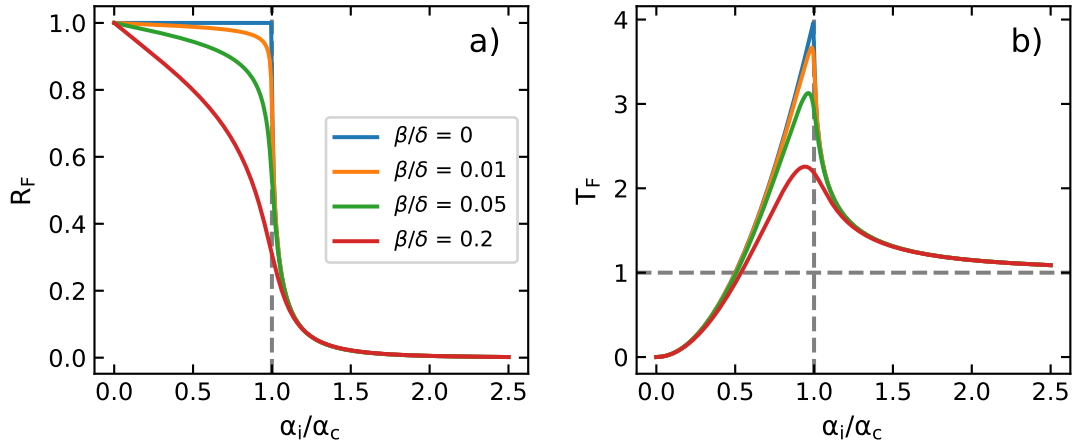

Figure 2.15
Fresnel reflection (R_F) and transmission (T_F) function for an exemplary Si sample with $\delta = 7.56 \times 10^{-6}$ and varying absorption β. a) Total reflection occurs for incident angles $\alpha_i < \alpha_c$ with a fast decay for $\alpha_i > \alpha_c$. b) Fresnel transmission shows an intensity maximum at the critical angle. Interference of the reflected and transmitted wave results in a four times enhanced intensity. Increased absorption ($\beta > 0$) yields in both cases a damped intensity.

and reflection coefficients for the z-component of the incident and transmitted beam are given as[80]

$$r = \frac{k_i - k_t}{k_i + k_t} \qquad t = \frac{2k_i}{k_i + k_t}, \tag{2.32}$$

with $k_i = k\sin(\alpha_i)$ and $k_t = k\sqrt{n^2 - \cos^2(\alpha_i)}$. The corresponding intensities $R_F = |r|^2$ and $T_F = |t|^2$ close to the critical angle α_c are depicted for different absorption coefficients β in Figure 2.15. The reflected intensity shows a constant total reflection for $\alpha_i < \alpha_c$ with a fast decay for $\alpha_i > \alpha_c$ and a damping of the signal for increasing absorption ($\beta > 0$). In contrast, the transmitted intensity shows an intensity maximum at the critical angle. At this point, the reflected and transmitted beam run together in phase for a short distance along the surface and constructively interfere, leading to an amplitude enhancement of the transmitted beam by the factor of two.[80] While the energy conservation still holds, the interference yields a four times enhanced transmission function T_F. Increased absorption ($\beta > 0$) again damps the transmission significantly.

2.5.2 Grazing-Incidence Small-Angle Scattering (GISAS)

According to Figure 2.14b, the scattering vector $\vec{q} = \vec{k}_\mathrm{f} - \vec{k}_\mathrm{i}$ is in general given by[88]

$$\vec{q} = \begin{pmatrix} q_x \\ q_y \\ q_z \end{pmatrix} = \frac{2\pi}{\lambda} \begin{pmatrix} \cos(\alpha_\mathrm{f})\cos(\psi_\mathrm{f}) - \cos(\alpha_\mathrm{i})\cos(\psi_\mathrm{i}) \\ \cos(\alpha_\mathrm{f})\sin(\psi_\mathrm{f}) - \cos(\alpha_\mathrm{i})\sin(\psi_\mathrm{i}) \\ \sin(\alpha_\mathrm{f}) + \sin(\alpha_\mathrm{i}) \end{pmatrix} \tag{2.33}$$

$$\overset{\psi_\mathrm{i}=0°}{\Rightarrow} = \frac{2\pi}{\lambda} \begin{pmatrix} \cos(\alpha_\mathrm{f})\cos(\psi_\mathrm{f}) - \cos(\alpha_\mathrm{i}) \\ \cos(\alpha_\mathrm{f})\sin(\psi_\mathrm{f}) \\ \sin(\alpha_\mathrm{f}) + \sin(\alpha_\mathrm{i}) \end{pmatrix}, \tag{2.34}$$

in dependence on the incident angle α_i, the exit angles α_f in the xz-plane and $\psi_\mathrm{f} = \psi$ in the xy-plane, respectively. The incident angle in the xy-plane is typically $\psi_\mathrm{i} = 0$, which simplifies the scattering vector to Equation 2.34. Furthermore, in the present thesis, only elastic scattering is considered. Thus, the modulus of the incident and final wave vector is not altered ($k_\mathrm{i} = k_\mathrm{f}$) and the photon energy is conserved.

In the present thesis, small angle scattering experiments are performed in grazing-incidence geometry. By choosing incident angles of $\alpha_\mathrm{i} < 1°$, a large area of the investigated sample is illuminated which allows probing of a large film volume. Grazing-incidence experiments are especially suitable for probing of thin films, as the penetration depth can be adjusted and the sample signal compared to the substrate is enhanced.[83] However, in grazing-incidence geometry, the representation of the incident and exiting beam as plane wave is not valid anymore. Due to the small incident angle, additional reflection and/or refraction events may occur at the sample and substrate interface. Therefore, the Born approximation is extended with first-order corrections that account for these additional events. In the framework of the so-called distorted-wave Born approximation (DWBA),[89–91] the incoming wave at a scattering object is approximated as a combination of the direct and reflected waves, whereas the outgoing wave is a combination of the directly scattered or scattered and subsequently reflected waves, or both. A simplified graphical representation of the DWBA is depicted in Figure 2.16. In the last years, several software projects have been developed in order to simulate diffuse scattering patterns of such grazing-incidence experiments in the framework of the DWBA.[88,92–94] Though, such simulations are rather costly regarding computational power. Therefore, in the present thesis, further simplifications and approximations are applied to analyze obtained GISAS scattering patterns.

The Fresnel transmissivity $T_\mathrm{F} = |t|^2$ reveals an intensity maximum close to the critical angle of the corresponding material, as shown in Figure 2.15b. The strongly enhanced diffuse scattering in this case was first observed by Yoneda in 1963 and was further referred to as Yoneda peak.[95] As the Yoneda peak depends on the critical angle of the material, it is considered as material sensitive. Whether the Yoneda peaks of several materials are distinguishable depends on the difference of their critical angles and thus on the scattering contrast (Equation 2.19). In order to extract lateral

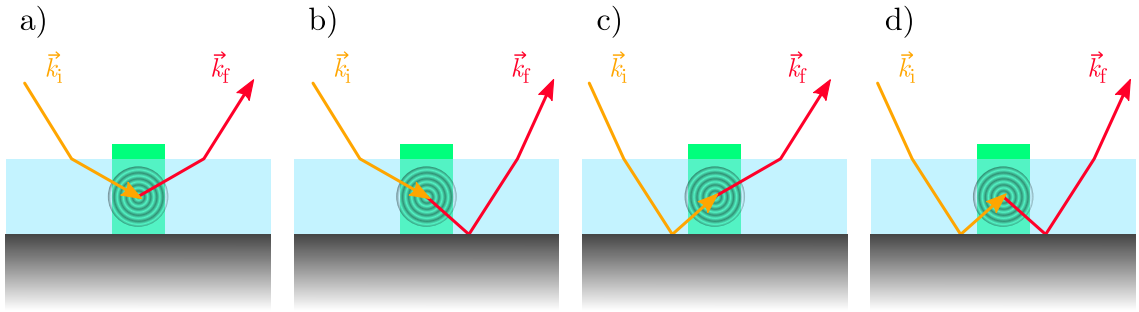

Figure 2.16
Schematic representation of the different combinations of scattering and reflection that are considered in the DWBA. a) Directly scattered beam; b) scattered and reflected beam; c) reflected and scattered beam; d) reflected-scattered-reflected beam. Additionally, the DWBA accounts for refraction and multiple reflection/scattering events, which are omitted here for the sake of clarity but typically are accounted for in simulation software.

structure information from the scattering pattern, it is sufficient to analyze so-called horizontal line cuts along the Yoneda peak position of the desired material. Thereby, the analysis is performed for a fixed q_z-value, where only lateral correlations in the film are considered. A further simplification can be obtained via the effective interface approximation (EIA)[96,97] where the height-height correlation function of the sample is described by one effective interface. Those simplifications speed up data modeling significantly and allow a quantitative analysis. The differential cross section of a scatterer on a sample is then given by[88,97]

$$\frac{\mathrm{d}\sigma}{\mathrm{d}\Omega} = \frac{A\pi^2}{\lambda^4} |\Delta n|^2 |t_\mathrm{i}|^2 |t_\mathrm{f}|^2 P(\vec{q}), \tag{2.35}$$

with the illuminated area A, the scattering contrast $|\Delta n|^2$, the Fresnel amplitude transmission coefficients of the incident and exiting beams $t_{\mathrm{i,f}}$ and the scattering factor $P(\vec{q})$. As mentioned in Subsection 2.5.1, the contrast difference of the investigated material towards its surrounding is of high importance in order to achieve structure information from the sample. The incident angle α_i and therefore the illuminated area A is typically fixed during a measurement. Furthermore, for horizontal line cuts the final angle α_f is kept constant. Together, this results in fixed transmission coefficients $t_{\mathrm{i,f}}$. Consequently, the scattering intensity only scales with the scattering factor $P(\vec{q})$.

Since in the small angle regime structures with length scales starting with a few nm in size are probed, the atomic form factor contributes little to the scattering. In contrast, a form factor $F(\vec{q})$ of mesoscopic objects with approximately homogeneous refractive index is assumed, that is calculated according to Equation 2.18. Considering the object's form factor and the corresponding structure factor $S(\vec{q})$ that takes coherent

interaction of scattered waves from identical, geometrical ordered objects into account, the overall scattering factor $P(\vec{q})$ is calculated by[97–99]

$$P(\vec{q}) \propto N \left|F(\vec{q})\right|^2 S(\vec{q}) \tag{2.36}$$

In this case, a homogeneous distribution of monodisperse scattering objects with number density N is assumed. However, the object size typically varies around a mean value and further approximations have to be taken into account. This is typically achieved via the local monodisperse approximation (LMA) or decoupling approximation (DA).[100]

In order to extract lateral structure information contained in horizontal line cuts obtained from GISAS scattering patterns, a model with differently sized geometrical objects is assumed that coexist under different length scales in the sample. Thus, the model describes in first approximation hierarchical structures in the investigated films. A more detailed explanation of the applied model is given in the PhD theses of Dr. Christoph J. Schaffer[54] and Dr. Johannes Schlipf,[101] respectively. Within this model, the full scattering function $P(\vec{q})$ is represented by an incoherent superposition of j scattering factors in the framework of the LMA. Contributions from different types of scatterers can then be treated as independently and the total scattering factor is calculated by the summation of each component type

$$P(\vec{q}) \propto \sum_j N_j \left\langle \left|F_j(\vec{q})\right|^2 \right\rangle S_j(\vec{q}). \tag{2.37}$$

In the present thesis, cylindrical or spherical form factors $F(\vec{q})$[88,100] are used in the frame of the EIA,[102] which correlates to the object size of the scatterer. Furthermore, the scattering objects are assumed to be arranged in a 1D paracrystal lattice after Hosemann et al.[103] with a (Gaussian) distribution and a mean inter domain distance, which defines the structure factor $S(\vec{q})$. This model provides a good approximation with low computational effort for determining the lateral object size, distance and order of a particular structure inside a sample.[104] It is noteworthy to mention that the above discussed model is valid for GISAS experiments with both, X-rays (GISAXS) or neutrons (GISANS). In the present thesis, a Python v2.7 based software, developed by Dr. Christoph J. Schaffer and David Magerl is employed to quantify structural differences in ZnO scattering layers in Chapter 5.

2.5.3 Grazing-Incidence Wide-Angle X-ray Scattering (GIWAXS)

Since scattering techniques rely on the momentum change of a wave vector in reciprocal space, the detection of the wide angle scattering range give access to very small length scales in the sub-nm regime that translates to lattice spacing of crystallites. In this case, single atoms serve as scattering centers and the signal is generated by the (periodic) structure of these scatterers. Thus, for X-rays, the scattering is related

to the periodic electron density cloud expanded by a lattice of single atoms, which can be approximated again by the atomic scattering factor shown in Equation 2.20.[81] Therefore, wide angle scattering experiments are used to investigate the crystalline structure of samples.

X-rays impinging on a crystalline regime in a sample are reflected on its periodic net layers $\{hkl\}$. Depending on the orientation of these net layers with respect to the incident beam, defining the scattering angle θ, constructive or destructive interference occurs. According to Bragg's law, intensity maxima are recorded for a path difference of the incident and outgoing beam by $n\lambda$. Thus, the obtained diffraction pattern allows determination of the net layer distance of the $\{hkl\}$ family by

$$n\lambda = 2\,d_{hkl}\,\sin(\theta), \qquad \text{with } n \in \mathbb{N} \tag{2.38}$$

$$\Rightarrow \quad d_{hkl} = \frac{n\,\lambda}{2\sin(\theta)} = n\frac{2\,\pi}{q}. \tag{2.39}$$

However, Equation 2.39 only holds for specular conditions, where the scattering vector $\vec{q}$ (Equation 2.34) only depends on the z-component. More generally, considering Huygens' principle, each scatterer is the origin of an elementary wave. Thus, constructive interference only occurs if the momentum transfer matches a reciprocal lattice vector $\vec{G}_{hkl}$ and fulfills the Laue condition

$$\vec{q} \equiv \vec{G}_{hkl} = ha^* + kb^* + lc^*, \tag{2.40}$$

with a^*, b^* and c^* being the reciprocal lattice vectors of the unit cell. Considering energy conservation ($|\vec{k}_\mathrm{i}| = |\vec{k}_\mathrm{f}|$), the Laue condition can be expressed by the Ewald sphere, depicted in Figure 2.17a. Hereby, the modulus of the (exiting) wave vector defines the radius of a sphere in reciprocal space. Therein, the scatterer are represented by reciprocal lattice points. Each intersection of the sphere's surface with a lattice point represents the fulfilled Laue condition and depicts a possible momentum transfer that leads to constructive interference and an intensity maximum in the diffraction pattern.

In GIWAXS experiments, the incident angle is typically fixed and the diffuse scattering is recorded by a 2D detector in close vicinity to the sample. The scattering pattern yields then information about the scattering angle α_f and ψ with respect to the incident beam. As those scattering angles are in the range of several tens of degrees, the small angle approximation applied for GISAS experiments does not hold anymore. Therefore, the contribution of the q_x-component cannot be neglected. As the recorded 2D scattering pattern represents a projection of the allowed Bragg reflexes of the 3D Ewald sphere, both, the q_z- and the q_y-component cannot be decoupled from q_x. Figure 2.17b provides a graphical representation of this projection. This leads to the typical representation of reshaped GIWAXS data in Figure 7.8 and 7.9, revealing a so-called missing wedge for the non-accessible q-values. Consequently, the pure q_z ($q_{xy} = 0$) or q_y ($q_{xz} = 0$) contributions are not accessible by GIWAXS measurements and can be obtained by complementary XRD experiments.

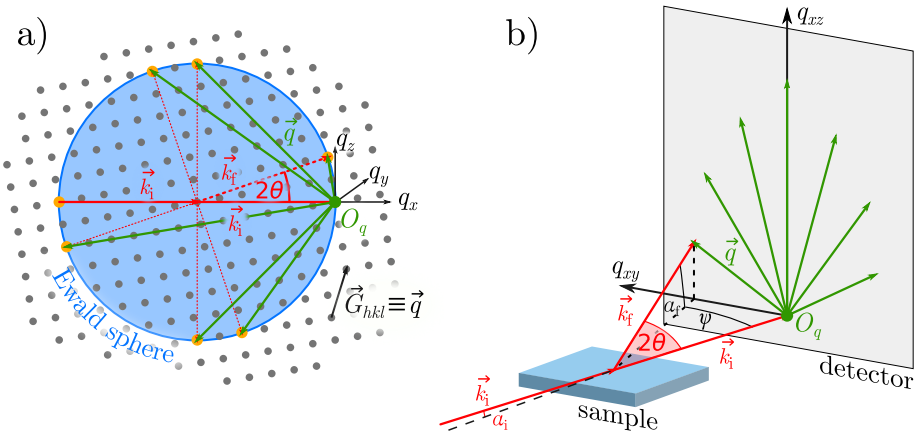

Figure 2.17
Graphical representation of Ewald sphere and GIWAXS pattern. a) Ewald sphere (blue) in reciprocal space, depicted in 2D for sake of clarity. If the Laue condition is fulfilled $\vec{G}_{hkl} \equiv \vec{q}$ (marked with orange dots), constructive interference occurs and the final X-ray beam $\vec{k}_\mathrm{f}$ is reflected at net layers under the angle 2θ with respect to the incoming beam $\vec{k}_\mathrm{i}$, resulting in the scattering vector $\vec{q} = \vec{k}_\mathrm{f} - \vec{k}_\mathrm{i}$. The intersections of the Ewald sphere surface with the reciprocal lattice points that fulfill the Laue condition are highlighted in orange. b) The Bragg reflexes become visible in a scattering pattern as a projection of the 3D Ewald sphere on the 2D detector. The intersection of the incident beam with the 2D detector yields the origin O_q (green) of the projected q_{xy}, q_{xz} coordinate system. The scattering angle 2θ is translated to the scattering angles α_f and ψ.

Additionally to the required reshaping of the obtained scattering images, several corrections have to be applied beforehand to consider the measurement geometry. Therefore, for data corrections and reduction, the MATLAB® based software GIXSGUI v1.7.1 is used. In the following a short overview of the most important corrections is given. However, a detailed discussion about the applied corrections can be found in the publication of Jiang.[105]

First of all, a **flat field** and **dark field correction** have to be applied on the measured data. The first one accounts for a different pixel sensitivity and is typically applied directly on the measurement server of the detector. This depends on the quality of the calibration files, measured beforehand with a homogeneous scatterer or provided by the manufacturer. The second one is accounted for by masking so-called *dead* or *hot* pixels and exclude them from data evaluation.

In wide angle scattering geometry, photons that are scattered under different angles have to travel different path lengths between the scattering center and the detector pixel. As a consequence, the scattered beam intensity is differently attenuated, e.g., by air, which can be reduced by measuring in vacuum. More important, the scattered photons hit the detector pixels under different angles, that result in different detection probability. Both effects are accounted for with the **efficiency correction**.

Typical lab sources provide unpolarized X-rays. However, synchrotron sources provide, due to the differently generated radiation, horizontally (linear) polarized radiation (~98 %). Dipole oscillations of the electrons in the probed material in the direction of polarization reduces the scattered intensity for small angles between the plane of polarization and the scattered beam $\vec{k}_f$. Thus, the scattering intensity for small angles is underestimated and has to be corrected by the **polarization correction**.

Since typically all pixels of a detector are of the same size and the SDD for GIWAXS experiments is small, every pixel covers a different amount of solid angles. The **solid angle correction** is applied in order to account for this purely geometrical effect.

After all corrections are applied, the scattering data can be processed and numerous information such as net layer distances, crystallite orientations and apparent crystallite size can be extracted. Furthermore, the general degree of crystallinity of a sample can be estimated. While the lattice spacing is obtained via Equation 2.39, the corresponding peak shape contains further information on the structure. Scherrer connected in 1918 the crystallite size D to the peak's full width at half maximum (FWHM) via[106]

$$D = \frac{K\lambda}{\mathrm{FWHM}\ \cos(\theta)}, \tag{2.41}$$

where θ is the scattering angle, λ the X-ray's wavelength and K the shape factor of the crystallite. The last one is often approximated by $K = 0.9$ which relates to an average spherical crystallite shape. Equation 2.41 is typically denoted as Scherrer equation. An infinite large crystal would therefore result in a delta function like scattering peak, while small crystallites reveal a strong peak broadening. It is noteworthy to mention that the instrument further contributes to the peak broadening. Additionally, large sample dimensions and consequently a large X-ray footprint in comparison to the SDD results in further peak broadening, caused by the different distance of the scatterers to the detector. Therefore, the crystallite size obtained by Scherrer's equation is typically referred as *apparent crystallite size*. However, as for polymers the crystallite size is in the range of several nm it typically dominates the peak broadening. In any case, Scherrer's equation allows determining a lower limit of the crystallite size and provide a good qualitative comparison within a sample series measured under similar conditions.

2.5.4 Time of Flight Mode of Neutron Experiments

According to Bragg's law (Equation 2.39), there are two possibilities to obtain a scattering pattern. Either monochromatic light is used and the incident angle (and consequently the scattering angle) is changed, or the incident angle is fixed and the energy of the incident beam is varied. For X-ray experiments typically the first case is used, as lab and synchrotron sources provide high flux, brilliance and low energy divergence. However, in the case of neutrons it is different. Typical sources provide continuously neutrons with a broad energy distribution. Consequently, narrowing the energy of the

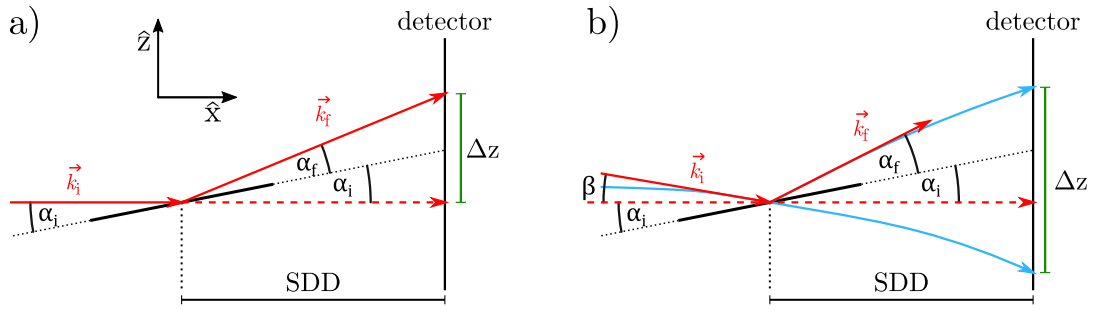

Figure 2.18
Graphical representation of gravitational effect on neutrons during measurements. The definitions of the angles in xz-plane without (a) and with the influence of gravity (b) in $-z$-direction. The deviation of the neutron beam results in a larger incident angle $\alpha_i' = \alpha_i + \beta$, as indicated by the blue parabola. The real incident angle for a given neutron energy is calculated from the pixel positions of the specular and direct beam (adapted from Rawolle[40]).

neutrons down to a small, monochromatic-like distribution would sacrifice most of the neutron flux. Therefore, the so-called time of flight (ToF) mode is typically used. First developed for NR,[107–109] it is also suitable for GISANS measurements.[110,111] However, in the present thesis only ToF-NR measurements are employed. Nevertheless, the basic principle discussed in the following holds as well for GISANS experiments.

By running the instrument in ToF mode, the neutron beam is cropped via several sets of choppers to a pulsed neutron bunch with a defined starting time and velocities, that translates to different wavelengths. After passing the sample, each single neutron is recorded on a 2D detector with its corresponding time of flight. From this, its velocity v_n and its corresponding de Broglie wavelength λ is calculated via

$$\lambda = \frac{h}{p(v_n)} \tag{2.42}$$

with Planck's constant h and the neutron's momentum $p(v_n)$. In contrast to X-rays, neutrons possess a mass and therefore are exposed to gravity. Its influence is strongest for the slowest neutrons with the lowest energy. Consequently, the real incident angle α_i' differs for each neutron energy from the horizontal angle α_i by $\alpha_i' = \alpha_i + \beta$, as indicated in Figure 2.18. Therefore, a correction of the neutron deviation is required. As the gravitational effect on the neutrons is the same for the direct transmitted and the specular reflected beam, the real incident angle α_i' can be calculated by

$$\tan(\alpha_i' + \alpha_f) \overset{\alpha_i' = \alpha_f}{=} \tan(2\alpha_i') = \frac{\Delta z}{\mathrm{SDD}} \tag{2.43}$$

$$\Rightarrow \alpha_i' = \frac{1}{2} \arctan\left(\frac{\Delta z}{\mathrm{SDD}}\right). \tag{2.44}$$

The recorded single neutrons of all bunches are then binned according to their wavelength and the scattering vector $\vec{q}$ can be calculated according to Equation 2.34. The energy resolution only depends on the binning size and can be adjusted as desired as the measurement is performed in single neutron detection mode. In ToF-NR geometry, as used in the present thesis, only the specular reflection is considered ($\alpha_{\mathrm{i}}' = \alpha_{\mathrm{f}}$). Together with the corrected incident angle and the corresponding wavelength of each neutron, the scattering vector simplifies then to

$$\vec{q} = q_z = \frac{4\,\pi}{\lambda}\,\sin(\alpha_{\mathrm{i}}') \tag{2.45}$$

and a reflection pattern similar to XRR is obtained, but enables a different sensitivity based on the different scattering contrast (see Subsection 2.5.1). Further information about the measurement technique and data analysis is provided by Cubitt et al.[112]

CHAPTER 3

Sample Preparation

The present chapter provides a detailed explanation about the various preparation steps for the samples investigated in the frame of this thesis. In Section 3.1, the material characteristics and the supplier information of the investigated functional materials and substrates are listed. Additionally, the cleaning and pattering procedure which were applied to the different substrates before deposition is given. The basic principles and standard parameters of the applied thin film deposition techniques and required finalizing steps, such as thermal annealing, is explained in Section 3.2. The general fabrication procedure of ZnO scattering layers, including the preparation steps of the sol-gel solution, is given in Section 3.3. The preparation steps required for fabrication of PEDOT:PSS polymeric electrodes, which are examined in Chapter 6 and Chapter 7, are covered in Section 3.4. Finally, Section 3.5 deals with the (ITO-free) OLED assembly itself in order to test the performance of the investigated polymeric electrodes in a working device.

3.1 Materials

In the following the materials used in the present thesis are introduced and the basic sample preparation steps including the applied deposition techniques are explained. The section is split into three parts, beginning with the used substrate materials including their preparation and cleaning procedure, followed by the functional materials, which behavior is actually investigated in the present thesis, and the used solvents that have different influence on the functional materials.

3.1.1 Substrate Types and Preparation

In this work a variety of different substrate materials are used depending on the desired purpose and measurement technique. Typically glass substrates are employed for experiments. However, some measurement setups require special substrate properties, e.g., high conductivity, high crystallinity, or low surface roughness with well defined edges. Therefore, silicon substrates are used especially for neutron reflectometry (NR) measurements. Further, two kinds of transparent conductive oxides (TCOs) are employed for XPS measurements and device fabrication, namely flurine-doped tin oxide (FTO) and indium-doped tin oxide (ITO), respectively. A short description of the employed substrate materials is listed in the following. In addition, the required electrode patterning and cleaning procedures prior to film deposition are introduced.

Glass Substrates

For most of the investigated thin films, glass substrates provide all necessary requirements. Due to their optical transparency in the visible range of light and their electrical insulating properties, glass is well suited for the purpose of electrical and optical characterization of thin films. In addition, it is used for X-ray scattering experiments. For this purpose, standard microscope glass slides made of soda-lime glass with dimensions of $76 \times 26\,\mathrm{mm}^2$ and 1 mm thickness, provided by Carl Roth GmbH + Co. KG, are used. The glass slides are cut with the aid of a diamond cutter to the desired substrate size of typically $\sim 25 \times 26\,\mathrm{mm}^2$. In order to clean the substrate surface before thin film deposition, glass substrates are subjected to a hot acid bath as described on page 48.

Silicon Substrates

Silicon substrates are used in the present thesis for NR, GIXS and cross section SEM measurements. The p-doped silicon wafers with a resistivity of $10\,\Omega\,\mathrm{cm} - 20\,\Omega\,\mathrm{cm}$ were provided by Silicon Materials (Kaufering, Germany). The round shaped wafers have a size of 100 mm in diameter with a polished side, which coincides with the $\langle 100 \rangle$ crystal direction. Thus, a surface roughness of the polished side of $R_\mathrm{q} < 0.5\,\mathrm{nm}$ is achieved for the 0.5 mm thick wafers. The wafers are cut along a crystal direction with a diamond cutter to the desired substrate size of typically $2 \times 2\,\mathrm{cm}^2$ for X-ray experiments and SEM measurements or to $7 \times 7\,\mathrm{cm}^2$ for neutron experiments. Hereby, the marking of the wafers is performed on the backside and cut over a sharp edge, e.g., an aluminum plate. In order to avoid unwanted scattering effects, attention has to be paid for well defined and sharp substrate edges. Prior to thin film deposition, the silicon substrates are subjected to the same cleaning procedure in a hot acid bath as the used glass substrates and as explained on page 48.

Fluorine-doped Tin Oxide (FTO) Substrates

Standard soda-lime glass covered with flurine-doped tin oxide (FTO) is used as conductive substrate for XPS measurements in order to prevent charge depletion during examination. Pre-cut FTO substrates (TEC7) are purchased from Solems (Palaiseau,

FRANCE) with dimensions of $22 \times 22\,\mathrm{mm}^2$ and 2.2 mm thickness. The 600 nm conductive FTO coating has been deposited by chemical vapor deposition and shows a sheet resistance of $7\,\Omega\,\square^{-1}$ – $10\,\Omega\,\square^{-1}$. Because the sensitive coating could not resist such an aggressive cleaning step as applied for glass and silicon substrates, FTO substrate cleaning is performed on the basis of organic solvents (see page 49).

Indium-doped Tin Oxide (ITO) Substrates

Indium-doped tin oxide (ITO) covered substrates (ITOSOL30) are purchased from SOLEMS (PALAISEAU, FRANCE). ITO substrates are used in the present work for fabrication of standard OLED devices in Chapter 7, which serves as reference for ITO-free OLEDs on the basis of PEDOT:PSS electrodes. The pre-cut substrates with dimensions of $25 \times 25\,\mathrm{mm}^2$ and thickness of 1.1 mm are covered with a 100 nm ITO layer, deposited by physical vapor deposition, and obtaining a sheet resistance of $25\,\Omega\,\square^{-1}$ – $35\,\Omega\,\square^{-1}$. In order to fabricate OLED devices, the ITO substrates are patterned and subsequently cleaned prior to thin film deposition according to an organic cleaning procedure described on page 49.

Electrode Patterning

Devices fabricated in the present thesis are typically contacted by applying spring contacts on the evaporated metal electrodes. Such pin contacts may penetrate the different functional layers of a device and may connect the top and the bottom electrode. In order to prevent such short circuits, the back electrode underneath the contact area has to be removed prior to film deposition. Hence, ITO or FTO coated substrates designated for device fabrication are subjected to a patterning process, which is depicted in Figure 3.1. Therefore, the TCO region of the desired bottom electrode is covered with sticky tape (TESAFILM®, 12 mm width) to protect it from the reactive etching solution (Figure 3.1b). The unprotected area is then partly covered with Zn powder by using a custom-made snap cap vial with a perforated lid. Note that Zn powder serves as catalyst in the following etching process. Thus, already small amounts of Zn are sufficient and the TCO does not need to be completely covered with zinc powder. HCl (37 %) is diluted with H_2O at 1:1 volume ratio and dropped via a glass pipette on top of the zinc powder covered TCO (Figure 3.1c), followed by mechanically wiping with a cotton bud. Afterwards, the substrates are excessively rinsed under tap water to remove the reagents before the sticky tape is detached. In the following, the substrates are scrubbed with a toothbrush dipped in ALCONOX® detergent solution ($16\,\mathrm{g\,L}^{-1}$) and subsequently rinsed with water in order to remove adhesive residuals on the substrate surface (Figure 3.1d). The so patterned bottom electrode is now suitable for the used eight-pixel device layout depicted in Figure 3.1e. Prior to film deposition the patterned substrates are subjected to an organic cleaning procedure explained on page 49.

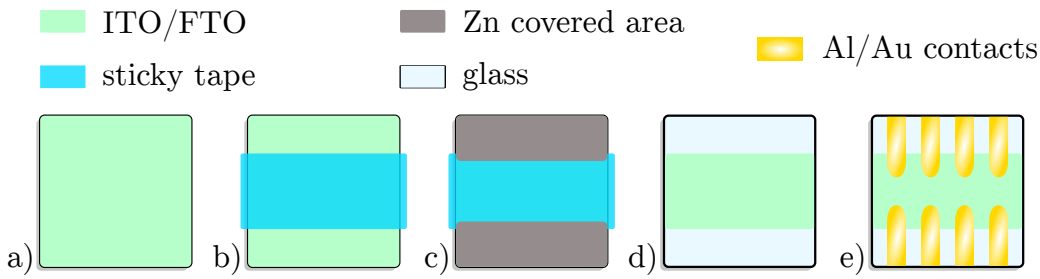

Figure 3.1
Electrode patterning procedure for ITO and FTO substrates intended for OLED fabrication. a) Initial ITO or FTO coated substrates. b) The center of the substrate is covered with sticky tape in order to protect the intended electrode region from etching. c) Zinc powder is peppered onto the uncovered region in order to serve as catalyst for the subsequent etching process with diluted HCl. d) After removing the sticky tape, the desired electrode pattern is revealed and the substrate is ready for further cleaning and deposition steps. e) Desired electrode layout for finished OLED devices. Functional layers are supposed to be sandwiched between the TCO electrode and the Al/Au contacts. The active area is defined as the overlap region of both electrodes.

Acid Cleaning

After cutting the glass and silicon substrates to the desired size and prior to thin film deposition, any impurities or organic traces on the substrate surface need to be removed. Thus, the substrates are subjected to a cleaning procedure based on a modified piranha bath.[113] The hot acid bath is prepared as following: Two nested beakers are placed on a combined magnetic stirrer/heater plate, while the outer one holds a water bath for safely heating of the inner one. The inner beaker is filled subsequently with 54 mL deionized water (H_2O), 84 mL hydrogen peroxide (H_2O_2, 30 %), and 198 mL concentrated sulfuric acid (H_2SO_4, 95 % – 98 %). The acid bath is heated up to 80 °C and is covered with a watch glass to avoid evaporation. Note that the mixing sequence must not be changed to avoid deflagration of the exothermic reaction. The substrates are placed upright in a special designed holder consisting of acid-resistant polytetrafluoroethylene (PTFE), colloquial known as Teflon™, and rinsed with water to wash away dust and glass or silicon splinters. Then, the holder, including the substrates, is placed for 15 min in the hot acid bath. Afterwards, the sample holder is immediately transferred and subsequently washed in three beakers, filled with 500 mL H_2O each. In order to fully dilute and remove any acid residuals, each individual substrate is finally taken and subsequently rinsed with water, followed by drying under a continuous nitrogen flow. The duration of the acid bath has a strong influence on the formation of SiO_x surface layers on the substrate, which is especially important for silicon substrates. Note that the highly reactive and oxidizing cleaning procedure results in a hydrophobic surface activation of the substrate. In order to obtain a hydrophilic surface, an oxygen plasma can be applied prior to film deposition, as explained on page 49.

Organic Cleaning

For (patterned) ITO and FTO substrates a different cleaning procedure is required to preserve the conductive coating. Thus, the substrates are placed upright into a PTFE substrate holder and rinsed with water to get rid of dust particles. Then, a step-by-step cleaning protocol is applied based on a 10 min ultrasonic bath in ALCONOX® detergent ($16\,\mathrm{g\,L^{-1}}$), ethanol, acetone and isopropyl alcohol (IPA). After each step, the substrates together with the sample holder are rinsed with the solvent of the subsequent step. In addition, after the ALCONOX® bath, the substrates are rinsed with water to flush any traces of the detergent before they are cleaned in ethanol. In the end, the substrates are removed one by one from the IPA solvent and are dried under a continuous nitrogen flow. Note due to time constraints it may be necessary to store the substrates in the IPA solvent until shortly before deposition of the thin films. In order to functionalize the substrate's surface an oxygen plasma is performed directly before deposition.

Oxygen Plasma

If necessary, the substrates are subjected to an oxygen plasma treatment after the chemical cleaning procedure. Plasma cleaning is performed with a NANO PLASMA CLEANER by DIENER ELECTRONIC. The substrates are placed in the vacuum chamber which is flooded with oxygen at a pressure of 0.4 mbar. By applying a frequency of 40 kHz for 10 min at a power of ~250 W, any organic compounds at the surface are decomposed by the produced oxygen radicals and the ultraviolet radiation from relaxing O_2/O_3 molecules. The combustion of the organic residuals creates mostly CO_2, which is – together with the excess O_2/O_3 – eventually extracted by the vacuum pump. Furthermore, the surface becomes more hydrophilic by activating polar chemical bonds, which improves the wettability of polar solvents such as PEDOT:PSS solution. It is noteworthy to mention that the adjuvant effect of the performed oxygen plasma treatment lasts only for several minutes. Therefore, thin films are deposited immediately after the oxygen plasma is carried out.

3.1.2 Functional Materials

In the following, the functional materials that are used in the present thesis are listed. In Chapter 5 scattering layers based on ZnO are investigated. In the fabrication process of such thin films, the inorganic precursor ZAD is used. The polymer template PS-*b*-PEO becomes important when the ZnO layers have to be structured, e.g., in order to form porous metal oxide layers. PS microspheres find application in the hierarchical structuring of the above mentioned ZnO layers, in order to obtain additional scattering centers in the wavelength region of the visible light. In Chapter 6 and Chapter 7 the polymer mixture PEDOT:PSS is investigated regarding its performance and durability in use as polymeric electrodes. SUPER YELLOW® is used as emitter material for OLED devices in order to test the performance of PEDOT:PSS electrodes in Chapter 7.

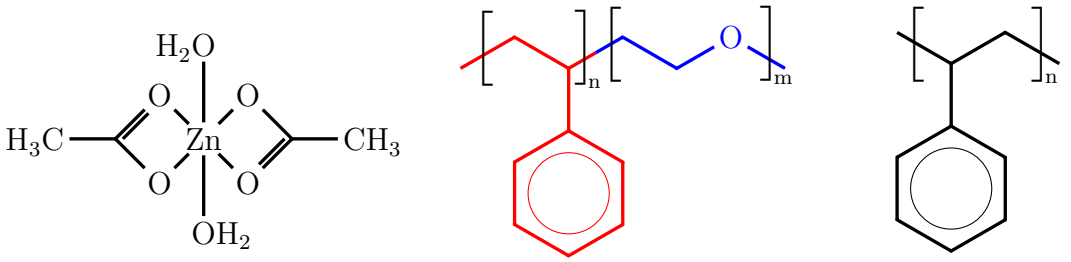

a) ZAD **b)** PS-*b*-PEO **c)** Polystyrene

Figure 3.2
Materials used for diblock copolymer assisted sol-gel synthesis of ZnO scattering layers.

ZAD

Zinc acetate dihydrate, abbreviated as ZAD, is used as inorganic precursor material for zinc oxide (ZnO) thin film fabrication. The precursor is purchased from Sigma-Aldrich with a purity of 99.999 % (trace metals basis). It has the appearance of a white powder and a density of $1.74\,\mathrm{g\,cm^{-3}}$ ($219.51\,\mathrm{g\,mol^{-1}}$). Its chemical structure is depicted in Figure 3.2a with its formula quoted as $Zn(CH_3COO)_2 \cdot 2\,H_2O$ (CAS: 5970-45-6). The dihydrate crystallizes in a monoclinic unit cell with dimensions $a = 14.50\,\text{Å}$, $b = 5.32\,\text{Å}$, $c = 11.02\,\text{Å}$, and $\beta = 100°$.[114] The chemical structure of ZAD indicates that the coordination geometry around the Zn atom is octahedral as Zn is bound to the oxygen atoms of the two hydration water molecules and four oxygen atoms of the acetate ligands. Forming ZnO from the ZAD precursor requires a high temperature treatment of above 300 °C which leads typically to a crystallization as wurtzite polymorph. Zinc oxide itself has a melting point of $T_\mathrm{m} = 1974\,°\mathrm{C}$ and can be considered as chemically very stable. It shows a direct optical band gap of 3.3 eV with a refractive index of $n \approx 2$, which allows the fabrication of transparent layers.[115,116] Hence, an application in OLED or OPV devices is possible. In addition, its abundance and non-toxic behavior makes ZnO to a promising material towards environmentally friendly device fabrication.

PS-*b*-PEO

The amphiphilic diblock copolymer polystyrene-*block*-poly(ethylene oxide), or short PS-*b*-PEO (Figure 3.2b), is used in the present study for structuring ZnO scattering layers in Chapter 5. Such a diblock copolymer acts as structure directing template in the sol-gel synthesis route and allows tailoring of the resulting nanostructures in the final thin film. In the case of PS-*b*-PEO the PS block acts as hydrophobic block, while the PEO block serves as hydrophilic block where the polar ZAD molecules are able to attach during synthesis. The present diblock copolymer is obtained from Polymer Source, Inc., Canada and is used as received. The total number average molecular mass is given as $M_\mathrm{n} = 28.5\,\mathrm{kg\,mol^{-1}}$, split up into $20.5\,\mathrm{kg\,mol^{-1}}$ and $8.0\,\mathrm{kg\,mol^{-1}}$ for the PS block and the PEO block respectively. Hence, the fraction of PS is calculated according to Equation 2.2 as $f_\mathrm{PS} = 0.52$. The polydispersity index (PDI) is characterized as 1.02. PDI and the molecular weight is determined by the supplier with size

exclusion chromatography, while the composition of the blocks is calculated from ^{1}H-NMR. The glass transition temperature of PS is given as T_g = 107 °C. Furthermore, the glass transition (T_g), melting (T_m) and crystallization (T_c) temperature of PEO is characterized as −65 °C, 63 °C and 43 °C, respectively.

PS Microspheres

Microspheres consisting of polystyrene (PS) are employed as additional structure giving templating material for ZnO thin film fabrication. The chemical structure of PS with its formula $(C_8H_8)_n$ is given in Figure 3.2c. As one block of the used polymer template PS-*b*-PEO consists of the same material, a good compatibility is expected. A large bunch of different sized microspheres are available, which allows adjusting the desired pore size of the achievable hierarchically structured ZnO films. Polybead® PS microspheres with a mean diameter of 500 nm are purchased from Polysciences, Inc. The microspheres are provided in a 2.6 % solids (w/v) aqueous suspension with a concentration of ~26 mg mL^{-1} and are used without further purification.

PEDOT:PSS

The polymer mixture poly(3,4-ethylene dioxythiophene):poly(styrene sulfonate), abbreviated as PEDOT:PSS, consists of two ionomers, namely the hydrophobic conducting PEDOT and the hydrophilic electrically insulating PSS. Their chemical structure is expressed with the formulas $(C_6H_4O_2S)_n$ and $(C_8H_7O_3S)_m$, which are depicted in Figure 3.3. PEDOT:PSS is commonly used in organic electronics for its advantageous properties like high conductivity, transparency and ease of processibility. Its conducting behavior is based on the conjugated backbone created by the alternating polythiophene rings of the PEDOT component. This enables high electrical conductivity of positively charged polarons along the PEDOT backbone that are introduced by the presence of the deprotonated sulfonic-groups of the PSS component. Therefore, due to the hydrophobic behavior of PEDOT, the hydrophilic PSS component serve a purpose of charge stabilization and providing solubility in water to the blend. The PEDOT:PSS polyelectrolyte tends to form a scrambled egg like structure in water,[117] which gives a tendency towards the formation of agglomerates.

In the present thesis, Heraeus Clevios™ PEDOT:PSS is used in two different mixtures listed in Table 3.1, both provided by Ossila Ltd, Sheffield UK in aqueous solution (CAS: 155090-83-8) and are stored at 4 °C in light absorbing bottles. Al 4083 (order code M121) with a mixing ratio of 1:6 is used as electron blocking layer in the device fabrication of Chapter 7. However, the main subject of investigation in this study is PEDOT:PSS PH 1000 (order code M122) with a mixing ratio of 1:2.5. Depending on the treatment, this material provides very high conductivities and therefore is investigated in the present study regarding its suitability as polymeric electrode. Note, while the viscosity of the stock solution is eligible for spin coating, for spray deposition the solution needs to be diluted with water in order to prevent plugging of the spray gun.

Table 3.1
Mixing ratios and physical properties of the used PEDOT:PSS solutions of Al 4083 and PH 1000 type, according to the supplier. In the present study, PH 1000 is mainly used in order to investigate its performance as polymeric electrode. Al 4083 has been applied as EBL in the fabrication of OLED devices.

PEDOT:PSS	ratio	solid content [wt.% (in H_2O)]	work function [eV]	viscosity [mPa s]
Al 4083	1:6	1.3 – 1.7	5.0 – 5.2	5 – 12
PH 1000	1:2.5	1.0 – 1.3	4.8 – 5.0	<50

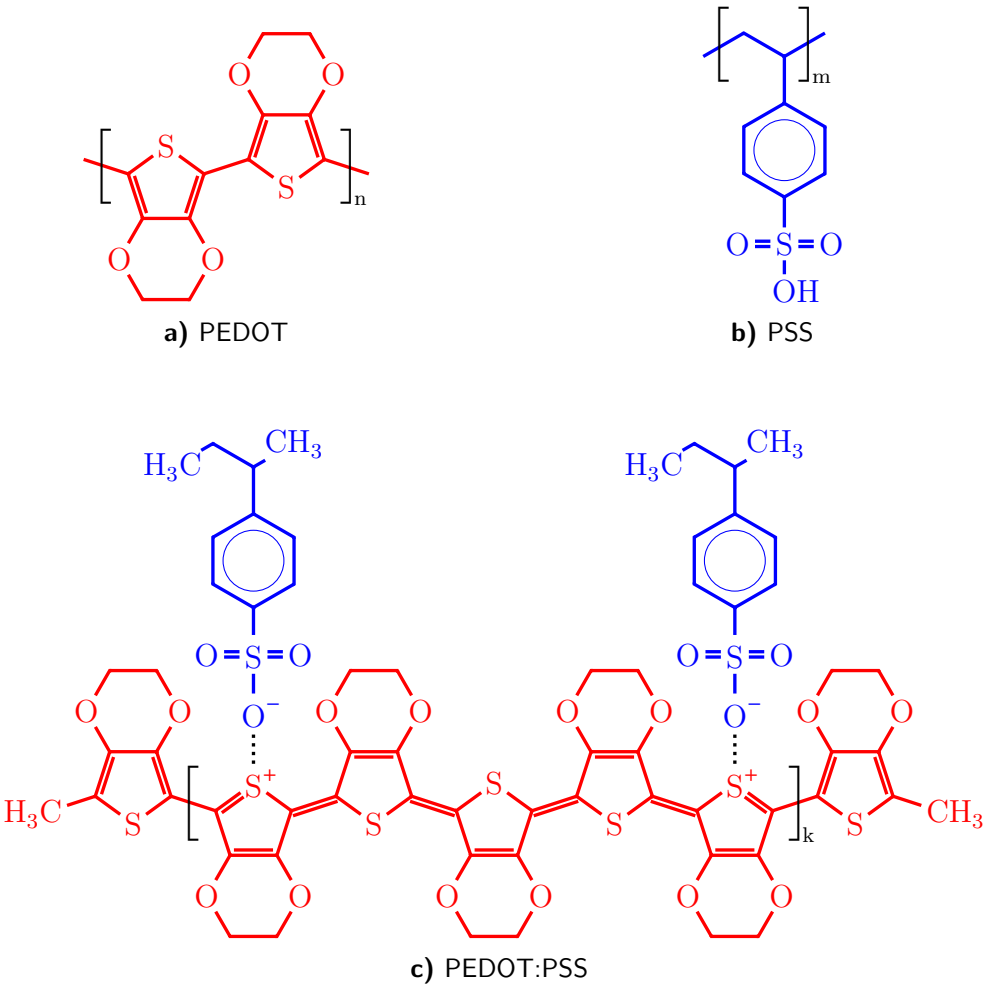

Figure 3.3 Chemical structures of a) PEDOT, b) PSS and c) the polymer mixture of both.

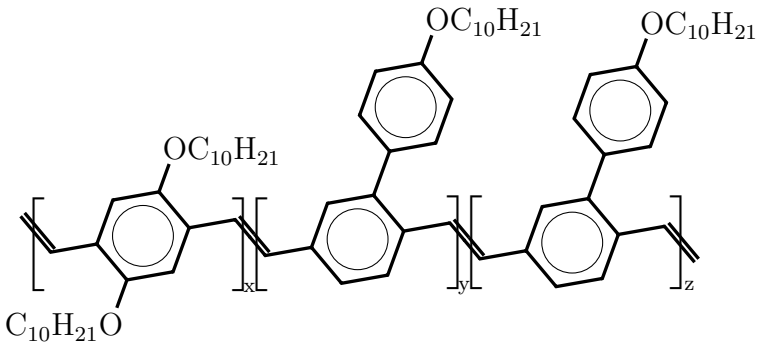

Figure 3.4 Chemical structure of the light emitting polymer Super Yellow®.

Super Yellow

Super Yellow® (PDY-132, Livilux®) is a PPV-based, light emitting copolymer, provided by Merck KGaA (CAS: 26009-24-5) and is shipped as clumpy yellow powder. Its molecular weight is $M_w > 1.3 \times 10^6\,\mathrm{g\,mol^{-1}}$ with a molecular number of $M_n > 4 \times 10^5$. Its chemical structure is depicted in Figure 3.4. PDY-132 belongs to the category of very robust singlet emitter materials, which makes it to an ideal choice for the fabrication of standard OLED devices in the present thesis. It is easily soluble in toluene, which is an orthogonal solvent to the water-based PEDOT:PSS that has to be deposited beforehand. The maximum efficiency of PDY-132 is given by the supplier with $11\,\mathrm{cd\,A^{-1}}$ with an external quantum efficiency (EQE) of 5.3 % in a standard device stack. In this case, the onset voltage is given with 2.2 V, which is slightly below the nominal electronic band gap between the HOMO (−5.4 eV) and the LUMO (−3.0 eV) level.[118] The emission maximum is located around 560 nm, which matches well with the onset voltage, while its absorption maximum is located around 440 nm.[119]

3.1.3 Solvents and Acids

In the following section, the solvents and acids used in the present thesis are listed. While DMF is used as solvent for the ZnO precursor ZAD, toluene finds its application as solvent for the light emitting polymer Super Yellow®. Zonyl is used as additive in PEDOT:PSS thin film preparation. Furthermore, the solvent ethylene glycol and the acids formic acid, hydrochloric acid, nitric acid, and sulfuric acid are used for post-treatment of PEDOT:PSS thin films. An overview of the chemical structures of the used solvents and acids is depicted in Figure 3.5.

Deionized Water (DI-H_2O)

If not other stated, a Purelab Chorus 1 by Veolia high-purity water system is used to produce deionized, cleaned water with a resistivity of >18.2 MΩ cm. Such purified water is used for all sample preparation steps throughout the whole present thesis. In order to achieve high contrast in neutron measurements typically heavy

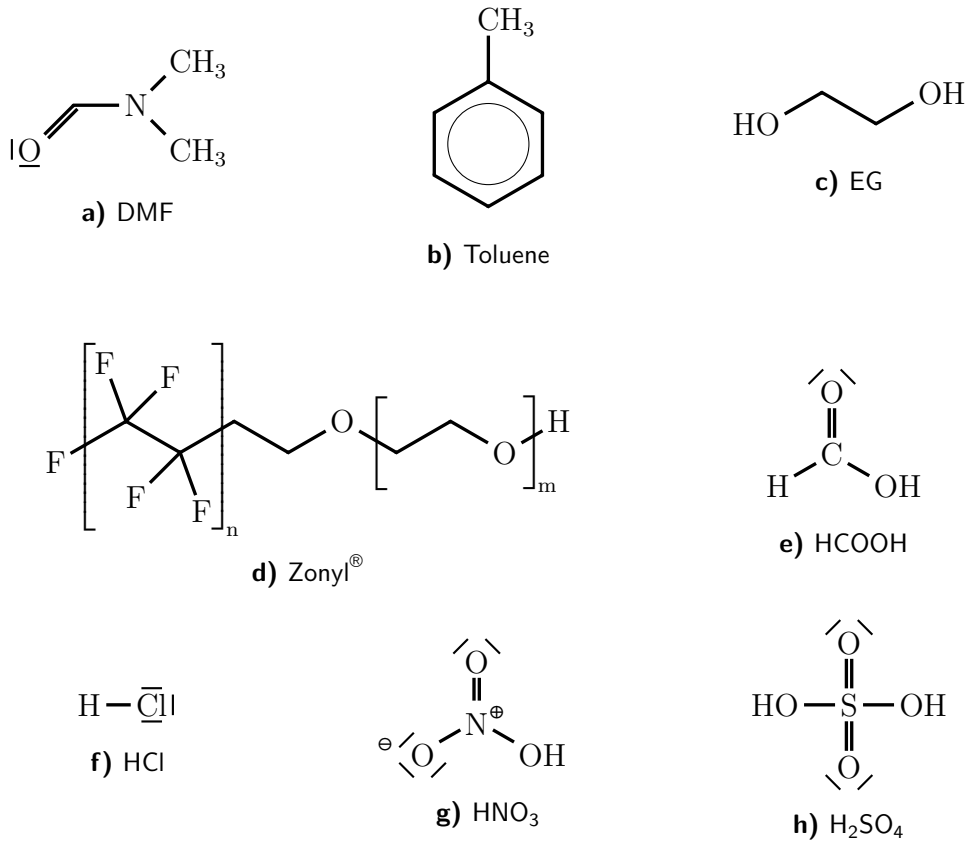

Figure 3.5 Chemical structures of solvents and acids used in the present thesis.

water instead of H_2O is employed. For this purpose, D_2O (99.95 %) is purchased from Deutero GmbH, Kastellaun (CAS: 7789-20-0).

N,N-Dimethylformamid

DMF is used as so-called good solvent in ZnO sol-gel synthesis in Chapter 5. Its chemical structure with the formula C_3H_7NO is given in Figure 3.5a. DMF is purchased from Carl Roth GmbH + Co. KG with a purity of ≥99.8 % and has a molecular weight of 73.10 g mol^{-1} (CAS: 68-12-2). The polar solvent with a density of 0.95 g mL^{-1} is well miscible with water and has a boiling point of ~153 °C.

Toluene

Toluene is used in the OLED fabrication process of the present thesis as solvent for the light emitting polymer Super Yellow®. It belongs to the category of non-polar solvents, which allow the use as orthogonal solvent after the deposition of the water-based PEDOT:PSS. Toluene is purchased from Carl Roth GmbH + Co. KG with a purity of ≥99.8 % (CAS: 108-88-3). Its chemical structure with the formula C_7H_8 is depicted in Figure 3.5b. Toluene's molar weight is given as 92.14 g mol^{-1} with a density of 0.87 g mL^{-1}. Its boiling point is given as 110 °C – 111 °C.

Ethylene Glycol

EG is used as secondary dopant for PEDOT:PSS post-treatment. Its chemical structure with the formula $C_2H_6O_2$ is depicted in Figure 3.5c. EG is purchased from SIGMA-ALDRICH with a purity of 99.8 % (CAS: 107-21-1). Its density is given as $1.113\,\mathrm{g\,mL^{-1}}$ with a molar weight of $62.07\,\mathrm{g\,mol^{-1}}$ and a boiling point of 195 °C – 198 °C.

Zonyl

The fluorosurfactant DUPONT™ ZONYL® FS-300 – henceforth referred to as Zonyl – is a registered trademark of E.I. DU PONT DE NEMOURS AND COMPANY (CAS: 197664-69-0). Its chemical structure is shown in Figure 3.5d. It is purchased from SIGMA-ALDRICH and produced through the company's subsidiary FLUKA® ANALYTICAL. Zonyl is provided as ~40 % fluorosurfactant in aqueous solution with a density of $(1.10 \pm 0.05)\,\mathrm{g\,mL^{-1}}$ at 20 °C. Further, it mixes well with water and its boiling point is ~80 °C.[120] Zonyl is used in the present thesis as additive in the fabrication routine of PEDOT:PSS thin films.

Formic Acid (≥98 %)

Formic acid (HCOOH) belongs to the organic acids and is used for post-treatment of PEDOT:PSS thin films in Chapter 7. It is purchased with a purity of ≥98 % from CARL ROTH GMBH + CO. KG (CAS: 64-18-6). The density of HCOOH is given as $1.22\,\mathrm{g\,mL^{-1}}$ with a molar weight of $46.02\,\mathrm{g\,mol^{-1}}$. Its boiling point is 101 °C. The chemical structure with the formula CH_2O_2 is given in Figure 3.5e. HCOOH is used without further purification or dilution.

Hydrochloric Acid (37 %)

HCl belongs to the inorganic acids with a strong dissociation behavior and is depicted in Figure 3.5f. Hydrochloric acid is purchased with a purity of 37 % (extra pure) from CARL ROTH GMBH + CO. KG (CAS: 7647-01-0). Its density is given as $1.19\,\mathrm{g\,mL^{-1}}$ with a molar mass of $36.46\,\mathrm{g\,mol^{-1}}$. HCl is used in the present thesis without further purification for post-treatment of PEDOT:PSS thin films in Chapter 7.

Nitric Acid (65 %)

HNO_3 belongs to the inorganic acids and is shown in Figure 3.5g. It is purchased with a concentration of 65 % (pure) from CARL ROTH GMBH + CO. KG (CAS: 7697-37-2). The density of HNO_3 is given as $1.3\,\mathrm{g\,mL^{-1}} - 1.4\,\mathrm{g\,mL^{-1}}$ with a molar mass of $63.0\,\mathrm{g\,mol^{-1}}$. Concentrated HNO_3 is used in Chapter 7 without further purification for post-treatment of PEDOT:PSS thin films. It is noteworthy to mention that nitric acid shows similar as H_2SO_4 a strong oxidation behavior.

Sulfuric Acid (95 % – 98 %)

H_2SO_4, shown in Figure 3.5h, belongs to the inorganic acids with high oxidizing behavior. Sulfuric acid is purchased from CARL ROTH GMBH + CO. KG with a concentration of 95 % – 98 % (CAS: 7664-93-9). Its molar mass is given as $98.08\,\mathrm{g\,mol^{-1}}$ with

a density of $1.84\,\mathrm{g\,mL^{-1}}$. Concentrated sulfuric acid is used without further dilution or purification in the post-treatment process of PEDOT:PSS thin films in Chapter 7. Note, the same sulfuric acid is used for the hot acid bath in the substrate cleaning process on page 48.

3.2 Thin Film Deposition

PEDOT:PSS and all other layers are deposited on solid substrates throughout the present thesis by two deposition techniques, namely spin coating and spray coating. While spin coating is an excellent method for lab scaled sample fabrication, spray coating allows the deposition on larger and complex shaped substrates. In this work, spray coating is used for deposition of ZnO scattering layers, while spin coating has been applied for the fabrication of PEDOT:PSS polymeric electrodes and OLED devices. In order to assure good contacting for the latter, evaporation of metal back electrodes is performed via physical vapor deposition.

3.2.1 Spin Coating

Spin coating is a commonly used technique for fabrication of thin films with ~100 nm thickness from solution with volatile solvents. Its main advantage is the fabrication of very thin, homogeneous films on a laboratory scale. However, the method is limited regarding the sample size and shape as well as the amount of samples one can produce. In the present thesis, a Delta 6 RC TT spin coater by Süss MicroTec Lithography GmbH is used. The setup consists of a rotating plate with well defined acceleration and rotation speed. The sample is fixed on the plate either by fitting in a cavitation or by applying vacuum. After covering the whole substrate surface with the solution (100 µL – 500 µL, depending on the substrate size), the spin coating process is started immediately. In order to maintain a reproducible sample environment the lid of the spin coater is kept closed during the deposition process. Hereby, the rotation speed, the acceleration time, the rotation time and the samples environment define the properties of the final thin film. In the end, a homogeneous film is formed,[121,122] whose thickness d highly depends on the angular velocity ω by $d \propto \omega^{-1/2}$ and can be determined by Schubert's Equation:[122]

$$d = C\, c_0\, \omega^{-1/2}\, M_\mathrm{w}^{1/4}, \tag{3.1}$$

with C being an experimental parameter that has to be determined for each sample system, c_0 the initial concentration, and M_w the molecular weight of the solute. The acceleration is typically set to ACL9, which corresponds to an acceleration time of ~6 s until the final rotation speed is reached and the timer is started. Typical spinning speeds of 750 rpm – 4000 rpm are used with rotation times of 60 s. Due to the increased

velocity on the outer parts of the sample, a thickness gradient from the rotation center to the sample edges cannot be avoided and limits the substrates size. Therefore, substrates of diameter ⌀ ≤ 10 cm are typically used. It is noteworthy to mention that for neutron measurements whole silicon wafers (⌀ 10 cm) are required, which should not be fixed by applying vacuum to avoid bending of the substrates.

3.2.2 Spray Coating

Spray coating is a widely used technique for solution based large scaled deposition on (complex) surfaces. The deposition process is commonly distinguished by wet and dry spray deposition. In the first case, the impinging material still contains a certain amount of solvent, which provides mobility during film formation. Contrary, in the second case, the solvent is already evaporated before the dried material hits the sample. Commonly, a spray is referred to a flow of small droplets coming out of a nozzle. These droplets are generated by a process called atomization, where a liquid is dispersed into small droplets by the energy of a compressed carrier gas.[123] The dispersion of the liquid jet depends on the solutions density, its kinematic viscosity and its surface tension. Lateral pressure differences lead to an angular and downward velocity of the solution at the exit point of the nozzle. Thus, the angular velocity drives the droplets apart, which leads to a widening of the spray, known as spray cone. Hence, the diameter of the cone enlarges and the density of droplets decreases.[124,125] A larger distance between the nozzle and the substrate yields a more homogeneous cone with smaller droplets and a larger coverage of the substrate. The carrier gas pressure, the nozzle diameter and shape as well as the flow rate of the solution are critical parameters that need to be adjusted. The optimization of these parameters is of high importance in order to achieve reproducibility of the fabricated films. Furthermore, the substrate temperature has a major impact on the sprayed solution and therefore the film creation. By adjusting the temperature, the evaporation of the residual solvent from the film, the spreading of the droplets on the surface and chemical reactions that take place in the sprayed solution and the final deposited material, can be tuned. The different regimes of the spray process, caused by different substrate temperatures, are described in more detail by a model by Viguié et al.[126] With increasing substrate temperature the phase and state of the particles that arrive at the substrate surface changes:

I. At low temperatures the droplets hit the surface in a liquid state and wet the substrate.
II. By increasing the temperature, the liquid is almost evaporated during the flight and non-reacted solid material hits the sample (commonly known as airbrush spray coating).
III. With higher temperatures, a vapor phase is reached, where the contained particles react or decompose during the flight or on the substrate (chemical vapor deposition).

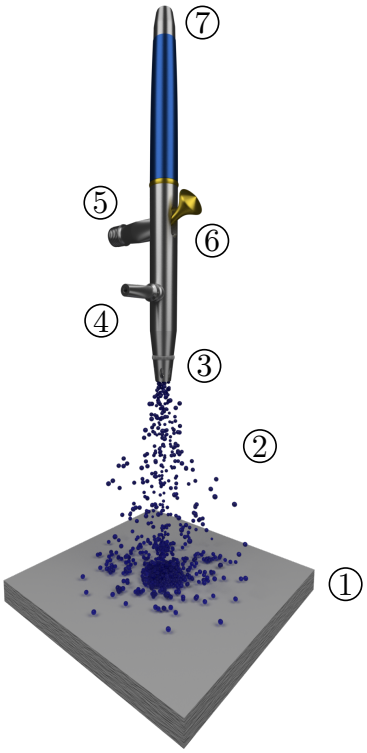

Figure 3.6
Schematic spray setup with substrate ① and spray cone ② exiting from the nozzle ③ of the spray gun of type Grafo T3 with the inlet for the spray solution ④ and the carrier gas ⑤. By pushing the knob at ⑥ the gas flow is opened and the spray process starts. The flow rate can be adjusted by fine tuning the opening of the nozzle with the control knob at ⑦.

IV. For even higher temperatures, the solvent is completely evaporated and the particles have already undergone a chemical reaction before they hit the substrate surface.

In the present thesis, an automatized spray setup is employed consisting of a rotatable mounting for a spray gun, a heatable sample stage with adjustable substrate to nozzle distance and a timer regulated carrier gas control. A schematic sketch of the spray process is depicted in Figure 3.6. If not other stated, the spray gun model Grafo T3 (nozzle ⌀ 0.4 mm) by Harder & Steenbeck is mounted with a substrate to nozzle distance of 16 cm and an incident angle of 90° (anti-parallel to surface normal of substrate). Dry nitrogen is chosen as carrier gas with a pressure of 2 bar. The nozzle opening is adjusted in order to set the flow rate of the solution to ~25 µL s^{-1}. A heating plate equipped with a massive copper block in order to ensure a homogeneous and stable temperature field is set to 80 °C. The sample is placed below the spray gun such that it is centered in the spray cone. Careful adjustment of the spray parameters to these settings reveals wet spray deposition (region I) for all samples fabricated in the present thesis. Hence, a certain degree of mobility is provided to the deposited material during film formation on the substrate. In total, 1 mL solution is sprayed with 10 s pulse duration and 5 s pause in between to allow the residual solvent to evaporate and to avoid rapid cooling of the heating stage caused by latent heat of vaporization. It is noteworthy to mention that solutions with high viscosity tend to spread inhomogeneous large droplets over the sample during the start of each spray

shot. Therefore, it is useful to adjust the spray protocol such that one single spray shot can be used. For spraying PEDOT:PSS thin films the spray protocol is slightly modified by using a larger substrate to nozzle distance of 19 cm and depositing the material in one single continuous shot with a flow rate of ~20 µL s^{-1}. In general, a low viscosity of the solution is required in order to achieve a high atomization yield. Thus, spray coating allows a reduced material consumption and coating of larger substrates as compared to spin coating.

3.2.3 Thermal Annealing

Thermal annealing is realized by holding a sample for a certain time at a defined elevated temperature. The annealing procedure is performed in order to serve several purposes. First, residual solvent evaporates and therefore the film is dried. Second, polymer chain relaxation is facilitated by keeping the samples at a certain temperature. This can have a strong influence on the nanometer scale morphology and crystallinity of polymer or polymer blend films.[127–129] In the present thesis, PEDOT:PSS thin films are annealed in the end of each deposition or post-treatment process for 10 min at 140 °C. For annealing, a RCT BASIC heat plate by IKA WERKE GMBH & CO. KG is used. A copper block fitted to the heater plate allows a homogeneous temperature distribution. Further, a contact thermometer is inserted into the copper block for active temperature control. After annealing, the samples are placed on a metal plate in order to rapidly cool down to room temperature.

3.2.4 Thermal Deposition

In order to characterize the performance of the investigated layers in a working device, the application of a back electrode is required. Thus, aluminum or gold contacts are evaporated by physical vapor deposition on top of the organic layers. Aluminum is used as back electrode in the OLED device stacks, while gold has been applied as electrodes for impedance measurements on highly conducting PEDOT:PSS electrodes. However, the evaporation procedure is kept the same for both devices. The samples are placed upside down on a shadow mask, which defines the position of the electrodes in the custom made setup, formerly implemented by Dr. Robert P. Meier.[130] Typically, an eight pixel electrode layout is used as depicted in Figure 3.1e. About 60 mg – 80 mg aluminum grains or gold are placed in a tungsten boat (BD482000-T, LEYBOLD OERLIKON) or tantalum boat (EVS7005TA, KURT J. LESKER), respectively. Both materials can resist a temperature of ~1600 °C, which is sufficient for melting of aluminum or gold. Under a working pressure of 1×10^{-5} mbar to 5×10^{-5} mbar, a high current of ~90 A (~180 A) is applied to evaporate a ~100 nm thick layer of aluminum (gold) on the samples. After the evaporation is finished, the chamber is vented and the samples are immediately measured.

3.3 Hierarchically Structured Porous ZnO

In the following section the fabrication of hierarchically structured porous zinc oxide layers is described. ZnO layers are cast from solution, which is prepared by sol-gel synthesis on the basis of the precursor material zinc acetate dihydrate (ZAD) and a sacrificial diblock copolymer. In this work, PS-*b*-PEO is used as structure directing template. In order to obtain the final scattering layers, various processes are carried out consisting of preparation of the sol-gel solution, the deposition of it on suitable substrates via spray coating, and a final calcination step where the polymer is combusted and removed while the crystallinity of the nanostructures is imparted. All preparation steps are carried out at ambient conditions. The resulting ZnO layers are investigated in the present work regarding their light scattering behavior for the use in organic light emitting diodes.

3.3.1 Sol-Gel Synthesis

In the beginning of the sol-gel synthesis all required glass ware and tools are pre-cleaned with the respective solvent. The ZAD precursor and the structure directing diblock copolymer PS-*b*-PEO are dissolved separately in different vials and are mixed in the end in order to obtain the final sample solution. The polymer concentration is kept constant at $25\,\mathrm{mg\,mL^{-1}}$. A schematic overview of the preparation steps for the final sample solution is depicted in Figure 3.7. The sol-gel synthesis starts with the dissolving of the copolymer template PS-*b*-PEO in a so-called good solvent, which dissolves both blocks equally well. In the present case, the solvent N,N-dimethylformamid (DMF) is used. The required amount of PS-*b*-PEO is weighed into a pre-cleaned glass vial which is filled up with the corresponding amount of solvent. As only half of the solvent volume is used it needs to be ensured that the polymer is dissolved completely in the reduced DMF volume. The remaining DMF is added to the required amount of ZAD, pre-weighed into another glass vial. Both vials are sealed and kept on magnetic stirrers for at least 30 min at room temperature in order to obtain clear solutions. Eventually undissolved parts or larger agglomerates are extracted by separately transferring both solutions into pre-cleaned glass vials each by using 0.45 µm pore sized PTFE filter, purchased from Carl Roth GmbH + Co. KG. Next, the required amount of water, which serves as so-called selective solvent (bad solvent), is added to the polymer/DMF solution. During another 30 min stirring procedure the micelle formation of the PS-*b*-PEO is started, induced by former addition of the selective solvent. After the second stirring step, the two solutions are mixed drop-wise into another pre-cleaned glass vial using a motorized syringe pump equipped with PTFE tubes. The pump of type PHD 2000 Infuse/withdraw by Harvard Apparatus is capable of controlling two syringes at the same time. The PTFE tubes, which are used to hold the sol-gel solution, have an inner diameter of 2 mm and a length of ~20 cm. The injection speed and therefore the mixing rate is kept constant at $1\,\mathrm{mL\,min^{-1}}$. The

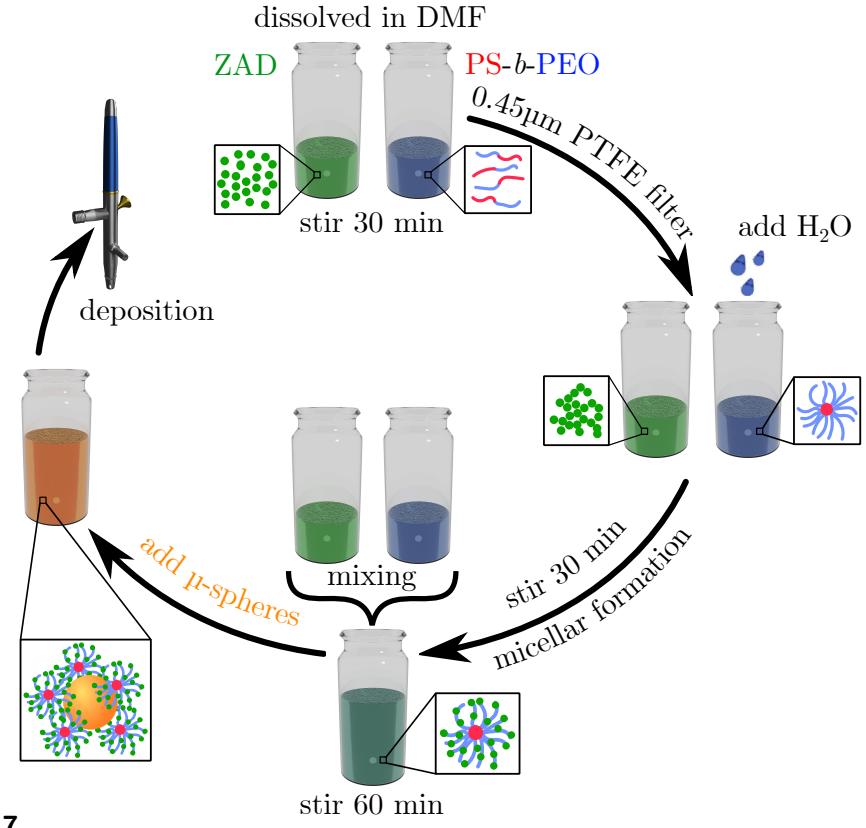

Figure 3.7
Graphical representation of sol-gel synthesis for ZnO thin films. Zinc acetate dihydrate (ZAD) and PS-*b*-PEO are dissolved in DMF in separate vials. After stirring for 30 min, both solutions are filtered using PTFE filters with a pore size of 0.45 µm. A small amount of the selective solvent H_2O is added to the polymer solution and both solutions are stirred for another 30 min in order to induce the micellar formation of the diblock copolymer. Then, both solutions are drop-wise mixed together and stirred for 60 min. Prior to deposition of the solution, the required amount of PS microspheres is added to the mixed sol-gel solution and the resulting one is immediately deposited via spray coating.

mixed solution is kept stirring during the whole process and for further 60 min after the solution transfer is finished.

In order to hierarchically structure the final ZnO layers, different amounts of PS microspheres are added into the solution in order to serve as additional template for larger sized pores. Therefore, the sol-gel solution serves as stock solution and is split into the required number of sample solutions that receive the different microsphere concentrations. As polystyrene is dissolved by DMF, the microspheres are added to the sol-gel solution shortly prior to deposition. The final solution is additionally stirred for ~10 s in order to support the mixture of the components and to minimize dissolution of the PS spheres. Then, the final solution is immediately deposited on the substrates.

The obtained thin films are stable at ambient conditions but require a calcination step in order to create the final scattering layers.

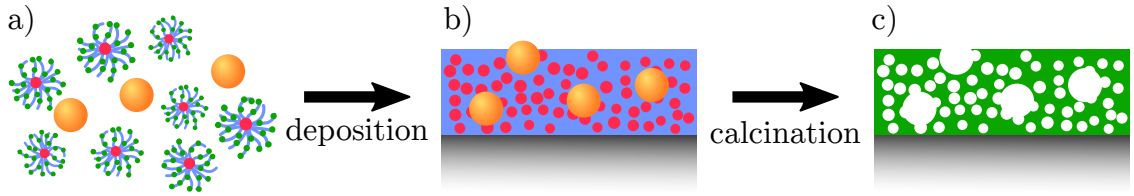

Figure 3.8
Sketch of fabrication process for hierarchically structured ZnO films. a) Micelle solution consisting of the structure directing diblock copolymer PS-*b*-PEO (micelles) with the aggregated ZnO nanoparticles (green) obtained from sol-gel synthesis. Addition of PS microspheres (orange) serve as template for a hierarchical structure. b) Composite film with embedded PS microspheres after deposition. c) Final ZnO film with hierarchical structure obtained after calcination and removal of the polymer template.

3.3.2 Thin Film Fabrication

As mentioned in Subsection 3.3.1 PS microspheres are added to the prepared sol-gel solution shortly prior to deposition. The time between the addition of microspheres and the deposition of the obtained mixture is kept <3 min. As thick films are required to serve as scattering layer, spray coating according to Subsection 3.2.2 is chosen for deposition of the sol-gel solution.

Therefore, acid cleaned glass substrates (see page 48) are placed on the 80 °C preheated sample stage. The spray gun is mounted in 16 cm distance to the substrate and is adjusted to a flow rate of 25 µL s^{-1}. In total, 1 mL solution is sprayed in 10 s long spray pulses separated by 5 s drying time in between. Prior to each film deposition, the setup is flushed with DMF in order to clean the spray gun. The deposited thin films are placed on a metal plate in order to rapidly cool down to room temperature and are calcined afterwards. High temperature treatment of the samples has two effects. Firstly, the polymer template is combusted and removed from the thin films. Secondly, calcination provides crystallinity and structural organization to the nanostructures generated by the diblock copolymer. Calcination is performed in ambient atmosphere using a tube furnace by GERO HOCHTEMPERATURÖFEN GMBH. The samples are placed in the center of the tube where the temperature is most stable and homogeneous. The two openings of the ceramic tube are closed with ceramic wool and aluminum foil. A calcination protocol using one ramp is programmed in order to expose the samples to a controlled temperature increase. A temperature ramp of 6.25 °C min^{-1} is set in order to slowly reach the desired temperature of 400 °C. The calcination time for the thin films is set to 30 min after that the furnace is automatically turned off and the samples cool slowly down to room temperature. Thus, the polymer template including the microspheres are removed and hierarchically structured thin films consisting of crystallized ZnO are obtained, as depicted schematically in Figure 3.8. As the whole process takes several hours, calcination of scattering layers is typically performed overnight.

3.4 PEDOT:PSS Thin Films

The second investigated layer for OLED applications consists of the polyelectrolyte poly(3,4-ethylene dioxythiophene):poly(styrene sulfonate) (PEDOT:PSS), introduced on page 51. Depending on the blend ratio listed in Table 3.1 it is either used as electron blocking layer (EBL) or as conducting polymeric electrode. The higher PSS amount in PEDOT:PSS Al 4083 leads to a lower viscosity and therefore thinner films via spin coating. More important is its work function, which fits better to the used adjacent functional layers and provides an optimized band alignment for enhanced charge carrier transport. Therefore, it is typically used as HTL/EBL between the electrode and the emitting layer. PEDOT:PSS PH 1000 on the other side shows a decreased amount of PSS in the blend, which has several effects. The most obvious one is the decreased solubility in water, which leads to an increased viscosity and strongly influences the deposition parameters. However, by reducing the amount of the insulating PSS, the conductivity of the thin film is raised and the work function is lowered. Those characteristics can be tuned by application of different treatments to the PEDOT:PSS solutions or thin films.[56] In this work, the focus is set on the characterization of PEDOT:PSS PH 1000 thin films as polymeric electrode. In the following, the sample preparation steps for the application of PEDOT:PSS thin films and their post-treatment are explained.

3.4.1 Solution Preparation and Deposition

As PEDOT:PSS is a polyelectrolyte consisting of hydrophobic PEDOT and hydrophilic PSS it forms a scrambled egg like structure in water[117] and tend to agglomerate, which has a negative impact on the deposition process and on the final film homogeneity. Therefore, before film deposition, the stock solution is placed for 15 min into an ultrasonic bath (US-B) in order to break up such agglomerates. Larger clusters and residual agglomerates are removed by transferring the ultrasonicated solution through a polyvinylidenfluorid (PVDF) filter with 0.45 µm large pores into a fresh glass vial. Such filtered PEDOT:PSS solution is stored until deposition on a shaker to prevent further agglomeration. The so-prepared PEDOT:PSS Al 4083 is directly used for deposition of the EBL in Chapter 7. All other PEDOT:PSS thin films in the present thesis are prepared using PH 1000 with lower PSS content. As depicted in the flow chart in Figure 3.9, further dilution of the purified stock solution is required depending on the desired deposition method.

Pristine

In order to achieve thin films with sufficient thickness, undiluted PEDOT:PSS is used in the fabrication process of polymeric electrodes from pristine thin films in Chapter 7.

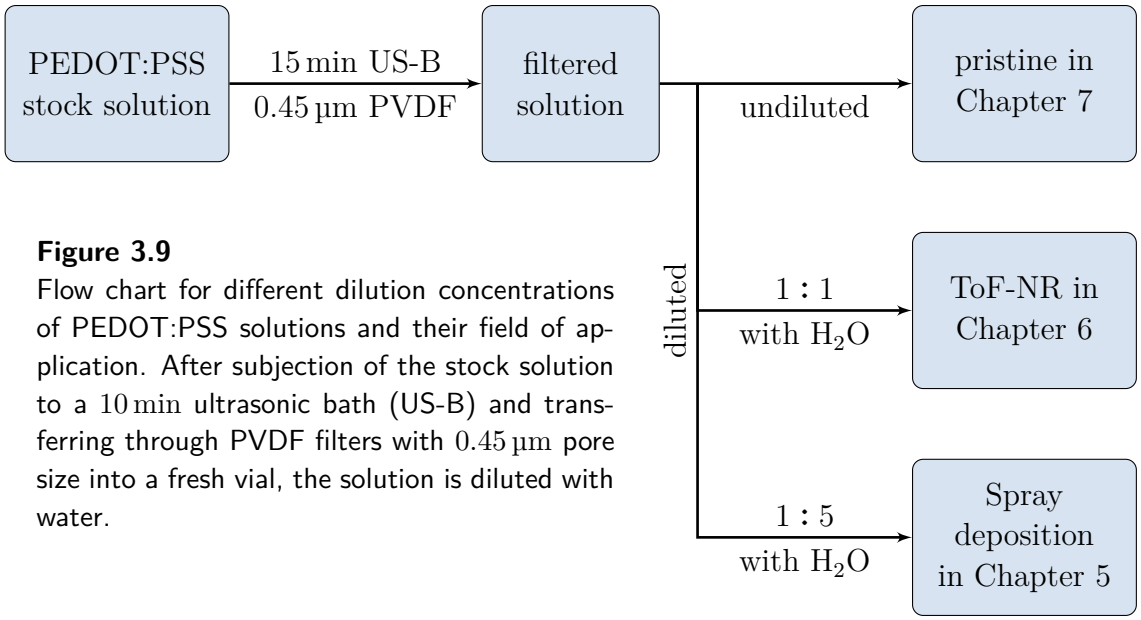

Figure 3.9
Flow chart for different dilution concentrations of PEDOT:PSS solutions and their field of application. After subjection of the stock solution to a 10 min ultrasonic bath (US-B) and transferring through PVDF filters with 0.45 µm pore size into a fresh vial, the solution is diluted with water.

Filtered : H_2O = 1 : 1

In order to achieve a sufficient homogeneous thin film on large substrates (Si, $7 \times 7\,cm^2$) for ToF-NR measurements in Chapter 6, a dilution of the stock solution is required. Therefore, the filtered PEDOT:PSS is diluted 1 : 1 by volume with H_2O and put for 1 min into the US-B to ensure full mixture.

Filtered : H_2O = 1 : 5

Spray deposition of PEDOT:PSS in Chapter 5 requires a significantly reduced viscosity of the stock solution to prevent plugging of the spray gun. Therefore, the filtered PEDOT:PSS PH 1000 is diluted 1 : 5 by volume with H_2O and subjected to a 1 min US-B to ensure full mixture.

Zonyl Additive for Structure Modification

The fluorosurfactant Zonyl is used in order to enhance the wettability of PEDOT:PSS on the substrate during thin film deposition. Furthermore, the surfactant induces a change in the morphology by phase separation of the PEDOT and PSS components that leads to an increased PSS capping layer thickness.[131] In addition, the overall film thickness is increased compared to the deposition of pristine PEDOT:PSS with the same parameters. The influence of Zonyl treatment on PEDOT:PSS thin films is analyzed in Chapter 6 regarding to the electrode performance. In contrast to all other treatments on PEDOT:PSS that are used in the present thesis, Zonyl is added prior to film deposition into the solution. Due to the amphiphilic nature of Zonyl, it is found to be easiest to first weigh the desired amount of Zonyl before adding the corresponding amount of PEDOT:PSS. In the present thesis, 1 wt.% Zonyl is added to the filtered 1 : 1 diluted solution of the latter and mixed for one to two hours on a shaker.

Deposition by Spin Coating

In this work, the mainly used deposition technique for PEDOT:PSS thin films is spin coating (Subsection 3.2.1). Hereby, the substrates are cleaned according to the acid cleaning protocol (glass, silicon) or organic cleaning protocol (ITO, FTO) on page 48 and page 49, respectively. Prior to deposition, the substrate surface is activated using an oxygen plasma cleaning procedure as explained on page 49. As the spin coating parameters vary with the used solution the detailed parameters are given at place in the chapters. However, the overall procedure is as following: The (diluted) PEDOT:PSS solution is dropped via a pipette on the substrate such that the surface is completely covered. After closing the lid, the spin coating process is started immediately according to Subsection 3.2.1. Then, the final thin films are subjected to a subsequent thermal annealing process according to Subsection 3.2.3. Thermal annealing is performed after each deposited PEDOT:PSS layer for 10 min at 140 °C. If thicker films are required, the spin coating with subsequent annealing steps are repeated as necessary.

Deposition by Spray Coating

As spin coating is not suitable for depositing homogeneous PEDOT:PSS electrodes on top of rough ZnO scattering layers, spray coating according to Subsection 3.2.2 is employed in Chapter 5. Therefore, a diluted PEDOT:PSS solution (1 : 5) is required to avoid plugging of the spray gun. While deposition on substrates requires a cleaning process containing acid or organic cleaning including a subsequent oxygen plasma, this step is skipped for already coated samples such as ZnO scattering layers in order to prevent damage to the layers. For deposition, the samples are placed on a heating plate equipped with a copper block, which is preheated to 80 °C. For PEDOT:PSS a substrate to nozzle distance of 19 cm is used and the flow rate is set to ~20 µL s^{-1}. After deposition, the samples are subjected to the same annealing procedure as described above (140 °C for 10 min on heating plate).

3.4.2 Post-Treatment

Untreated PEDOT:PSS PH 1000 thin films reveal typically an electrical conductivity of ~1 S cm^{-1} and therefore can be considered as insulating. In order to raise their conducting properties to elevated values in the region of typically used TCOs, several treatments have been developed, either by adding the additives into the solution or treating the final films after deposition (post-treatment). Those treatments are often based on high boiling point solvents and are expected to have an influence on the thin film morphology. Consequently, they are referred to as secondary doping. In the present thesis, only post-treatments are applied and their impact on PEDOT:PSS thin films is examined. In the following, the applied post-treatment procedures for the different used materials are explained in detail.

High Boiling Point Solvents

Besides the typical used solvent DMSO, ethylene glycol (EG) is a widely used solvent for enhancing the conducting properties of PEDOT:PSS thin films. Therefore, EG is chosen as representative among the various possible solvents for PEDOT:PSS conductivity enhancement and serves for fabrication of reference samples in Chapter 7. In the present thesis, EG post-treatment is performed with both, spin coating and spray deposition techniques.

Post-treatment via spin coating is realized by pipetting EG on top of the annealed PEDOT:PSS thin film, which is placed on the spin coating stage beforehand. For typical used substrate sizes of $2.5 \times 2.5\,\mathrm{cm}^2$ a volume of 400 µL – 500 µL is necessary to cover the whole film. Larger sample sizes such as $7 \times 7\,\mathrm{cm}^2$ silicon substrates used for ToF-NR in Chapter 6 require ~7 mL for full coverage of the sample. After 3 min reaction time with a closed lid, the excess amount of EG is spun off via spin coating with a rotation speed of 1500 rpm for 60 s. In order to remove residual solvent and dry the film completely an additional annealing step for 10 min at 140 °C is performed.

Post-treatment via spray coating requires less material compared to spin coating as the spray cone defines the homogeneous coverage of the sample instead of the surface tension of the sample in the case of spin coating. Therefore, 200 µL of EG is sufficient to wet the whole sample surface. The annealed PEDOT:PSS thin films are placed on the heated sample stage (80 °C) and centered in the spray cone. In order to avoid inhomogeneous spattering over the sample of the high viscous solvent, the whole amount of EG is completely deposited in one single continuous spray pulse with a flow rate of $\sim 15\,\mu\mathrm{L\,s}^{-1}$. The flow rate and further the substrate to nozzle distance (19 cm) is kept the same as for spray deposition of PEDOT:PSS. Finally, the post-treated samples are transferred to a second heating plate and subjected to 10 min annealing at 140 °C in order to evaporate the residual EG and support polymer chain relaxation.

Acid Treatment

In order to extract excess PSS from PEDOT:PSS thin films, acid post-treatment is performed. The influence of such acid treatment on the morphological structure, film composition and electrode performance of PEDOT:PSS thin films is subject of investigation in Chapter 7. Therefore, the prepared pristine PEDOT:PSS thin films are subjected to a post-treatment with different acids. In addition, the resilience against water of the post-treated films is tested by a subsequent washing step.

Acid post-treatment is realized at room temperature by placing the PEDOT:PSS coated samples on a flat, acid resistant base plate. The acid is dripped on the sample via a glass pipette such the whole sample of $2.5 \times 2.5\,\mathrm{cm}^2$ size is covered. In the present thesis, an amount of 700 µL was necessary for HCl, HNO_3 and H_2SO_4, while 300 µL of HCOOH was sufficient due to its better wetting on the PEDOT:PSS films. After a 10 min reaction time, the samples are fixed with tweezers and dried by carefully blowing away the residual amount of acid using a continuous, dry nitrogen flow. As

the acid soaked PEDOT:PSS films easily tear off during this treatment, the gas flow rate should be kept low in order to avoid destroying of the film. The drying procedure is finalized by transferring the samples to a heating plate and anneal them for 10 min at 140 °C according to Subsection 3.2.3.

If required, washing of the acid treated samples is performed in H_2O. Hence, the dried samples are slewed with the aid of tweezers subsequently for ~5 s in three different beakers containing 300 mL H_2O each. The excessive washing procedure has two effects. On one hand, it is performed in order to assure the removal of any residual acid components from the film. On the other hand, it is used to test the resilience of the acid treated films against water. As a final step, the washed samples are again subjected to a last drying procedure as described above. Thus, the wet samples are carefully dried under a continuous flow of dry nitrogen gas and subsequently transferred to a heating plate and annealed for 10 min at 140 °C following the well known annealing protocol given in Subsection 3.2.3.

3.5 OLED Assembly

This section explains the general procedure and sequence of OLED sample preparation used in the present thesis. As the focus of the present work is set on the investigation of additional functional layers in a typical OLED device stack, namely scattering layers and polymeric electrodes, a standard emitter is selected for device fabrication. Thus, Super Yellow® (PDY-132) (see page 53) is used in fabrication of OLED devices. Below, the preparation of the emitter solution is given and followed by the two used device stacks. As the subject of investigation are ZnO scattering layers and polymer electrodes consisting of acid treated PEDOT:PSS PH 1000, the fabrication of all other layers is kept constant. Therefore, the thickness of the electron blocking layer (PEDOT:PSS Al 4083), the emitting layer (Super Yellow®) and the top electrode (aluminum) for the prepared layers is measured as (34 ± 7) nm, (42 ± 5) nm, and (200 ± 10) nm, respectively. In contrast to a common OLED device as introduced in Section 2.4, here, no electron transport layer (ETL) or hole blocking layer (HBL) is applied between the aluminum back electrodes and the emitting material. This drawback is owed to conditional of manufacturing limitations, which has to be taken into account when evaluating the obtained device performance, as the omitted ETL/HBL lowers the maximum achievable device efficiency. However, the obtained OLEDs are considered as suitable to serve as test devices for comparative evaluation of the investigated functional layers.

3.5.1 Preparation of Emitter Solution

The Super Yellow® solution is prepared one day in advance to assure full dissolution of the solute. Hence, the required amount of solution is calculated and the correspond-

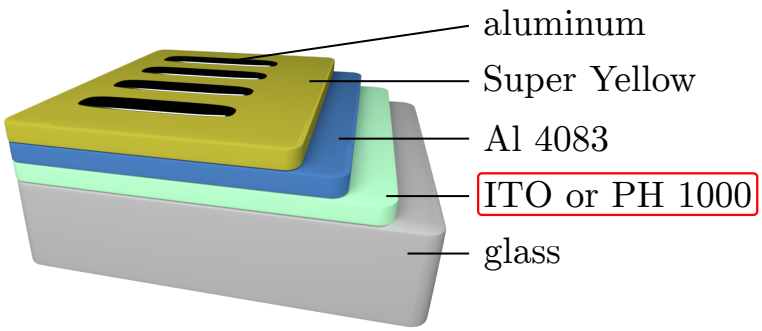

Figure 3.10
OLED stack of the prepared devices. For all devices the material and deposition of the top electrode (aluminum), the emitting layer (SUPER YELLOW®) and the EBL (PEDOT:PSS Al 4083) is kept constant. The red box marks the layer which is exchanged and investigated in the present thesis. ITO coated glass substrates are used for fabrication of reference devices, while for ITO-free devices the ITO layer is replaced by two layers of subsequently spin coated PEDOT:PSS PH 1000 subjected to different treatments. Note: Due to conditional of manufacturing limitations the application of an ETL or HBL is omitted.

ing amount of PDY-132 is weighed into a pre-cleaned glass vial using a micro balance by SARTORIUS AG. Cleaning of the vials and other used items with contact to the sample is performed by rinsing with the corresponding solvent and subsequent drying under a nitrogen flow. The weighed SUPER YELLOW® is dissolved in toluene with a concentration of $3\,\mathrm{mg\,mL^{-1}}$. The sealed vial is wrapped into aluminum foil in order to prevent degradation by incident light and stirred over night. The prepared emitter solution is then ready for spin coating. Note, for spray coating of the emitter solution a concentration of $1\,\mathrm{mg\,mL^{-1}}$ is found to be sufficient.

3.5.2 Reference OLED Stack

The standard OLED device stack used in the present thesis is based on an ITO bottom electrode and is depicted in Figure 3.10. All investigated ITO-free devices are compared to the performance of the here described one. The fabrication is performed as following: First, the ITO substrates are patterned in order to avoid short circuits between the bottom electrode and the contact pins during device characterization (see page 47). Then, the structured ITO substrates are subjected to the organic cleaning protocol with subsequent oxygen plasma, described on page 49. PEDOT:PSS Al 4083 serves as electron blocking layer and is spin coated on top of the ITO layer according to Subsection 3.2.1 (2500 rpm, 60 s) and followed by an annealing step as described in Subsection 3.2.3 (10 min at 140 °C), which yields a film thickness of ~34 nm. 300 µL of PEDOT:PSS Al 4083 are sufficient to completely cover the $25 \times 25\,\mathrm{mm^2}$ sized substrates. As toluene is an orthogonal solvent for the deposited PEDOT:PSS layer, 400 µL of the previously prepared PDY-132 solution can safely be applied by spin

coating with a rotation speed of 1500 rpm for 60 s, yielding a film thickness of ~42 nm. After a second annealing step, the bottom electrode is exposed at two positions for contacting purpose by mechanically wiping with a toluene soaked cotton stub. 200 nm aluminum contacts are thermally evaporated according to Subsection 3.2.4 in order to serve as top electrodes and to define the eight pixel layout of the samples. The freshly prepared OLED devices are immediately characterized by their current voltage characteristics and emission efficiency.

3.5.3 ITO-free OLED Stack

In order to test the performance of the investigated polymeric electrodes in a working device, ITO-free OLEDs are fabricated. The ITO-free OLED stack only distinguishes from the reference OLED by replacing the ITO layer with two layers of subsequently spin coated PEDOT:PSS PH 1000 (Figure 3.10). A graphical representation of the general ITO-free OLED preparation routine is depicted in Figure 3.11. Glass substrates are cleaned according to the acid cleaning protocol described on page 48 with a subsequent oxygen plasma (page 49). Two layers of filtered pristine PEDOT:PSS PH 1000 solution are spin coated (500 µL each, 1200 rpm, 60 s) on top of the cleaned glass substrates according to Subsection 3.2.1. After each layer subsequent annealing following Subsection 3.2.3 is performed. The PH 1000 layers are subjected to different post-treatments according to Subsection 3.4.2 in order to achieve highly conducting polymeric electrodes that serve as bottom electrode.

On top of the polymeric electrodes an additional PEDOT:PSS Al 4083 layer is applied to serve as electron blocking layer. In order to be able to contact the bottom electrode during later measurements, the Al 4083 layer is structured by covering two edges of the PH 1000 electrodes with PTFE tape (Figure 3.11d). The deposition and annealing of the Al 4083 layer is performed in the same way as for the reference device (300 µL, 2500 rpm, 60 s).

After application of all PEDOT:PSS layers, the polymeric electrode needs to be patterned in the same way as ITO electrodes such that the top electrode can be contacted without the risk of short circuits. Therefore, the two edges adjacent to the previously masked ones are mechanically wiped with an acetone soaked cotton stub in order to expose the underlying glass substrate (Figure 3.11e).

The deposition of the emission layer (PDY-132) and the aluminum top electrodes are performed in the same way as for the reference device.

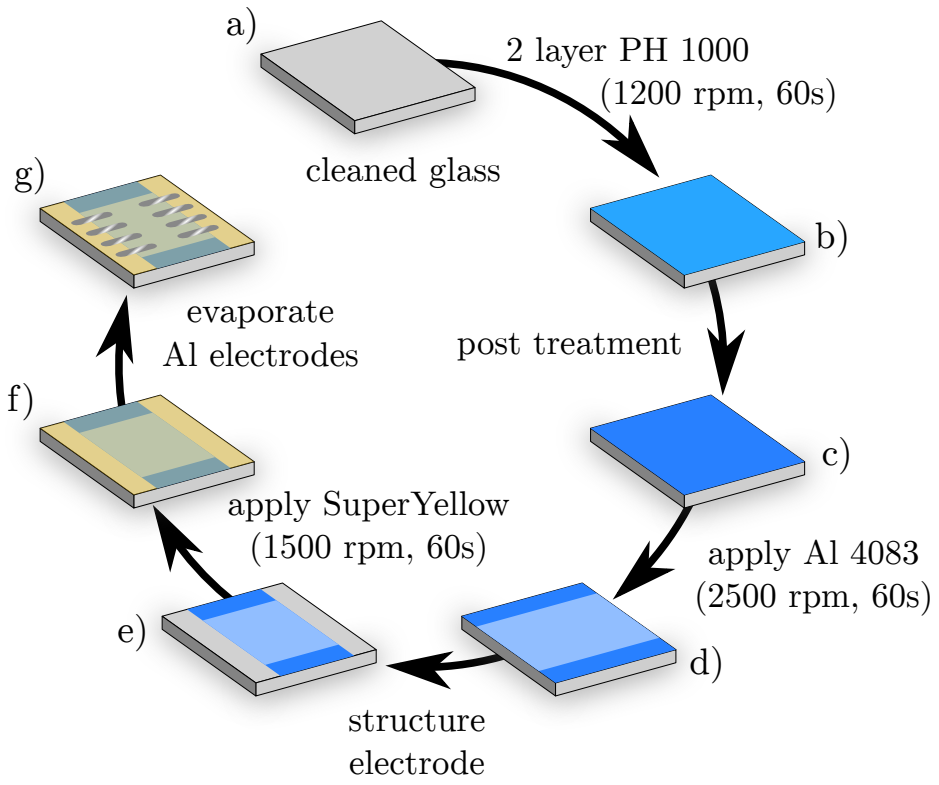

Figure 3.11
Graphical representation of the fabrication process for ITO-free OLEDs. a) Glass substrate (acid cleaned, O_2 plasma). b) Spin coating of two layers of PEDOT:PSS PH 1000. c) Post-treatment in order to make PEDOT:PSS PH 1000 highly conductive. d) Masking and application of PEDOT:PSS Al 4083 as EBL. e) Structuring of PEDOT:PSS back electrode. f) Application of SUPER YELLOW® as emitting layer. g) Thermal evaporation of aluminum top electrodes. Furthermore, thermal annealing ($10\,\mathrm{min}$, $140\,^{\circ}\mathrm{C}$) is performed after deposition of each single layer.

CHAPTER 4

Sample Characterization

The focus of the present thesis is on the characterization of functional layers employed in OLED devices. Hence, thin film characterization techniques are utilized to determine their physical properties. Since for light emitting devices the transmissive behavior of the investigated functional layers is of major interest, UV-Vis spectroscopy is employed to determine the absorption behavior (Section 4.1). Additional to the transmittance, the chemical composition of polymeric electrodes is probed with X-ray photoelectron spectroscopy (XPS). The methods used to characterize the electronic properties of thin films are treated in Section 4.2. Four-point probe measurements and impedance spectroscopy are employed in order to determine the DC and AC response of polymeric electrodes. Methods for basic structural characterization in real space are explained in Section 4.3. Thereby, optical microscopy is used to evaluate the homogeneity of films and obtain the pixel size of OLEDs. Profilometry and atomic force microscopy (AFM) is performed to determine the film surface roughness and thickness of the functional layers, while scanning electron microscopy (SEM) is used to evaluate the real space structure in detail. Furthermore, cross-sectional imaging is used to investigate layer stacks of ZnO/PEDOT:PSS bilayers. As real space imaging techniques are limited to a small section of a sample, scattering methods are employed to obtain structural information with more statistical relevance (Section 4.4). Here, the thin films are probed with X-rays or neutrons to obtain (in situ) structure information. X-ray reflectometry (XRR) and time of flight neutron reflectometry (ToF-NR) are employed to characterize the vertical film composition of polymeric electrodes upon the exposure to saturated water atmosphere. Grazing-incidence X-ray scattering techniques are used to probe the lateral structure of ZnO light-scattering layers in the range of nm

(GISAXS). As the crystallinity of polymeric electrodes has strong impact on their electronic properties, GIWAXS measurements are conducted to determine the influence of different treatments upon the device performance. In order to obtain a structure-function relation of ZnO light-scattering layers, the angular resolved scattering has to be measured. Therefore, the construction and working principle of a goniophotometer setup is given in Section 4.5. The custom-built setup is capable to measure the angular and wavelength dependent scattering of thin films or the emission of OLEDs, respectively. Furthermore, the total emission of OLEDs is determined via an optional integrating sphere. The investigated OLEDs are connected to a KEITHLEY source meter to obtain simultaneously the current-voltage characteristic of the investigated devices.

4.1 Spectroscopic Characterization

4.1.1 UV-Vis Spectroscopy

In order to characterize the optical properties of thin films regarding their absorption and transmission behavior from the ultraviolet (UV) to the near-infrared (IR) region of light, UV-Vis spectroscopy measurements are performed. This enables an analysis of the samples regarding their optical band gap and the overall transmissive behavior, which is of crucial importance for the performance of transparent electrodes. Spectroscopic measurements are performed with two different instruments, both supplied by PERKINELMER, namely LAMBDA 35 and LAMBDA 650 S. Those instruments are equipped with a deuterium and a tungsten-halogen light source to cover the whole visible light spectrum and beyond, from the UV to IR range. For both instruments the measurement procedure and working principle is the same. A mirror directs the emitted light from one of the lamps towards a filter and collimator setup. Afterwards, the wavelength is selected by a monochromatic mirror and a subsequent slit, which is set to 1 nm width. The monochromatic light is equally split into two beams, whereby one passes the sample and the other one serves as reference. Afterwards, the intensity of both beams is detected via photodiodes. The transmitted light intensity I is compared to the unobscured intensity I_0, which defines the transmittance $T(\lambda)$ of the material. In general, the transmittance of a sample is given by the Lambert-Beer's law, whereas losses due to reflection and scattering are neglected:

$$T(\lambda) = \frac{I(\lambda)}{I_0(\lambda)} = \exp\left(-\beta(\lambda)\, d\right), \tag{4.1}$$

with the absorption coefficient β and the sample film thickness d. In order to account for the transmittance of the substrate (e.g. glass), a reference measurement

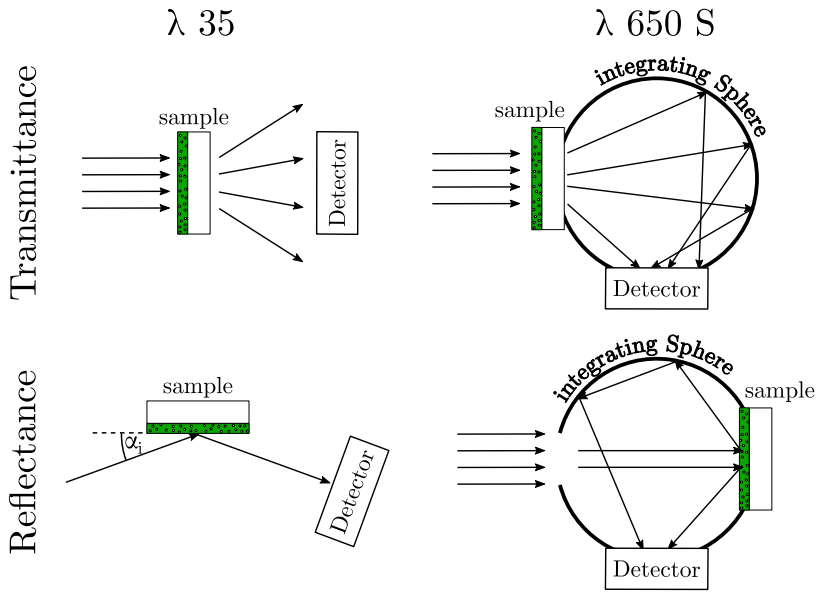

Figure 4.1
Available UV-Vis measurement setups. PerkinElmer Lambda 35 (left column) enables direct transmittance and reflectance ($\alpha_i = 45°$) measurements, omitting scattered and refracted light. PerkinElmer Lambda 650 S (right column) enables measurement of the total transmitted/reflected light intensity by the built-in integrating sphere with 150 mm diameter.

is performed in the beginning and the transmittance of the thin film is obtained by correcting the raw signal of the whole sample:

$$T(\lambda) = \frac{T_{\text{raw}}(\lambda)}{T_{\text{ref}}(\lambda)}, \tag{4.2}$$

with the measured transmittance T_{raw} and the substrate contribution T_{ref}. In spectroscopy often the absorbance $A(\lambda)$ of a material is of interest, which can be deduced from the transmittance by:

$$A(\lambda) = \frac{\beta(\lambda)\, d}{\ln 10} = -\log_{10} T(\lambda) \tag{4.3}$$

$$\tag{4.4}$$

Therefore, the absorption coefficient β can be expressed either as a function of the absorbance or the transmittance:

$$\beta(\lambda) = \frac{1}{d} A(\lambda) \ln 10 = -\frac{1}{d} \ln T(\lambda) \tag{4.5}$$

The absorption coefficient is normalized to the sample's film thickness and therefore is a material specific parameter, which enables a comparison of differently prepared samples.

The setups for the measurements performed with these two instruments are depicted in Figure 4.1. The instruments distinguish regarding the detectable wavelength range and the detectable solid angle. The detectable range of the LAMBDA 35 instrument is 190 nm – 1100 nm with a scanning speed set to 240 nm min^{-1}. The lamp change from tungsten-halogen to the deuterium light source is performed at 326 nm. For this instrument scattered or refracted light is omitted and thus, only direct transmittance or reflectance spectra are recorded. For reflectance measurements, a PELA1025 mirror from PERKINELMER is used, which provides a specular reflectance measurement with an incident and exiting angle of 45°.

The second instrument LAMBDA 650 S is equipped with an integrating sphere of 150 mm diameter (Lambertian surface), which allows the detection of the total transmitted (reflected) light intensity. The spectra are recorded with a scanning speed set to 266 nm min^{-1} in a wavelength range from 250 nm – 950 nm. The lamp change is performed at 319.2 nm. Before a measurement is conducted, the spectrometer sensitivity of both devices is calibrated according to 100 % and 0 % transmitted intensity, the so-called auto-zero (blank beam) and blocked-beam measurement, respectively. After each measurement, the recorded transmittance is normalized to 1.

4.1.2 X-ray Photoelectron Spectroscopy (XPS)

A widely used technique to study the compositions of materials is X-ray photoelectron spectroscopy (XPS). Its principle is based on the absorption of light and the resulting photoelectric effect. In order to avoid scattering of the emitted photoelectrons on air, XPS measurements are usually performed under high vacuum. While UV, visible light, or lasers are often used as light source to determine the work function of a material, X-rays render the examination of stronger bound core electrons. Due to the characteristic electron binding energy for different elements and their core levels, the identification of different species in a sample is possible. Furthermore, by comparing the number of detected electrons of the identified species a quantitative determination of the composition is enabled. The sample is hit by monochromatic X-rays, typically in the range of several keV, and eventually emits photoelectrons. The electrons then pass through an electromagnetic lens system, where the exposure to an electric field allows deflection and sorting according to their kinetic energy before they are recorded via an hemispherical detector array. By measuring the kinetic energy of the emitted photoelectrons, one can determine their binding energy E_B to the emitting element by:

$$E_\text{B} = E_\text{ph} - (E_\text{kin} + \Phi_\text{spec}), \tag{4.6}$$

where E_ph is the energy of the incident X-ray photons, E_kin the kinetic energy of the emitted electrons, and Φ_spec the work function of the spectrometer/detector itself. Φ_spec is an adjustable correction factor of the instrument, taking into account the

loss in kinetic energy of the photoelectrons as they are absorbed by the detector. In addition, surface charges on the sample may cause an energetic deviation and therefore a positive or negative shift in binding energies. In order to overcome this shift, typical XPS spectra need to be corrected according to a charge reference. For this purpose, adventitious carbon is commonly used, due to its presence on the surface of all air exposed samples. Therefore, all spectra in this work are shifted according to the C 1s signal, which is set to 285.0 eV.

In addition, different bonding types with different elements cause a change in the electronic environment of the probed species. Depending on the difference in electronegativity of the involved elements, the emitted photoelectrons vary slightly in binding energy based on Coulomb repulsion/attraction of the partly charged element in comparison to its neutral state. XPS enables high resolution spectra of a specific energy band in the range of tens of eV for a core level. Thus, the small shifts in binding energy are detectable, which permit to draw conclusions about the bonding environment and the related oxidation level of species. Hence, XPS renders not only for determining the quantitative chemical composition of a sample, but also for the different oxidation states of the same element. It is noteworthy to mention that despite of the high penetration depth of X-rays, the path length of the generated electrons is typically in the range of a few nm. Therefore, the information depth for XPS is very limited and the method is considered as surface sensitive. The obtained binding energy can be compared to several databases such as NIST[132] to identify specific elements and their bonding environment.

The measurements in this work were performed in the group of Jonathan Veinot at the University of Alberta, Canada. The used instrument was an AXIS 165 by Kratos, which was operated with a Mg-K_α X-ray source producing photons with an energy of E_{ph} = 1.254 keV. Thin PEDOT:PSS films were prepared on FTO substrates to avoid charging effects on the sample surface due to released photoelectrons. Data analysis was performed using the software CasaXPS v 2.3.13.

4.2 Electronic Characterization

4.2.1 Four-Point Probe Measurements

The sheet resistance of the investigated thin films is determined with a four-point probe setup equipped with a Tektronix Keithley 2400 source meter in combination with a Cascade Microtech C4S 54/5 3208 probe. The probe consists of four equally distant tungsten carbide test prods (l = 1.27 mm) with tip radii of 127 µm. The pins are pressed onto the sample surface with a spring force of 40 g – 70 g to assure good electrical contact. By sweeping a current I from pin 1 to pin 4 through the thin film, the voltage drop V between pin 2 and 3 can uniquely be measured. Thus, the measurement method is free of resistance contribution from wires or contacts. In

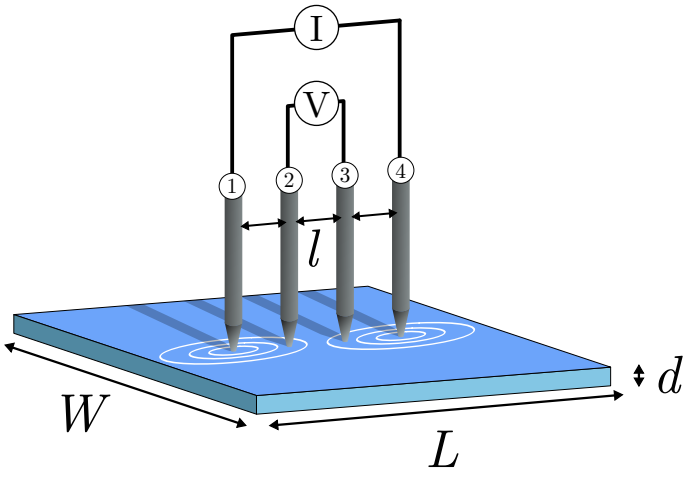

Figure 4.2
Scheme of a four-point probe for sheet resistance measurement. Four pins $(1-4)$ with equal distance l are brought into contact with the sample surface. The sample's dimensions are described with the width W, length L, and film thickness d. While running a current I from pin 1 to 4, the established potential V between pin 2 and 3 is measured.

Figure 4.2 a schematic depiction of the measurement setup is shown. In this case, the electrical conductivity σ between two probes is given by Equation 4.7, where ρ is the film's resistivity, I the current, V the established potential between two probes in distance l and a geometry correction factor F that takes into account the dimensions of the sample[133]

$$\sigma = \frac{1}{\rho} = \frac{I}{V}\frac{1}{2\,\pi\,l\,F}. \tag{4.7}$$

To obtain a reliable measurement the sample dimensions must be much larger than the tip distance l. Thus, the current flow between the tips is not impaired by edge effects of the sample. For $l \ll W \wedge l \ll L$, the sample can be considered as infinite large compared to the measurement probe. In the case of thin films is $l \gg d$ and the correction factor becomes $F = 1$. Thus, Equation 4.7 yields the sheet resistance $R_\square$ of a thin film, which is used in the present thesis:

$$R_\square = \frac{1}{\sigma\,d} = \frac{\rho}{d} = \frac{V}{I}\frac{\pi}{\ln 2}. \tag{4.8}$$

To clearly distinguish the sheet resistance, its unit is given as $\Omega\,\square^{-1}$. Hereby, the value describes the resistance through a square of any size perpendicular to the current flow. Thus, the $\square$ shows that the given value is related to a thin film and not a bulk material. The measurement requires an ohmic behavior of the investigated thin film, resulting in a linear dependence of $V(I)$. Therefore, current sweeping is set to ranges smaller than $-100\,\mu\text{A} - 100\,\mu\text{A}$ with the compliance set to $100\,\text{V}$ to avoid charging effects at the contacts. Equation 4.8 shows the sheet resistance is dependent on the film thickness.

Therefore, typically the conductivity σ is used to compare the performance of thin film electrodes.

As for transparent electronic devices the transmittance $T(\lambda)$ of the used materials is of high importance, it is often related to the sheet resistance to obtain a figure of merit (FoM) for the performance of a transparent electrode, i.e. a transparent conducting organic thin film such as PEDOT:PSS.

$$T(\lambda) = \left(1 + \frac{Z_0}{2\,R_\square}\frac{\sigma_{\mathrm{op}}(\lambda)}{\sigma_{\mathrm{dc}}}\right)^{-2}$$

$$\Rightarrow \mathrm{FoM} = \frac{\sigma_{\mathrm{dc}}}{\sigma_{\mathrm{op}}(\lambda)} = \frac{Z_0}{2\,R_\square\left(\dfrac{1}{\sqrt{T(\lambda)}} - 1\right)}, \tag{4.9}$$

where $\sigma_{\mathrm{op}}(\lambda)$ and σ_{dc} are the optical and the direct current conductivities, respectively and $Z_0 = 377\,\Omega$ is the impedance of the free space.[134] The minimum requirements for transparent electrodes is considered as $T > 90\,\%$ and $R_\square < 100\,\Omega\,\square^{-1}$. Therefore, the minimum industry standard corresponds to a FoM > 35.[135,136]

4.2.2 Impedance Spectroscopy

Potentiostatic electrochemical impedance spectroscopy (PEIS) is used to measure the frequency dependent response of a material between two contacts upon an AC signal. In the frame of this work it is applied to examine the possible application of PEDOT:PSS electrodes for AC electronic components. The measurement is performed by applying a small sinusoidal voltage around a constant potential and recording the current flow through the sample. Thus, the AC dependent resistance is measured as the impedance Z, consisting of a real and an imaginary part:

$$Z = R + \mathrm{i}\,X = \mathrm{Re}(Z) + \mathrm{i}\,\mathrm{Im}(Z) = |Z|\exp(\mathrm{i}\,\Phi). \tag{4.10}$$

The obtained data reveal information about the ohmic resistance R and the phase shift Φ between the applied and the recorded signal and therefore can be used to evaluate the usable frequency range for AC devices. The collected data is typically depicted as $-\mathrm{Im}(Z)$ versus $\mathrm{Re}(Z)$, the so-called Nyquist plot. In addition, representation in the so-called Bode plot is as well widely used, where the absolute value of the impedance $|Z|$ and the phase shift Φ are plotted versus the logarithmic frequency f. For most systems a detailed physicoelectrical model is unavailable.[137] Thus, modeling of the obtained data is typically realized using an equivalent circuit that reveals the electrical characteristics of the investigated samples. Such an equivalent circuit is in this case built up by combinations of ideal resistors R, inductors L and capacitors C, which can have a non-ideality factor α in order to account for sample inhomogeneities.

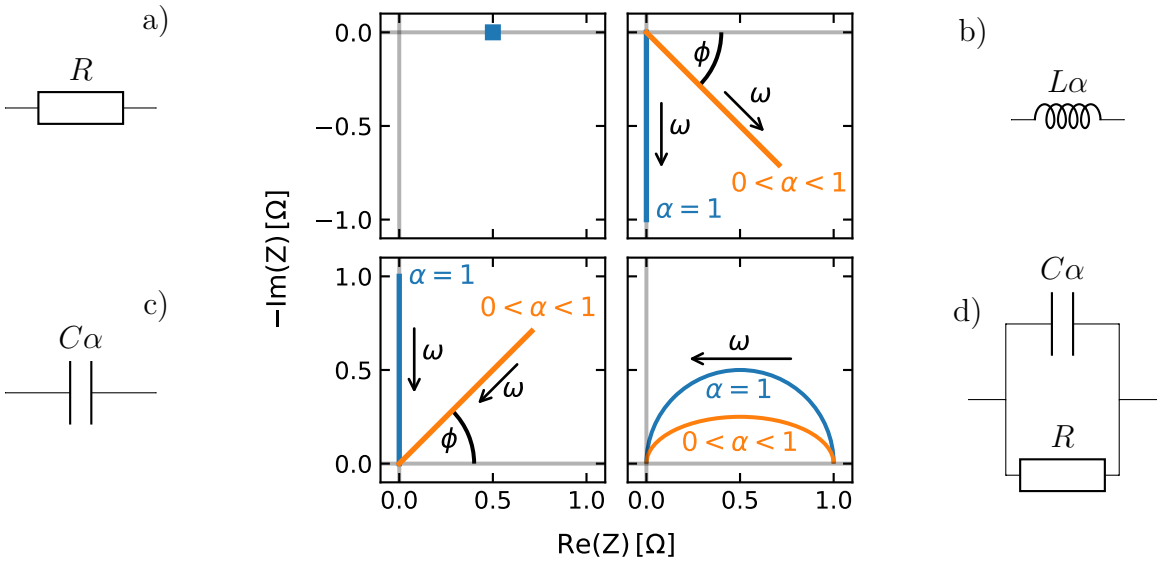

Figure 4.3
Nyquist plots of some basic components used in equivalent circuit modeling for impedance spectroscopy. The corresponding equivalent circuit is depicted next to the impedance spectrum it creates. a) Resistor, b) non-ideal inductor, c) non-ideal capacitor, d) parallel circuit of capacitor and resistor, also known as constant phase element.

Each different element in an equivalent circuit has its own contributions to the overall impedance Z, which is described in the following equations:

$$Z_{\mathrm{R}} = R \tag{4.11}$$

$$Z_{\mathrm{L}\alpha} = (\mathrm{i}\,\omega)^{\alpha}\, L \overset{\alpha=1}{=} \mathrm{i}\,\omega\, L \tag{4.12}$$

$$Z_{\mathrm{C}\alpha} = \frac{1}{(\mathrm{i}\,\omega)^{\alpha}\, C} \overset{\alpha=1}{=} \frac{1}{\mathrm{i}\,\omega\, C} \tag{4.13}$$

The dimensions for the modified inductance and capacitance are $\mathrm{H\,s}^{\alpha-1}$ and $\mathrm{F\,s}^{\alpha-1}$, respectively, in order to maintain the correct units. For $\alpha = 1$ the modified versions of $L\alpha$ and $C\alpha$ are equivalent to an ideal inductor and capacitor. Except for the resistor, all other components depend on the applied signal frequency $f = 2\pi\omega$. Therefore, a sinusoidal voltage over a wide range of frequencies f is applied to the system in order to reveal information about the values and arrangement of the single components and hence the properties of the investigated samples.

In Figure 4.3, typical Nyquist plots of the above mentioned basic components are depicted. As seen in Equation 4.11 the imaginary part of the impedance for an ohmic resistor becomes $\mathrm{Im}(Z) = 0$ and only the real part contributes. Therefore, an ohmic resistor results in a point on the $\mathrm{Re}(Z)$ axis in Figure 4.3a for all applied frequencies. An ideal inductor and an ideal capacitor ($\alpha = 1$) produce a vertical line in the bottom and top sector of the Nyquist plot, corresponding to a phase shift Φ of 90° and −90°, respectively. Non-ideal inductors and capacitors, described by Equation 4.12 and 4.13,

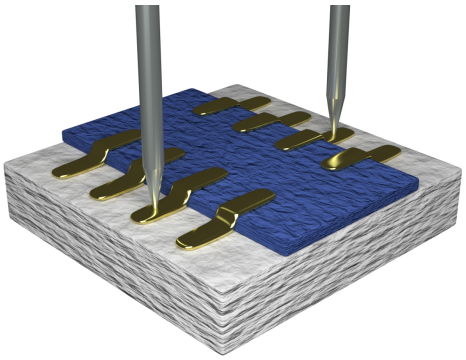

Figure 4.4
Exemplary electrode pattern for impedance measurements. The gold pins are placed on two oppositely evaporated gold electrodes in order to measure the in-plane film response between those contacts. The film is patterned such the evaporated gold contacts cover half of the film and the substrate.

contain an additional contribution of $\mathrm{Re}(Z)$. The resulting phase shift of $0° < \Phi < |90°|$, which is considered with an ideality factor $0 < \alpha < 1$, is depicted in Figure 4.3b,c as a slope in the Nyquist plot. Figure 4.3d shows a parallel circuit of a non-ideal capacitor and a resistor, also known as constant phase element, which is used to model the behavior of an insulating material such as untreated PEDOT:PSS. For a perfect capacitor the graph shows a semi-circle in the Nyquist plot, which is damped for non-ideal capacitors with $0 < \alpha < 1$.

If the sample's geometry is known, impedance spectroscopy allows to calculate the DC conductivity σ from the measured resistance R by Equation 4.14.

$$\sigma = \frac{s}{R\,A} = \frac{1}{R}\,\frac{s}{b\,d}, \tag{4.14}$$

with the electrode distance $s = 4.96\,\mu\mathrm{m}$, the cross-sectional area $A = b\,d$, the width of the electrodes $b = 3.53\,\mu\mathrm{m}$, and the film thickness d.[138] Thus, the measurements obtained from impedance spectroscopy are comparable to the data obtained from four-point measurements and can be further verified.

In the present thesis, impedance spectroscopy were performed with a SP-150 device by BioLogic Science Instruments. In order to obtain reproducible measurements, the sample's substrate is exposed at the edge to allow contacting of evaporated electrodes above the substrate instead of the film. This results in contacting the sample with conducting needles attached to micromanipulators without putting pressure on the investigated film, as depicted in Figure 4.4. Measurements are performed with a single sine signal with an amplitude of 10 mV and the constant potential set to 0 V against the open circuit potential between the two gold contacts. The applied signal's frequency is swept from 1 MHz to 1 Hz with 20 data points per decade (logarithmic spacing). In order to increase the measurement statistics, data acquisition is performed with 10 measurements per frequency and 0.1 s waiting time between each acquisition. The working electrode potential E is set to a maximum measurement range of $-10\,\mathrm{V} - 10\,\mathrm{V}$, with the current measurement sensitivity set to automatic. The band pass filter is set to 5, corresponding to a bandwidth of 62 kHz. Data modeling with equivalent circuits is performed with the included software EC-Lab® v11.20 (5.3.2018) by BioLogic Science Instruments.

4.3 Structure Investigation in Real Space

4.3.1 Optical Microscopy

In order to evaluate the thin film homogeneity and to determine the active area of OLEDs, optical microscopy has been employed. An AXIOLAB A microscope by CARL ZEISS was used to obtain microscopy images with 1.25×, 2.5×, 10×, 50× and 100× magnification. A reflected-light geometry is chosen to permit the measurement of non-transparent films or substrates. Digital micrographs are recorded with a PIXELINK PL-S621CU CMOS sensor ($1280 \times 1024\,\mathrm{px}^2$, 8.52 mm sensor diagonal). Real space distances are calculated according to the transformation factors listed in Table 4.1. Image processing and analysis is performed using the software IMAGEJ V1.44P.[139] The resolution limit in the focal plane is given according to the Rayleigh criterion:

$$R = \frac{1.22\,\lambda}{2\,NA}, \tag{4.15}$$

with the numerical aperture NA and the wavelength λ.

Table 4.1
Available magnifications for optical microscopy images with corresponding numerical aperture NA, spatial resolution R and transformation factor from pixel size to real space length. The spatial resolution is calculated according to Equation 4.15 for $\lambda = 700\,\mathrm{nm}$. Distances in real space correspond to a distance of 1 pixel in digital micrographs. The factors have been formerly determined empirically.

magnification	NA	$R(\lambda = 700\,\mathrm{nm})$ [µm]	factor $\left[\mu\mathrm{m\,px}^{-1}\right]$
1.25	0.035	12.2	6.258
2.5	0.075	5.7	3.2
10	0.20	2.1	0.8
50	0.70	0.61	0.16
100	0.75	0.57	0.08

4.3.2 Profilometry

Profilometry is a fast technique to determine the thickness and the surface profile of thin films. In order to determine the film thickness, the samples are scratched and the height-profile across the scratch is measured. In the present thesis a DEKTAKXT

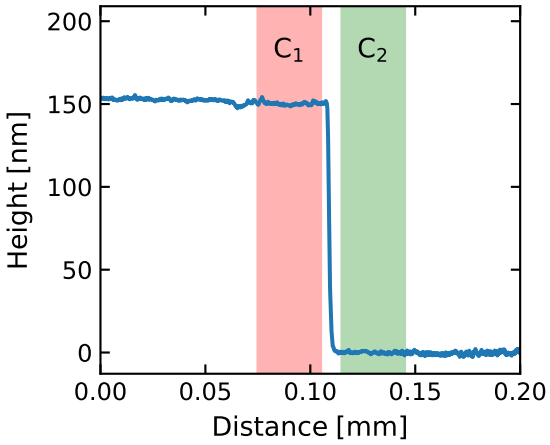

Figure 4.5
Exemplary height profile across a scratched thin film of spin coated PEDOT:PSS. The film thickness is calculated by taking the absolute difference of the mean height at cursor C_1 and C_2. In addition, the film roughness P_q can be determined. For the present example a film thickness of $(150.3 \pm 1.5)\,\mathrm{nm}$ and a root mean square roughness of $1.0\,\mathrm{nm}$ is obtained at C_1.

by Bruker Nano Surface Division is used. This device is equipped with a stylus mounted above a high precision xy-stage. The sample is placed on the stage such that the scratch is perpendicular to the movement direction of the sample stage. The diamond tip of the stylus has a radius of $2\,\mu\mathrm{m}$ and is used with a contact pressure corresponding to the weight of $1\,\mathrm{mg}$. While moving the xy-stage with the additional equipped actuator, which permits a continuous precise movement in measurement direction, the vertical deflection of the probe is recorded and translated into a height-profile. An exemplary measurement is depicted in Figure 4.5. For a more quantitative comparison of measurements, the root mean square roughness P_q and the average step height ASH is extracted from such profiles using the included software Vision64. The ASH is calculated by taking the mean height outside (Figure 4.5, C_1) and inside (C_2) the scratched area of nine different measurement spots distributed across the sample yielding the average film thickness. Typical measurements were performed over a scan range of $350\,\mu\mathrm{m}$ with a scan speed of $35\,\mu\mathrm{m\,s^{-1}}$. Hence, a lateral resolution of $117\,\mathrm{nm\,pt^{-1}}$ is obtained. It is noteworthy to mention that, due to the contact pressure, the tip might penetrate soft materials such as polymers. Furthermore, brittle materials might even be damaged and the measurement might be imprecise by agglomeration of particles at the tip. Thus, in combination with possible material residuals within the scratched area, the obtained film thickness might be underestimated. However, the technique provides good starting values for the fitting of XRR data (Subsection 4.4.1), which provides more precise information about the vertical film structure of polymer thin films.

4.3.3 Atomic Force Microscopy

A main constraint in optical microscopy and SEM, where only a two dimensional projection of the investigated surface is observable, is the limitation of the height information that can be accessed from such measurements. In contrast, atomic force

microscopy (AFM) enables very precise imaging of a sample's topography. Therefore, a three dimensional map of the sample is attainable with accurate height information in nm-resolution. This is achieved by a sharp tip which is scanned over the sample surface line-by-line. A wide field of different tips can be chosen to probe samples with very different properties. Thus, the kind of contrast can be adjusted to the sample's characteristic of interest and can be combined with the spatial nm-resolution, e.g., mapping its 3D surface topography or conductivity. In this thesis, basic AFM is used to probe the sample's topographical information and therefore is applicable for electrically insulating polymers that are not capable for SEM measurements.

The working principle of an AFM is based on the interaction of the very small tip with the atoms on the sample surface. Therefore, the tip is brought into close proximity with the surface such that an inter-atomic force is detectable. Thus, the resolution is based on the size of such a tip with typical curvature radii in the range of <10 nm. A Lennard-Jones potential is used to describe the short-range repulsive and long-range attractive interaction. This allows for three different modes of operation, namely contact, tapping, and non-contact mode. In order to avoid damaging of soft matter surfaces, the measurements in the present thesis are conducted in tapping mode. Hereby, the cantilever, where a sharp tip is mounted, oscillates near its resonance frequency and is brought into close proximity to the sample surface. The interaction with the nearby surface atoms of the sample affects the amplitude of the oscillation. A laser is focused to the back of the cantilever whereas a multi-sector photodiode detects its reflection and therefore the movement of the cantilever. Thus, any variation in the oscillation's amplitude is recorded and translated into a height information. A feedback loop is applied to keep the cantilever in a constant distance to the sample surface in order to prevent damaging of the tip or the sample. Using piezoelectric actuators the cantilever is scanned line-by-line over the sample to map the topographic information with the lateral structure size of the sample.

In the present thesis a MFP-3D AFM by Oxford Instruments Asylum Research is used at ambient conditions. The cantilever is driven in tapping mode with a scan rate of 0.1 Hz. $40 \times 40\,\mu m^2$ micrographs with a pixel density of 512 px/line are obtained for ZnO samples in order to analyze the surface topography and film roughness. The software Gwyddion v2.45[140] is used for data analysis and image post-processing. Obtained AFM images are corrected according to tilt (leveling) and polynomial background subtraction. Height profiles are extracted by line-cuts in direction of the fast scanning axis. Similar to SEM data analysis described in Subsection 4.3.4, RPSDs are extracted in order to obtain the dominating surface structure size.

4.3.4 Scanning Electron Microscopy

Structural investigations with nm-resolution are performed with scanning electron microscopy (SEM). In contrast to optical microscopy, electrons are used to probe the sample surface, which renders a much higher resolution in real space and a large depth of field. On the downside, high vacuum and conducting samples are required. Considering a typical used acceleration voltage of $V = 5\,\mathrm{keV}$ the de Broglie wavelength for an electron becomes:

$$\lambda = \frac{h}{p} = \frac{h\,c}{\sqrt{2\,m_\mathrm{e}\,c^2\,e\,V + (e\,V)^2}} \approx 17.3\,\mathrm{pm} \tag{4.16}$$

with Planck's constant h, the electron momentum p, the speed of light c, the rest mass of an electron m_e and its elementary charge e. Hence, resolutions of less than 1 nm are possible.

The working principle of a SEM is as following: First, electrons with a well defined kinetic energy are generated in an electron gun. Electrons are either generated by thermal or field emission, while the best quality is usually provided with a combination of both. Such thermally assisted field emission guns (Schottky cathode) provide a high electron flux in combination with a stable and well defined kinetic energy and enable low acceleration voltages ($<5\,\mathrm{kV}$). Therefore, the latter type is typically used to achieve good quality images. The generated electron beam is condensed by a set of electromagnetic lenses and is cut down by an aperture to a specific beam size. The quality and the adjustment of these lenses defines the size and shape of the electron beam, which has a strong influence on the final image resolution and quality. Scan coils are used to guide the beam to the desired position on the sample surface in order to scan over the whole region of interest line-by-line. The incident electrons (primary electrons) penetrate the sample and get scattered, which releases mainly low energy secondary electrons ($\approx 10\,\mathrm{eV} - 50\,\mathrm{eV}$) resulting from inelastic scattering on the sample's surface which provide a strong topographical contrast. In addition, material contrast is possible by detecting the elastic backscattered electrons or eventually generated Auger electrons. Furthermore, characteristic X-rays may be detected for a chemical mapping via energy-dispersive X-ray spectroscopy (EDX). Primary electrons create a so-called scattering plume where the detected signal comes from, which is typically larger than the beam size. While secondary electrons are released close to the surface, backscattered electrons and X-ray radiation are originated from deeper regions of the sample and provide lower resolution due to the widened scattering volume. Therefore, in practice, the resolution is limited by the diameter of the electron beam and the size of the generated scattering plume. This yields typical resolutions for secondary electron detection in the range of $1\,\mathrm{nm} - 10\,\mathrm{nm}$.

The image quality highly depends on the contrast of the detected signal. For secondary electrons, which are used in this work, the contrast depends on the atomic number of the element, the work function of the surface and the local curvature/sample

topography. Therefore, high structures (hills) and edges appear bright, due to a shorter working distance at this point whereas low structures (dips) appear dark, even if they composed of the same material. In order to prevent charging effects of the sample, which can lead to loss in contrast, the depletion of electrons at the sample's surface needs to be compensated. Therefore, investigated samples are cast on conducting substrates such as silicon, FTO, or ITO.

In this work a Gemini NVision 40 FIB-SEM by Zeiss is used. This instrument is equipped with a thermally assisted field emission gun and an in-lens detector for secondary electron detection, which allows low acceleration voltages and a small working distance. The smallest aperture of 10 µm is chosen to obtain a small beam size and thus a high resolution. An acceleration voltage of 5 kV with a working distance of ~3 mm is used for most of the measurements. However, for insulating samples with a low electron yield such as polymers, an acceleration voltage of 1 kV – 2 kV and a small working distance of ~1 mm is required to achieve a sufficient image quality and a reduction of charging effects.

For cross-sectional imaging, the desired samples are quick-frozen in liquid nitrogen and subsequently broken on a sharp edge. By this means, the soft or porous samples are hardened and well defined breaking edges are obtained. Samples for cross-sectional imaging are typically deposited on silicon substrates which guide the thin film to brake along a well defined crystal direction of the wafer. In this thesis cross-sectional imaging is typically performed with a 45° tilt of the sample towards the electron beam. The obtained distorted images are directly corrected by the measurement software during the data acquisition process.

For evaluation of the SEM images the software ImageJ v1.44p[139] is used to adjust contrast and sharpness. Fast Fourier transform of the micrographs permits the identification of dominating structure sizes. Radial integration of the Fourier transformed image yields a radial power spectral density (RPSD), which enables a quantitative analysis of the surface structures that can be compared to the volume structures obtained by GISAXS measurements (Subsection 4.4.3).

4.4 Structure Investigation in Reciprocal Space

4.4.1 X-ray Reflectometry

In order to analyze the vertical film composition and thickness of thin films, X-ray reflectometry (XRR) measurements have been employed. The measurement method is sensitive towards different scattering length densities (SLDs). Concerning X-rays, the SLD is linked to the material's electron density and increases with atomic number and material density. Therefore, it enables the identification of different layers inside the film, e.g., enrichment layers of components and the interface in between for blend

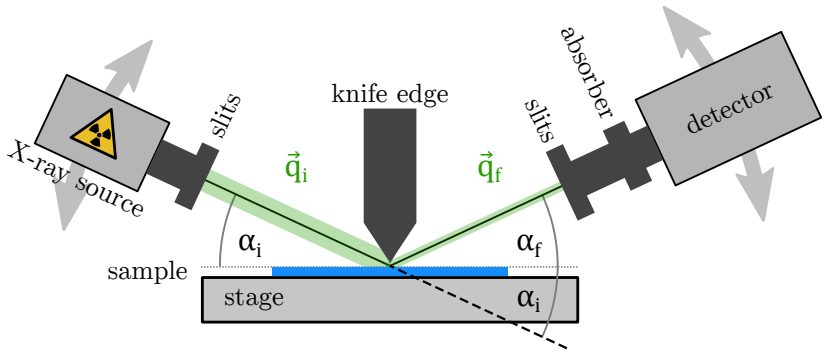

Figure 4.6
Schematic sketch of a XRR setup. Monochromatic X-rays ($\vec{q}_i$) are generated by a Cu-K$_\alpha$ anode and impinge the sample surface under the angle α_i. The specular reflected beam ($\vec{q}_f$) under the angle $2\alpha_i$ (with respect to the incident beam) is recorded by a scintillation detector. The so-called coupled $\theta - 2\theta$, or in this case $\alpha_i - 2\alpha_i$, measurement yields the reflected intensity in dependence on the incident angle, which can be translated to a momentum transfer with Equation 4.17. The tantalum knife edge prevents over-illumination of the sample.

systems. Within this thesis XRR is used to investigate the vertical layer composition of PEDOT:PSS polymeric electrodes.

Figure 4.6 shows a schematic sketch of a typical XRR setup. Monochromatic X-rays hit the sample surface under a defined angle α_i. The specular reflected beam exits the sample under $\alpha_i + \alpha_f = 2\alpha_i$ with respect to the incident beam. The reflected intensity is then recorded with a detector as a function of α_i. As the photons are scattered elastically, their energy does not change, i.e. $|\vec{q}_i| = |\vec{q}_f|$ and a change in the momentum $\vec{q}$ only depends on a redirection of the photons. Thus, the momentum transfer from Equation 2.34 simplifies to:

$$\vec{q} = q_z = \frac{4\pi}{\lambda} \sin \alpha_i \tag{4.17}$$

For angles smaller than the critical angle $\alpha_i < \alpha_c$ total reflection occurs. Once the increasing incident angle surpasses the critical angle, the beam starts to penetrate the film. This becomes apparent in an intensity drop in the reflection curve, also known as critical edge. For higher angles ($\alpha_i > \alpha_c$) the beam is split into a reflected and transmitted part at each interface with a change in refractive index n, according to Fresnel's equations (Subsection 2.5.1). Thus, multiple reflections and refractions at different vertical positions inside the film occur. Superposition of the reflected beams result the characteristic Kiessig fringes of the reflectivity pattern. From the distance Δq_z between adjacent Kiessig fringes one can determine the film thickness d by:

$$d \approx \frac{2\pi}{\Delta q_z}, \qquad \text{with } \Delta q_z = |q_{z,1} - q_{z,2}| \tag{4.18}$$

By dividing the probed film into a hypothetical stack of layers, each of them with different refractive index, the internal vertical structure of the probed film can be modeled applying the Paratt algorithm.[141] Thus, a detailed vertical SLD profile can be obtained, which renders specific enrichment layers and their thickness in the film. A detailed discussion about XRR on soft-matter thin films is provided by Tolan.[80]

In this thesis, a D8 Advance Diffractometer by Bruker is used. X-rays are generated with a copper anode and a monochromatic wavelength (Cu-K_α) of $\lambda = 1.54\,\text{Å}$ is selected by a Goebel mirror. Before impinging the sample's surface the incident beam is collimated with 0.2 mm sized slits. A tantalum knife edge is placed above the point of incidence to cut down the beam for very small angles. Thus, the illuminated area, also called footprint of the incident beam, can be controlled to prevent over-shooting of the sample, i.e. illuminating the sample stage. The exciting beam is collimated with a second set of slits with size 0.1 mm and 0.05 mm before hitting the detector. Additionally, the detector is equipped with a rotary absorber to prevent over-saturation or damaging. The typical scan range is set to 10°. The obtained reflectivity curves are modeled according to the Paratt algorithm with the software plugin Motofit[142] for IGOR Pro v6.37 by WaveMetrics.

4.4.2 Time of Flight Neutron Reflectometry (ToF-NR)

Neutron reflectometry (NR) measurements have been performed at the REFSANS instrument at the Heinz Maier-Leibnitz Zentrum MLZ, Garching, Germany.[143] The instrument was operated in ToF mode (see Subsection 2.5.4), which means each single neutron is recorded with its position on the detector and its corresponding time of flight. Therefore, the time resolution of this instrument is only limited by the intensity of the scattering signal, which enables kinetic measurements with a time resolution of <1 min. Considering Equation 4.17, a reflectivity curve can be obtained by either fixing the wavelength λ of the incident photons/neutrons and varying the incident angle α_i or vice versa. Thus, with the latter, a certain q_z-range is covered without the need of changing the incident angle. This is achieved by a chopper system that selects neutron pulses with a wavelength band ranging from 2.1 Å – 20.0 Å.

In this work static and kinetic measurements of PEDOT:PSS thin films have been performed in Chapter 6. The static states were measured with incident angles of $\alpha_{\text{i},1} = 0.6°$ and $\alpha_{\text{i},2} = 2.4°$ and with acquisition times of 20 min and 100 min, respectively. Afterwards, both recorded reflectivity curves were merged together to cover a q_z-range up to $0.15\,\text{Å}^{-1}$. To obtain a good time resolution with reasonable statistics, the incident angle for the kinetic measurement was set to $\alpha_\text{i} = 0.76°$. After the measurement, a 30 s time resolution was achieved by binning the detected single neutrons and summing up their signal to one reflectivity curve.

The obtained static and kinetic curves are modeled according to Subsection 4.4.1 using the IGOR plugin MOTOFIT.[142] Out of the analysis of the NR data a thickness change and a SLD_N change are extracted independently. The film thickness evolution is obtained from the total thickness of all modeled polymer layers. The mean film SLD_N is obtained by taking into account the SLDs of each individual layer, which is weighted regarding to its layer thickness in order to obtain one representative value for each film. In addition, the thickness change is normalized to the starting value of the as-prepared films at ambient conditions to obtain the swelling ratio. The water content $\Phi(D_2O)$ for the films is calculated according to Equation 2.7 by comparing the measured SLD_N to the ones of the dry polymer film and pure D_2O. The resulting curves are fitted according to a humidity sensitive model introduced by Magerl et al.[51] The obtained set of equations from Section 2.2 results in an implicit function that depends on the relative humidity and the relative swelling ratio which both are time dependent measures. By applying this model, the diffusion time constant τ, the effective Flory-Huggins interaction parameter χ_{eff}, and the fitting parameter B are obtained (Section 2.2).

4.4.3 Grazing-Incidence Small-Angle X-ray Scattering (GISAXS)

Grazing-incidence small-angle X-ray scattering (GISAXS) describes a scattering technique to probe the inner film structure of thin films. By varying the sample-to-detector distance (SDD) of typical 1 m – 5 m, the detectable range of the scattering angles in vertical (α_f) and lateral (ψ) direction is adjustable, which permits to probe length scales in the range of 1 nm up to 1 µm. GIWAXS in contrast covers the sub-nm range with SDDs <50 cm and is explained in more detail in Subsection 4.4.4. Compared to real space imaging techniques such as AFM or SEM, which provide only a snapshot of a small surface area, GISAXS/GIWAXS measurement techniques have been developed to probe the inner film structure of thin films with a thickness of typically $\lesssim 100$ nm. By choosing a small angle under grazing-incidence, the effectively illuminated area on the sample can reach sizes of a few cm^2 and therefore provide high statistical significance. In Figure 4.7 a schematic setup of the common GISAXS/GIWAXS techniques is depicted. The sample is tilted around the $\hat{y}$-axis by the incident angle α_i, which typically amounts <1.0°, versus the incoming X-ray beam, that usually defines the $\hat{x}$-axis of an orthonormal Cartesian coordinate system. The incoming X-rays with momentum $\vec{q}_i$ are diffusely scattered and leave the sample with the momentum $\vec{q}_f$ under the vertical exit angle α_f with respect to the sample surface ($\alpha_i + \alpha_f$ with respect to the incident beam) and the lateral angle ψ with respect to the specular plane (xz-plane). The specular plane is spanned under the incoming beam and the sample's surface normal. A 2D detector placed at the SDD records the diffusely scattered intensity in dependence on the scattering angles, which translates to the scattering vector $\vec{q}_f$.

For incident angles above a material's specific critical angle ($\alpha_i > \alpha_c$) the X-rays

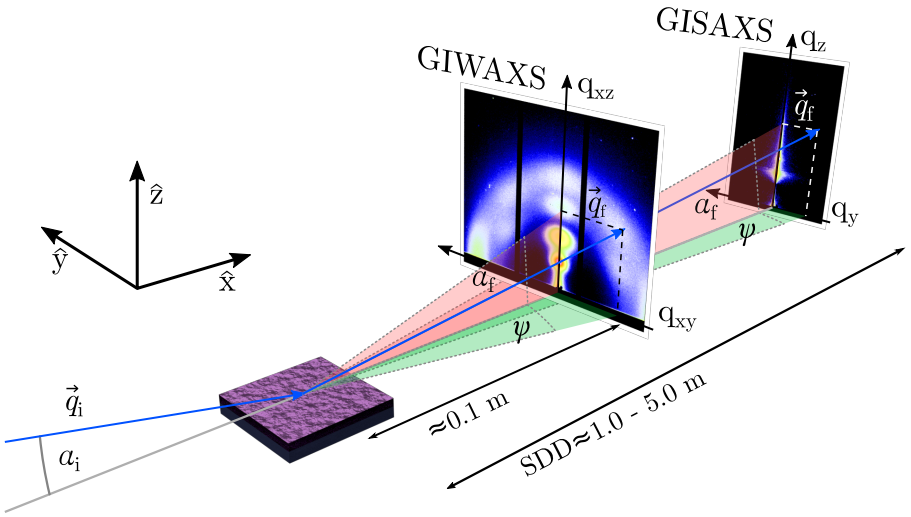

Figure 4.7
Schematic GISAXS/GIWAXS setup. The X-rays impinge the sample surface under the incident angle α_i and become diffusively scattered. The X-rays leave the sample under the lateral scattering angle ψ with respect to the yz-plane and the vertical scattering angle α_f with respect to the sample surface. The 2D detector is placed at the SDD where the scattered X-rays ($\vec{q}_f$) are eventually detected. Depending on the SDD the setup is either used for wide angle (small SDD, GIWAXS) or small angle (large SDD, GISAXS) scattering.

penetrate the sample's surface and induce an evanescent wave in the film which couples out at the critical edge of the material. The observed pronounced scattering intensity (located at $\alpha_f = \alpha_c$) is the so-called Yoneda peak, which reveals information about the lateral structure of the corresponding material within the film volume, as explained in Subsection 2.5.2. By decreasing the incident angle below the critical angle ($\alpha_i < \alpha_c$) of the investigated material, the Yoneda peak moves towards the specular reflection and eventually joins it. Thus, total reflection occurs and the measurement becomes strongly surface sensitive. Hence, by adjusting the incident angle, the X-rays penetration depth can be varied and therefore the sensitivity towards probing the sample volume or surface can be adjusted. Typically, the incident angle for GISAXS experiments is set to a larger value than the material specific critical angle ($\alpha_i > \alpha_{c,material}$) such that the Yoneda peak and the specular reflection are distinguishable. Thereby, the penetrating X-rays reveal information from the inner film volume and the lateral structure of the probed material is accessible via horizontal cuts at the Yoneda peak position.

Due to the well defined and fixed incident angle α_i and SDD, the detector image can be mapped to a q_y-q_z-scattering pattern. Hereby, the momentum transfer $\vec{q}$ is given by the momentum difference of the exiting (α_f, ψ) and the incoming beam (α_i) and is calculated according to Equation 2.34. Since the incoming and scattering angles are

small, it is reasonable to apply a small angle approximation. With the well defined SDD, the incident angle can be calculated by Equation 4.19

$$\alpha_\mathrm{i} = \frac{1}{2}\arctan\left(\frac{\left(y_\mathrm{spec} - y_\mathrm{DB}\right)p}{\mathrm{SDD}}\right), \tag{4.19}$$

with the y pixel position of the specular reflection (y_spec) and the direct beam (y_DB) on the 2D detector and its pixel size p. Further, the lateral (ψ) and vertical (α_f) deflection angles can be determined according to Equation 4.20

$$\begin{pmatrix}\alpha_\mathrm{i} + \alpha_\mathrm{f}\\ \psi\end{pmatrix} = \begin{pmatrix}\arctan\left(\dfrac{(y - y_\mathrm{DB})\,p}{\mathrm{SDD}}\right)\\ \arctan\left(\dfrac{(x - x_\mathrm{DB})\,p}{\mathrm{SDD}}\right)\end{pmatrix} \tag{4.20}$$

Further information about the theory behind the GISAXS technique can be found in Section 2.5.

Data Evaluation

In practice, the SDD is determined with a calibration sample, i.e. fresh silver behenate, with the aid of the software IGOR Pro v6.37 and the Nika macro package.[144] Figure 4.8a shows an exemplary GISAXS pattern already mapped to q_y-q_z-representation. For smooth films, the highest intensity of such a scattering pattern is originated in the specular reflection of the incident beam. Thus, it is often covered by a beamstop to prevent over-saturation of the detector. Its position on the detector is used together with the direct beam position to determine the exact incident angle α_i and the specular scattering plane. For data analysis so-called vertical (in-plane) and horizontal (out-of-plane) cuts in q_z- and q_y-direction are performed, respectively. Data reduction is performed using the open source software DPDAK v1.3.1[145] or self written Python scripts. Similar to XRR, the vertical line cuts (Figure 4.8b) exhibit information about the vertical film structure (Kiessig fringes). Furthermore, the Yoneda peak positions of the used materials are visible, which are used to calculate the material's critical angle and the related average mass density. Thus, e.g., the porosity of metal oxide films is determined. On the other hand, horizontal line cuts (Figure 4.8c) are typically performed at the Yoneda peak position and reveal lateral structure information of the probed film volume. For a quantitative analysis the horizontal line profiles are modeled using a Python 2.7 script written by Dr. Christoph J. Schaffer.[54] A more detailed explanation is shown in Subsection 2.5.2. The model is based on a 1D paracrystal in the framework of the distorted-wave Born approximation (DWBA) with a local monodisperse approximation (LMA) and neglects possible correlations between the interfaces (EIA). A central aspect is the assumed radial isotropy of scattering objects, which are represented by either spherical or cylindrical shaped form factors. Furthermore, the mean distances between the scattering objects are represented by the structure factor.

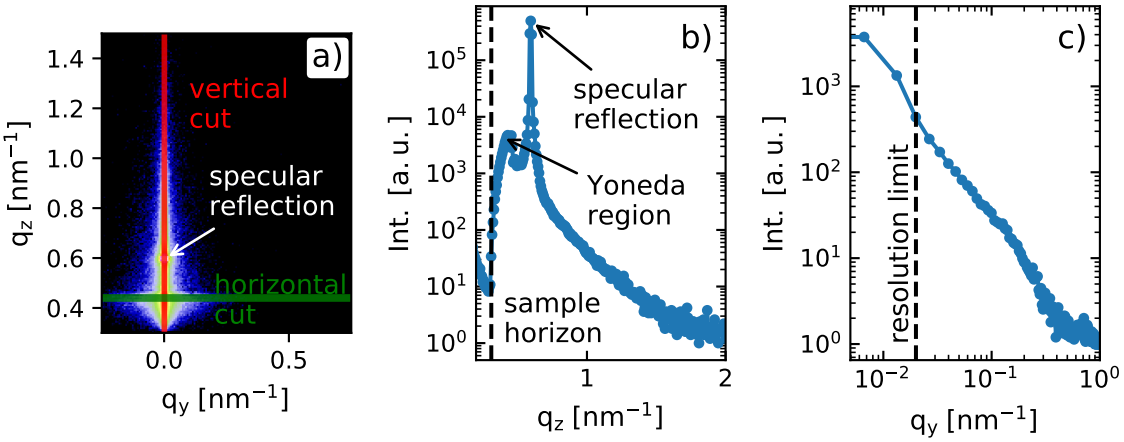

Figure 4.8
a) Exemplary GISAXS scattering pattern mapped to q_y-q_z-representation of PEDOT:PSS thin film. The specular reflection is typically covered by a beam stop to prevent oversaturation of the detector. From its position the exact incident angle α_i can be determined. Exemplary horizontal line cuts (green) along the Yoneda peak position in q_y-direction and vertical line cuts (red) in q_z-direction are shown. b) Corresponding vertical scattering profile along q_z-direction shows the specular reflection, Yoneda peak and sample horizon. c) Corresponding horizontal line cut along the Yoneda peak position with marked resolution limit.

Both, radii and distances typically follow a Gaussian distribution around their mean values. This is especially the case for non highly ordered systems. Within the present thesis typically two or three structure and form factors are used to model the intensity profiles. For low q_y-values (large structure sizes) the resolution is limited by the instrument and is accounted for with a Lorentzian shaped resolution function. Thus, structure sizes below the resolution limit (marked with a dashed line in Figure 4.8c) are not resolvable.

4.4.4 Grazing-Incidence Wide-Angle X-ray Scattering (GIWAXS)

Grazing-incidence wide-angle X-ray scattering (GIWAXS) describes a scattering technique to obtain information about the crystal structure and orientation of crystallites in thin films. Similar to the GISAXS technique, described in Subsection 4.4.3, the diffuse scattering intensity is imaged using a 2D detector. However, for GIWAXS a shorter SDD is required, typically in the range of 10 cm – 50 cm, to cover the larger scattering angles (Figure 4.7). The incoming X-ray beam is diffusively scattered on polymer crystallites or agglomerates in the thin film. Thus, intensity maxima under the Bragg-angle θ are observed on the 2D detector. According to Bragg's law (Equation 2.39) the scattering angles 2θ refer to a net layer spacing d on a length scale of a few Å up to a few nm. In order to probe a maximized sample volume and therefore increase the scattering signal and statistical significance – as mentioned in

Subsection 4.4.3 for GISAXS – a small angle α_i is applied. For materials with critical angles smaller than those of the used substrate, which is usually the case for polymer thin films, the incident angle can be set to a value between those. Thus, by setting $\alpha_{c,sample} < \alpha_i < \alpha_{c,substrate}$, the substrate contribution to the recorded scattering pattern is suppressed while the sample signal is enhanced. This procedure is especially important for investigations on semi-crystalline polymer thin films coated on amorphous substrates such as glass. Otherwise, the amorphous broad glass peak around $q \approx 1.8\,\text{Å}^{-1} - 1.9\,\text{Å}^{-1}$ may overlay the weak sample signal, e.g., the π-π-stacking signal at $q \approx 1.8\,\text{Å}^{-1}$ arising from PEDOT. Therefore, additional background subtraction is performed in order to highlight the scattering signals of interest.

Caused by the geometry of GIXS experiments, the substrate-film interface of thin films yields a loss in symmetry due to an anisotropy of the scattered signal (see Subsection 2.5.3). In contrast to GISAXS no small angle approximation is retained. Therefore, the q_x-component of the scattering vector $\vec{q}$ must not be neglected and $\vec{q}$ splits into a q_{xz}-component in the specular plane and a q_{xy}-component (also referred as q_r) in the sample plane (Figure 4.7). Thus, the bare $q_z = \sqrt{\left(q^2 - q_x^2 - q_y^2\right)}$ component perpendicular to the sample surface is only accessible for $q_y = q_x = 0$. According to Equation 2.34, this condition is fulfilled for zero lateral divergence ($\psi_f = 0$) and specular reflection ($\alpha_f = \alpha_i$). Thus, for diffuse scattering such as GIWAXS, the so-called missing wedge needs to be taken into account when mapping the 2D scattering patterns to q_r-q_z-representation. In order to cover the non-detectable region, XRD can be performed as a complementary measurement technique. Since for XRD the specular reflection is measured, the condition $\alpha_i = \alpha_f$ holds and the q_z-component is directly accessible.

For data reduction the MATLAB® based software GIXSGUI v1.7.1[105] is used, which provides a graphical user interface for the GIXSDATA toolbox. The software package takes into account several corrections such as polarization and geometry corrections as explained in more detail in Subsection 2.5.3. Furthermore, it allows correct pixel splitting and binning, yielding the typically used reshaped scattering images in q_r-q_z- and χ-q-representation style. Furthermore, sector integrals have been applied to extract intensity profiles along specific q-directions for further analysis. The obtained intensity profiles are evaluated according to the stacking distance and azimuthal orientation (χ-orientation) of crystallites in the thin films.

In the present thesis the lab system GANESHA 300XL SAXS-WAXS by SAXSLAB is used for GIWAXS measurements. The instrument is equipped with a copper K_α X-ray source (Xenocs GeniX^{3D}), powered with 49.79 kV and 0.59 mA, which generates photons exhibiting an energy of 8.047 keV corresponding to a wavelength of $\lambda = 1.5408$ Å. Beam collimation is achieved by a three slit system set to $0.4 \times 0.4\,\text{mm}^2$, $1.0 \times 1.0\,\text{mm}^2$, and $0.1 \times 0.5\,\text{mm}^2$ to achieve GIWAXS measurements with a high resolution in vertical direction with respect to the sample surface. For alignment purpose and GISAXS measurements, the slit system is set to $0.4 \times 0.4\,\text{mm}^2$, $1.0 \times 1.0\,\text{mm}^2$,

and $0.1 \times 0.1\,\mathrm{mm}^2$, respectively. The incident angle $\alpha_\mathrm{i} = 0.2°$ is set slightly below the critical angle of glass to penetrate the PEDOT:PSS films and suppress the substrate contribution. The scattered X-ray photons are recorded with a PILATUS 300K detector by DECTRIS, consisting of $619 \times 487\,\mathrm{px}^2$ with a pixel size of $172 \times 172\,\mu\mathrm{m}^2$ and a thickness of 0.32 mm. The detector is placed in a SDD of 106 mm and is considered as noise free, due to the employed cooling system. Furthermore, in order to address anisotropic detector sensitivity, flat-field and dark-field corrections are directly applied on the measurement server. In order to reduce the background caused by air scattering, the whole setup – including sample stage and detector – is placed in a vacuum chamber with a pressure of 1.87×10^{-2} mbar. If not other stated an acquisition time of 36×20 min is chosen, resulting in a total measurement time of 12 h of the summed images.

4.5 Goniophotometer Setup

In the frame of the present thesis functional layers for potential application in OLED devices are investigated. Hence, the evaluation of the scattering capability of ZnO layers regarding visible light and the angular dependent emission characteristic of OLED devices are required. Therefore, an instrument was constructed that renders angular and wavelength dependent measurements of the scattering and emission characteristics of thin films and OLEDs, respectively. The setup had to fulfill several requirements:

- Characterization of thin film scattering layers and OLEDs in operation
- Angular and wavelength dependent measurement
- Lifetime experiments
- Automatized measurement
- Lightproof sample environment

In Figure 4.9a the setup for angular dependent measurements is depicted. Figure 4.9b shows a magnification of the sample stage consisting of sample holder ① and the light source ②. The LED is glued with thermal adhesive on an aluminum plate, which serves as heat sink and allows sufficient cooling. The sample is placed upright in front of the LED light source, which is equipped with an aperture in order to adjust the illuminated area of the sample. The whole sample stage consisting of the sample holder, LED and aperture can be rotated by the aid of a stepper motor ③ around the scattering angle φ. Therefore, the incident angle of the incoming light is fixed to 90° with respect to the sample surface. The sample stage is designed such that the rotation axis lies in the surface plane of the investigated sample. The light is then collected under the angle φ by an optical probe ④ and redirected to the spectrometer via a glass fiber cable. In order to adjust the angular resolution, the distance of the probe to the rotation axis is adjustable from ~10 cm – 100 cm along the optical axis (depicted in yellow). If not other stated a SDD of 37 cm is used. Further, additional

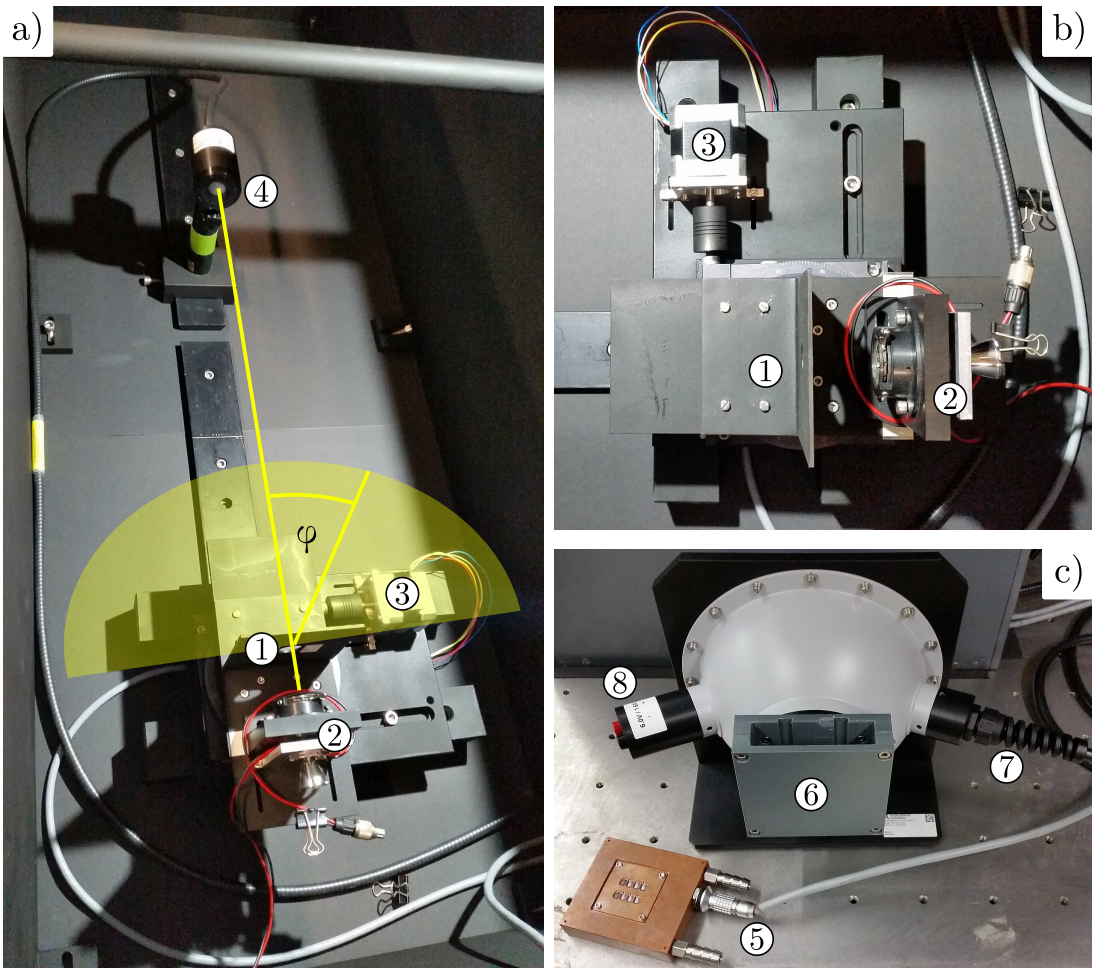

Figure 4.9
Photograph of the constructed goniometer setup for angular dependent spectroradiometric measurements of scattering layers and OLEDs. a) Setup for angular resolved measurements at the angular offset $-90° < \varphi < 90°$ from the optical axis ($\varphi = 0°$), both depicted in yellow. The distance between the sample and the optics (4) for collecting the scattered light under the angle φ is movable along the optical axis. b) Top view of goniometer with the sample stage consisting of sample holder (1) and LED light source with slit (2). The sample stage is rotated by the Arduino controlled stepper motor (3). c) Integrating sphere for measurements of the hemispherical emission characteristics of OLEDs. The specimens are placed in the sample holder (5) equipped with $8 + 2$ gold coated spring contacts for contacting the eight pixels and the back electrode. The sample holder is mounted with the attachment (6) at the integrating sphere opening. The glass fiber cable (7) redirects the collected light to the spectrometer. An auxiliary halogen light source (8) can be used for correcting the self absorption of the specimen.

Table 4.2
Color code of the cables connected to the measurement cell and the corresponding pin and pixel order. The different OLED pixels $1-8$ can be selected by a rotary switch for individual pixel measurement. Pin 9 and 10 are connected to the counter electrode of the OLED device.

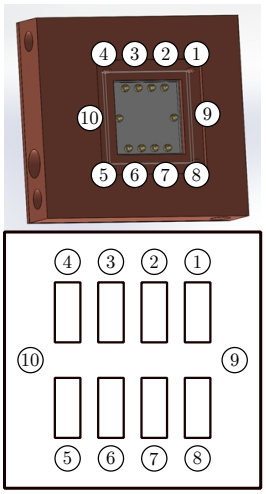

pin #	pixel #	cable color
1	1	brown
2	2	white
3	3	red
4	4	blue
5	5	pink
6	6	grey
7	7	yellow
8	8	green
9	CE	purple
10		black

apertures may be added along the optical axis to minimize secondary scattering effects. In order to prevent ambient light and increased light scattering effects at the setup and housing during measurements, the whole sample environment is placed in a black coated, light-tight PVC box, while all electrical and optical cables are directed through cable bushings to the measurement instruments outside of the measurement chamber.

In order to measure OLED devices, the sample holder can be exchanged with a measurement cell (5) designed by Dr. Johannes Schlipf,[101] that allows to contact each of the eight pixels on lab scaled OLED devices for individual measurement. The pixels are selected by an additional rotary switch and the whole cell can be set to a specific temperature via a water cycle through the cell housing (not used in this thesis). Therefore, the angular dependent emission characteristic of OLEDs can be measured. The pixel assignment to the pins of the measurement cell including the related color code of the connected wires is listed in Table 4.2. For voltage current characterization and degradation measurements of the investigated OLEDs a Keithley 2614B source meter by Tektronix is employed.

In the present thesis, the total emission of the produced OLED devices is of particular interest. In order to collect the total emitted light of a specimen, an integrating sphere is required. In Figure 4.9c the second part of the setup is depicted, which consists of a so-called Ulbricht sphere as optical probe. The measurement cell (5) is mounted in a housing (6) in front of the integrating sphere, which permits the detection of the total hemispherical emission of the OLED. The collected light is further redirected via an optical cable (7) to the spectrometer. Additionally, the integrating sphere is

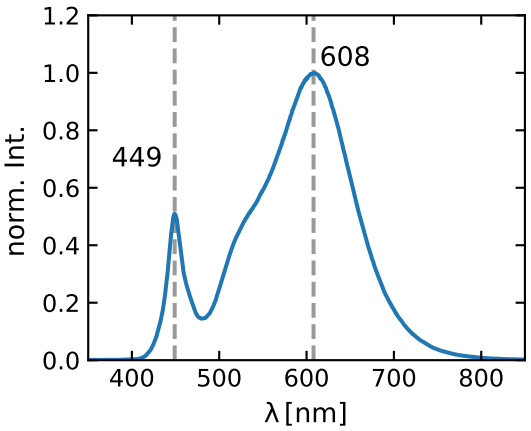

Figure 4.10
Emission spectrum of the LED mounted as white light source in the Goniometer setup. The emission peaks of the emitting material and the phosphor are clearly visible at 449 nm and 608 nm, respectively. The whole spectrum covers the most important regions for OLED devices which are the supposed field of application for the investigated scattering layers. The emission spectrum is normalized to its peak intensity.

equipped with an auxiliary halogen light source (8) in order to take self absorption of the investigated specimen into account.

The spectrometer and both of the optical probes are purchased and calibrated from Instrument Systems, Munich in order to be capable to measure absolute values of the radiant flux. For the angular resolved measurements the scattered/emitted light is collected by an EOP-120 optical probe with a ⌀ 25.4 mm entry window and a spectral range of 190 nm – 1350 nm. The integrating sphere used for total emission measurements is of type ISP-150L-250 with a ⌀ 35 mm opening and a potential spectral range of 380 nm – 1600 nm. To measure the collected light in wavelength dependency, a CAS 140CT-154 array spectrometer with a spectral range of 220 nm – 1020 nm and a spectral resolution of 3.8 nm (100 µm slit) is used. The spectrometer is equipped with a set of different absorbers in order to enable measurements of a wide range of intensities. A $1024 \times 128\,\mathrm{px}^2$ CCD sensor is used as array detector, which is cooled down to $-10\,^{\circ}\mathrm{C}$ via Peltier elements in order to reduce measurement noise. Communication with the measurement computer is provided via an USB port.

As light source for characterizing scattering layers a warm white LED of type XLamp® XM-L2 T2 by Cree®, Inc. with a luminous flux of ~380 lm (@1.4 A) is used. The LED is powered by a constant current source KSQ1400 (1400 m A) that allows adjusting the intensity of the LED by PWM. Both devices are purchased from Lumitronix® and are glued with thermal adhesive on aluminum heat sinks to encounter thermal dissipation. The normalized emission spectrum of the LED is depicted in Figure 4.10, showing a sharp peak at ~449 nm for the emitting material and a broad peak around 608 nm for the phosphor that is responsible for the warm white color. Therefore, its emission spectrum is suitable to characterize scattering layers for application in OLEDs.

The scattering/emission angle dependent measurements require for a motorized movement of the sample stage mounted on top of the goniometer. Therefore, a stepper motor QSH 4218 with 200 steps/rotation is connected to the goniometer stage

and allows precise rotation of the sample. The stepper motor is powered by a DMOS microstepping driver A4988. The correct rotation of the goniometer and the LED light source is controlled by an Arduino Nano based controller, which takes care of the power supply, the adjustment of the stepper motor and the LED including their corresponding drivers. The electrical circuit diagram and the corresponding board of the controller is depicted in Figure 4.11. The controller including its connected devices require a power supply of 12 V and >1.2 A.

In order to perform automatized measurements, a software was written in Python 2.7 including a graphical user interface based on PyQt 4. The program enables IV-characterization of OLEDs by sweeping a voltage and measuring the current density through the device, as well as for lifetime experiments by applying a constant voltage or current and measuring the opposed one. Simultaneously, the OLED emission can be characterized regarding its total amount or its angular characteristics by using the integrating sphere or the Arduino Nano based goniometer, respectively. By replacing the OLED sample holder with the normal sample stage equipped with the LED light source (Figure 4.9a,b), the angular dependent scattering of thin films can be measured. The main advantage of this setup is the capability of fast automatized characterization of the specimen's spectral and angular emission/scattering behavior simultaneously.

It is noteworthy to mention that for measurements the setup needs typically to be calibrated regarding the scattering angle φ. Therefore, an empty angular scan is performed without any sample to set the angle of the highest measured intensity to $\varphi = 0°$. This angle corresponds to the detection of the direct transmitted/scattered light parallel to the sample's surface normal.

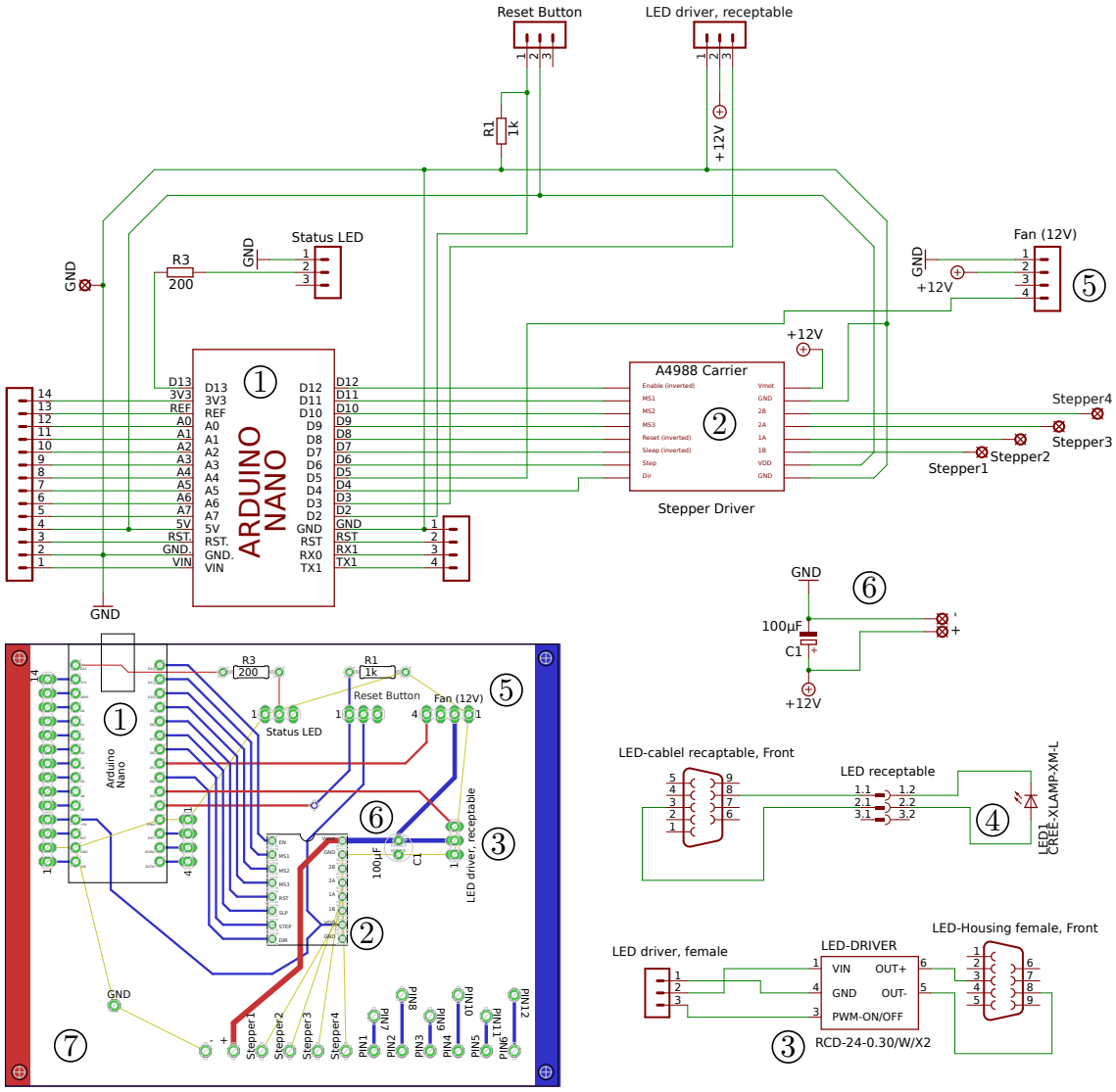

Figure 4.11

Electrical circuit diagram of the goniometer controller consisting of an ARDUINO NANO microcontroller ①, a stepper driver ② for moving the sample stage, and a LED driver ③ to power the connected light source ④. A power supply for a cooling fan is provided at ⑤ and a capacitor ⑥ is used to stabilize the input power and protect the electronics from voltage peaks. The corresponding board layout ⑦ is provided in the bottom left.

CHAPTER 5

Hierarchically Structured ZnO Scattering Layers

The present chapter tackles the question how the efficiency of OLEDs can be enhanced with the implementation of scattering layers. Therefore, the need for such scattering layers in OPV and OLEDs is discussed in Section 5.1. Hence, ZnO thin films are investigated regarding their scattering behavior in the visible range of light. Hierarchically structured scattering layers were fabricated via spray deposition from solution. This is obtained by combining a structure directing diblock copolymer template with sol-gel chemistry on the basis of the ZnO precursor ZAD. As templating material the diblock copolymer PS-*b*-PEO is used, as described in Section 5.2. Since sol-gel chemistry typically leads to structures in the nm-range, PS microspheres are added to the system in order to provide an additional template for larger structures. The size of the microspheres is chosen to be 500 nm in order to be in the range of visible light's wavelengths and thus can be used for light scattering in OPV and OLEDs. The influence of the PS microsphere concentration in the sol-gel preparation step on the final ZnO morphology and the resulting scattering behavior in the spectral range of visible light is investigated. Therefore, their spectral response is examined in Section 5.3 regarding the transmission and reflection behavior with UV-Vis spectroscopy. Furthermore, the angular resolved scattering behavior is quantified with measurements obtained from the custom built setup described in Section 4.5. The surface topography is probed in Section 5.4 via surface sensitive AFM and SEM measurements. In order to examine the inner film morphology, GISAXS measurements were conducted at the I22 instrument at the Diamond Light Source, UK with the help of Dr. Paul Staniec. The

obtained results about the inner structure are discussed in Section 5.5. The morphological changes of the surface and inner film morphology of fabricated ZnO scattering layers are linked to the PS microsphere concentration during sol-gel preparation. Finally, ZnO/PEDOT:PSS bilayers were tested in the frame of the Bachelor's thesis of Irina Ilicheva[146] and are discussed in Section 5.6 regarding their performance as transparent polymeric electrodes for application in OLED devices.

5.1 Demand for Scattering Layers

In the recent years, the efficiency and lifetime of OLEDs reached values which render them suitable for industrial applications. The large variety of available organic emitters enables OLEDs to cover a wide range of the visible color spectrum. By using phosphor emitters, the internal quantum efficiency reached values close to the theoretically possible maximum of 100 %.[24] As described in detail in Subsection 2.4.3, the overall efficiency still suffers from the extraction of photons from the device.[68]

Several approaches exist to overcome this drawback, e.g., attaching micro-lenses on the substrate surface[27] or applying Bragg scattering layers into the device.[147] Both of them have the disadvantage of high wavelength dependent scattering due to their high order, which leads to a color shift of the scattered light. A promising approach to enhance the light outcoupling of OLED devices consists in the implementation of an additional scattering layer. Such a layer might redirect generated photons and, thereby, suppress total reflection back into the device. Consequently, substrate modes can be reduced to reach a higher photon outcoupling efficiency. The integration of a nanostructured scattering layer consisting of a transparent metal oxide holds high potential, due to its chemical stability and high refractive index. By matching the refractive index to the adjacent layers, both, substrate and organic modes might be suppressed, which would enhance the EQE significantly. The basic idea for such a layer is represented in Figure 5.1, where the scattering layer is implemented between the substrate and the transparent electrode. In such a case, the commonly used brittle metal oxides such as ITO and FTO need to be replaced by an electrode with less destructive deposition techniques. With an optical band gap of ~3.3 eV and a refractive index of ~2.0, ZnO is a suitable material for this approach as it reveals high transmittance in the visible range of light.

In order to tailor the ZnO scattering layer, the structure directing diblock copolymer template PS-*b*-PEO is combined with sol-gel chemistry. This procedure allows the fabrication of custom-tailored, nanoporous ZnO layers with tuned overall porosity.[47] Thereby, the correlated refractive index of the respective layer can be precisely controlled. Thus, the refractive index mismatch of the different functional layers to the substrate can be adjusted in order to provide a gradient interface that can reduce organic modes. By introducing microspheres with a larger size as secondary template, an

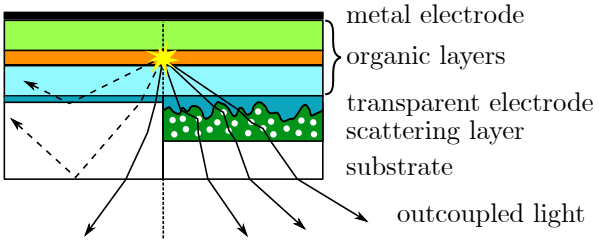

Figure 5.1
OLED device with integrated scattering layer. Without scattering layer (left), light extraction is limited by total reflection. With scattering layer (right), generated photons are redirected in order to suppress total reflection.

additional structure size can be implemented.[148,149] Therefore, a hierarchically porous structure can be achieved, which allows to introduce additional scattering centers that match the desired wavelength of interest. By mixing various sized microspheres, the scattering can be further adjusted in order to cover the emission spectra of white OLEDs and therefore minimize spectral shifts of the scattered light and provide a high angular dependent color stability.

5.2 Investigated Samples

A detailed sample preparation for the ZnO scattering layers investigated in the present chapter is given in Section 3.3. The required sol-gel solution is prepared, according to Subsection 3.3.1, using the diblock copolymer PS-*b*-PEO that serves as structure directing agent. The polymer is dissolved in DMF with a constant concentration of $25\,\mathrm{mg\,mL^{-1}}$ for all samples. In this case, DMF is used as so-called good solvent, as it dissolves both blocks of PS-*b*-PEO equally well. The dissolved polymer is mixed with the selective solvent H_2O and the precursor ZAD. By addition of H_2O, the micelle formation is induced, where the PS block forms the inner core, causing nanopores in the final film, and the PEO block forms the ZAD enriched shell. To achieve a porous nanostructure, the mixing ratio is kept constant for all samples by a weight ratio of $w_{\mathrm{DMF}} : w_{\mathrm{H_2O}} : w_{\mathrm{ZAD}} = 0.92 : 0.01 : 0.07$.[47] The obtained parent solution is split and separately mixed with varying PS microsphere concentrations, ranging from 0 wt.% – 8.45 wt.%. All used concentrations are listed in Table 5.1. A PS microsphere size of ⌀ 500 nm is selected to provide additional scattering centers for visible light. Since PS is dissolved by DMF, the viscosity of the sol-gel is increased with higher microsphere concentrations, which might lead to inhomogeneous deposition. Therefore, the microspheres are added shortly before deposition. Acid cleaned glass slides with a size of $2.4 \times 2.4\,\mathrm{cm^2}$ are used as transparent substrates (see page 48). Thin films are deposited via spray coating at ambient conditions ($T = 22.4\,^{\circ}\mathrm{C}$, $RH = 23\,\%$), according to Subsection 3.3.2. High temperature treatment at $400\,^{\circ}\mathrm{C}$ is used to finalize the ZnO scattering layers by extracting the structure giving polymer templates via calcination.

Table 5.1
PS microsphere concentrations used for fabrication of ZnO scattering layers. Microspheres are added shortly before deposition into the prepared sol-gel solution. Concentrations are calculated from relations of the microsphere's mass ($26\,\mathrm{mg\,mL^{-1}}$) to the solution's volume[†] and the diblock copolymer mass[‡].

sample #	1	2	3	4	5	6	7
$c\ \left[\mathrm{mg\,mL^{-1}}\right]^{\dagger}$	0	0.11	0.23	0.56	1.09	1.61	2.10
$c\ [\mathrm{wt.\%}]^{\ddagger}$	0	0.46	0.91	2.26	4.41	6.48	8.45

5.3 Optical Properties

As the above introduced ZnO thin films are supposed to serve as scattering layers in OLED applications, their performance regarding visible light scattering is of high interest. In Figure 5.2, selected ZnO samples are depicted and compared to a bare glass substrate. The samples are fabricated with precursor solutions taken at different stages of the sample preparation routine depicted in Figure 3.7. The diffuse scattering for the pure ZnO precursor is already visible with bare eyes. Addition of the structure giving diblock copolymer PS-*b*-PEO and further addition of PS microspheres leads to an even more enhanced diffuse scattering, apparent by the blurry letters underneath the samples in Figure 5.2. For a more detailed analysis, the scattering layers are characterized regarding their scattering ability of visible light. For this purpose, the present section covers the transmittance, reflectance and angular dependent scattering characteristic of the investigated samples in Subsection 5.3.1 and Subsection 5.3.2, respectively. The data is obtained by employing UV-Vis spectroscopy and a custom built angular dependent scattering setup, as described in Subsection 4.1.1 and Section 4.5, respectively.

5.3.1 UV-Vis

The ZnO thin films were characterized with different setups of UV-Vis spectroscopy. As depicted in Figure 4.1, the two used instruments allow measuring of the direct and the total amount of reflectance R and transmittance T of thin films. By comparing the results of all measurements one can draw conclusions about the diffuse scattering behavior and the amount of forward directed light.

In Figure 5.3 the transmittance of the as-prepared samples (marked with U) are depicted and compared to a bare glass substrate and an exemplary calcined ZnO sample. All of the uncalcined samples reveal an almost identical transmittance, independent on the used PS microsphere concentration. Their transmission is almost as good as the used glass substrate, which dominates the transmittance and the beginning absorp-

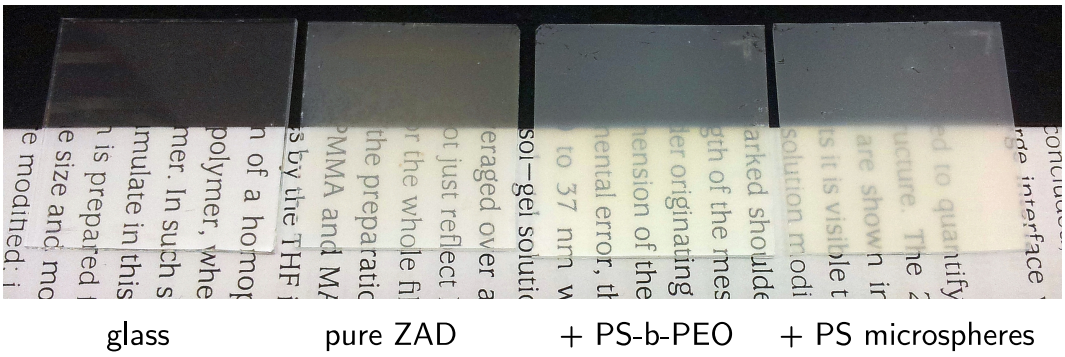

Figure 5.2
Photograph of selected ZnO scattering layers. Films are fabricated from casting solutions taken at different stages of the sample preparation procedure depicted in Figure 3.7, as indicated in the subtitle of each column. Application of pure ZAD precursor leads already to diffuse scattering compared to the bare glass substrate. Addition of the block copolymer PS-*b*-PEO and further addition of PS microspheres yields enhanced diffuse scattering, indicated by blurry letters underneath the samples.

Figure 5.3
Transmittance of as-prepared ZnO layers, measured with an integrating sphere. Uncalcined films (U) consist of deposited PS-*b*-PEO with incorporated ZAD precursor and embedded PS microspheres. Transmittance is just slightly reduced for as-prepared films and independent on microsphere concentration. Absorption edge is dominated by absorption of glass substrate (dashed grey). Exemplary calcined film (solid line) shows clearly the absorption edge for ZnO, indicating crystallization.

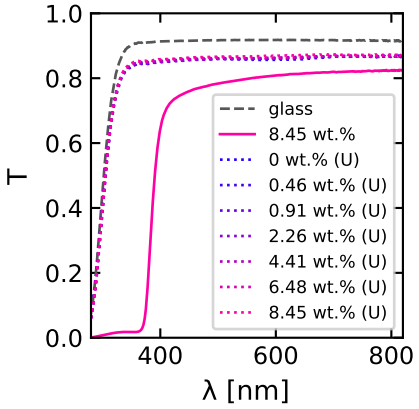

tion around 310 nm. After calcination at 400 °C, the templating diblock copolymer together with the introduced PS microspheres are removed by combustion and the provided heat leads to transition of the ZAD precursor to ZnO crystallites. Thus, the final ZnO scattering layers are formed. The crystallization becomes clearly visible in the shift of the absorption edge towards ~380 nm, corresponding to the ZnO band gap of ~3.3 eV.[115,116]

In Figure 5.4, the optical response of all calcined samples is depicted. The direct transmittance (Figure 5.4a) shows a clear wavelength dependency with decreasing transmission for smaller wavelengths down to full absorption at the band gap energy of ZnO. Furthermore, the transmittance is continuously reduced for increasing PS microsphere concentrations. The direct reflectance (Figure 5.4d) draws a similar picture regarding wavelength dependency and reduced reflectance for increased PS microsphere concentrations. As the reflectance was measured according to Subsection 4.1.1 with

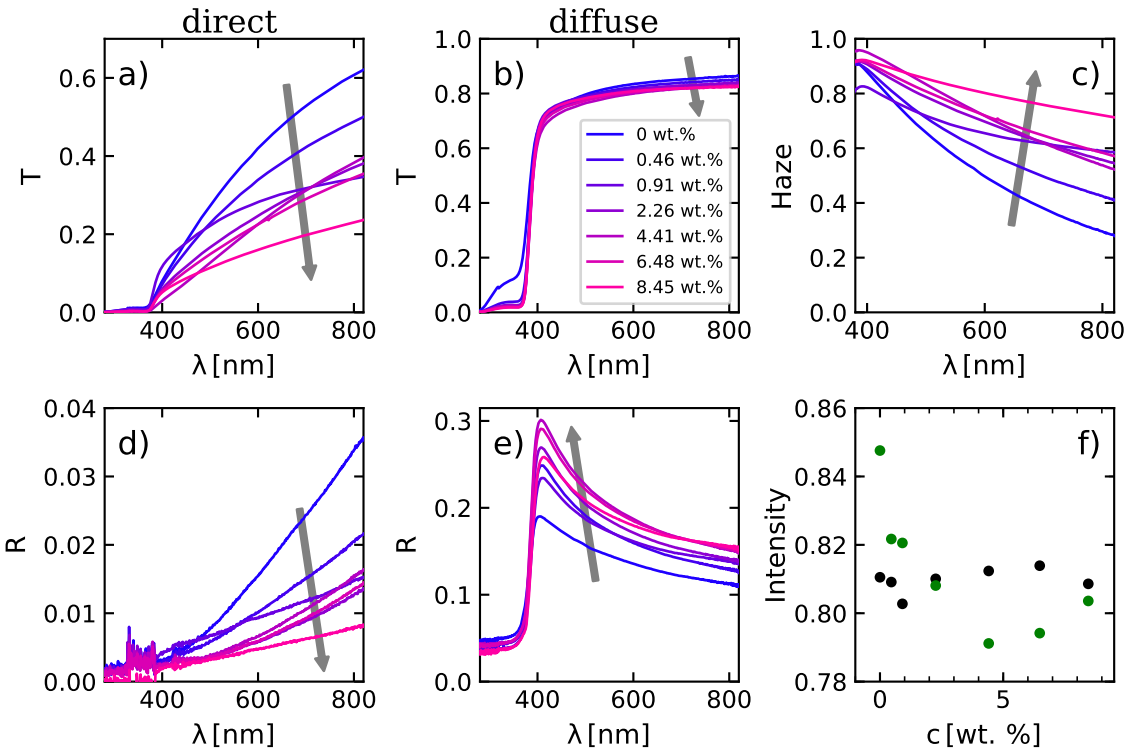

Figure 5.4
UV-Vis spectra of calcined ZnO scattering layers measured according to Subsection 4.1.1. Scattering layers are fabricated with different amounts of PS microspheres ranging from $0\,\mathrm{wt.\%} - 8.45\,\mathrm{wt.\%}$. Direct transmittance (a) and reflectance (d) decreases with increasing concentration. The total transmittance (b) decreases slightly, while the total reflectance (e) is increased. c) The resulting transmission haze, calculated from a) and b), increases with PS microsphere concentration. f) The integral from $280\,\mathrm{nm} - 820\,\mathrm{nm}$ of the sum of total reflectance and transmittance I_t (black) shows no significant increase in absorbance, while the ratio I_f (green) of forward scattered/transmitted light to the total amount reveals a small drop to ~$80\,\%$, indicating increased reflectance.

an incident angle of $\alpha_\mathrm{i} = 45°$, it serves additionally as a measure for the specular gloss of the examined samples. Consequently, due to the very low direct reflectance/gloss, a high surface roughness can be concluded for all samples. In order to exclude absorption effects, the total transmittance and reflectance is further measured for all samples using an integrating sphere. The obtained results are depicted in Figure 5.4b,e, respectively. The total diffuse transmittance is almost constant for all samples, showing only a small reduction for increasing microsphere concentrations in the larger wavelength region. Overall, the total transmittance is considered as constant. Taking into account the reduced direct transmittance, it becomes obvious that the diffuse scattering is enhanced for increasing microsphere concentrations. This is in accordance to the measured diffuse reflectance, which is enhanced for increased microsphere concentrations as well. This strong increase can partly be related to the measurement setup itself. As depicted

in Figure 4.1, the measurement setup for diffuse reflectance requires an opening in the integrating sphere for the incoming beam. The incident light is impinging the sample anti-parallel to its surface normal. Therefore, directly reflected light might leave the integrating sphere through the same opening and is not detected by the instrument, while an enhanced diffuse scattering reduces the amount of such reflected light, which increases the overall detectable intensity. However, as the direct reflectance depicted in Figure 5.4d is very low, the above described relation has only a small contribution to the diffuse reflectance. Consequently, the diffuse reflectance is enhanced while the direct one is reduced, which is a further indication for enhanced diffuse scattering with increasing microsphere concentration.

To evaluate the amount of enhanced scattering further, the wavelength dependent transmission haze is calculated from the measured diffuse and direct transmittance. The haze value is defined as the ratio of diffuse transmittance to the total transmittance[150] and therefore is calculated according to

$$\text{Haze} = \frac{T_{\text{diffuse}} - T_{\text{direct}}}{T_{\text{diffuse}}}, \tag{5.1}$$

where T_{direct} is the measured direct transmittance of the sample and T_{diffuse} is the total transmittance obtained via an integrating sphere measurement, both depicted in Figure 5.4a,b, respectively. The calculated haze is depicted in Figure 5.4c and shows a strong increase in the large wavelength region, which is in accordance to the reduced gloss and direct transmittance. Hence, the implementation of PS microspheres leads to haze values of up to 0.82 (λ = 550 nm) and 0.72 (λ = 800 nm) for the highest microsphere concentration. Thus, the diffuse scattering is clearly enhanced.

In order to quantify the obtained results further, the total intensity I_{t} of the transmitted and reflected light as well as the fraction of the transmitted to the total intensity I_{f} is calculated by

$$I_{\text{t}} = \int_{280\,\text{nm}}^{820\,\text{nm}} T(\lambda) + R(\lambda)\,\text{d}\lambda \left(\int_{280\,\text{nm}}^{820\,\text{nm}} \text{d}\lambda \right)^{-1}, \tag{5.2}$$

$$I_{\text{f}} = \int_{280\,\text{nm}}^{820\,\text{nm}} T(\lambda)\,\text{d}\lambda \left(\int_{280\,\text{nm}}^{820\,\text{nm}} T(\lambda) + R(\lambda)\,\text{d}\lambda \right)^{-1}, \tag{5.3}$$

with T and R being the total measured transmittance and reflectance, respectively. The results of the total intensity I_{t} and its amount of forward transmitted light I_{f} are depicted in Figure 5.4f. The total intensity shows an almost constant behavior for increasing microsphere concentrations, proving no change in the overall absorption. The amount of forward directed scattering I_{f} is slightly reduced for increasing concentrations, indicating a slightly increased diffuse back scattering of the incident light, which is in accordance to the total reflectance measurements (Figure 5.4e). However,

the available data suggest a strongly enhanced diffuse scattering for visible light, which can be beneficial for the light outcoupling in OLED devices. The slight increase for high concentrations might be related to the increased viscosity of the sprayed sol-gel solution which resulted in inhomogeneities on the film. In order to investigate the scattering of the visible light in more detail, angular dependent measurements are evaluated in the following section.

5.3.2 Angle Resolved Light Scattering

UV-Vis spectroscopy employed with an integrating sphere is not capable to resolve the angular scattering in more detail. Thus, a custom built setup is used in order to characterize the angular dependent transmittance through a thin film as introduced in Section 4.5. Thereby, a white LED light source is used to illuminate the scattering layers and detect the angle resolved scattering intensity after passing through the sample. For this purpose, the incident angle of the incoming light is kept anti-parallel to the surface normal and the whole sample stage (sample including light source) is rotated around the scattering angle φ.

Hence, the angle φ is scanned from $-30° - 30°$ in $1°$ steps and the transmitted spectral irradiance under the given angle is detected. The obtained 1D spectra are linked to the scattering angle and stitched together in order to create a 2D scattering pattern that represents the wavelength and angular dependent scattering of the investigated samples. The obtained results are depicted in Figure 5.5, where the diffuse scattering patterns of ZnO films, fabricated with PS microsphere concentrations ranging from 0 wt.% – 8.45 wt.% (Figure 5.5c-i), are given. The empty beam measurement and the scattering pattern of a bare glass substrate are shown in Figure 5.5a,b, respectively. For the sake of comparability, the measured irradiance for all samples is normalized to the maximum intensity of the empty beam measurement. The visible pattern for the empty beam is mainly dominated by the used light source, whose emission spectrum is given in Figure 4.10, showing emission peaks around 449 nm and 608 nm. Furthermore, the beam widening and the detector dimensions yield a naturally broad pattern of around ~8° width for the empty beam (Figure 5.5a). The glass substrate itself, depicted in Figure 5.5b, does not alter the scattering pattern significantly. The application of a ZnO scattering layer in Figure 5.5c has two main effects. Firstly, the peak intensity drops, which is in accordance to the earlier discussed UV-Vis study of the direct transmittance. Secondly, a clearly enhanced diffuse scattering is apparent, visible by the intensity signal for higher scattering angles φ of up to 30° and beyond. Further addition of PS microspheres seems to intensify this effect. Scattering depends highly on the size and shape of the scattering objects in relation to the scattered wavelength. However, the obtained 2D scattering patterns reveal no clear change in the wavelength dependent scattering, as no wavelength shift along the φ-axis is observable. Therefore, the scattering layers create a weak wavelength dependency with a high color stability

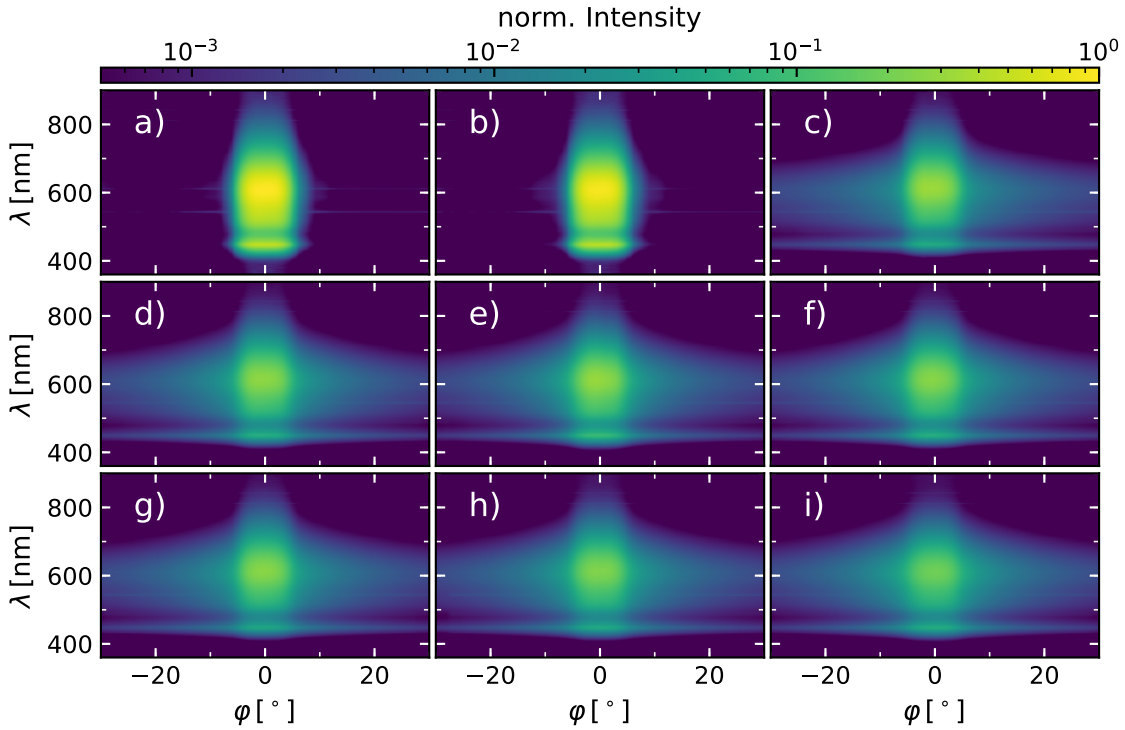

Figure 5.5
Angular and wavelength dependent scattering of ZnO thin films performed with the setup described in Section 4.5. The spectral irradiance is normalized to the highest intensity of the empty beam. Measurement of empty beam a) and glass substrate b) serve as reference. Amount of diffuse scattering for higher angles φ is enhanced for ZnO scattering layers with increasing PS microsphere concentrations ranging from $0\,\mathrm{wt.\%} - 8.45\,\mathrm{wt.\%}$ in c-i).

in the visible range of light, which will be especially beneficial for scattering of white light.

In order to analyze the angular dependent scattering in more detail, the 2D patterns are integrated along the wavelength range of $400\,\mathrm{nm} - 850\,\mathrm{nm}$ to obtain an angular dependent scattering curve of the total irradiance $E_\mathrm{e}(\varphi)$. The resulting spectra are obtained from the non-normalized spectral irradiance $E_\mathrm{e}(\varphi, \lambda)$ in order to distinguish the total transmitted amount of light. The drop in the peak intensity compared to the bare glass substrate is clearly visible in Figure 5.6a for the application of a ZnO layer and is mainly related to the increased reflectance, as seen in Subsection 5.3.1. In addition, the sides of the scattering curve shift to larger angles, which is visible for the normalized irradiance depicted in Figure 5.6b and further shows enhanced diffuse scattering. Consequently, the implementation of PS microspheres leads to an enhanced peak widening with slightly decreased peak intensity. Hence, a beneficial effect of the addition of PS microspheres becomes more apparent.

In order to quantify the changes of the peak width depending on the used PS microsphere concentrations, the scattering curves are further analyzed: the total scattering

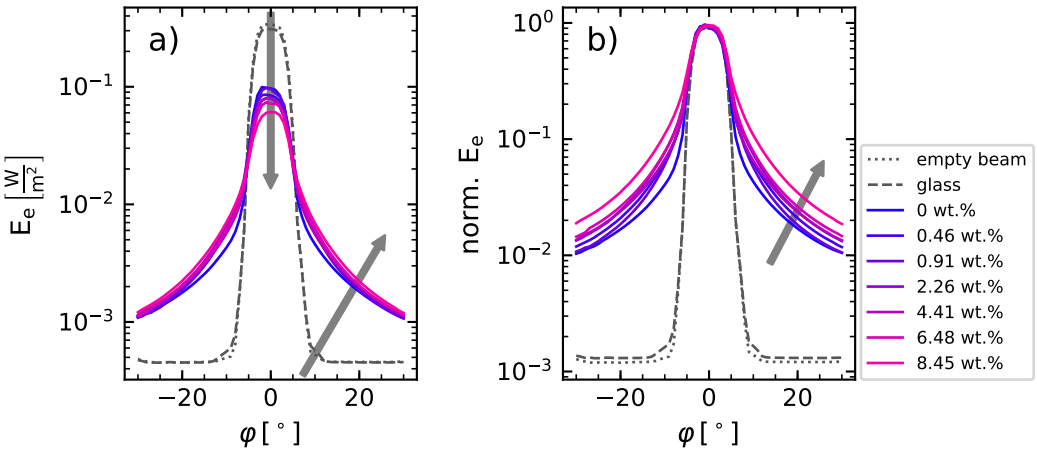

Figure 5.6
Evaluation of goniometer measurements on ZnO scattering layers with varied PS microsphere concentrations. a) Angular dependent irradiance E_e obtained from the spectral irradiance (Figure 5.5) integrated along the wavelength range $400\,\mathrm{nm} - 850\,\mathrm{nm}$. b) Normalized irradiance E_e. Empty beam (dotted grey) and glass substrate (dashed grey) measurements serve as reference for the ZnO layers. Decreased height and increased width indicates peak spreading for increasing PS microsphere concentrations of $0\,\mathrm{wt.\%} - 8.45\,\mathrm{wt.\%}$ (blue to pink).

intensity is obtained by integrating the irradiance E_e over all scattering angles and normalizing to the empty beam intensity. The results in Figure 5.7 show a reduced intensity for the glass substrate and a large drop for ZnO scattering layers. Both decreases are mainly related to the corresponding reflectance in the given region of $400\,\mathrm{nm} - 850\,\mathrm{nm}$ of ~8 % for glass and up to ~30 % for the ZnO scattering layers. Thus, the large drop in intensity compared to the reference glass measurement can be explained with the increased reflectance of the scattering layers as depicted in Figure 5.4e. Here, one should note, the measurement setup geometry only covers the scattering on a semicircular arc behind the sample. Consequently, only a spherical segment of the full hemispherical scattering is detectable. Thus, the detected total intensity is underestimated and the intensity drop is overestimated for enhanced scattering. This drawback is canceled out by the previously discussed UV-Vis study, which shows for the different treatments an almost constant total transmitted intensity above 80 %. A more representative peak characteristic is given by the FWHM and the integral breadth, which allow a quantitative measure of the peak spreading and therefore the increased diffuse scattering ability. The obtained results are depicted as well in Figure 5.7 and marked with guides to the eye, which show a similar increase for both. The FWHM is rising from $(7.4 \pm 0.2)°$ for the empty beam to $(8.5 \pm 0.1)°$, showing a clear peak widening. As the FWHM highly depends on the peak shape, the integral breadth is a more reliable measure for peak spreading. The integral breadth is increasing from 0.11 ± 0.01 for the empty beam to 0.18 ± 0.01 for the highest microsphere concentration, which corresponds to an enhancement of about 61 %. Thus, the

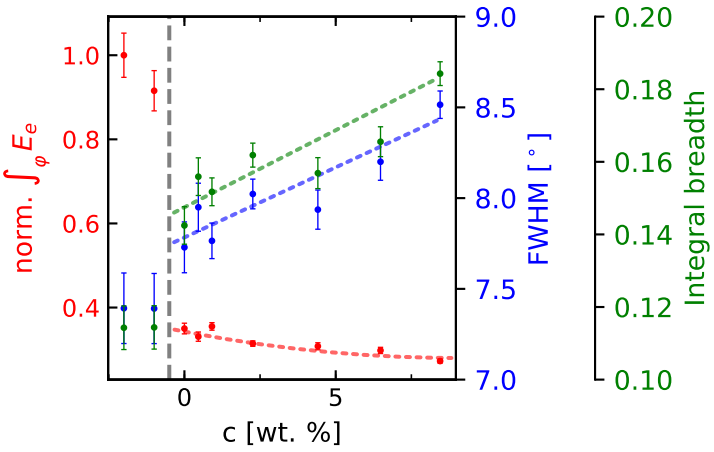

Figure 5.7
Evaluation of angular dependent scattering extracted from Figure 5.6. The total irradiance (red) in dependence on the PS microsphere concentration is obtained by integration along the scattering angle φ and is normalized to the empty beam measurement. The large drop in the total transmitted intensity is followed by a slight decrease for the ZnO samples. The first drop is related to the enhanced reflectance compared to glass (see Figure 5.4e), the second one is related to the increased PS microsphere concentration. FWHM (blue) and integral breadth (green) of the corresponding peaks are increased, verifying peak spreading. The colored dashed lines serve as guide to the eye. The grey dashed line separates the reference measurements of empty beam and glass substrate (left) from the ZnO scattering layers (right).

obtained results are in agreement with the previously discussed UV-Vis study. From the given data it is evident that the application of ZnO layers, commonly prepared with a structure directing diblock copolymer, already leads to a clear peak spreading and therefore enhanced diffuse scattering abilities. The application of additionally implemented PS microspheres is capable to enhance this scattering ability even further, which makes thin films fabricated in such a way to an ideal candidate for scattering layers.

5.4 Surface Morphology

In order to fathom the origin of the enhanced diffuse scattering for ZnO thin films fabricated with a diblock copolymer and PS microsphere additive the surface structure of those films is examined employing different scanning probe techniques. Therefore, surface profilometry, AFM and SEM measurements were performed in order to examine the film thickness, roughness and surface morphology.

5.4.1 Surface Roughness

To determine the film's thickness, surface profilometry was performed with a DektakXT instrument according to Subsection 4.3.2. Therefore, the sample's surface is scratched down to the substrate and a profile scan is performed across the scratches on several spots per sample. From the resulting profiles, the average step height and surface roughness is extracted in order to obtain the mean film thickness d and the root mean square (rms) surface roughness P_q with their corresponding standard deviation, respectively. The results in dependence on the used PS microsphere concentrations are depicted in Figure 5.8. The average film thickness shows values around 1.0 µm – 1.5 µm with a slight decrease for medium microsphere concentrations (Figure 5.8a). All samples show a film thickness that is large enough to fully cover the implemented PS microspheres of 500 nm in diameter. Thus, the microspheres are likely embedded into the ZnO films and create a hierarchical structure with additional scattering centers in the large nanometer sized region. The large deviation of the film thickness is presumably related to the high surface roughness, already indicated by the former UV-Vis study in Section 5.3 and proven by the rms surface roughness P_q, depicted in Figure 5.8b. A mean roughness of ~0.4 µm with a large deviation is observed for all samples. The variation in thickness and its deviation might be related to the spraying process itself and the finalizing calcination step. Together, this could lead to a rough and inhomogeneous surface. In general, spray deposition causes rougher films as compared to spin coating. Nevertheless, the films fabricated with PS microsphere templates, though of similar roughness as the reference spray sample, show enhanced diffuse scattering.

In order to improve the statistics of the surface roughness measurement and get an impression about the surface morphology, AFM measurements were performed according to Subsection 4.3.3. The obtained micrographs cover an area of $40 \times 40\,\mu m^2$ and are depicted in Figure 5.9a-g. For a better comparability, the limits of the height information are fixed to 0 µm and 5 µm for all images. All samples reveal a differently pronounced surface structure, dominated by randomly oriented wrinkles with varying size and elongation. The appearance of such wrinkles was observed earlier and is typical for ZnO films fabricated via a sol-gel approach.[151,152] The formation of this structure is related to a slow evaporation time of residual solvent, which provides mobility to the gel particles and leads to a reorganization and piling up during drying.[153,154] Hence, the rather low annealing temperature of 80 °C of the heating plate during wet spray deposition together with the slow heating ramp of 6.25 °C min^{-1} during calcination leads to the observed wrinkles. Thus, faster heating up during calcination should result in smoother films. Additionally, such a structure can be easily obtained for thick films.[39] However, the obtained structure sizes of the wrinkles are typically in the range of 50 nm – 200 nm with distances of 500 nm – 1000 nm and therefore are referred to as nano-ridges.[151,152,155–157] In contrast, in the present case, the structure sizes are in the range of a few µm with distances of tens of µm and thus are about 10

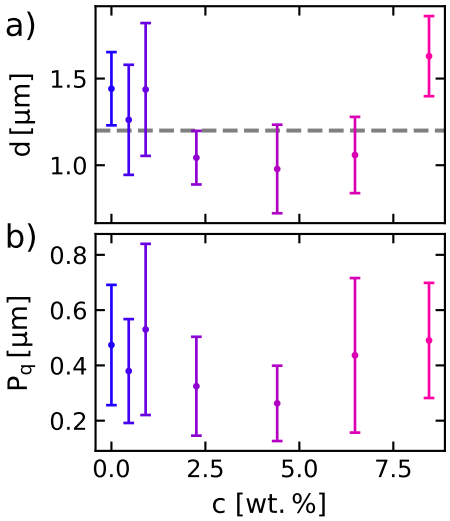

Figure 5.8
a) Average film thickness d and b) average root mean square roughness P_q of ZnO thin films. Measurements were performed at various positions on the samples and averaged in order to obtain a mean value and the standard deviation of d and P_q. The average film thickness of ~1.2 µm (dashed line) is sufficient to bury microspheres of 0.5 µm size. The large deviation for both values is originated in a high surface roughness.

times larger as the typically obtained structures. Therefore, much larger length scales of such wrinkles can be obtained with the use of a diblock copolymer, revealing an enhanced hierarchical structure in the µm-range. On one hand, no clear correlation of the microsphere concentration to the surface structure is observed. On the other hand, the implementation of PS microspheres provides an additional amount of homopolymer to the diblock copolymer and therefore dissolution of the PS might alter the final structure. Furthermore, the scattering of visible light indicates a structural change in the thin films with dependence on the microsphere concentration. For all cases, the random surface structure is in accordance to the high surface roughness determined by profilometry measurements, which reveals a strongly enhanced interfacial area and additionally also contributes to the diffuse light scattering.[151]

In order to quantify the surface structure further, data reduction in combination with a statistical evaluation is performed. For this purpose, the mean height $\langle z \rangle$ is extracted for all samples from the micrographs and plotted together with the rms roughness as deviation in Figure 5.9h. The mean height is located in the same region as the average film thickness, indicating a large influence of the peak height, corresponding to the wrinkled structure. Therefore, the surface morphology and the average film thickness is dominated by the formation of wrinkles with peak to valley differences of up to 5 µm.

The rms roughness P_q is calculated for each line of the micrographs. The final roughness with its deviation is then calculated by the mean value and standard deviation of all lines and is depicted in Figure 5.9i. Here, the 0.91 wt.% sample shows an outlier position, which might be related to surface inhomogeneities caused by spraying of the viscous sol-gel solution. For all samples, a large surface roughness is determined ranging from 0.5 µm – 1 µm, which shows comparable values to the ones obtained from surface profilometry measurements, depicted in Figure 5.8b. Therefore, a macroscopic rough surface with heights and valleys is obtained, resulting in highly hierarchically

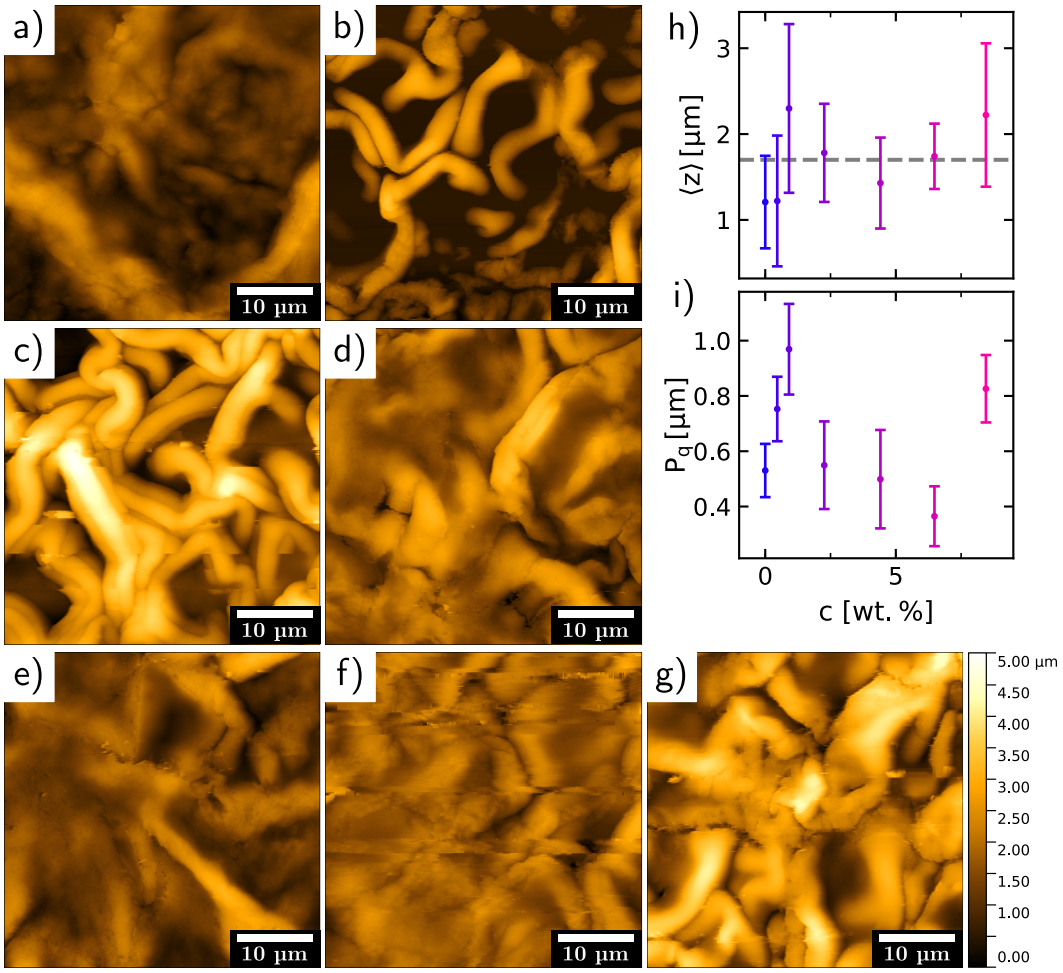

Figure 5.9
a-g) AFM micrographs of ZnO scattering layers fabricated with varying PS microsphere concentrations ranging from $0\,\mathrm{wt.\%} - 8.45\,\mathrm{wt.\%}$. Typical randomly wrinkled structures are visible for all samples. A high surface roughness with a mean height of $\sim 1.7\,\mu\mathrm{m}$ and a maximum peak height of up to $5\,\mu\mathrm{m}$ is obtained for all samples, leading to large diffuse scattering. h) Extracted mean height value $\langle z \rangle$ and rms roughness deviation of the corresponding AFM measurements. i) Rms roughness P_q extracted from AFM micrographs. The depicted deviation of P_q is calculated from the standard deviation of each scanned line.

structured samples. All samples reveal a large surface roughness in combination with a randomly wrinkled structure. Overall, the implementation of PS microspheres has low correlation to the surface roughness but shows an increased light scattering ability. Consequently, a morphological change in the thin film is reasonable. It is noteworthy to mention that the addition of PS microspheres into the sol-gel leads to partial dissolving of the PS that results in an increased viscosity for higher concentrations. This leads to a reduced flow rate during spray deposition, which requires steady control of the process. Therefore, the obtained wrinkled structure and surface roughness is probably also altered by the fabrication process itself and the resulting film formation.

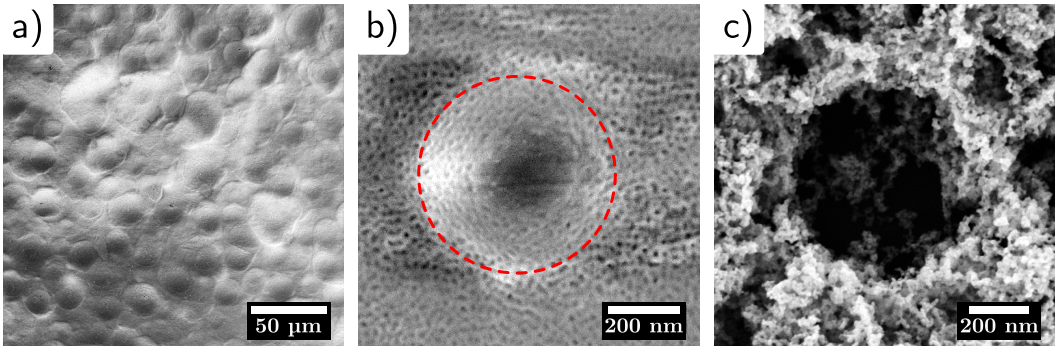

Figure 5.10
Exemplary SEM images of (un)calcined spray deposited ZnO thin films. a) Uncalcined samples revealing spray droplets with ⌀ ~20 µm. b) Zoom in of uncalcined sample shows an embedded PS microsphere of ⌀ 500 nm (red dashed circle). The templating effect of the used PS-*b*-PEO diblock copolymer towards porous ZnO is clearly visible. Dark spots represent the non-polar PS block, while bright spots represent the ZAD enriched PEO block. c) The combusted PS microspheres lead to additional large pores in the final calcined ZnO layer. The small porous structure originates from the removed PS-*b*-PEO template.

5.4.2 Surface Structure

As surface profilometry and AFM measurements suggest a randomly macroscopic structured surface with high roughness, SEM measurements with various magnifications were performed on the samples in order to evaluate the surface morphology further. To check the influence of the spray deposition itself on the surface morphology, uncalcined samples were additionally investigated with SEM. An exemplary measurement of an uncalcined sample is given in Figure 5.10a, showing the typical formation of spray droplets on the sample's surface. The size of such droplets vary for the used spray settings around 20 µm and is an additional reason for the macroscopic surface roughness. However, the size of those droplets is too large to contribute to the wrinkled surface structure, which is in the range of a few µm and is mainly dominated by the evaporation kinetics of the residual solvent and the subsequent calcination process.[151,153,154]

As described in more detail in Section 5.3, the influence of the microsphere concentrations on the visible light scattering is evident. However, the appearance of hollow spheres created by the removal of the PS microspheres is not proven yet. In Figure 5.10b, a well embedded PS microsphere is observed for an increased magnification. The visible microsphere maintains a size of ~500 nm and therefore is not significantly dissolved by the solvent DMF. As the microspheres are nicely embedded into the structured PS-*b*-PEO/ZAD mixture and the film thickness is sufficient, additional buried microspheres are reasonably assumed inside the film. The resulting pores of such combusted buried microspheres contribute to the scattering of visible light, as seen in the UV-Vis and goniometer measurements in Section 5.3. For an approximately homoge-

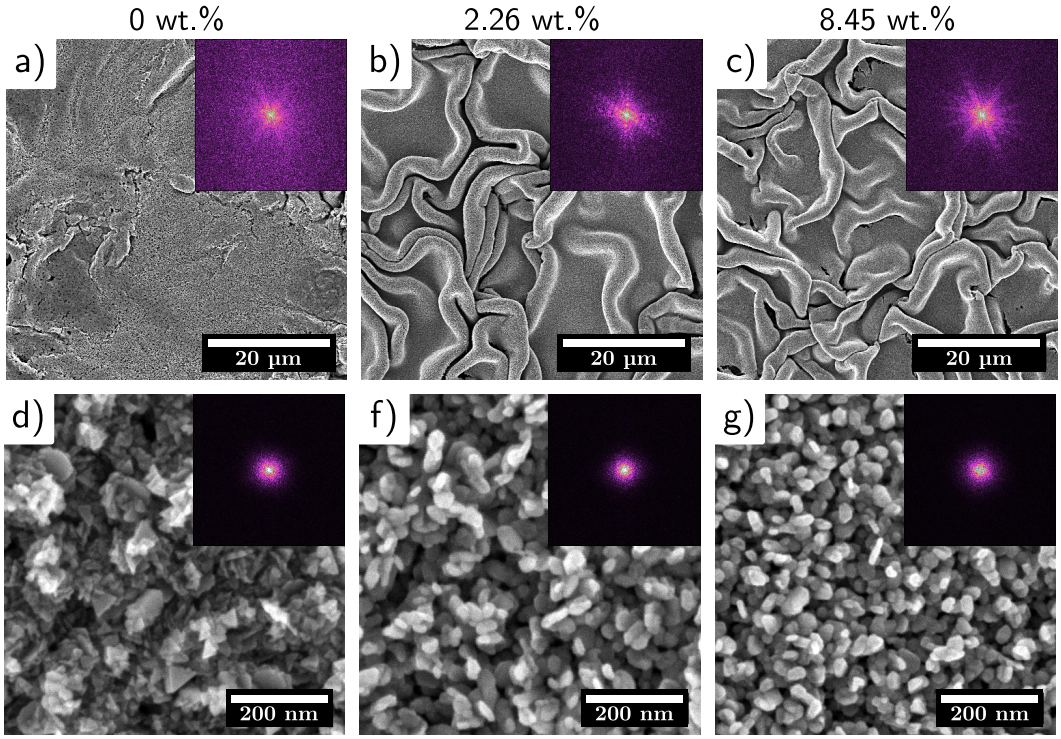

Figure 5.11
SEM images with corresponding 2D FFT (inset) of calcined ZnO thin films fabricated with different amount of PS microspheres additive. Increasing microsphere concentration leads to a wrinkled structure in the µm-range (top row), while the nanostructures are changing towards spherical shape leading to a densification at the surface (bottom row). A hierarchical structure is obtained for increased microsphere concentrations, while a porous structure is maintained for all samples.

neous topography and as explained in Subsection 4.3.4, bright spots in SEM images are correlated to a high electron density, originated in a large amount of ZAD/ZnO. Dark spots on the other hand, are correlated to a low electron density and therefore are linked in the present case to a polymer rich phase. Hence, dark spots are assigned to the PS-block, whereas bright spots are allocated to the ZAD enriched PEO block of the used diblock copolymer. The micelle formation during sample preparation leads to the nanostructured porous-like surface of the uncalcined films with ~10 nm pore size, as depicted in Figure 5.10b. An exemplary sample after calcination is depicted in Figure 5.10c, showing a maintained porous nanostructure with an additional large hole inside. The depicted large hole with size of ~500 nm proves the successful removal of the implemented PS microspheres, introducing an additional structure size into the final thin films. Thus, besides the increase of the surface roughness achieved with spray coating and the wrinkled structure formation, the PS microspheres provide a further templating.

In Figure 5.11, selected SEM images of calcined ZnO scattering layers fabricated

with increasing PS microsphere concentrations are depicted with magnifications of 1×10^3 and 80×10^3. The insets show the corresponding FFT of the image. The scattering layer fabricated without additional PS microspheres show a rather homogeneous macroscopic surface. With the addition of PS microspheres, the earlier observed wrinkled structure gets intensified, which is consistent to the AFM measurements. However, further increase of the microsphere concentration has low impact on the randomly wrinkled structure, as seen in Figure 5.11a-c. Taking a look to the high magnified images, depicted in Figure 5.11d-g, the reference sample with no microsphere additive reveals a plate-like porous nanostructure. With increased microsphere concentration, the nanostructure changes to more round shaped spherical-like particles with a slight densification at the surface. This might be related to a slower drying/calcination time[158] for increased microsphere concentrations, which is in accordance to the seemingly intensified wrinkled structure.

In order to quantify the morphological changes at the surface, the radial power spectral density (RPSD) was calculated for all samples, using the software GWYDDION v2.45.[140] The RPSDs for large and small structures were extracted from SEM images with 1×10^3 and 80×10^3 magnifications, respectively and are depicted in Figure 5.12. The reference sample without PS microsphere additive shows a small peak around $q \approx 13 \times 10^{-3}\,\mathrm{nm}^{-1}$ in the RPSD for large structures (Figure 5.12a), corresponding to a comparable homogeneous surface with a dominating structure size of ~480 nm, as depicted in Figure 5.11a. For small microsphere concentrations, more prominent peaks arise around $q \approx 6 \times 10^{-3}\,\mathrm{nm}^{-1}$ and $20 \times 10^{-3}\,\mathrm{nm}^{-1}$, corresponding to a structure size of ~1 µm and 300 nm. The occurrence of these peaks is related to the wrinkled surface structure and reflects their average size, as already shown in AFM and SEM images. The addition of PS microspheres during the sample fabrication supports the formation of this typical ZnO structure. With increasing microsphere concentrations the peaks become more pronounced and shift apart to around $q \approx 4 \times 10^{-3}\,\mathrm{nm}^{-1}$ and $24 \times 10^{-3}\,\mathrm{nm}^{-1}$, corresponding to a structure size of ~1.5 µm and 260 nm. Furthermore, the more pronounced peaks indicate a higher order within the size and spatial distribution of the wrinkles, as depicted in Figure 5.11c. Hence, the evolution of the surface structure shows a dependency of the PS microspheres on the wrinkle formation, which was not clearly seen in AFM and SEM micrographs and might be related to a surplus of PS homopolymer in the sol-gel.

The RPSD corresponding to smaller structures, depicted in Figure 5.12b, draws a different picture. A peak around $\sim 0.28\,\mathrm{nm}^{-1}$ and a poorly defined shoulder around $\sim 1.6\,\mathrm{nm}^{-1}$ are visible for the 0 wt.% sample, corresponding to the average structure size of the porous surface, depicted in Figure 5.11d. With increasing microsphere concentrations, the peak shifts to larger q-values to around $\sim 0.7\,\mathrm{nm}^{-1}$, overlaying the signal of the shoulder and indicating a reduced surface structure from ~22 nm to ~9 nm. The almost constant q-value of the shoulder corresponds to a roughly constant size of ~4 nm, which is related to an additional small surface structure. As the shoulder is

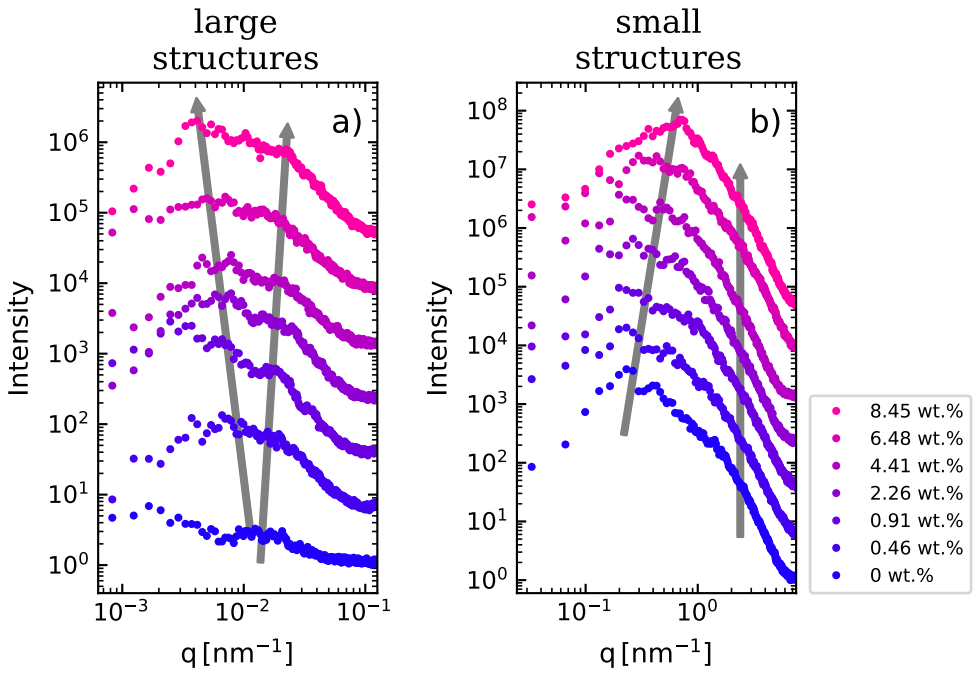

Figure 5.12
RPSD extracted from SEM images of ZnO scattering layers with 1×10^3 (a) and 80×10^3 (b) magnification (see Figure 5.11). a) For large structures, the $0\,\mathrm{wt.\%}$ sample shows a small peak around $\sim 13 \times 10^{-3}\,\mathrm{nm}^{-1}$ which splits up into two peaks around $\sim 4 \times 10^{-3}\,\mathrm{nm}^{-1}$ and $24 \times 10^{-3}\,\mathrm{nm}^{-1}$, corresponding to the wrinkled structure. b) Smaller structures reveal a peak around $0.28\,\mathrm{nm}^{-1}$ which shifts towards a low pronounced shoulder at almost constant $q \approx 1.6\,\mathrm{nm}^{-1}$, indicating a densification of the surface structure. Note that the curves are shifted in intensity for better representation.

not distinguishable anymore from the main peak, one dominating surface structure in the nm-range is concluded from SEM measurements and assigned to the average particle size. The shift of the main peak matches the observation in the SEM images, where a densification of the surface structure is observed, caused by a reduced average particle size and distance as depicted in Figure 5.11. Since such wrinkled structures are obtained via a slow drying and calcination processes, there is enough time for the film to relax before crystallizing, which results in a denser film.[151,158] Hence, the presence of the PS microspheres seems to provide additional mobility to the system during calcination, which leads to a densification of the surface structure caused by changed drying kinetics.

In summary, the combination of a structure directing diblock copolymer with larger sized PS microspheres and spray deposition technique leads to a highly hierarchically structured sample surface. This structure is composed of small and large pore sizes created by the block copolymer and the microspheres, respectively. Those pores are embedded in a randomly wrinkled sample surface that creates in addition to the generally present nm-roughness a high surface roughness in the µm-range. While the first

one strongly enhances the diffuse light scattering, the latter one is too large to significantly contribute to the scattering of visible light, but provides with its randomly wrinkled structure a large interfacial area. In contrast to the nanostructure, which is defined by the PS microsphere and block copolymer mixture, the randomly oriented superstructure in the µm-range is related to a slow drying process during sample fabrication and to a slow heating ramp during calcination. By using a diblock copolymer, much larger structures were obtained compared to the commonly observed nano-ridges for ZnO films cast from sol-gel solution. Furthermore, the wrinkled structure seems to be enhanced and homogenized with increasing microsphere concentrations, indicating an influence on the drying kinetics. Consequently, the presence of the PS microspheres seem to alter the film relaxation during the drying process.

5.5 Inner Film Morphology

The surface morphology investigations of the previous section show a hierarchical structure, consisting of small and large pores. Those are originated in the polymer/microsphere template and are embedded in a highly randomly structured surface. All together, this has a strong influence on the diffuse light scattering. As the above discussed scanning probe techniques only allow an examination of the sample's surface, the question arise how the inner film morphology changes upon PS microsphere addition. In order to probe the structure changes in the film, X-ray measurements were employed. Typically used SAXS measurements rely on a large sample thickness to achieve a suitable signal that is not dominated by the substrate itself. Therefore, GISAXS measurements were performed according to Subsection 4.4.3. This technique allows probing a large sample volume thanks to the large illuminated area on thin films, which is originated in the small incident angle. Hence, the inner film volume can be probed with high statistical relevance, allowing a more meaningful argumentation on the film's structure as the spatial and surface restricted scanning probe techniques.[39,97]

The GISAXS data presented in the upcoming section was collected with the help of Dr. Paul Staniec at the I22 instrument at the Diamond Light Source, UK. The measurements were performed with a photon energy of 12.4 keV, corresponding to $\lambda = 1\,\text{Å}$. The ZnO scattering layers deposited on top of glass substrates were probed under an incident angle of $\alpha_\text{i} = 0.18°$. The diffuse scattering was recorded with a Dectris Pilatus 2M detector, providing 1475×1679 pixels with a size of $172 \times 172\,\mu\text{m}^2$ each.[159] With the SDD set to 3915 mm, the setup enables the detection of low to medium nm-sized structures. The obtained 2D scattering patterns were further analyzed according to Subsection 4.4.3 to determine the lateral structure size in the thin film's volume. An exemplary 2D GISAXS scattering image representative for the investigated samples is depicted in Figure 5.13, revealing for all samples a strong diffuse scattering in q_z- and q_y-direction, which indicates a rough surface and

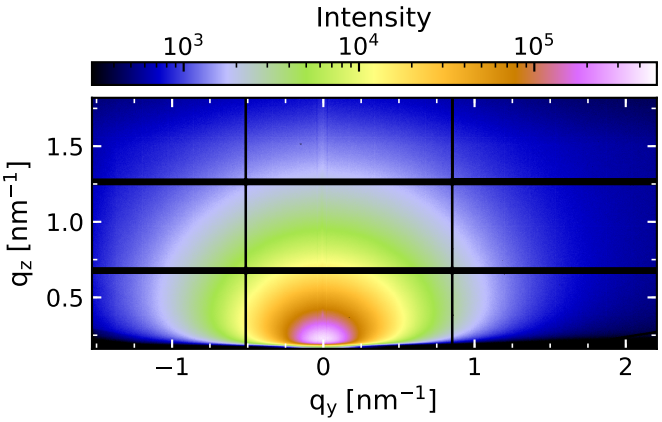

Figure 5.13
Exemplary GISAXS pattern of a ZnO scattering layer fabricated with $8.45\,\mathrm{wt.\%}$ PS microsphere concentration. Strong diffuse scattering and the absence of a specular reflection are observed. Horizontal line cuts are performed for quantitative analysis at the Yoneda peak position ($q_y = 0.24\,\mathrm{nm}^{-1}$).

inner structure. The high surface roughness is further evident by the smeared specular reflection around $q_z = 0.37\,\mathrm{nm}^{-1}$.

As the film's inner structure is of interest for scattering layers, a detailed quantitative analysis was carried out according to Subsection 4.4.3. Therefore, horizontal line cuts were performed on the 2D data at the ZnO's Yoneda peak position, revealing the lateral structure information of the sample's volume. In order to increase the measurement statistics further, the cuts were averaged over a width of five pixels. The obtained data was normalized to the Yoneda peak intensity for enhanced comparability and plotted in Figure 5.14a. The plateau-like feature for all samples results from the absence of a well-defined ordered structure, as already suggested by the surface morphology investigations and observed by Sarkar et al. for a similar system.[39] Furthermore, no prominent peaks are identified, additionally indicating a high surface roughness and a poly-disperse structure size. Therefore, the inner ZnO nanostructure morphology is randomly oriented. Besides the poorly defined nanostructure that dominates the signal, a shift from large to smaller q_y-values is observable and marked with a grey arrow in Figure 5.14a. This shift implies that an increased PS microsphere concentration leads to increased nanostructures inside the film. For a more quantitative analysis, the obtained cuts are analyzed according to Subsection 2.5.2 and Subsection 4.4.3. For this purpose, the scattering data is modeled in the frame of the DWBA, applying an EIA and LMA. The best results are obtained when assuming the presence of two substructures. Each substructure correspond to a set of spherical shaped particles with a certain mean radius and a corresponding inter-domain distance. The obtained modeled curves are depicted together with the corresponding scattering data in Figure 5.14b. For clarity reasons, the curves are shifted along the intensity and the shift of the observed shoulder towards smaller q_y-values is again marked with a grey arrow.

As concluded from the surface measurements in Section 5.4 and suggested by the 2D GISAXS scattering images, a high surface roughness with no dominant ordered structure is found. Therefore, further discussion is concentrated on the used two form factors (FF) together with their variance, which are depicted in Figure 5.14c,d,

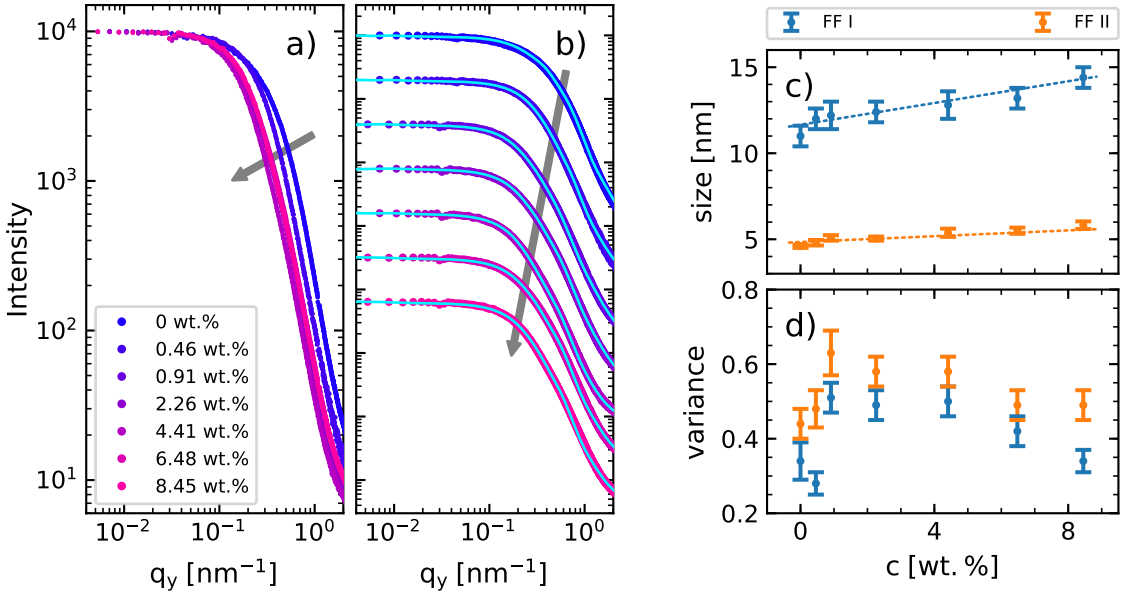

Figure 5.14
GISAXS investigation on ZnO thin films fabricated with varying PS microsphere concentrations from $0\,\mathrm{wt.\%} - 8.45\,\mathrm{wt.\%}$. a) Horizontal line cuts at the Yoneda peak position of ZnO showing a shift towards smaller q_y-values with increasing microsphere concentration, corresponding to an increase in particle size. b) The same horizontal line cuts including the corresponding model (turquoise) depicted with shifted intensity for better visibility. The microsphere concentration increases from top to bottom. The data is modeled with two form factors, while no dominant structure factor is found. c) From models extracted average particle size (diameter) for form factor I (blue) and II (orange). An increased particle size ranging from $\sim 11\,\mathrm{nm} - 15\,\mathrm{nm}$ is visible, while smaller particles stay at almost constant size around $\sim 5\,\mathrm{nm}$. The dashed lines serve as guide to the eye. d) The extracted variance of the corresponding particle size depicted in (c) shows a large deviation for both particles, indicating a polydisperse size distribution.

respectively. The form factors represent in this case the mean size of the particles found, whereas the variance give information about the deviation of this mean particle size and therefore is a measure for their polydispersity. The small form factor ($FF\ II$) correspond to a particle size around 5 nm, which is almost constant for increasing PS microsphere concentrations and is in accordance to the weakly pronounced shoulder observed in the RPSD (Figure 5.12b). The large form factor on the other hand ($FF\ I$) shows a value of ~11 nm for the reference sample with 0 wt.% microspheres. In contrast to the surface nanostructure discussed in Section 5.4, the inner structure shows an opposite trend with an increase in the particle size to up to ~15 nm for the highest microsphere concentration. In the present case, due to the high surface roughness, the randomly ordered large µm-structure and the large pores obtained from the 500 nm sized PS microspheres cannot be resolved anymore.

The solvent used during sample preparation is expected to dissolve the implemented PS microspheres very well. In order to avoid full dissolution of the microspheres and therefore a highly increased viscosity of the sol-gel, the microspheres are added shortly before deposition. On one hand, a slight dissolution of the microspheres cannot be avoided. On the other hand, the SEM study discussed in Section 5.4 proofed the presence of microspheres in the deposited film, which excludes a full dissolution. Nevertheless, an increased amount of dissolved PS in the sol-gel solution is reasonably expected. Providing the same homopolymer to the system that is present in one of the blocks of a diblock copolymer results in an increased accumulation of this material in the corresponding block during sol-gel preparation. In the present case, this leads to a swelling of the non-polar PS group of PS-*b*-PEO, which becomes apparent in micelles with an increased core size. This effect was already observed for a similar system by Kaune et al.[148] Such a swelling of the micellar core results in an increased pore size inside the final thin films. Therefore, the particle size observed with the present GISAXS study is assigned to an increased pore size from ~11 nm – 15 nm. Hence, an increased film porosity of the samples can be concluded. The corresponding deviation of both form factors, depicted in Figure 5.14d, shows a large variation around 40 % – 60 %. Therefore, the determined mean pore size is also considered as polydisperse.

Overall, the conducted GISAXS study reveals a high surface roughness, which strongly contributes to the diffuse light scattering and is in accordance to the previous results. Furthermore, nm-sized particles with increasing size and broad size distribution are found. This inner film structure is assigned to nanopores, generated by selective swelling of the diblock copolymer micelles in the presence of a surplus of the homopolymer PS. Consequently, the addition of PS microspheres increases the inner film porosity, while at the same time the nanostructure at the sample's surface shows an increased densification, as observed in SEM measurements in Subsection 5.4.2. Hence, a density gradient can be achieved and allow to tune the refractive index of the scattering layer. Thus, by adjusting the PS microsphere concentration and the sol-gel processing parameters, a refractive index gradient can be obtained in order to gradually match the adjacent organic layers and the substrate and thus reduce organic and substrate modes in OLED devices.

5.6 ZnO/PEDOT:PSS Bilayers

The previously investigations showed the influence of the PS microsphere concentration on the meso- and nanostructure of ZnO thin films, which are supposed to be used as scattering layers for OLED applications. An enhanced diffuse scattering with no observable color shift is found, originating from a hierarchically structured and rough film. For a successful implementation of such a scattering layer into a working device, the application of a conducting bottom electrode on top of the rough scattering layer is crucial. The application of ITO or FTO on such a layer is hardly practicable.

Since polymers are processable from solution and require less damaging treatment to the scattering layer, the deposition of a polymeric electrode is pursued. An excellent candidate among the various potential materials[160] is the so-called PEDOT:PSS,[117] which is introduced on page 51 and further investigated in Chapter 6 and Chapter 7. This material allows easy deposition from solution and enables the adjustment of work function and conducting properties via numerous treatments. In the following, the application of this versatile polymer mixture on top of exemplary ZnO scattering layers is tested via spin coating and spray deposition techniques in order to proof their use in scattering layer assisted ITO-free OLEDs. Additionally, as OLED devices require typically flat surfaces, the use of PEDOT:PSS to compensate the high surface roughness is tested. For this purpose, ZnO/PEDOT:PSS bilayers were fabricated in the frame of the Bachelor's thesis of Irina Ilicheva.[146]

5.6.1 Structural Investigations

Bilayers prepared with the typically used spin coating technique, as described in Subsection 3.2.1, turned out to yield insufficient results (see Figure 5.15a,b). Firstly, the foam-like structure in combination with the high surface roughness of the ZnO layers leads to soaking and infiltration of PEDOT:PSS solution into the scattering layer (Figure 5.15d). At first sight, this is a desired behavior as it leads to a slight back-filling of the ZnO and thus creates a well integrated network of conducting material. Additionally, the surface roughness can be smoothed to meet the requirements of OLED devices. In fact, the required high concentration and amount of material for spin coating leads to incorporation of to much polymer, resulting in thick layers such that the film's absorption is highly increased. Therefore, the transparency is strongly reduced and the bilayers are not suitable as transparent electrodes.

Secondly, the high surface roughness of several hundreds of nm results in an inhomogeneous distribution of material by spin coating. The rough surface reasonably leads to a fill up of valleys during spin coating, whereas the heights are insufficiently covered, resulting in an inhomogeneous distribution of PEDOT:PSS.

Finally, the high wettability of the porous ZnO with water (and the dispersed PEDOT:PSS) is expected to diminish the adhesive force between the ZnO layer and the substrate. In combination with the high film roughness the high rotation speed might then lead to strong centripetal forces on the wrinkles which can result in a detaching of the composite film, as depicted in Figure 5.15a,b. The subsequent annealing of the films might further intensify this effect by different thermal expansion coefficients of the materials. Therefore, spin coating is considered as inadequate for the application of polymeric electrodes on top of such scattering layers.

The disadvantage of the high centripetal force and large amount of solvent/material on the sample can be overcome by switching to another deposition technique such as spray coating. Therefore, PEDOT:PSS films are deposited on ZnO scattering lay-

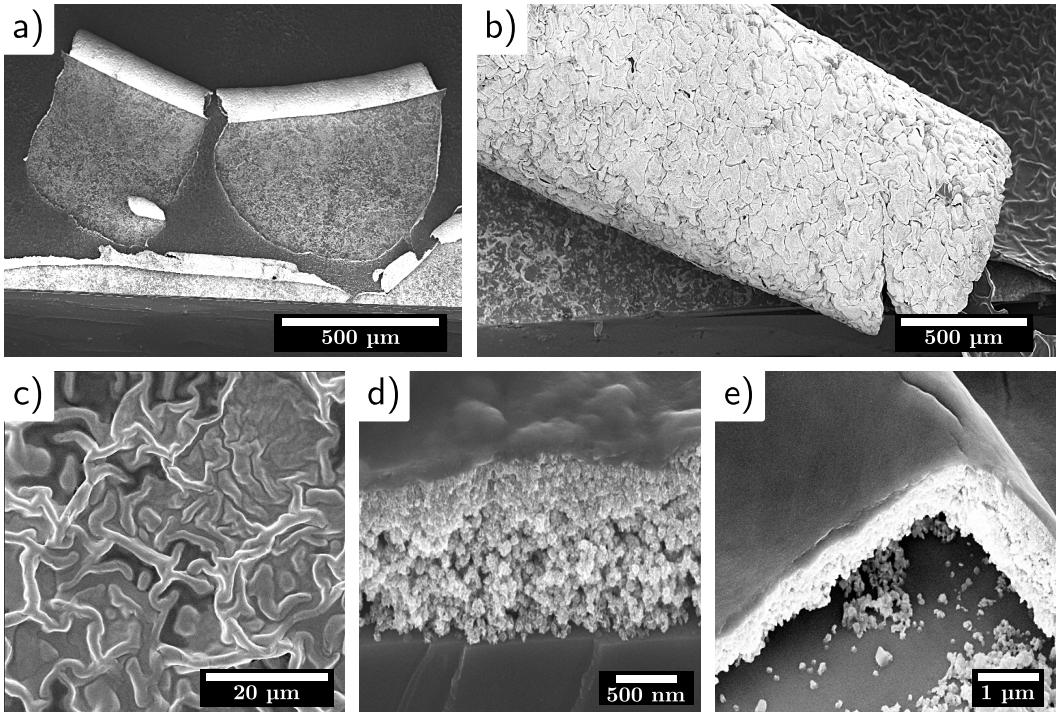

Figure 5.15
SEM images of ZnO/PEDOT:PSS bilayers. ZnO scattering layers are fabricated via spray deposition. Spin coating of PEDOT:PSS on top of the scattering layers leads to peeling of the bilayer (a, b). c) Spray deposition of PEDOT:PSS yields almost homogeneous coating of the hierarchically structured ZnO layer. d) Cross-sectional image of a bilayer shows a thick ZnO layer with decreased porosity from bottom to top which is partly infiltrated by the top PEDOT:PSS layer. e) Cross-sectional image of bilayer reveals hollow wrinkles.

ers as explained on page 65 and according to Subsection 3.2.2, using 1 : 5 diluted PEDOT:PSS PH 1000 with subsequent spraying of EG and thermal annealing. In total, 1 mL diluted PEDOT:PSS solution is deposited in a single spray pulse on the previously prepared ZnO layers. For thickness and conductivity calculations, a PEDOT:PSS reference sample is fabricated under the same conditions on an acid cleaned glass substrate. The top view of such a prepared bilayer is depicted in Figure 5.15c, revealing the typical wrinkled structure is maintained. Cross-sectional imaging in Figure 5.15d shows the well-defined surface coverage and infiltration of the deposited PEDOT:PSS into the nanoporous ZnO film with a total thickness of ~1.4 µm. Furthermore, an increased porosity at the substrate/ZnO interface and an increased density at the ZnO/PEDOT:PSS interface is observed, which is in agreement with the findings from the SEM and GISAXS study. The main advantage of spray deposition is the possibility to homogeneously coat complex surface structures such as the present scattering layers. Figure 5.15e shows the cross-sectional image of such an uniformly coating of a ZnO wrinkle. Additionally, the cross-section reveals voids underneath the wrinkled structure contributing to the insufficient adhesion of ZnO layers during PEDOT:PSS

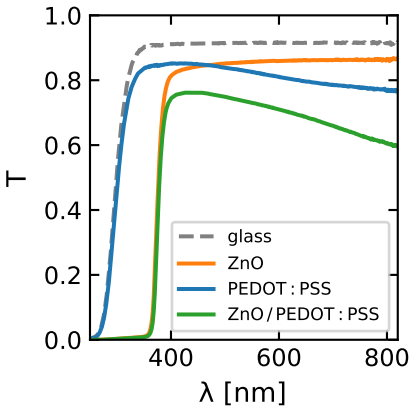

Figure 5.16
Transmittance of ZnO, PEDOT:PSS and bilayers, measured with an integrating sphere. All films are prepared via spray deposition. For proof of principle, the ZnO layer is fabricated without PS microspheres. PEDOT:PSS is sprayed on top of the scattering layer. Subsequent EG post-treatment is performed with spray deposition and annealing. High transmittance is obtained for the bilayer which allows the use as conductive scattering layer.

spin coating. The hollow wrinkles easily explain the increased peak heights in AFM measurements that exceed the general layer thickness, as discussed in Section 5.4. In addition, the voids proof the highly hierarchical morphology across the film and provide further random structure to the system. The formation of such wrinkles can be tuned via adjusting drying and calcination times. On one hand, compensation of the µm-roughness with PEDOT:PSS is not possible as it creates non-transparent films. However, fast heating ramps during calcination are potentially able to suppress such largely pronounced wrinkles and consequently reduce the macroscopic surface roughness. On the other hand, in the present case, the high interfacial area provided by the randomly wrinkled structure might also be beneficial in order to enhance the OLED efficiency.

5.6.2 Transparent Electrode Performance

In order to test the suitability of such prepared ZnO/PEDOT:PSS composite films, UV-Vis measurements have been employed according to Subsection 4.1.1 by detecting the transmittance via an integrating sphere. Figure 5.16 shows the obtained transmittance of the reference glass substrate in comparison to the single ZnO and PEDOT:PSS layers together with the bilayer of both. The ZnO layer shows the known behavior of high transmittance in the visible range of light for wavelength of $\lambda \gtrsim 380\,\mathrm{nm}$. The EG post-treated PEDOT:PSS layer shows a slightly reduced transmittance for long wavelength while the absorption around $\lambda \lesssim 310\,\mathrm{nm}$ is dominated by the glass substrate itself. As expected, the bilayer reveals a combination of both transmittance spectra with slightly reduced intensity. The transmittance in the range of the visible light is still >60 %, showing the highest transmittance of ~76 % around ~450 nm. Therefore, a high total transmissibility of the ZnO/PEDOT:PSS bilayer is maintained.

In order to evaluate the electrode performance of the bilayer, four-point probe measurements are performed according to Subsection 4.2.1. The average thickness for the pure PEDOT:PSS layer is determined as $d = (0.25 \pm 0.03)\,\mu\mathrm{m}$ and is used for further

conductivity calculations of the reference and bilayer samples. For the PEDOT:PSS reference sample, a sheet resistance of $R_{\square} = (24 \pm 5)\,\Omega\,\square^{-1}$ is obtained, leading to a conductivity of $\sigma_{\mathrm{dc}} = (1728 \pm 627)\,\mathrm{S\,cm^{-1}}$. The example bilayer yields a sheet resistance of $R_{\square} = (191 \pm 78)\,\Omega\,\square^{-1}$. As the bilayer does not allow to determine the PEDOT:PSS layer thickness separately via surface profilometry measurements, the film thickness of the reference PEDOT:PSS layer is used, assuming a comparable and homogeneous thickness for the bilayer. Thus, a conductivity of $\sigma_{\mathrm{dc}} = (213 \pm 115)\,\mathrm{S\,cm^{-1}}$ is obtained.

Obviously, the conductivity for the bilayer is significantly lowered in comparison to the PEDOT:PSS reference. This is most probably related to the macroscopic large surface roughness originated in the wrinkled structure of the ZnO scattering layer. Therefore, the measurement procedure using a four-point probe might be error-prone, as the investigated film cannot be considered as flat and thin. Furthermore, the high roughness of the underlying ZnO layer leads to large deviations of the measurement at different sample positions. Therefore, the average sheet resistance shows a large error. In addition, the determined PEDOT:PSS layer thickness might be underestimated, which would result in a larger conductivity. Furthermore, the large area of the ZnO/PEDOT:PSS interface might influence the work function and the doping of the polymeric electrode.

All together, the conductivity of the bilayer lacks behind a single PEDOT:PSS or an ITO electrode and therefore is not suitable for the application in an OLED. As OLED devices require typically very flat surfaces, it might be necessary to overcome the macroscopic roughness towards a full OLED device stack. The compensation of this roughness with PEDOT:PSS is not suitable, as the light absorbance would be highly increased and the photon emission significantly reduced. Consequently, it might be essential to reduce the µm-sized structure by a fast heating ramp during calcination of ZnO. However, the macroscopic roughness could even be beneficial for the application in an OLED device. Besides the light scattering behavior, the increased roughness reveals in fact an increased interfacial area of the different functional layers. Assuming such a randomly structured film can be homogeneously coated, which is possible with spray deposition, such films may provide an increased luminance for OLED devices originated in the increased interfacial area. In any case, the measurement successfully demonstrated the realization of a conducting semi-transparent scattering layer via fabrication of PEDOT:PSS coated ZnO bilayers. Therefore, such bilayers could be used for enhanced light outcoupling of ITO-free OLED devices. However, besides the high macroscopic roughness, the main limiting factor towards a working ITO-free OLED is the reduced conductivity of the composite layer, which stays behind its potential. Therefore, the conductivity of such PEDOT:PSS polymeric electrodes needs to be further enhanced, which is subject of investigation in Chapter 7.

5.7 Summary

The performance of the obtained ZnO films upon visible light scattering is analyzed by comparison of direct and diffuse scattered visible light in forward (transmittance) and backward (reflectance) direction. UV-Vis spectroscopy reveals an enhanced diffuse scattering and slightly enhanced diffuse reflectance with increasing PS microsphere concentration, while no increased absorption is found. Angular and wavelength dependent goniometer measurements are conducted in order to resolve the scattering characteristics of the structured thin films. A significantly enhanced angular scattering of up to 30° and beyond is observed, while the maximum intensity is decreased. The high surface roughness already provides a strong diffuse scattering ability. However, the apparent peak spreading of the transmitted intensity proofs further enhancement with increasing microsphere concentrations. The increased FWHM and integral breadth of the scattered intensity of up to 61 % proves the successful implementation of additional scattering centers into the ZnO films. Furthermore, no wavelength dependent scattering is observed, revealing no apparent color shift, which is a precondition for the application as scattering layer for white OLEDs.

Morphological investigations of the different scattering layers on the surface are performed via surface profilometry, AFM and SEM measurements. The topographical study reveals a high deviation in the average film thickness of each sample, probably related to the increased sol-gel viscosity during deposition. Therefore, increased microsphere concentrations might result in flow rate variations during spray coating, which leads to local inhomogeneities on the sample. However, the film thickness is determined as >1 µm, which is sufficient to bury the implemented microspheres and leads to spherical voids inside the film. Additionally, a very high surface roughness of ~0.4 µm – 0.6 µm is found, which is the supposed main contribution to the strong diffuse scattering. The suggested relation is proofed via SEM and AFM analysis. Furthermore, an intense wrinkled structure in the µm-scale is observed, which provides a high roughness together with a randomly oriented structure. The wrinkles are found to be hollow and create additional voids in the film. Therefore, a hierarchical structure is achieved. Furthermore, successfully embedded PS microspheres are proven for uncalcined samples that reveal spherical shaped voids in the final thin films. With increasing microsphere concentrations, a densification of the surface nanostructure is observed, related to a slow drying and calcination process that also leads to the wrinkled structure.[151] Consequently, this might be related to the enrichment of the PS block of the copolymer by slight dissolving of the additional PS microspheres.

The inner nanostructure is examined via GISAXS measurements, revealing a highly randomized morphology with no defined order. Additionally, an increased nanopore size from ~11 nm – 15 nm is found inside the films, which allows tuning of the thin films porosity and thus of the ZnO refractive index. The increased pore size is assigned to

a swelling of the non-polar PS block via partly dissolved PS microspheres, as observed earlier for a similar system.[148]

In summary, the fabrication of hierarchically structured ZnO is achieved, revealing three length scales ranging from a few nm to several µm. The latter mainly provides a large interfacial area and has only a low contribution to the scattering. The origin of the enhanced diffuse scattering is found to be a combination of the increased surface roughness in the nm-scale and spherical voids introduced by the 500 nm sized PS microsphere templates. Additionally, slight dissolution of the microspheres results in a swelling of the nanopores, created by the sol-gel assisted block copolymer template. Therefore, an increased and tunable film porosity with a dense surface can be obtained.

Hence, such scattering layers provide high potential to enhance the OLED efficiency via increased photon outcoupling. For this purpose, the implementation of a conducting polymer on top of the scattering layer is tested via spin coating and spray deposition of PEDOT:PSS PH 1000 with subsequent EG post-treatment. A ZnO/PEDOT:PSS bilayer is successfully fabricated via spray deposition, while spin coating shows a detaching of the underlying ZnO films. For the spray coated film, a conductivity of $(213 \pm 115)\,\mathrm{S\,cm^{-1}}$ and a transmittance of >60 % with a peak transmittance of ~76 % at $\lambda = 450\,\mathrm{nm}$ is achieved. Due to the low conductivity and the high macroscopic roughness, the obtained bilayers failed in the fabrication of ITO-free OLEDs. On one hand, further research might be required to suppress the wrinkled structure and produce ZnO scattering layers with a flat surface. Additionally, backfilling with PEDOT:PSS to compensate the surface structure is considered as not suitable, as the light absorbance would be highly increased. A promising approach to smooth the surface could be the use of a faster heating ramp during calcination, which would reduce the time for the film to relax and therefore could suppress the formation of the typical wrinkled structure. On the other hand, homogeneous coating of the scattering layer leads to an increased interfacial area of adjacent functional layers. In combination with an enhanced light outcoupling via the scattering layer this might lead to an increased luminance of OLEDs. Hence, the efficiency of ITO-free OLED devices might be enhanced by the application of such bilayers. In any case, the lack in conductivity of the PEDOT:PSS electrode needs to be overcome and is further investigated. Therefore, the characteristics of the PEDOT:PSS electrode are examined in Chapter 6 and Chapter 7 in order to understand its conductivity's origin and to improve the electrode performance.

CHAPTER 6

Following the Humidity Induced Swelling of PEDOT:PSS Electrodes

The following chapter is mainly based on the publication "Monitoring the Swelling Behavior of PEDOT:PSS Electrodes under High Humidity Conditions" (Bießmann et al., *ACS Applied Materials & Interfaces*, 2018, DOI: 10.1021/acsami.8b00446).[29] Reproduced with permission from American Chemical Society, Copyright 2018.

An important contribution to the device performance in organic electronics depends on the stability of its electrode. A key aspect to understand the degradation of organic electronic devices is their sensitivity towards water. Thus, the present chapter covers the influence of high humidity on differently treated poly(3,4-ethylene dioxythiophene):poly(styrene sulfonate) (PEDOT:PSS) electrodes with respect to their water sorption and the resulting swelling behavior. Therefore, different treatments are applied to the thin films (Section 6.2) and the impact on their water sensitivity and swelling response is tested. The as-prepared films are characterized via XRR (Section 6.3) and static ToF-NR (Section 6.5) measurements before they are exposed to a saturated water atmosphere. The applied measurement protocol is given in Section 6.4. The film response is then monitored in Section 6.6 with time resolved neutron reflectometry measurements in ToF mode.[109] The experiments were conducted at the REFSANS instrument at the MLZ, Garching, Germany. Further details about the instrument and the measuring technique itself are given in Subsection 2.5.4 and Subsection 4.4.2, respectively.

6.1 The Multifaceted Behavior of PSS

One main advantage of organic electronic devices is their semi-transparency and inherent flexibility, depending on the used organic layers. These characteristics enable the realization of flexible devices. However, to broadly switch to such types of components, it is necessary to replace commonly used brittle and costly electrodes such as indium-doped tin oxide (ITO) or flurine-doped tin oxide (FTO). Among the various available materials, PEDOT:PSS – introduced on page 51 – is a promising candidate to cover the requirements for such flexible electronics.[161–164] PEDOT:PSS can be described as a polyelectrolyte complex consisting of the hydrophilic PSS and the hydrophobic PEDOT.[117] The presence of PSS is a necessary requirement during the synthesis of the polymer mixture. Thereby, the PSS part itself shows a multifaceted behavior. It serves as counterion, stabilizing charge carriers introduced by primary doping on the PEDOT chains, which leads to a closely intermixing on the molecular scale of both components. Therefore, a certain amount of PSS is required for electrical conductivity. Furthermore, due to its hydrophilicity, PSS makes the polyelectrolyte soluble in water and therefore solution processable in an environmentally friendly way. To ensure good solubility and prevent agglomeration, the PSS amount is usually much higher than the one of PEDOT. Some typical mixture ratios are listed in Table 3.1, all of them used for very different purpose. In this chapter the high conducting PEDOT:PSS PH1000 is used, in the following only called short PEDOT:PSS. The mixing ratio of this specific blend is given by the supplier with $1:2.5$, yielding thin films with a comparable small PSS content. Nevertheless, without further treatment, the conductivity of $\sim 1\,\mathrm{S\,cm^{-1}}$ of such prepared pristine films stays behind its potential.

However, the hydrophilic behavior of PSS – being beneficial during solution processed film deposition – becomes to a detrimental property in the final thin films. In this case, the conducting PSS doped PEDOT-rich crystallites are embedded in an insulating matrix of excess PSS. Thus, the extent of this network and therefore the distance between neighboring PEDOT domains depends on the amount of excess PSS, which hinders the charge transport between neighboring PEDOT crystallites and therefore limits in the end the overall electrical conductivity. Furthermore, it is also known that PSS forms an insulating enrichment layer on top of thin films, due to the different solubility of PEDOT and PSS. As a consequence, this has a negative impact on the overall conductivity and on the charge transport to neighboring transport or active layers.[131,165,166]

Therefore, several methods have been developed to reduce the insulating capping layer and extract the excess PSS from the thin films. Those techniques are mainly based on high boiling point solvents, which are either added into the PEDOT:PSS dispersion before or were applied as post-treatment after film deposition.[9,120,167–171] The induced structural rearrangement is assumed to be caused by a phase separation of PEDOT and PSS and yields an improved charge transport in lateral film direction. Consequently,

such conductivity enhancement by morphological optimization is commonly referred to as secondary doping. For instance, Kim et al. used EG post-treatment in combination with thermal annealing to achieve conductivities of up to $1418\,\mathrm{S\,cm^{-1}}$, which is in the same order of magnitude as ITO.[169] Furthermore, by modifying the PSS capping layer, the work function can be adjusted and therefore the charge transport from the PEDOT:PSS electrode to adjacent layers can be tailored.[172]

However, besides being insulating, the excess amount of PSS adds further problems to PEDOT:PSS electrodes. In general, the presence of H_2O leads to degradation effects in organic materials. In the case of PEDOT:PSS, the hygroscopic behavior of PSS yields a high potential for water uptake, which has a negative influence on the film's conductivity and might harm the whole device performance.[173] In addition, film swelling induced by water uptake of the PSS is expected, which can cause mechanical stress onto the other functional layers in an organic device. Even encapsulation cannot completely prevent the device from moisture. Moreover, it is important to understand the underlying kinetics of water uptake and film swelling in PEDOT:PSS thin films, for instance for a cost-effective pre-processing under ambient conditions.

6.2 Investigated Samples

The aim of this chapter is a better understanding of the water sorption and the connected swelling kinetics of typically treated PEDOT:PSS thin films exposed to humid atmosphere. In the following, three PEDOT:PSS thin films were prepared with commonly used treatments. Namely, pristine PEDOT:PSS PH1000 was compared to a film prepared with Zonyl additive. Zonyl is a commercially available fluorosurfactant, which leads to an enhanced wetting behavior of the dispersion on the substrate and therefore is widely used in the preparation routine for PEDOT:PSS thin films.[120] Furthermore, the induced phase separation leads to morphological changes which result in a larger PSS capping layer. This increased insulating capping layer influences the work function and conductivity of the final film, which is detrimental for controlling the selective charge transport to adjacent layers in electronic devices.[9,131] The second investigated method is the earlier mentioned EG post-treatment, which is an often used technique to enhance the film's conductivity of PEDOT:PSS electrodes.[169] Using a high boiling point solvent such as EG leads to a structural rearrangement in the film (secondary doping) and is supposed to partly dissolve and remove the above mentioned PSS capping layer.

All samples were prepared according to Section 3.4 from 1 : 1 diluted PEDOT:PSS stock solution. The prepared solution was spin coated on acid cleaned[113] p-doped silicon wafers (⌀ 100 mm). In order to assure a comparable film thickness of ~20 nm for all investigated samples, the spin coating speeds were adjusted to 1500 rpm, 2500 rpm and 1200 rpm for the pristine, Zonyl and EG treated sample, respectively. As the viscosity and wettability of the different solutions vary, an amount of 4 mL – 6 mL was

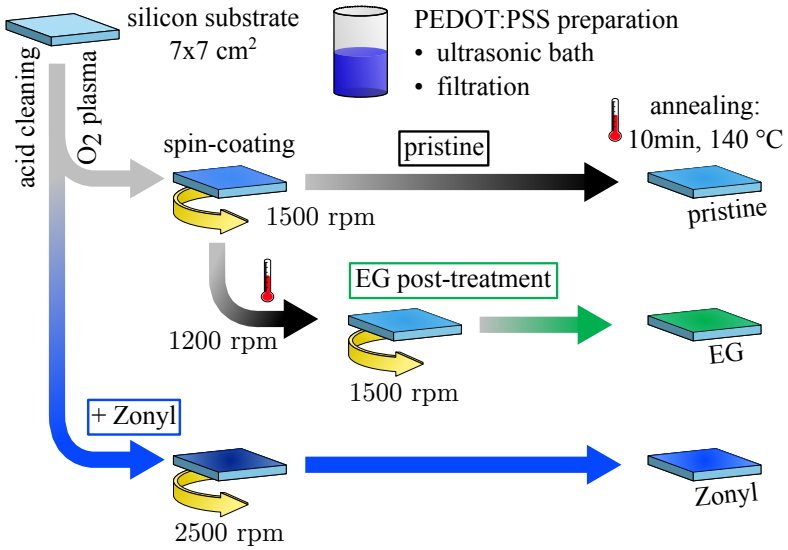

Figure 6.1
Schematic overview of the investigated PEDOT:PSS samples:
Pristine (black), Zonyl additive (blue) and EG post-treated (green). The samples were prepared using different spin coating settings and annealing steps. While Zonyl was added into the solution before deposition, EG post-treatment was applied on a pristine PEDOT:PSS thin film. A more comprehensive description is written in Section 3.4. Adapted with permission from American Chemical Society, Copyright 2018.[29]

used in order to fully cover the whole substrate. The Zonyl surfactant was added prior to deposition, whereas the EG post-treatment was performed after deposition of the thin films. Either way, an annealing step at 140 °C for 10 min was performed for all samples. A short overview about the sample preparation steps and the different treatments used is given in Figure 6.1.

Both treatments are expected to have an influence on the film's morphology and most probably influence the PEDOT-to-PSS ratio. Besides the well studied change in electric conductivity resulting from these treatments, the question arise how sensitive the different films are upon high moisture conditions and how fast the films respond to a change in relative humidity. Therefore, the film response regarding swelling ratio and water uptake induced by a change in relative humidity was investigated by means of ToF-NR.

6.3 PEDOT:PSS Films

The prepared samples are investigated and characterized regarding their conductivity, film thickness and average X-ray scattering length density (SLD_x). All of the results are listed in Table 6.1. Due to conducting silicon substrates, all conductivity measurements were carried out on an additional sample set prepared on glass substrates.

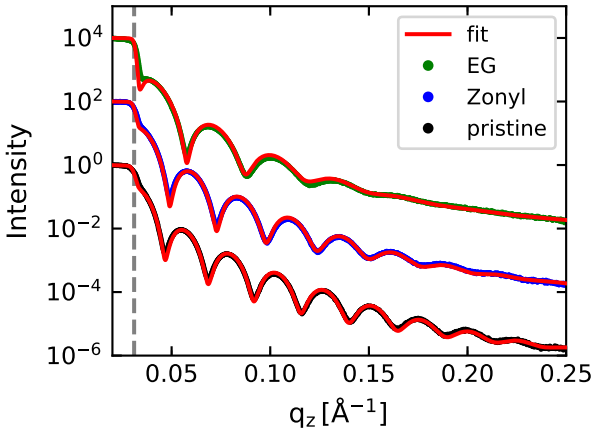

Figure 6.2
XRR measurements on PEDOT:PSS films for verification of sample's suitability for ToF-NR measurements. Depicted are pristine (black), Zonyl (blue), and EG-treated (green) samples including their corresponding fits (red). The data gives reference values for the average film thickness and SLD_x for upcoming ToF-NR examination. The critical edge is marked with a grey dashed vertical line.

Employed four-point measurements reveal typical conductivities for pristine, Zonyl, and EG treated samples, giving a slightly decreased conductivity for Zonyl and a significantly enhanced conductivity for EG post-treated films. The decreased conductivity for Zonyl treated samples is assumed to be related to an increased PSS capping layer thickness. The enhanced conductivity for EG treated samples is often explained with a structural rearrangement inside the film in combination with a reduced PSS capping layer.

Due to the large beam size and footprint for NR measurements, samples providing a small roughness and a good film homogeneity in a cm-range are of high importance to obtain good data quality. In order to assess if the prepared samples are suitable for ToF-NR, XRR measurements are performed. The obtained data is fitted considering a constant SiO_2 layer on the Si substrate and using a one-layer model according to Subsection 4.4.1 to account for the investigated polymer film. The conducted measurements give information about the film thickness and roughness. Therefore, the film homogeneity can be determined. In addition, the reflectivity curves give information about the average film SLD_x, which is related to the materials mass density with Equation 2.22. The obtained XRR measurements are depicted in Figure 6.2 together with their corresponding fits. All curves show several Kiessig fringes and a well defined critical edge (grey dashed line), indicating a smooth surface and a sharp polymer-air interface. The extracted film thickness for the pristine, Zonyl added and EG treated PEDOT:PSS samples are found to be 25.2 nm, 23.4 nm and 19.0 nm, respectively. Therefore, the samples provide comparable thicknesses, which gives good reference values for the upcoming fitting of the NR data. The obtained surface roughness for all films is around 1 nm and therefore can be presumed as smooth. Consequently, the homogeneity of the films is considered as suitable for ToF-NR measurements.

The third important parameter extracted from the XRR fits is the X-ray scattering length density (SLD_x) which is listed in Table 6.1 as well. As explained in Subsection 2.5.1, the SLD_x is related to the average electron density of the material. The

Table 6.1
Results of sample characterization on PEDOT:PSS thin films. Conductivity σ is obtained on an additional sample set prepared on glass substrates. The average mass density ρ is calculated from the average SLD_x. Thickness, roughness and SLD_x were determined from the best XRR fits.

quantity	**pristine**	**Zonyl**	**EG**
$\sigma\left[\mathrm{S\,cm^{-1}}\right]$	1.35 ± 0.15	0.12 ± 0.02	883 ± 130
thickness [nm]	25.2 ± 0.1	23.4 ± 0.1	19.0 ± 0.2
roughness [nm]	1.00 ± 0.08	1.24 ± 0.10	1.72 ± 0.13
$SLD_x\left[10^{-6}\,\mathrm{Å^{-2}}\right]$	14.11 ± 0.47	13.86 ± 0.42	14.63 ± 0.35
$\rho\left[\mathrm{g\,cm^{-3}}\right]$	1.59 ± 0.05	1.56 ± 0.05	1.65 ± 0.04

electron density can be estimated by taking into account the scattering factors for each component of the polymer, its molar mass and its mass density. Due to the very similar scattering factors and molar mass for PEDOT and PSS, it can be assumed the SLD_x for each component (Table 6.2) mainly depends on the mass density, which translates to an average electron density (see Equation 2.22). Therefore, an average mass density for the different films can be estimated, which is listed in Table 6.1. The slightly decreased density for the Zonyl-added and increased density for the EG post-treated sample compared to the pristine one is in accordance to literature.[172,174] However, in the frame of the error range, the different densities are very similar.

In addition, due to the lack of knowledge about the exact mixing ratio of PEDOT and PSS in the final film, an accurate calculation of the mass density of each individual component is not possible. This makes a density calculation using the neutron scattering length density for PEDOT:PSS meaningless, because the difference in SLD_N for PEDOT and PSS is more pronounced for neutrons than for X-rays, as seen in Table 6.2 for a hypothetical mass density of $1\,\mathrm{g\,cm^{-3}}$ for both components. On the other side, this higher sensitivity of NR measurements towards the different components enhances the contrast between PEDOT and PSS. Thus, possible enrichment layers of one material are more pronounced. Analogously, a large SLD difference between the applied solvent and the polymer yields a high contrast, which enables a good distinguishability between them. In order to investigate the water content in a humid environment, it is necessary to take into account the SLDs for the different water isotopes.

Table 6.2
Theoretical values for X-ray (8 keV) and neutron SLDs for H_2O, D_2O, PEDOT:PSS and its single components. Values are calculated according to Subsection 2.5.1 assuming the theoretical PEDOT:PSS mixing ratio of $1:2.5$ for PEDOT:PSS PH1000 and a mass density of $1\,\mathrm{g\,cm^{-3}}$.

quantity	PEDOT	PSS	PEDOT:PSS	H_2O	D_2O
$\mathrm{SLD_x}\left[10^{-6}\,\text{Å}^{-2}\right]$	8.78	8.90	8.87	9.45	9.41
$\mathrm{SLD_N}\left[10^{-6}\,\text{Å}^{-2}\right]$	1.69	1.42	1.49	−0.56	6.36

6.4 PEDOT:PSS Electrode Humidity Study

For investigating the influence of varying humidity on PEDOT:PSS electrodes, in situ ToF-NR measurements were performed at the REFSANS instrument at MLZ, Garching, Germany. The ToF-NR measurement was conducted in single neutron detection mode, which enables a time resolution that is limited by the signal's intensity only. A 30 s time binning was chosen to provide a very good time resolution combined with reasonable statistics. This enables to follow the film response almost in real time.

One main advantage of applying NR is the very suitable scattering contrast of neutrons for the different used materials. The average $\mathrm{SLD_N}$ for pristine PEDOT:PSS thin films is determined from static NR measurements to be $(1.765 \pm 0.013) \times 10^{-6}\,\text{Å}^{-2}$, whereas the $\mathrm{SLD_N}$ literature values for H_2O and D_2O are given as $-0.56 \times 10^{-6}\,\text{Å}^{-2}$ and $6.36 \times 10^{-6}\,\text{Å}^{-2}$, respectively (see Table 6.2). Those values were calculated using the NIST SLD calculator according to the bound coherent scattering length collected by Sears.[84] The large difference between the $\mathrm{SLD_N}$ of D_2O to H_2O and PEDOT:PSS provides a very good contrast between the absorbed deuterated water and the polymer. Therefore, using D_2O as solvent, the water content in the film can be monitored by the change in $\mathrm{SLD_N}$, which is mainly represented by the critical edge in the reflectivity pattern. Furthermore, the film swelling can be followed by the q_z-spacing of the visible Kiessig fringes. Thus, ToF-NR enables for a decoupled, time resolved measurement of the water content in the film and its swelling ratio. Therefore, the measurement provides not only information about the vertical layer composition and the film thickness, but is also capable to yield a vertical SLD profile through the film, which can be transformed into a D_2O content in the film.[175]

Measurement Protocol:

To expose the PEDOT:PSS electrodes to a controlled environment, a special designed humidity chamber made from high purity aluminum is used and equipped with a temperature and humidity sensor (Sensirion SHT21). A typical humidity and temperature curve of the chamber environment for the conducted measurements is depicted

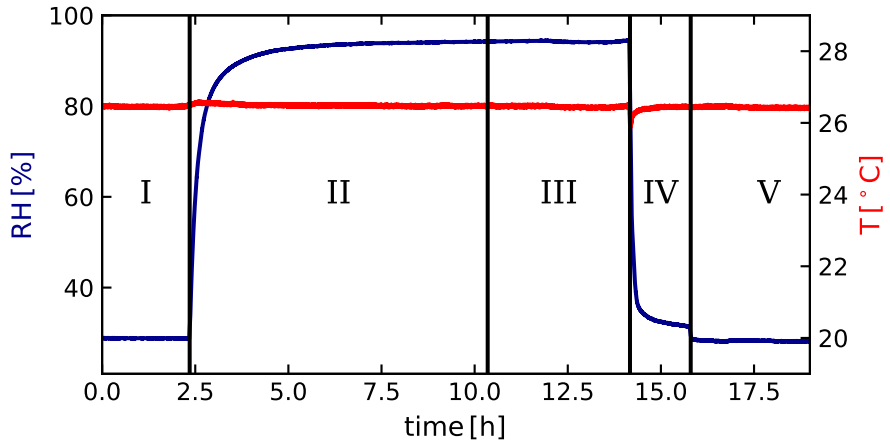

Figure 6.3
Temporal evolution of relative humidity (RH) and temperature (T) in the used humidity chamber, shown together with the different steps of the measurement protocol: I) Static measurement of as-prepared film. II) Kinetic measurement of hydration. III) Static measurement of humid film. IV) Kinetic measurement of dehydration. V) Static measurement of dehydrated/dry film. Adapted with permission from American Chemical Society, Copyright 2018.[29]

in Figure 6.3. In addition, the different states I to V of a single measurement are marked in the plot. For all measurements, the temperature in the chamber was kept slightly above ambient conditions to prevent condensation effects on the chamber windows. Therefore, the temperature was kept at a constant value of 26.5 °C to achieve equal conditions for the evaporation process of all samples. Each measurement was performed as following:

I. Static measurement of the as-prepared PEDOT:PSS films at ambient conditions.
II. Injection of 8 mL D_2O via a syringe into the water reservoir inside the humidity chamber. The reservoir is placed below the sample to avoid spilling of it. The rising humidity is tracked and the film response is monitored with a kinetic ToF-NR measurement.
III. After no change in the reflectivity curve is detectable (≈8 h), equilibrium conditions are attained and a second static measurement of the humid film is performed.
IV. Extraction of the residual water via a syringe and subsequent drying of the samples by removing the saturated atmosphere utilizing a vacuum pump.
V. In the end, a static measurement of the dehydrated film (further referred to as *dry* film) is conducted to record the final film state.

The three static measurements (as-prepared, humid, dry) were performed at an incident angle of 0.6° and 2.4° with an exposure time of 20 min and 100 min, respectively and are combined to one reflectivity curve. The kinetic measurement (step II) is

performed with an incident angle of 0.76°. The detected single neutrons are afterwards binned to achieve a 30 s time resolution.

The obtained NR data is evaluated using the MOTOFIT package by Nelson.[142] In combination with the high contrast of PEDOT:PSS and D_2O and the selective water uptake of the hygroscopic PSS part, different enrichment layers in the films are distinguishable. Hence, the best fits for the static measurements are obtained using a three-layer model to account for such enrichment layers. The analysis of the kinetic NR measurements focuses on changes of the film thickness and the SLD_N change, from which the water incorporation in the film can be deduced.

6.5 Static NR Measurements

In Figure 6.4 the static NR measurements are depicted together with their fits and calculated SLD_N profiles. From the static measurements, one can conclude, that the as-prepared (green) and dried (red) films in Figure 6.4b posses the same thickness and SLD_N profile for each individual sample, which is a hint for a good reversibility of the swelling process itself. However, the SLD_N for the EG post-treated film is slightly decreased by the humidity treatment. As reported in literature, EG post-treatment leads to a densification of the PEDOT:PSS film, which results in a higher SLD.[169,174] The swelling caused by the incorporated water seems to reverse this densification, which is already an indication for a structural change inside the film. The pristine PEDOT:PSS sample and the Zonyl treated sample show average SLDs of $(1.765 \pm 0.013) \times 10^{-6}\,\text{Å}^{-2}$ and $(1.755 \pm 0.009) \times 10^{-6}\,\text{Å}^{-2}$, respectively. The average SLD_N for the EG post-treated film is calculated to be $(1.917 \pm 0.003)\,\text{Å}^{-2}$. Therefore, the mass density is slightly decreased by the Zonyl treatment, whereas it is increased for an EG post-treatment compared to that of pristine PEDOT:PSS. The differences in the determined average film's mass density is in agreement with reported changes in the crystalline structure of PEDOT and PSS.[131]

In the SLD_N profiles in Figure 6.4b the strong thickness increase during swelling of about 100 % can easily be seen. In addition, the SLD_N increases through the whole film, which is an indication for a strong D_2O incorporation caused by the hygroscopic PSS and translates to a high water content. Furthermore, in the SLD_N profiles of the swollen films, two enrichment layers of low and high water content can be identified. While the pristine film shows a good intermixing of the enrichment layers with the bulk polymer, which is even more mixed for the Zonyl treated sample, the EG post-treated sample reveals a very sharp transition from the bulk to the enrichment layers. In addition, the enrichment layer at the polymer-air interface is drastically reduced for EG post-treatment and the whole thickness increase due to swelling seems to be lowered. Therefore, the low SLD_N enrichment layer at the substrate-polymer interface is identified as a hydrophobic PEDOT layer with few water incorporation. The high SLD_N enrichment layer at the polymer-air interface can be assigned to the

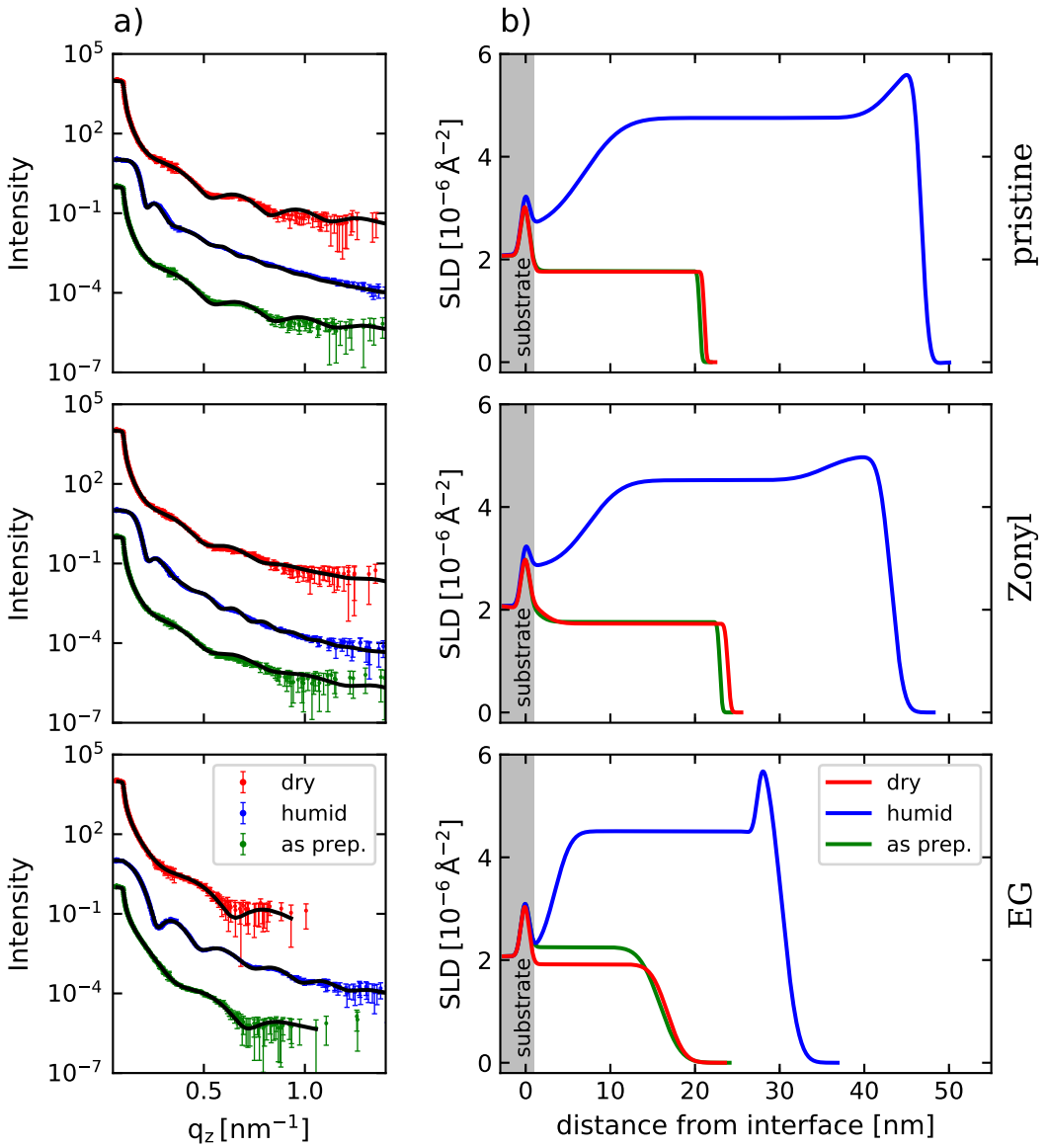

Figure 6.4
a) Static NR measurements of pristine, Zonyl-added and EG post-treated PEDOT:PSS thin films (top to bottom). b) The corresponding SLD_N profiles show the tremendous increase in thickness and average SLD_N of all films from the as-prepared (green) to the humid (blue) film, followed by a decrease for the dry (red) film. An enrichment layer of hydrophobic PEDOT at the substrate-polymer interface and an enrichment layer of hydrophilic PSS at the polymer-air interface are clearly identified for all films. The Zonyl-treated film shows a better intermixing of the enrichment layers, whereas the EG-treated film shows a more distinct separated interface for the enrichment layers and a reduced PSS capping layer. Adapted with permission from American Chemical Society, Copyright 2018.[29]

hydrophilic PSS, which is reduced due to EG post-treatment. This reduction of the PSS capping layer by EG treatment is responsible for the enhanced conductivity, as literature reported.[169]

Taking a look to the films after exposure to high humidity, the Zonyl and EG treated samples show a reduced water incorporation and swelling ratio compared to the pristine sample. Thus, the different treatments indeed impact the film's sensitivity under high humidity conditions. In order to elaborate the film response upon changing relative humidity, in situ ToF-NR measurements of the swelling (step II in Figure 6.3) are analyzed in detail and discussed in the following section.

6.6 Swelling Kinetics

After the static measurement of the as-prepared film is finished, D_2O is injected into the measurement chamber and the humidity starts to rise. The film response is detected with 30 s time resolution by ToF-NR and is linked to the actual relative humidity. Thus, during the swelling ~1000 data curves were collected and subsequently analyzed according to Section 2.2 and Subsection 4.4.2. For the pristine and Zonyl sample a three layer model was necessary to account for the different enrichment layers and to obtain accurate fitting results. However, a two layer model was sufficient to fit the kinetic ToF-NR data measured for the EG sample. In Figure 6.5 a selection of the kinetic dataset is depicted together with their corresponding fits. The color scale represents the changing humidity in the chamber from low (turquoise, bottom) to high (blue, top) humidity. For better visibility the critical edge of the dry polymer is marked with a vertical solid line and the swelling process is illustrated with an arrow. In accordance to the static measurements of the as-prepared and humid films, all wet PEDOT:PSS films show a clear shift of the critical edge towards larger q_z-values. This effect is related to an increasing SLD_N, which corresponds to a strong D_2O incorporation into the film. Furthermore, the high water incorporation leads to a film swelling, which is represented by additional appearing and shifting reflectivity maxima from large q_z- to small q_z-values.

The different film responses of the pristine, Zonyl and EG samples are distinguishable already with bare eyes. While the Zonyl treated sample (Figure 6.5b) shows a very similar behavior as the pristine one (Figure 6.5a), the EG treated sample (Figure 6.5c) draws a different picture. The shift of the critical edge is much less pronounced, which corresponds to a reduced water incorporation into the film. Furthermore, the shift of the reflectivity maxima towards smaller q_z-values is limited as well. This supports the earlier mentioned presumption about a reduced water incorporation and therefore an enhanced resistivity and stability against water.

In order to compare the treatments in a more quantitative way, the obtained film thickness of each film is normalized to its corresponding initial value of the as-prepared

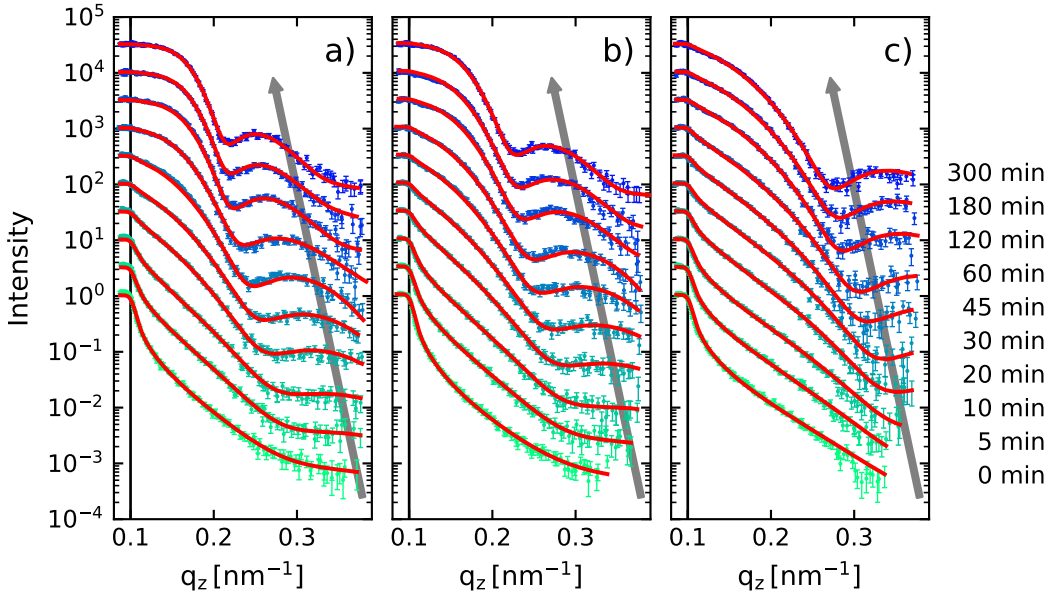

Figure 6.5
Selected ToF-NR reflectivity data (symbols) and fits (red) of PEDOT:PSS thin films under increasing humidity conditions, measured at times as indicated. For easier visibility, the data curves are shifted along the log-scaled intensity. a) Pristine film, b) Zonyl additive in solution, and c) EG post-treated films. The color gradient represents the increasing humidity (turquoise to blue). Vertical black solid lines represent the critical edge of the dry polymer film. The shift of the critical edge towards higher q_z-values indicates an increased D_2O incorporation. Appearing and shifting reflectivity maxima towards smaller q_z-values indicate a thickness increase (grey arrow). Adapted with permission from American Chemical Society, Copyright 2018.[29]

film, resulting in the so-called swelling ratio. Knowing the SLDs for the different components, namely the as-prepared polymer and the D_2O, it is possible to calculate the amount of water $\Phi_{D_2O}(t)$ in the film. Thus, Equation 2.7 becomes to

$$\Phi_{D_2O}(t) = \frac{SLD_{meas}(t) - SLD_{init}}{SLD_{D_2O} - SLD_{init}} \tag{6.1}$$

and allows calculation of the water content in the film, where $SLD_{meas}(t)$ is the measured mean SLD_N of the film at time t, and SLD_{init} and SLD_{D_2O} are the SLDs for the initially as-prepared polymer film and pure D_2O, respectively.

The resulting curves for the swelling ratio $^{d(t)}/_{d_0}$ and the water content $\Phi(t)$ are depicted in dependence on the time and the relative humidity in Figure 6.6a,c and Figure 6.6b,d, respectively. The decreased swelling ratio for the Zonyl and the EG post-treated sample is clearly visible for both cases, with the EG-treated sample showing the least response. Furthermore, a decreased water content is also seen, with both of the treated samples showing a similar behavior.

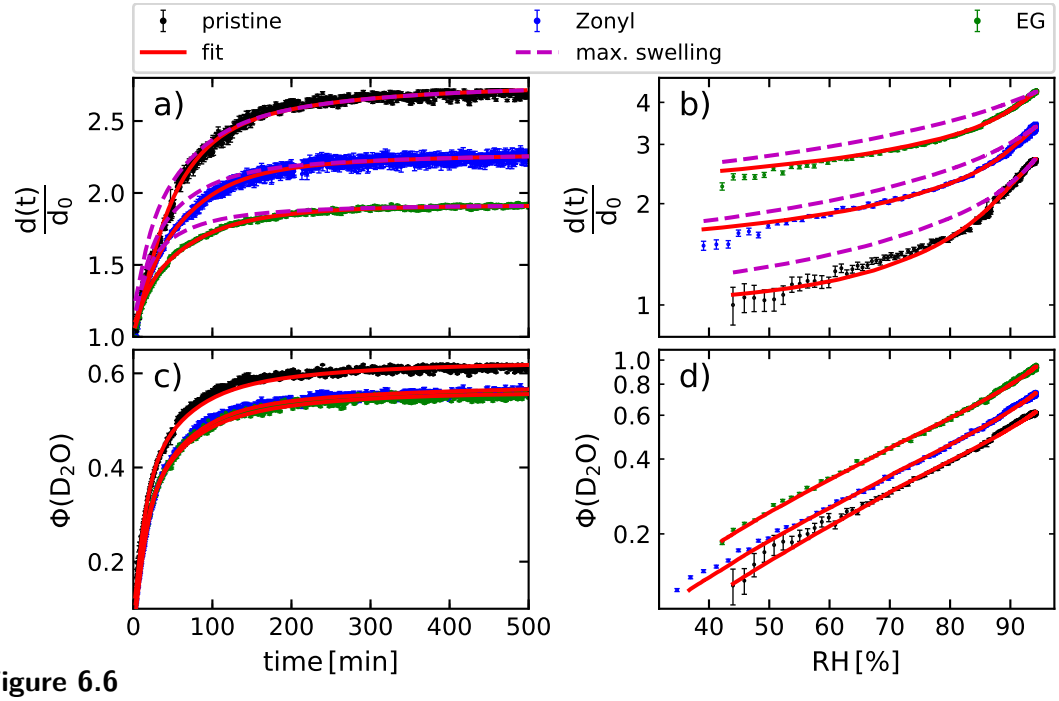

Figure 6.6
Results from the kinetic investigation of differently treated PEDOT:PSS films depicted in Figure 6.5. Swelling ratio $^{d(t)}/_{d_0}$ in dependence of measurement time (a) and time dependent relative humidity (b), respectively. The corresponding fits (red) and maximum swelling ratio (violet) for pristine (black), Zonyl (blue) and EG treated (green) samples are shown. c,d) Analogous representation of water content $\Phi(D_2O)$ in dependence on time and corresponding relative humidity. Swelling ratio and water incorporation are significantly decreased for Zonyl and EG treated films due to increased hydrophobicity. b) The difference in maximum swelling ratio and measured data is clearly visible, indicating a diffusion limited processes in the beginning. d) The water content is mainly dominated by the increased, time dependent relative humidity. Note: b) and d) are shifted along the log-scaled y-axis for better visibility. Adapted with permission from American Chemical Society, Copyright 2018.[29]

Using a swelling model accounting for a non-constant humidity, the resulting data is fitted using Equation 2.8 and 2.10 to obtain more information about the time dependency of the swelling process.[51–53] The selected swelling model (Section 2.2) takes into account the swelling driven by the increasing humidity and an intrinsic swelling kinetic, which is dominated by diffusion of the D_2O molecules through the thin film with a specific time constant τ. From this model it is possible to extract the effective Flory-Huggins interaction parameter χ_{eff} between the polymer film and the solvent D_2O, which is a measure for the hydrophobicity of the film. The maximum swelling ratio $^{d_\infty}/_{d_0}$ as a function of the time-dependent humidity and depending on χ_{eff} can be obtained numerically from Equation 2.9 and is shown together with the measured swelling ratio in Figure 6.6a,b. The maximum swelling of the film is related to the amount of water molecules the polymer chain can adsorb. The difference of the max-

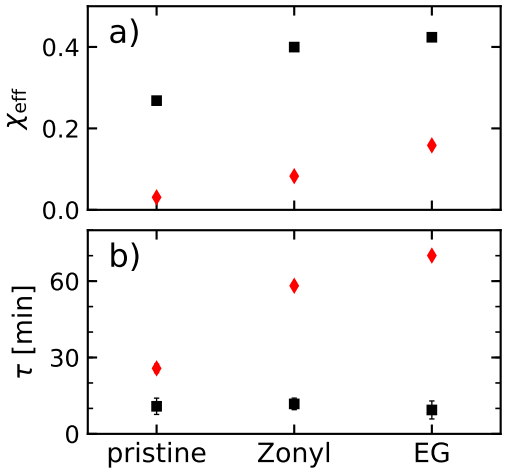

Figure 6.7
a) Effective interaction parameter χ_{eff} and b) specific time constant τ obtained from ToF-NR fit analysis. The values are extracted from swelling ratio fits (red) and water content fits (black) from Figure 6.6. The fast saturation represented by the small time constant τ for the water content fits (black) is in accordance with Figure 6.6d where the film response is dominated by the increasing relative humidity. The detailed values are listed in Table 6.3. Adapted with permission from American Chemical Society, Copyright 2018.[29]

imum achievable swelling ratio of the film d_∞/d_0 for a given humidity to the measured swelling ratio shows that the process is initially limited by the diffusion of D_2O into the film. At later stages, when the model fit and the maximum swelling ratio merge, the film swelling is dominated by the relative humidity changes. This effect is in accordance to the humidity dependent representation in Figure 6.6b, where the difference of the maximum and the real swelling ratio becomes clearly visible. For a higher relative humidity, both curves merge together.

In contrast, the water content depicted in Figure 6.6d shows a clear dependency on the relative humidity, as visible in the exponential behavior. The measured water content uniformly follows the increasing relative humidity in good agreement and no delay due to diffusion effects is visible. Hence, the water content in the film is mainly humidity driven. Consequently, the water content in the thin film is continuously saturated with increasing relative humidity. It is noteworthy to mention that the data depicted in Figure 6.6b,d are obtained under non-equilibrium conditions and only render the measured data in a different representation style. For an infinite slow increment of the relative humidity a perfect match of the maximum swelling ratio and the measured swelling ratio is expected. The onset where the maximum swelling ratio and the measured values merge is clearly different for the three investigated films and occurs after around 2.0 h for the pristine film and after 3.5 h and 4.5 h for the Zonyl-treated and the EG post-treated film, respectively. Hence, the swelling process is limited by the diffusion of the D_2O molecules into the film the most for the EG post-treated sample, which clearly indicates a reduced water sensitivity. Figure 6.7 shows the corresponding χ_{eff} and τ values extracted from the swelling ratio and the water content fits. Additionally, the detailed fitting values are listed in Table 6.3.

As seen in Figure 6.7a, the χ_{eff} parameter and thus the hydrophobicity is increased in both cases for the Zonyl sample and is even more enhanced for the EG post-treated sample. Consequently, the sensitivity against water is significantly reduced by both treatments. Figure 6.7b shows the specific time constants of the different films ex-

Table 6.3
Fitting results of kinetic ToF-NR measurements. Extracted from swelling ratio $^{d(t)}/_{d_0}$ and water content $\Phi_{D_2O}(t)$ fits (see Figure 6.6). The obtained values are depicted in Figure 6.7.

parameter		pristine	Zonyl	EG
$\frac{d(t)}{d_0}$	τ [min]	25.7(17)	58.2(9)	70.0(9)
	χ_{eff}	0.0309(1)	0.0828(1)	0.1584(1)
	B	0.780(69)	0.375(5)	0.396(6)
Φ_{D_2O}	τ [min]	10.8(32)	11.8(23)	9.4(35)
	χ_{eff}	0.2682(6)	0.3997(5)	0.4238(4)
	B	0.339(163)	0.222(65)	0.219(143)

tracted from the swelling and the water incorporation processes, respectively. There is an obvious difference between the τ obtained from the swelling ratio and the τ obtained from the water content. The former shows an increase, similar to the effective Flory-Huggins interaction parameter, indicating a slower swelling process and a reduced water sensitivity. Accordingly, the diffusion of the water molecules into the film, which causes the intrinsic swelling, is hindered. This is in agreement with the delayed onset of the humidity-limited swelling mentioned above. The latter instead shows an almost continuous small specific time constant for all three samples, indicating a fast saturation and a weak dependency of the treatment method on the water incorporation rate. Consequently, the specific time constant is in this case dominated by the time evolution of the relative humidity itself, which is kept the same for all measurements. Thus, the water incorporation is strongly humidity driven. The third required fitting parameter B listed in Table 6.3, takes into account the sample's geometry of a thin film according to Li and Tanaka.[52]

The above results indicate a faster response of the films to the water uptake in comparison to the film thickness increase. Thus, the response regarding the swelling ratio is a delayed process, decelerated by the diffusion of the D_2O molecules into the film. This behavior is attributed to local structural changes in the polymer chain conformation. In the case of Zonyl an amphiphilic surfactant is introduced during sample preparation which interacts with the PEDOT and the water molecules. As reported by Palumbiny et al., the longer hydrophilic PSS molecules coil around the shorter PEDOT molecules and screen them from the aqueous solution.[131] By addition of Zonyl, the interaction of PSS and PEDOT is reduced and PSS molecules are allowed to move more freely during film formation. Hence, less PSS is bound to PEDOT and the unbound PSS can be accumulated at the top surface. This leads to an enhanced phase separation of PEDOT and PSS. Therefore, the PSS amount in the bulk layer is

reduced. This is in agreement with the static humid measurement of the Zonyl-treated sample seen in Figure 6.4b, where the SLD_N and therefore the D_2O content in the bulk region is reduced in comparison to that of the pristine PEDOT:PSS sample (pristine: $4.755(9) \times 10^{-6}$ Å^{-1}, Zonyl: $4.523(9) \times 10^{-6}$ Å^{-1}). Furthermore, the transition from bulk to PSS enrichment layer is less pronounced for the Zonyl sample, which indicates a better intermixing of these layers. In addition, one can assume that the accumulated excess PSS at the top surface is also partly spun off during the spin coating process. This leads to a slightly increased PSS top layer thickness, whereas the total PSS amount in the bulk is reduced. Zonyl itself has a boiling point of ~80 °C and therefore it is unlikely to stay in the film after the annealing process at 140 °C.[120]

In the case of EG post-treated films, the PEDOT crystallites get reoriented, smaller and denser packed.[169,174] Furthermore, some of the excess PSS content, especially from the top surface, is dissolved and washed away during the spin coating process. The loss of PSS during spin coating is much more significant in the case of EG post-treatment due to the second spin coating step and the high boiling point of EG compared to water. This reduces the overall PSS content in the PEDOT:PSS and therefore the water sensitivity of the final thin film.[174] Thus, it is very likely to suppress the water sensitivity even further by applying similar treatments to PEDOT:PSS, which are able to reduce the PSS content inside the film. For instance, the application of sulfuric acid may perform very well in this case, which is part of the investigation in Chapter 7.

6.7 Summary

In summary, the swelling of pristine PEDOT:PSS thin films were compared to Zonyl additive and EG post-treated films serving as polymeric electrodes. In situ ToF-NR measurements under increasing high humidity conditions enabled to probe the swelling kinetics. As-prepared, humid and dehydrated/dry PEDOT:PSS films were compared. PEDOT and PSS enrichment layers were clearly identified at the substrate-polymer and polymer-air interface, respectively. The increased PSS capping layer by Zonyl addition and the reduced PSS content using EG post-treatment were proven. A significant decrease in film swelling and water uptake was observed for the Zonyl additive film. This decrease is enhanced by EG post-treatment which originates from an increased hydrophobicity and the hindered diffusion of water into the films. The differences in water uptake and film swelling are also reflected in the specific time constants τ and effective interaction parameters χ_{eff}. Hence, the water sensitivity and related instabilities of PEDOT:PSS films are remarkably reduced if Zonyl additive or an EG post-treatment is applied. The improvement for both treatments is mainly attributed to morphological changes and the reduction of PSS content inside the film. Therefore, besides the well-known impact on conductivity of both treatments, its beneficial influence on the water sensitivity also needs to be considered when selecting a suitable treatment for PEDOT:PSS electrodes in organic electronic applications.

CHAPTER 7

Highly Conducting PEDOT:PSS Electrodes

The following chapter is mainly based on the publication "Highly Conducting, Transparent PEDOT:PSS Polymer Electrodes from Post-Treatment with Weak and Strong Acids" (Bießmann et al., *Advanced Electronic Materials*, 2019, DOI: 10.1002/aelm.201800654).[30] Reproduced with permission from John Wiley & Sons, Copyright 2019.
Impedance spectroscopy measurements were performed in the frame of the Bachelor's thesis of Raphael Maier.[176] ITO-free OLED test devices were fabricated and investigated in the frame of the Bachelor's thesis of Lina Maria Todenhagen.[177]

On the way towards flexible electronics, the dependency on brittle TCOs has to be overcome. As mentioned earlier in this thesis, thin films cast from the polymer electrolyte PEDOT:PSS provide essential characteristics in order to replace such conducting metal oxides and allow the fabrication of ITO-free organic electronics. Thus, the application of such a transparent and flexible polymeric electrode can pave the way towards devices such as flexible OLEDs. Furthermore, ZnO scattering layers, such as introduced in Chapter 5 for enhanced photon outcoupling, proved the use of spray deposited PEDOT:PSS electrodes on top of such layers. However, the obtained ZnO/PEDOT:PSS bilayers fabricated with commonly available post-treatments lacked in conductivity, which reveal the necessity for significant conductivity improvements.

As shown in Chapter 6, the PSS component serves a multifaceted purpose in the PEDOT:PSS blend. On one hand, it allows dissolution of the polyelectrolyte complex in water and therefore is necessary for processing from solution. Furthermore, the presence of PSS is required during synthesis and induces charge carriers on the PEDOT backbone. On the other hand, the insulating PSS component diminishes the electrode performance of final PEDOT:PSS thin films. In addition, its hygroscopic behavior leads to film swelling and degradation effects that may eventually harm the final device.[29] Thus, the use of PSS is essential during film fabrication, but disadvantageous in the final thin film or device.

Therefore, the upcoming chapter handles the question how the PSS component may be reduced via more effective post-treatment methods. The aspired PSS reduction is expected to modify the films' morphology and impart improved conductivity. In order to evaluate the performance of the obtained PEDOT:PSS transparent electrodes, the examined treatments are studied regarding their influence on the thin films. Hence, their electrical and optical properties are examined in Section 7.3 and Section 7.4, respectively. The obtained results are further linked to the compositional and structural changes in Section 7.5 and Section 7.6. Finally, the performance of selected polymeric electrodes in comparison to a standard device stack is examined in ITO-free OLEDs.

7.1 Conductivity Enhancement by Structure Modification

As described before, PEDOT:PSS consists of the conducting and water-insoluble polymer PEDOT and the electrically insulating, water-soluble PSS. PEDOT itself is a polymer chain with a large conjugated π-electron system, which is the origin of its conducting properties.[178] In contrast, PSS consists of a non-conjugated linear backbone with randomly oriented side groups. Despite its electrically insulating properties, PSS is required during synthesis and serves as counter-ion for induced charge carriers in PEDOT (primary doping). In order to ensure a successful synthesis and good water solubility, PSS is usually added with excess amount. Thus, PSS takes up a multifaceted behavior, as shown in Chapter 6. On one hand, it is required for charge carrier introduction/stabilization and easy processibility, which is essential for high conductivity. On the other hand, high amounts of excess PSS diminish inter-domain charge carrier transport when fabricated as thin film, since the conducting PEDOT-rich domains are usually embedded into an electrically insulating excess PSS matrix.[179] In addition, the high amount of hygroscopic PSS is known to have a negative influence on the conductivity of the polymer electrode and might lead to degradation in the final device.[29] Therefore, intense research has been done to develop treatments for enhancing the electrical conductivity of PEDOT:PSS films. Over time, different treatments have been developed by applying various chemicals prior to film deposition or as

post-treatments, ranging from high boiling point solvents (EG, DMSO, etc.)[169,180,181] to acids and bases.[20,182–185] The improvement of electrical conductivity originates in a manifold of different factors, aiming mostly on the reduction of insulating excess PSS in the film and in an increased structural order of PEDOT-rich domains. To date, high conductivities of $>4000\,\mathrm{S\,cm^{-1}}$ have been obtained by H_2SO_4 treatment. Thus, values have reached the same range as the commonly used ITO. Kim et al. reported on a reduced PSS content due to the use of H_2SO_4, which dissolves and extracts the PSS, yielding an improved overall order of the polymer film.[184,186] Mengistie et al. reached similar high conductivities of $>2000\,\mathrm{S\,cm^{-1}}$ with the much weaker formic acid and attributed the change to Coulomb screening of charged PEDOT and PSS due to a high dielectric constant of the acid.[183] Palumbiny et al. showed how the in situ formation of preferred edge-on orientation of PEDOT crystallites is realized by ethylene glycol (EG) post-treatment during printing.[187] Therefore, PEDOT:PSS has become a viable alternative to transparent conductive oxide electrodes.

In this chapter, the influence of various strong and weak acids, together with a commonly used EG post-treatment is investigated upon PEDOT:PSS conductivity. In addition, the acid treatments were subjected to a H_2O washing step to ensure full removal of acid residuals and to investigate the water sensitivity and reversibility of the expected structural improvement of the polymer electrode. An overview of the investigated samples and their preparation is given in Section 7.2. To elaborate on the impact of the different treatments, the electrical and optical properties are measured in Section 7.3 and Section 7.4 in order to evaluate the polymer electrode performance by a figure of merit (FoM, see Subsection 4.2.1). In Section 7.5, the compositional changes regarding the PEDOT-to-PSS ratio are investigated with XPS, which is expected to have a positive influence on the conductivity. In Section 7.6, these findings are linked to the morphological change and the films' crystallinity, obtained by GIWAXS, and put together in a morphological model on the reorganization of PEDOT- and PSS-rich domains. In Section 7.7, the best promising electrodes are implemented into a standard OLED device stack in order to test their working performance.

7.2 Investigated Samples

A detailed overview of the fabricated samples with the introduced color code for the present chapter is depicted in Figure 7.1. $25 \times 25\,\mathrm{mm^2}$ sized soda-lime glass substrates were cleaned in a hot acid bath with subsequent oxygen plasma (see page 48 & 49). PEDOT:PSS PH 1000 stock solution was prepared according to Section 3.4 and two layers of PEDOT:PSS were spin coated according to Subsection 3.2.1 with 1000 rpm for 60 s with subsequent thermal annealing (10 min, 140 °C).

Post-treatment was performed according to Subsection 3.4.2 by drop casting concentrated hydrochloric acid (HCl), formic acid (HCOOH), nitric acid (HNO_3), and

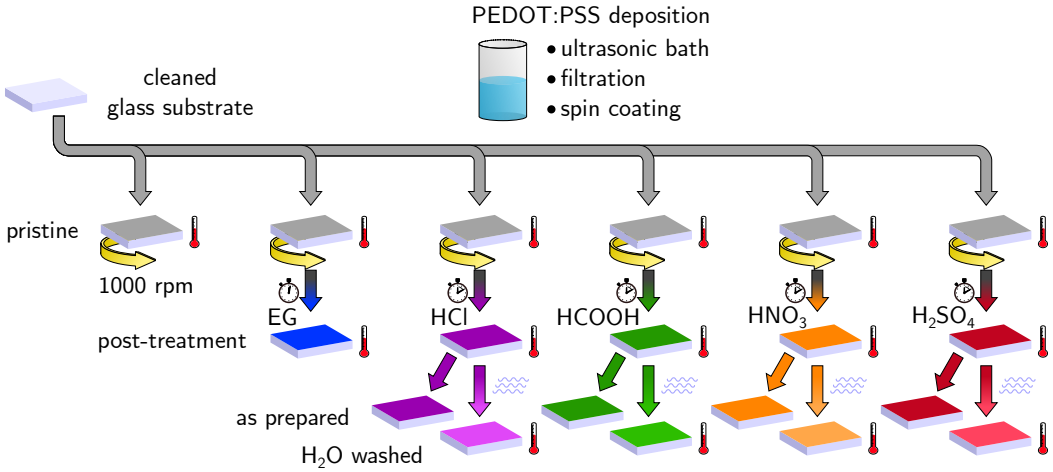

Figure 7.1
Sketch of sample preparation of investigated PEDOT:PSS thin films. All pristine films (grey) were spin coated in the same way followed by different post-treatments (see Section 3.4). EG and acid treated samples were dried after 3 min and 10 min reaction time, respectively. Excess EG was spun of, while acid treated samples were dried under a continuous nitrogen flow. Additionally, a second set of acid treated samples was subjected to a H_2O washing step. Each preparation step was followed by 10 min annealing at 140 °C on a hot plate. Reproduced with permission from John Wiley & Sons, Copyright 2019.[30]

sulfuric acid (H_2SO_4) cautiously on top of the pristine PEDOT:PSS thin films such the whole surface was covered. After 10 min reaction time the samples were dried under a continuous nitrogen flow and placed on a hot plate for 10 min at 140 °C.

Additionally, a second set of acid treated samples were subjected to a H_2O washing step – marked with (W) – to ensure full removal of any possible acid residuals in the film and to investigate the stability of the improved structure. These samples were dried following the same procedure as explained above. As a reference, a pristine PEDOT:PSS film together with the well established EG post-treatment was taken, where EG was drop cast on the thin films and spun off after 3 min soaking time, followed by additional annealing for 10 min at 140 °C.[169]

7.3 Electrical Characterization

The performance of the polymeric electrodes is described by their DC and AC conductivity. The in-plane DC conductivity of the present samples was obtained via four-point probe measurements (see Subsection 4.2.1) and used for further evaluation in Subsection 7.3.1. However, many electronic devices rely on alternating current. For example OLED devices may be operated with pulse-width modulation in order to save energy and increase the device lifetime. More important is the material behavior for application in integrated circuit components such as OFETs, where fast switching and

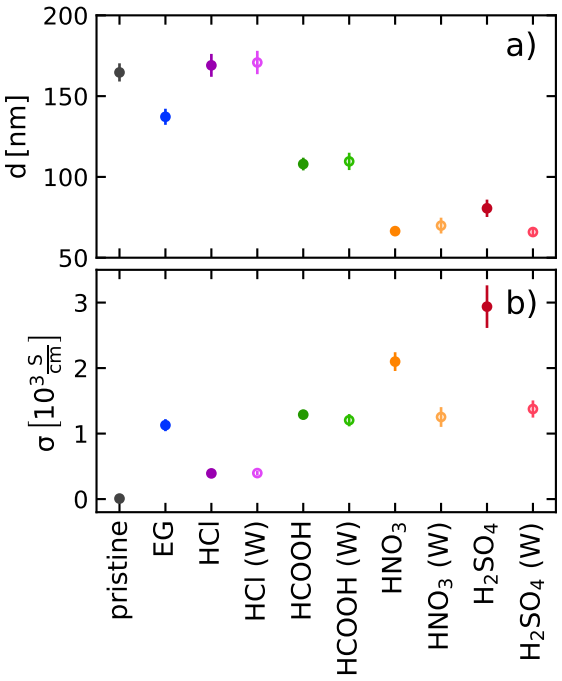

Figure 7.2
a) Film thickness and b) conductivity of post-treated PEDOT:PSS films. A correlation between decrease in film thickness and increase in conductivity can be observed. Non-washed treatments are depicted with dot-symbols for pristine (grey), EG (blue), HCl (purple), HCOOH (green), HNO_3 (orange), and H_2SO_4 (red). Subsequent washing with water after the respective acid treatment is represented with circles and the label (W). For high dielectric solvents, a decrease in conductivity after washing is observed. Reproduced with permission from John Wiley & Sons, Copyright 2019.[30]

thus a change of the direction of current with high frequency is required. Therefore, the electrode response regarding an alternating current was measured in addition via impedance spectroscopy (see Subsection 4.2.2) and is discussed in Subsection 7.3.2.

7.3.1 DC Conductivity

The obtained thin films were investigated regarding their DC conductivity by performing four-point measurements on several positions on each sample. The corresponding thicknesses were determined and considered for the in-plane conductivity calculations. Figure 7.2 shows the thickness along with the corresponding conductivity for the different treatments employed. All treatments – except for HCl – yield a decrease in the original film thickness. The initial thickness of $(165 \pm 6)\,\mathrm{nm}$ for the pristine films is reduced to a minimum value of $(66 \pm 2)\,\mathrm{nm}$ for HNO_3 treated films, which is an indication for material loss and is in agreement with earlier studies.[182,184] The conductivity for all treatments increases significantly up to three orders of magnitude from $(7 \pm 1)\,\mathrm{S\,cm^{-1}}$ (pristine) up to $(2940 \pm 330)\,\mathrm{S\,cm^{-1}}$ (H_2SO_4).

The loss in material is mainly attributed to a selective removal of insulating excess PSS in the film, which enhances the inter-grain charge transport between PEDOT-rich domains. Thus, the conductivity rises. The effectiveness of the removal seems to be related to the acids' strength and to their dielectric constants.[183] The corresponding values of the used acids are listed in Table 7.1. Interestingly, HCl treatment did not lower the film thickness significantly, which is probably related to the low di-

Table 7.1 Dissociation constants pK_a and dielectric constants ϵ_r of the used acids.

	EG	HCl	HCOOH	HNO_3	H_2SO_4
pK_a	15.1[188]	-7[189]	3.75[188]	-1.3[189]	-3[189]
ϵ_r	41.4[188]	4.6[190]	51.1[188]	50[190]	101[191]

electric constant compared to the other acids. Anyhow, the conductivity is increased to $(392 \pm 29)\,\mathrm{S\,cm^{-1}}$ without any loss in material, which supports the notion that the conductivity also depends on structural rearrangement and phase separation of the PEDOT- and PSS-rich regions.[184,187] Interestingly, the H_2O-washed HNO_3 and H_2SO_4 samples show a drop in conductivity to $\sim 1000\,\mathrm{S\,cm^{-1}}$ without a large thickness reduction, which indicates a reversibility of the adjuvant effect of phase separation induced by acid treatments. Meanwhile, washing of the HCl and the HCOOH treated samples seems to impact neither the film's thickness nor its conductivity.

7.3.2 AC Conductivity

As the field of application in organic electronics is not limited to DC powered devices it is of interest to investigate the AC response of polymeric electrodes. Therefore, their potential use for integrated circuits such as OFETs or PWM powered OLEDs was tested in the frame of the Bachelor's thesis of Raphael Maier.[176] In order to examine the conducting behavior for an alternating current on highly conducting polymeric electrodes, impedance spectroscopy measurements on selected PEDOT:PSS electrodes were performed according to Subsection 4.2.2. Beside pristine PEDOT:PSS, samples treated with EG, HCOOH and H_2SO_4 including subsequent H_2O-washing were tested regarding their AC response from 1 MHz to 1 Hz. The so-called Nyquist plot of the pristine PEDOT:PSS sample depicted in Figure 7.3d shows clearly a semicircle in the positive sector, which is typical for a high contribution of a combined capacitor and resistor. The response to the AC input becomes more obvious in the so-called Bode plots (Figure 7.3b,c). In this case, the modulus ($|Z|$) and the phase ($\Phi(Z)$) of the impedance Z are separately plotted in dependence of the applied frequency. Consequently, an ohmic behavior shows a constant horizontal line, while a conductance and an inductance show a drop and an increase for higher frequencies, respectively. In the case of pristine PEDOT:PSS the dependency of the absolute impedance from the applied frequency in Figure 7.3e shows a high value of $|Z| \approx 25\,\mathrm{k\Omega}$ for low frequencies and a decay for higher frequencies. The phase shift shown in Figure 7.3f represents the typical behavior of a capacitor with an increasing shift down to $\Phi \leq -75°$ for higher frequencies. Therefore, the AC response of pristine PEDOT:PSS can be modeled with an equivalent circuit consisting of a parallel connected capacitor and resistor, as

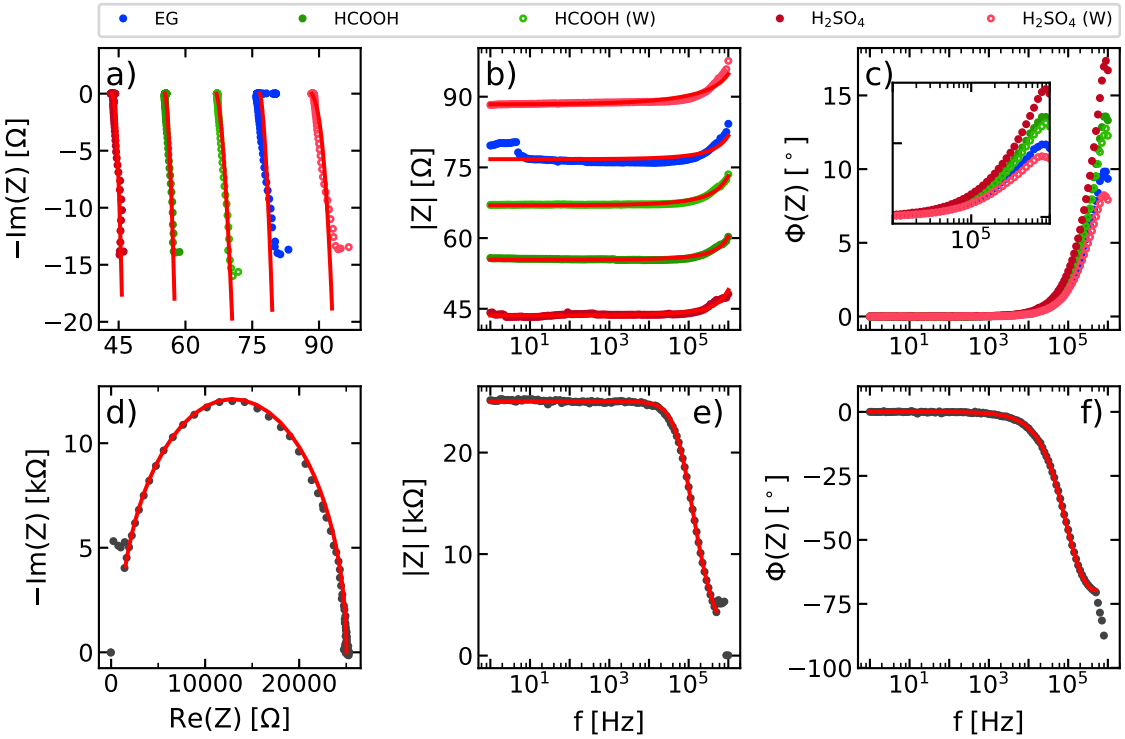

Figure 7.3
Impedance spectroscopy measurements including their fits (red) for selected high conducting polymeric electrodes. EG, HCOOH and H_2SO_4 treated PEDOT:PSS electrodes including H_2O-washed ones (top row) and pristine PEDOT:PSS (bottom row). The data is represented in so-called Nyquist plots (a, d) and Bode plots (b, c, e, f). While pristine PEDOT:PSS clearly shows the behavior of a capacitor, the polymeric electrodes are best described via a combination of resistance and inductance.

depicted in Figure 7.4c. Thus, values of $R_3 = 793\,\Omega$, $R_4 = 24.2\,\mathrm{k}\Omega$, and $C_4 = 74.8\,\mathrm{pF}$ for the resistances and the capacitance are obtained, respectively. The contribution of the wiring and contacts for all fits is addressed by a serial connection of a $R_1 = 10.5\,\Omega$ resistance and a $L_1 = 2.5\,\mu\mathrm{H}$ inductance (Figure 7.4a), which is connected in series to the equivalent circuits depicted in Figure 7.4b,c. The high resistance for low frequencies is in accordance to the measured DC conductivity discussed earlier and can be explained with the high PSS content and the presence of a PSS capping layer. This capping layer inhibits charge introduction into the conducting regions of the polymer and serves as insulating high dielectric material between the evaporated gold contacts, yielding the capacitive behavior for high frequencies.

The examined polymeric electrodes draw a different picture. As depicted in the Nyquist and Bode plots in Figure 7.3a-c, all samples reveal a typical inductive behavior and are only shifted on the $\mathrm{Re}(Z)$ axis. Therefore, they show ohmic behavior over a wide range of frequencies as seen in Figure 7.3b. The impedance starts to rise for $f > 100\,\mathrm{kHz}$, which becomes apparent in the positive phase shift in the same frequency

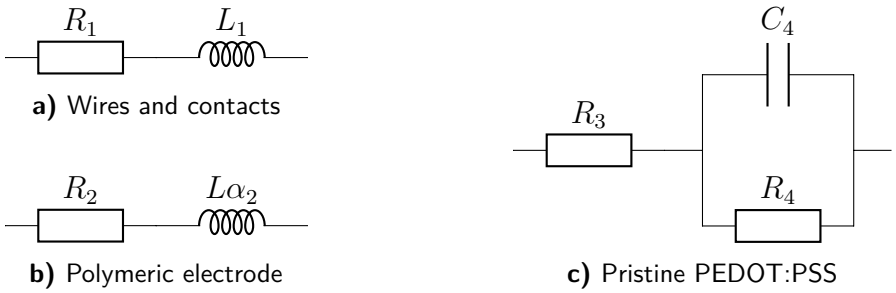

Figure 7.4
Used equivalent circuits of wiring and contacts (a), acid treated highly conducting PEDOT:PSS electrodes (b) and untreated pristine PEDOT:PSS (c). For all fits the contribution of wires and contacts is considered in an additional serial connection of a) with b) or c). a) Wires and contacts are considered as serial connection of resistance R_1 and inductance L_1. b) Highly conducting PEDOT:PSS is modeled with a resistance R_2 and a modified inductance $L\alpha_2$. c) The model for untreated PEDOT:PSS consists of the resistances R_3 and R_4 and the capacitance C_4.

region in Figure 7.3c. Therefore, the polymeric electrodes can be modeled with an equivalent circuit consisting of a serial connected resistance and a modified inductance as depicted in Figure 7.4b. As a perfect inductance would be present with a vertical line in the Nyquist plot, the ideality factor α is introduced in order to consider for the slight slope of the data curve visible in Figure 7.3a. The deviation from the ideal inductance is commonly referred to surface defects and the interface roughness between the contact and the probed sample. Since impedance spectroscopy is an integrative measurement technique, such defects cannot be resolved and are typically accounted for by the ideality factor of the measured inductance.[137] The fit results are depicted in Figure 7.5, where the ideality factor is $\alpha \approx 0.5$ for all fits. The inductance for all samples is fairly small around ~1 mH and is increased for the washed H_2SO_4 sample, as depicted in Figure 7.5a. Thus, the inductance for the samples is found to be ~10^3 larger than the contribution of the wires, which is probably related to the slower charge carrier mobility caused by counter-ion movement. The obtained ohmic resistances for the different samples are lower compared to the DC sheet resistance obtained from four-point measurements (Figure 7.5b). This lower value is most probably related to the measurement geometry and the contacting method. To obtain reproducible measurements, it was necessary to partly remove the PEDOT:PSS film and evaporate the gold contacts across the exposed film's ridge. As shown in Figure 4.4, the needle contacts are placed on the gold covered area of the substrate. On one hand, the measurement is then not disturbed by the varying contact pressure of the needles to the PEDOT:PSS thin film (see Subsection 4.2.2). On the other hand, the gold contacts provide a connection to the sample's surface and its edge, which results in additional channels for current flow through the sample that reduces the obtained resistance. Therefore, the offset is most probably related to effects caused by the

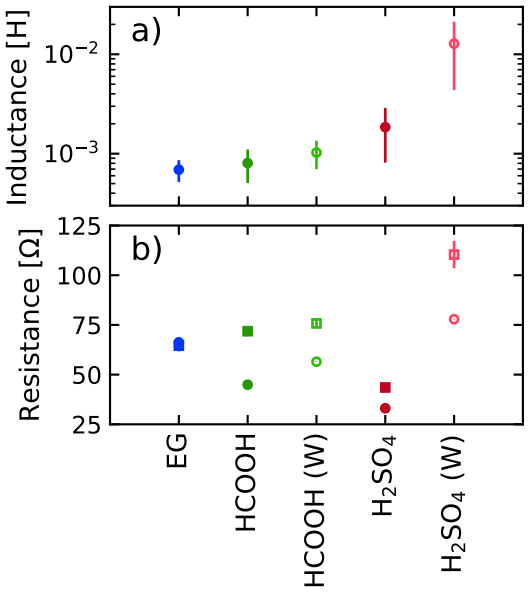

Figure 7.5
Fit results for EG, HCOOH and H_2SO_4 treated PEDOT:PSS electrodes (including H_2O-washed ones). Fits were performed with an equivalent circuit consisting of a non-ideal inductance (a) and a resistance (b). The resistance is underestimated compared to the plotted DC sheet resistance obtained from four-point measurements (□), most probably related to the measurement geometry setup, as explained in the main text.

described sample geometry leading to a deviation in the measured resistance. However, the measured resistance from impedance spectroscopy follows the same trend as the sheet resistance obtained from four-point measurements. Taking into account the Bode plots in Figure 7.3b,c, it becomes obvious that the selected polymeric electrodes are highly conductive and only show an influence of the inductance for frequencies >100 kHz. Below this critical value, the electrodes behave like ohmic resistors with high conductivity, as seen in Subsection 7.3.1. Therefore, the investigated samples might be used for applications with alternating current and could be employed for ICs up to operational frequencies of ~100 kHz.

7.4 Optical Properties

Beside the electrical conductivity, the light transmission through a transparent electrode is of high importance as well. The aim for well performing transparent electrodes is a high electrical conductivity in combination with low absorbance in the visible region of light. In Figure 7.6 the absorption coefficient and the figure of merit (FoM) for the different treated films are depicted. The FoM is a measure for the performance of transparent electrodes and considers its DC conductivity. It is calculated as function of the optical wavelength according to Scardaci et al. (Equation 4.9).[134] Values above 35 are considered as suitable for industrial applications. Therefore, all treatments obtain a well performing transparent electrode. The main change in the absorption spectra is located in the near infrared region, while the absorption around 400 nm stays almost constant, which is the reason for the intensified blueish color of the treated films. The absorption coefficient reveals an up to three times higher ab-

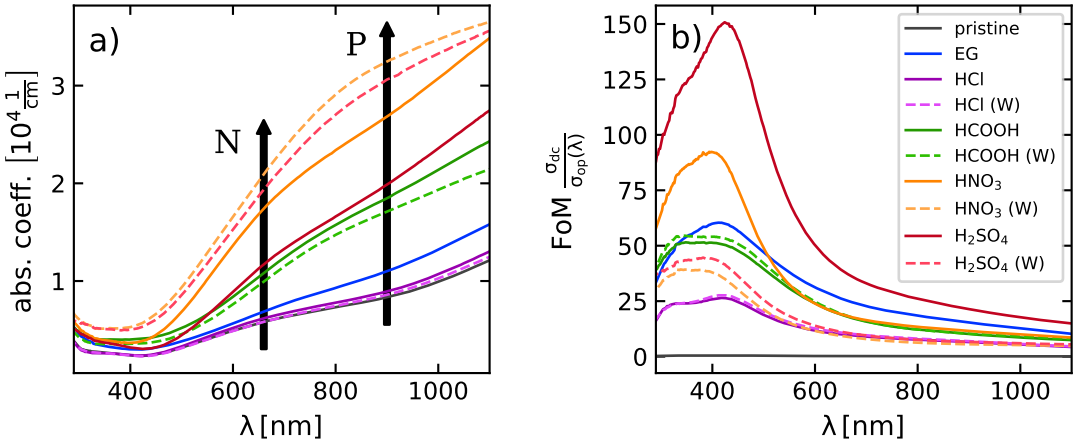

Figure 7.6

a) Absorption coefficient and b) figure of merit (FoM) of treated PEDOT:PSS thin films: pristine (black), EG (blue), HCl (purple), HCOOH (green), HNO_3 (orange), H_2SO_4 (red), with subsequent H_2O-washing (dotted lines). Absorption coefficients (a) are increased for acid treated samples, indicating a higher charge carrier density. Neutral (N) and polaronic (P) states are enhanced for H_2O-washed HNO_3 and H_2SO_4 samples. In contrast, subsequent H_2O-washing on HCl and HCOOH samples show no change in absorption spectra. Reproduced with permission from John Wiley & Sons, Copyright 2019.[30]

sorption in the near infrared region for acid treated samples, indicating a densification of thin films and an increased number of charge carrier states.[170,192] This effect is related to an additional secondary doping of PEDOT chains, caused by structural rearrangements in the film and goes along with increasing conductivity. Furthermore, washing of the high conducting HNO_3 and H_2SO_4 samples yields an increasing absorption around 600 nm – 900 nm, indicating a reduced number of bipolaronic states (>1250 nm) in favor of increased polaronic (~900 nm) and neutral (~660 nm) states caused by a dedoping effect of the PEDOT chains.[192]

7.5 Surface Compositional Analysis via XPS

X-ray photoelectron spectroscopy (XPS) was used to examine the impact of acid treatment upon PSS extraction. All spectra were referenced to the C 1s level set to 285.0 eV[167] and are shown in Figure 7.7. The high resolution spectra reveal two dominating features in the S 2p spectral region that are readily attributed to the presence of PSS and PEDOT at a binding energy of ~168 eV and ~164 eV, respectively.[167,193] The energy splitting and the intensity ratio of S $2p_{1/2}$ and S $2p_{3/2}$ were fixed at 1.2 eV and 1 : 2, respectively. In addition, the FWHM of these features is reasonably expected to be identical for both components of the doublet.[167,182,193] A comparison of the relative intensities of these spectral components is expected to provide insight into the effectiveness of PSS removal. Qualitative inspection of the spectra of the EG-

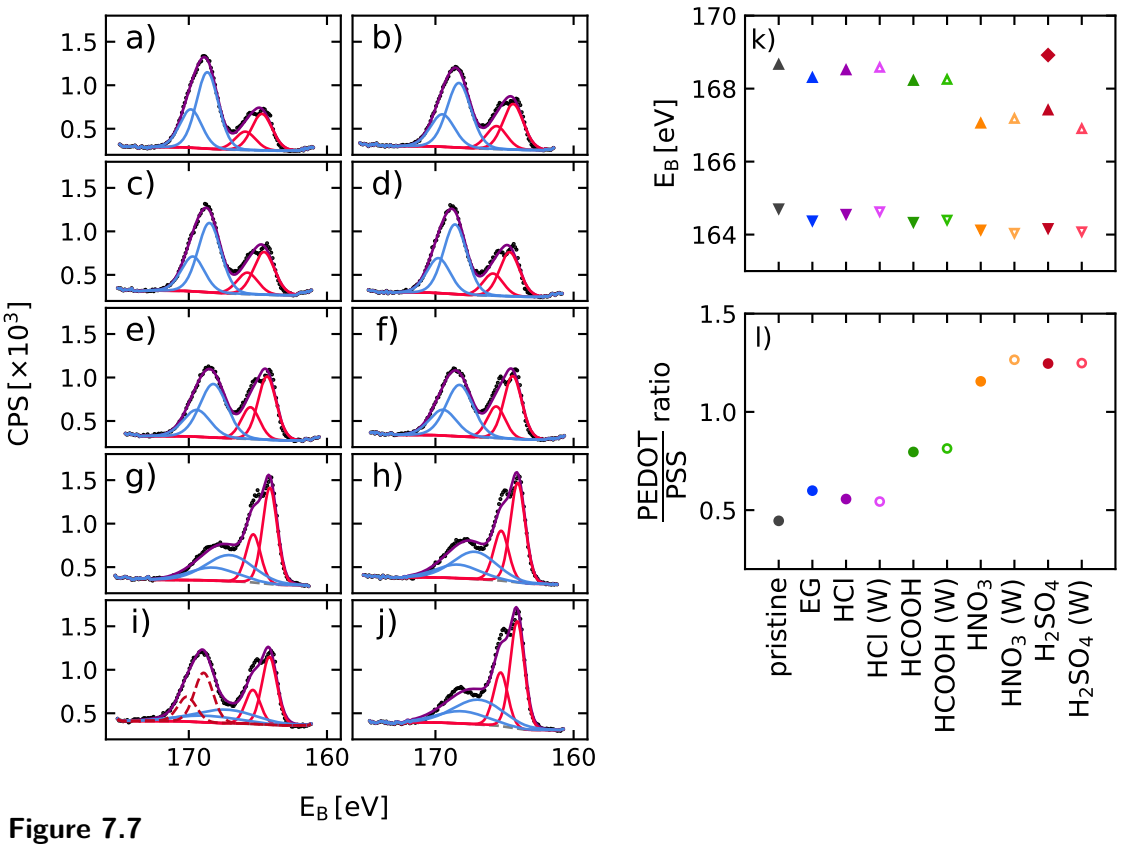

Figure 7.7
S 2p high resolution XPS spectra including fits for PEDOT (red), PSS (blue) and its superposition (purple). a) Pristine PEDOT:PSS, b) EG; c,d) HCl, e,f) HCOOH, g,h) HNO_3, i,j) H_2SO_4 treatment and their washed counterparts, respectively. Each peak is fitted according to the S 2p doublet ($S\,p_{1/2}$, $S\,p_{3/2}$). k) Binding energy of $S\,p_{3/2}$ contribution for PEDOT (~164 eV, ▼-symbols) and PSS (~168 eV, ▲-symbols). The third signal (◆) for H_2SO_4 treatment around ~169 eV arise from sulfuric acid residuals. l) PEDOT:PSS ratio calculated from area comparison of S 2p fits. Hollow symbols represent washed samples. Adapted with permission from John Wiley & Sons, Copyright 2019.[30]

treated samples (Figure 7.7b) compared to the pristine samples (Figure 7.7a) shows a slight change in intensity towards higher PEDOT content. This is in agreement with the reported reduced PSS capping layer for EG post-treatment.[174] Otherwise, the spectra for HCl, and HCl (W) (Figure 7.7c,d) were seemingly indistinguishable from the pristine sample (Figure 7.7a), indicating negligible PSS removal. In contrast, HCOOH-treated (Figure 7.7e) and subsequent H_2O-washed samples (Figure 7.7f) reveal a reduced PSS signal in combination with an increased PEDOT signal, indicating extraction of PSS. Finally, for HNO_3 and H_2SO_4 treated samples (Figure 7.7g,i), including their H_2O-washed counterparts (Figure 7.7h,j), the reduction of the intensity of the PSS spectral feature is more clearly visible, which is consistent with a substantial lowering of the PSS content. Washing treated samples with water (Figure 7.7d,f,h,j) has only a limited impact on the composition regarding PSS extraction. It is of inter-

est to note that the H_2SO_4-treated sample (Figure 7.7i,j) shows an additional broad emission at ~169 eV that can be attributed to residuals of sulfuric acid,[194] which were dissolved and removed in the subsequent H_2O washing step.

In addition to providing a probe of the material atomic composition, XPS allows the evaluation of changes in the oxidation states of atomic species, which becomes apparent in a shift in binding energy. In order to evaluate the impact of the acid treatments on the oxidation states of the sulfur containing components of the present polymers the binding energies of the S $2p_{3/2}$ emission for PEDOT and PSS was determined (Figure 7.7k). The maximum shift of ~0.6 eV towards lower binding energies of the PEDOT emission indicates a change in the electronic environment of the sulfur atom, which can be ascribed to a reduced average oxidation level of the thiophene sulfur of PEDOT. This might be a result of the reduction of the insulating PSS component and a possible ion-exchange by acid treatment, as observed by Wang et al. for a similar system.[195] Furthermore, a reduced oxidation level could indicate a dedoping effect, which would lead to a reduced charge carrier concentration.[20,185] Additionally, the binding energy of the sulfone group in PSS is reduced by ~1.7 eV consistent with protonation of the PSS-SO_3^--groups;[20] this protonation is expected to be beneficial for efficient PSS Coulomb screening and the subsequent removal during acid treatment/H_2O-washing. To quantify the PSS extraction, the S 2p peak areas of PEDOT and PSS were compared. The calculated PEDOT-to-PSS ratio is depicted in Figure 7.7l, showing a notable reduction of PSS after HNO_3 and H_2SO_4 treatment; this is beneficial for enhanced conductivity (vide supra). The present evaluation also indicates that the effectiveness of PSS removal correlates with the acid's strength and the Coulomb screening potential of the solvents/acids employed, which is discussed in more detail later on.

In addition, high resolution XP scans of Cl 2p and N 1s core-level regions exhibit no detectable increase in chlorine or nitrogen content for HCl and HNO_3 treated samples, respectively. Therefore, an intercalation of Cl^- or NO_3^--ions is less likely. In contrast, sulfuric acid treated samples show a strong emission at ~169 eV, which is attributed to H_2SO_4;[194] the appearance of this suggests an exchange of partially charged PSS with HSO_4^--ions may have occurred.

7.6 Structural Analysis via GIWAXS

As mentioned earlier, the spectroscopic investigations together with the reduced thickness and the XPS measurements suggest an extraction of excess PSS yielding an enhanced PEDOT-to-PSS ratio in favor of conducting PEDOT. However, taking a look at the increased conductivity for HCOOH, EG and especially HCl treated samples, in which cases almost no decrease in film thickness is observable, the extraction of PSS alone cannot explain the tremendous increase in the conductivity of the films. There-

fore, the films were examined with GIWAXS, which enables to probe the crystalline part of the films in terms of orientation and structure. In addition, information about the PEDOT-to-PSS ratio in the crystalline regions can be extracted. In contrast to XPS, where the information depth of the detected electrons is limited to the top-most layers of the film and therefore can be considered as surface sensitive, GIWAXS allows probing the inner film structure in combination with a large film volume. This reveals detailed information from the inner film with high statistical relevance.

7.6.1 Crystal Orientation

In Figure 7.8 the obtained 2D GIWAXS patterns are depicted for pristine PEDOT:PSS (a) films, together with EG (b), HCl (c), HCOOH (e), HNO_3 (g) and H_2SO_4 (i) treated ones. Figure 7.8d,f,h,j shows HCl, HCOOH, HNO_3, H_2SO_4 treated films additionally subjected to H_2O-washing. Figure 7.9 shows the same measurements in different representation style, for better visibility of the crystallite orientation and their absolute q-values. The 2D patterns clearly show distinct Bragg peaks in q_z-direction, indexed with {100}, coming from an alternating lamellar stacking of PEDOT and PSS, which was often seen in GIWAXS and XRD investigations on PEDOT:PSS films.[182,197,198] The H_2SO_4-treated sample in Figure 7.8i shows the most distinct Bragg peaks in q_z-direction, which can be attributed to a very high morphological order and goes along with the highest conductivity values among the investigated samples. This supports the link between a well developed order of the crystalline structure and high conductivity. However, this high order is obviously destroyed by subsequent H_2O-washing. In addition, for the pristine sample (Figure 7.8a) a very intense non-oriented signal is observed around $q \approx 1.3\,\text{Å}^{-1}$, which is attributed to the amorphous PSS π–π stacking distance of $d \approx 4.8\,\text{Å}$.[197] Interestingly, the amorphous PSS signal is reduced for the different treatments, confirming removal of the excess PSS in the films. The least amorphous PSS signal is seen for the HNO_3- and H_2SO_4-treated films, which goes along with the remarkable thickness decrease caused by these treatments as seen in Figure 7.2a. From below the reduced amorphous PSS signal, additional distinct and oriented Bragg peaks appear especially pronounced for HNO_3- and H_2SO_4-treated films (Figure 7.8g,i). Figure 7.9 shows, these distinct Bragg peaks are located around $\chi = 60°$ and $q = 1.25\,\text{Å}^{-1}$. Those peaks might originate from an oriented PSS π–π stacking, which might be induced through a templating effect of neighboring and crystallizing PEDOT domains that forces the PSS to a higher morphological order. Along with the reduced PSS content an additional oriented Bragg peak around $\chi = 40°$ and $q = 1.75\,\text{Å}^{-1}$ is revealed and might be related to an additional orientation of PEDOT π–π stacking between the face-on and the edge-on (020) stacking. These additional peaks are usually hidden under the signal coming from the non-oriented PEDOT π–π stacking. Thus, typically, they are not distinguishable from the very broad signal coming from the face-on and edge-on orientation and were formerly assigned to a shift

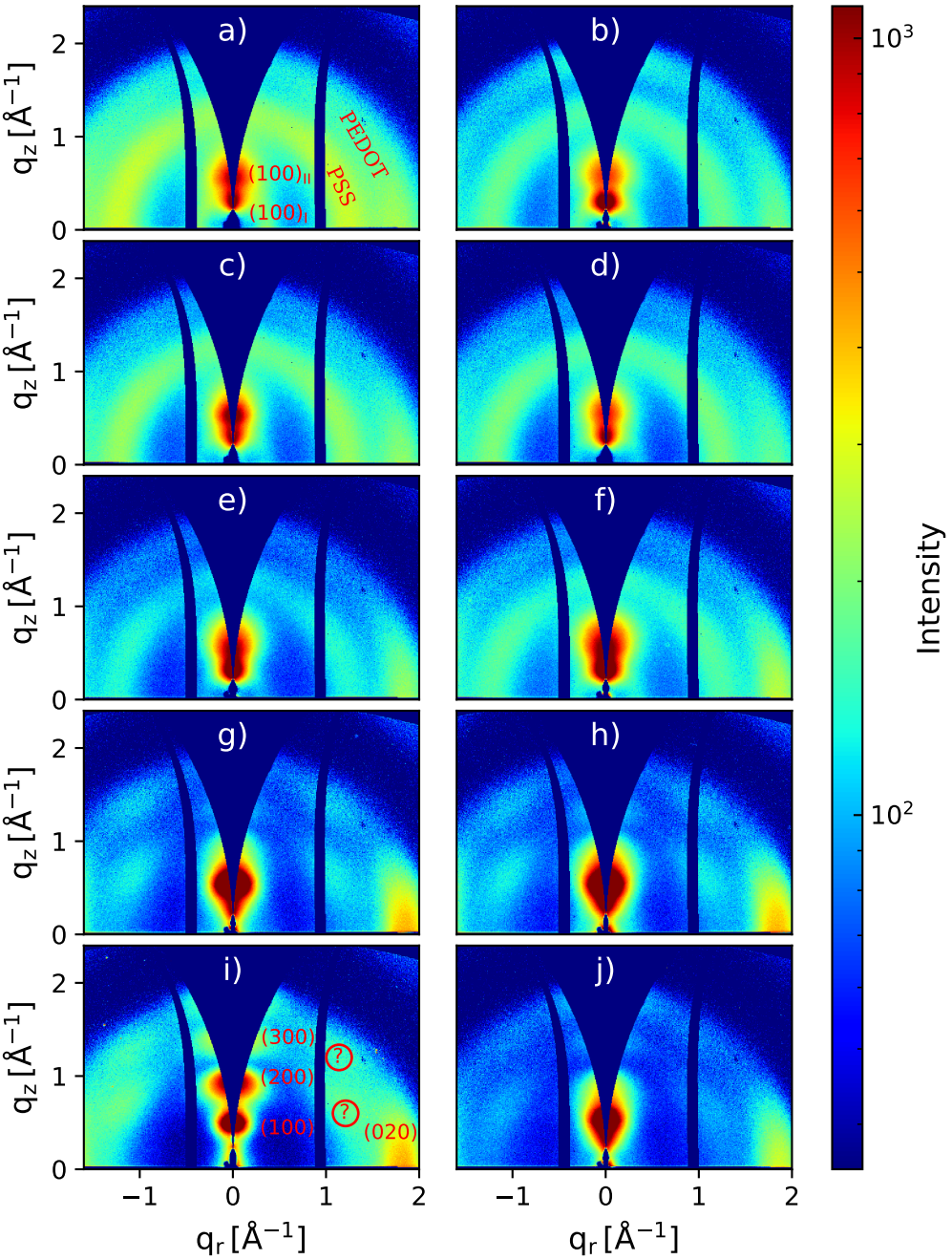

Figure 7.8
2D GIWAXS data of treated PEDOT:PSS samples: a) Pristine, b) EG, c,d) HCl, e,f) HCOOH, g,h) HNO_3, i,j) H_2SO_4 treatment and their H_2O-washed counterparts, respectively. Acid treated samples reveal a reduced amorphous PSS signal and high crystalline order. Different vertical lamellar stacking (marked with I/II in a) and increased PEDOT edge-on π–π stacking is observed. Reflexes corresponding to lamellar and PEDOT π–π stacking of (100) and (020) are exemplarily marked in a) and i) together with the π–π stacking attributed to PSS. The unassigned reflexes marked with (?) might be related to a (111) reflex.[196] Adapted with permission from John Wiley & Sons, Copyright 2019.[30]

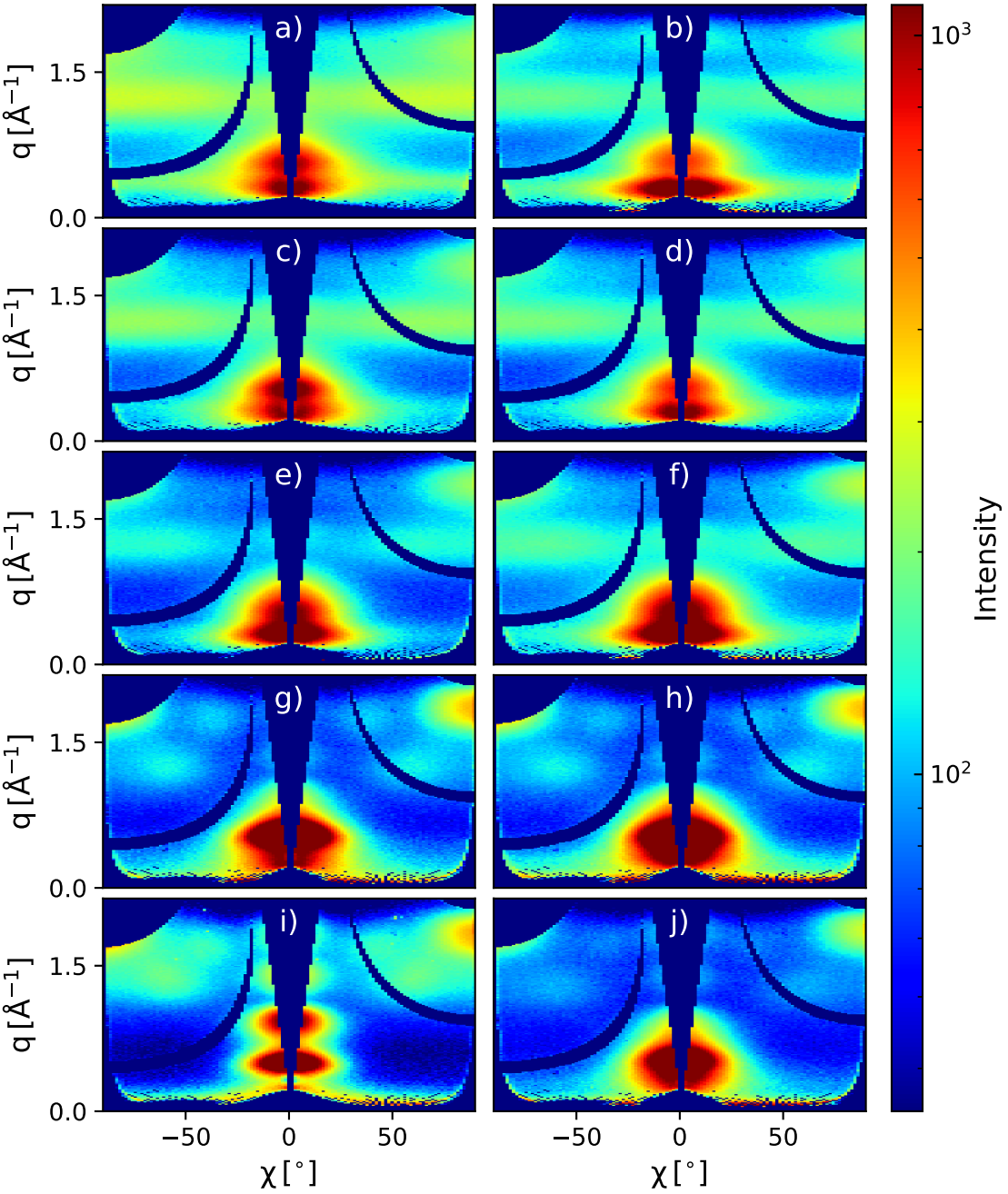

Figure 7.9

χ-reshaped 2D GIWAXS data, showing the absolute q-value in relation to the azimuthal orientation angle χ of its crystallites in PEDOT:PSS thin films. a) Pristine, b) EG; c,d) HCl, e,f) HCOOH, g,h) HNO_3, i,j) H_2SO_4 treated films and their H_2O-washed counterparts. The scattering signal around $q \approx 1.3\,\text{Å}^{-1}$ coming from the amorphous PSS is significantly reduced for HNO_3 and H_2SO_4 treated films, which reveals a high ordered signal around $\chi \approx 60°$ orientation angle. High orientation and lamellar stacking is altered by subsequent H_2O-washing. Reproduced with permission from John Wiley & Sons, Copyright 2019.[30]

in the PEDOT π–π stacking distance.[187] In the present case, the signal is clearly separated from the PEDOT face-on and edge-on π–π stacking and therefore is identified as an additional peak. Furthermore, Aasmundtveit et al. predicted for a similar system of PEDOT:Tos the appearance of an intense (111) reflex, which is only visible for a highly ordered system.[196] Hence, the appearing peaks might be related to the predicted reflex. In any case, the aforementioned scattering features are an additional indication for high crystallinity and order. For a detailed analysis, sector integrals in edge-on ($\chi = 70° - 85°$) and face-on ($\chi = -16° - 16°$) direction were performed, which are depicted in Figure 7.12 and Figure 7.15, respectively and are discussed later on in detail.

7.6.2 PEDOT-to-PSS Ratio

The assignment of the non-oriented ring located at $q \approx 1.3\,\text{Å}^{-1}$ to the amorphous PSS π–π stacking allows for using the signals' intensity as measure for the amount of excess PSS in the film. Therefore, it enables for a comparison of the PEDOT-to-PSS ratio for the different treatments by comparing the signals' intensities of PEDOT and PSS. In order to achieve better statistics, so-called powder integration cuts ranging from $\chi = -50° - 85°$ were performed and are depicted in Figure 7.10. Comparing the peak areas attributed to the PSS and the PEDOT π–π stacking ($q \approx 1.8\,\text{Å}^{-1}$) allows to make statements on the PEDOT-to-PSS ratio inside the films, which is depicted in Figure 7.11d and is in agreement with the XPS results shown in Figure 7.7l. The pristine PEDOT-to-PSS is calculated to be 0.8, which is not altered by the HCl treatment. EG and HCOOH post-treatment show a slight increase towards 1.3 and 1.6, respectively. HNO_3 and H_2SO_4 reveal a strong increase in PEDOT-to-PSS ratio to 2.8 and 2.4, following the reduced thickness trend and indicating an enhanced conductivity for these treatments as shown in Figure 7.2. Taking a look at the dissociation (pK_a) and dielectric (ϵ_r) constants of the used acids, the ability to extract PSS from the film and therefore increase the conductivity appears enhanced for strong acids, except for HCl treatment (Figure 7.11a,b). This is in agreement with the earlier discussed data and is confirmed with the PEDOT-to-PSS ratio in dependence on the dissociation and dielectric constants in Figure 7.11c,d. Especially, the different conductivities with very similar dielectric constants for EG, HCOOH and HNO_3 treated samples show the importance of the acids' strength on PSS removal.

This indicates a separation of PSS and PEDOT if the acid's dissociation constant is smaller than the one of sulfonic acid. Hence, protonation of the PSS' sulfonate group can happen, which is in agreement with its reduced binding energy for HNO_3- and H_2SO_4-treatments (Figure 7.7k). Therefore, the Coulomb interaction between PEDOT and PSS chains is altered. Furthermore, it has been shown by several groups that efficient extraction of PSS from the film is related to the Coulomb screening ability of the used solvent towards the PSS' sulfonic group.[182–184,199] The conductivity

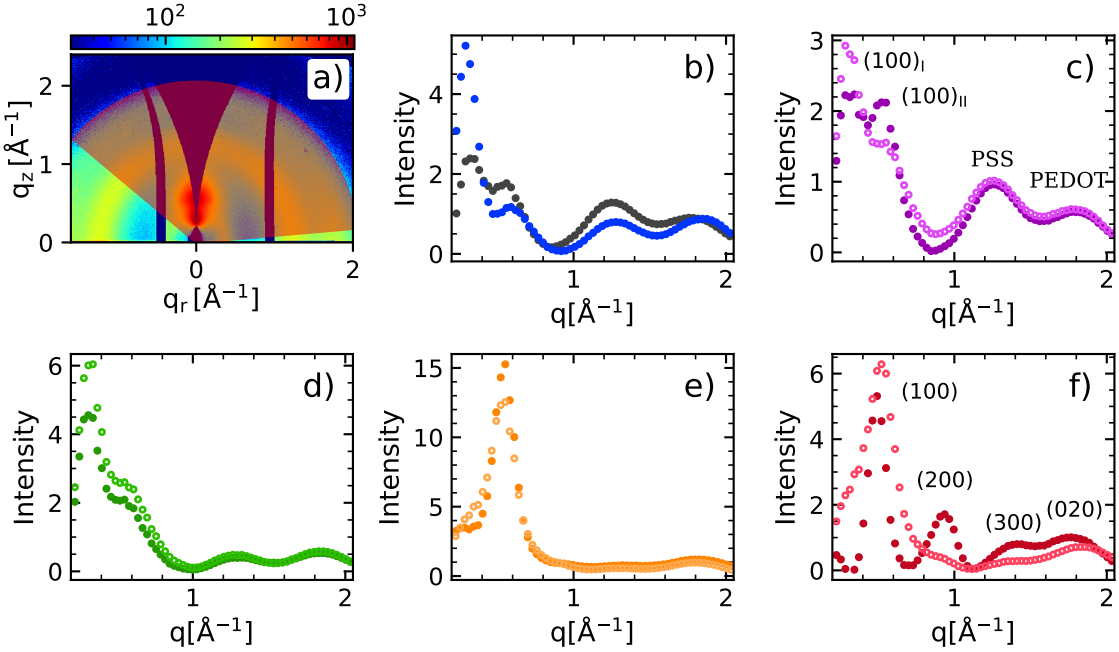

Figure 7.10
a) Exemplary powder integration of $\chi = -50° - 85°$ on pristine PEDOT:PSS. The color scale represents the measured intensity in arbitrary units. b) Corresponding cuts for pristine (black) and EG treated (blue) sample. Powder integration cuts for acid-treated (filled dots) and subsequent H_2O-washed (hollow circles) samples for c) HCl, d) HCOOH, e) HNO_3, and f) H_2SO_4, respectively. Different types of lamellar (100) stacking are exemplarily marked with I/II in c). Peaks around $q = 1.3\,\text{Å}^{-1}$ and $1.8\,\text{Å}^{-1}$ are attributed to the (non-)oriented PSS and PEDOT π–π stacking, respectively. Adapted with permission from John Wiley & Sons, Copyright 2019.[30]

dependence on the dielectric constant of the used solvent is depicted in Figure 7.11b. High dielectric solvents perform very well in screening the positive charge of PEDOT chains from the negative charge of PSS, respectively. Therefore, PSS and PEDOT chains can undergo phase separation more easily and PSS is extracted together with the solvent in subsequent washing and/or drying steps. This explains why HCl having a dielectric constant of ~5,[190] even being a strong acid, performs poorly regarding PSS extraction, while the weaker formic acid (HCOOH) with a dielectric constant of 51.1[188] performs very well. Therefore, it can be concluded that a dissociation constant smaller than that of PSS in combination with a high dielectric constant is beneficial for efficient PSS extraction.

Furthermore, except for the H_2SO_4 treatment, the following H_2O washing step shows less influence on the thickness and on the PEDOT-to-PSS ratio, indicating almost no additional removal of PSS. By considering the argument that an enhanced PEDOT-to-PSS ratio is beneficial for enhanced conductivity, the increased ratio for the washed

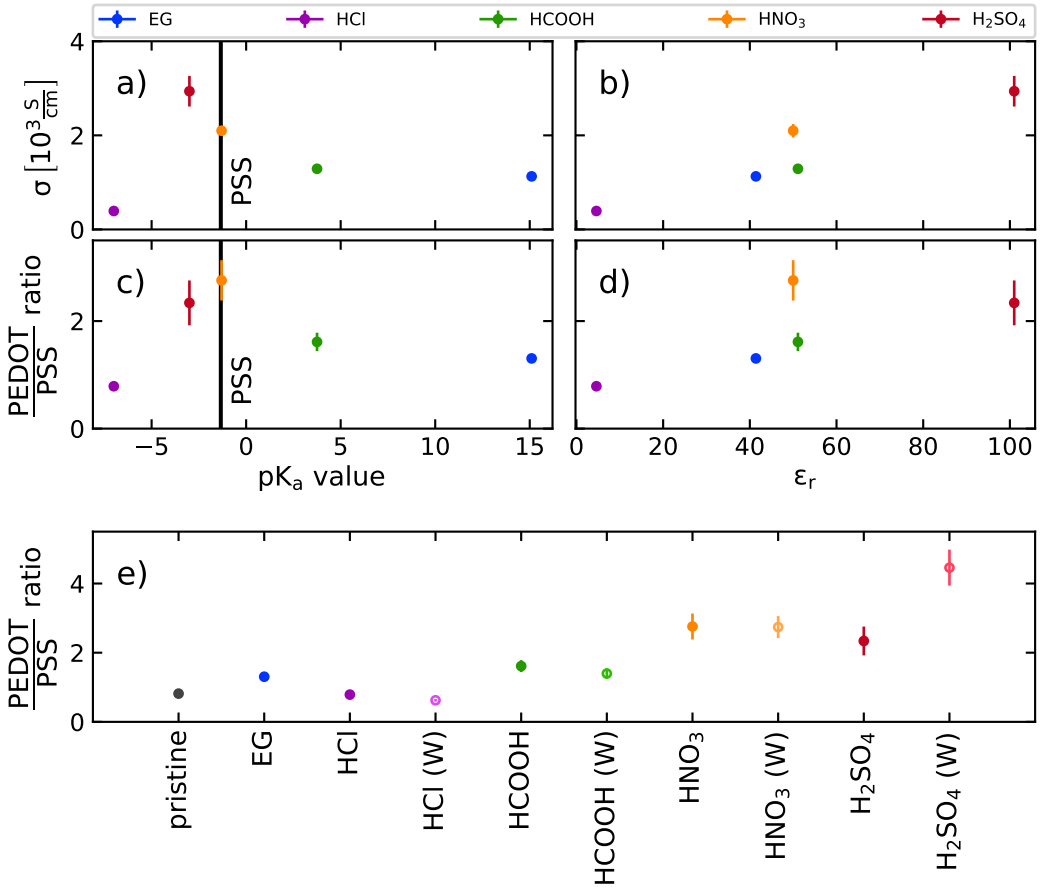

Figure 7.11

Dependency of DC conductivity σ on a) dissociation constant pK_a and b) dielectric constant ϵ_r of the used acids/solvent. The used values are listed in detail in Table 7.1. e) The PEDOT-to-PSS ratio was extracted from powder integration cuts ($\chi = -50° - 85°$) on 2D GIWAXS patterns depicted in Figure 7.10. The same PEDOT-to-PSS ratio in dependence on pK_a and ϵ_r is shown in c) and d), respectively. HCl treatment (purple) shows no change in PEDOT-to-PSS ratio, while EG (blue) and HCOOH (green) reveals a slight change. HNO_3 (orange) and H_2SO_4 (red) shows a strong change towards an increased PEDOT-to-PSS ratio, indicating PSS removal. The increased ratio for H_2SO_4 (W) might be related to a loss in crystallinity in the region of the PSS signal. Comparison of HNO_3, HCOOH and EG shows a combination of high dielectric constant and small dissociation constant is beneficial for efficient PSS extraction. Adapted with permission from John Wiley & Sons, Copyright 2019.[30]

H_2SO_4 treatment is counterintuitive. This might be related to a decreased crystallinity and order of crystallites, which is indicated by the reduced intensity of the newly exposed peaks around $\chi = 60°$ and $q = 1.25\,\text{Å}^{-1}$ in Figure 7.8i. In fact, the subsequent H_2O treatment reveals a maximum conductivity of $\sigma \approx 1000\,\text{S cm}^{-1}$, showing no change in conductivity for HCl and HCOOH treated samples, but a significant reduction for HNO_3 and H_2SO_4 treated samples. This is evidence for a structural rearrangement inside the film and might be an indication for a reversal of PEDOT and PSS phase separation.

7.6.3 Morphological Reorientation

The conductivity enhancement of PEDOT:PSS thin films upon different treatments is related to the ratio of electrically conducting PEDOT to insulating PSS and to the degree of short-range and long-range order of PEDOT crystallites. The edge-on sector integrals depicted in Figure 7.12 were fitted applying several Gaussians to reproduce the entire scattering curve. The three distinct peaks at $\sim 0.30\,\text{Å}^{-1}$, $\sim 1.25\,\text{Å}^{-1}$ and $\sim 1.8\,\text{Å}^{-1}$ are attributed to a stacking of alternating PEDOT and PSS, the PSS π–π stacking, and the PEDOT π–π stacking, respectively.[196,200]

It has been shown that a high content of edge-on stacked PEDOT crystallites is favorable for in-plane charge carrier transport, due to the strong π-overlap of the sp^2 hybrid orbitals of stacked PEDOT chains.[187,201] Therefore, a small stacking distance is favorable for good conductivity. Figure 7.13a shows the corresponding stacking distance d of PEDOT crystallites, determined from the fits on the edge-on sector integrals. The peak positions change slightly by the different treatments compared to the pristine sample depicted in Figure 7.12b. The stacking distance changes from 3.57 Å for pristine PEDOT:PSS towards more densely packed PEDOT crystallites with 3.38 Å for H_2SO_4-treated samples and goes along with the enhanced conductivity upon the different treatments. This densification is in agreement with the increased absorption of visible light in Figure 7.6a. Applying Scherrer's equation (Equation 2.41) with the FWHM of the fitted peaks one can calculate the apparent crystallite size D, which is depicted in Figure 7.13b and shows an increased value for the different treatments. In combination with the fitted stacking distance one can estimate the average number $\overline{N}$ of stacked PEDOT chains (Figure 7.13c). This quantity ranges from 3.17 ± 0.04 for the pristine sample to 4.45 ± 0.06 for the HNO_3 treated one. Therefore, the PEDOT crystallite size increases while the stacking distance of the single chains decreases on average, which goes along with the enhanced conductivity for the different treatments. The large difference in electrical conductivity for HNO_3- and H_2SO_4-treated samples compared to their H_2O-washed counterparts – despite the almost constant PEDOT π–π stacking distance – draws attention to the later on discussed lamellar stacking of PEDOT:PSS chains in the low q-region.

Furthermore, the intensities and shapes of the distinct edge-on peaks in Figure 7.12

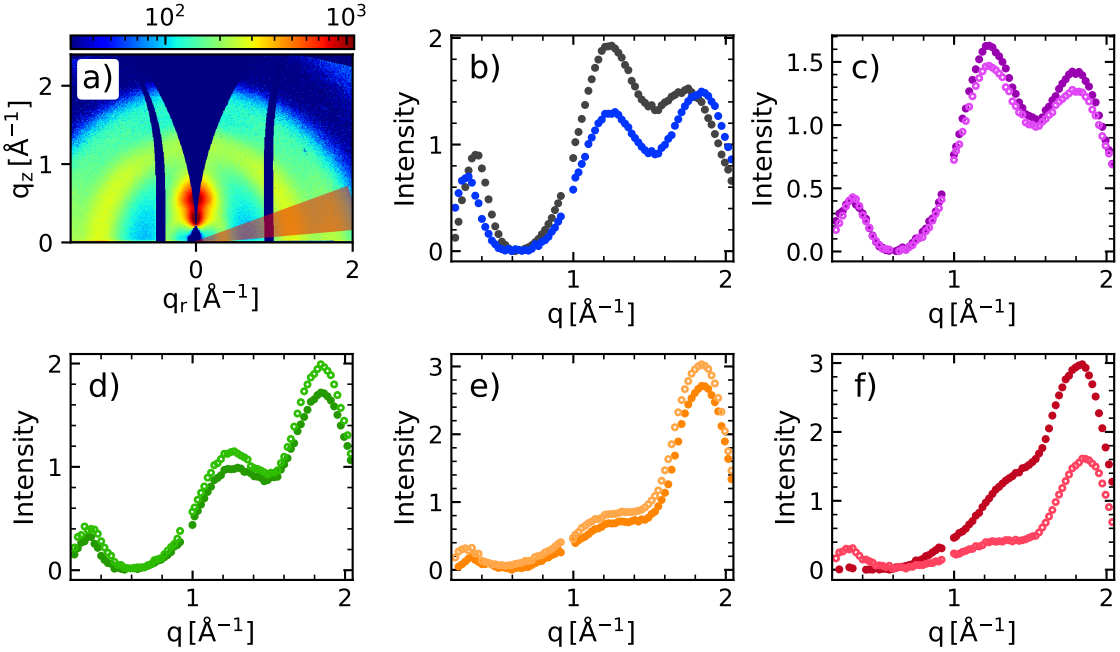

Figure 7.12
a) Exemplary edge-on sector integration of $\chi = 70° - 85°$ on pristine PEDOT:PSS. The color scale represents the measured intensity in arbitrary units. b) Corresponding cuts for pristine (black) and EG treated (blue) sample. c-f) Edge-on cuts for acid treated (filled dots) and subsequent H_2O-washed (hollow circles) samples for HCl, HCOOH, HNO_3, and H_2SO_4, respectively. Adapted with permission from John Wiley & Sons, Copyright 2019.[30]

change significantly with the treatment. Comparing the signal which is attributed to the PSS π–π stacking, the reduced PSS content for the different treatments is clearly visible and already discussed earlier on Figure 7.11. The HCl-treated samples in Figure 7.12c show almost the same shape as the pristine sample, indicating no significant PSS extraction, which is in accordance to the calculated PEDOT-to-PSS ratio and the comparable low conductivity. Treatments that yield higher conductivities show a reduced PSS signal while the signal coming from the edge-on oriented PEDOT π–π stacking is enhanced, e.g., for HNO_3 and H_2SO_4 treatment in Figure 7.12e,f. Furthermore, the signal located around $q \approx 0.30\,\text{Å}^{-1}$ can be attributed to a non-oriented lamellar stacking of type I for PEDOT and PSS (Figure 7.14a). This stacking is most pronounced for pristine PEDOT:PSS and least for H_2SO_4 treatment, which goes along with the strong orientation in q_z-direction of the latter. In addition, the position of the non-oriented stacking shifts from $\sim 0.36\,\text{Å}^{-1}$ (pristine) to $\sim 0.29\,\text{Å}^{-1}$ (EG) while the peak intensity is reduced for all treatments, indicating a reduced amount of non-oriented PEDOT:PSS. Furthermore, the influence of the subsequent H_2O washing can be seen in an increased intensity for HNO_3 (W) and H_2SO_4 (W), while the Bragg peak is not changing for the washed HCl- and HCOOH-treated samples. Thus, the drop in

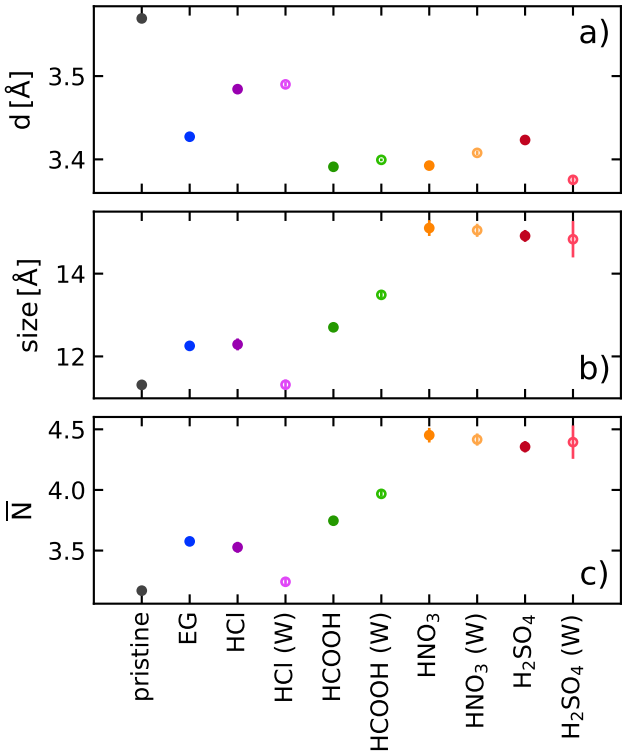

Figure 7.13
a) π–π stacking distance of edge-on oriented PEDOT crystallites. b) Apparent crystallite size of edge-on oriented PEDOT. c) Average number of stacked PEDOT chains per crystallite. Decreased stacking distance goes along with increased crystallite size and number of stacked chains. Adapted with permission from John Wiley & Sons, Copyright 2019.[30]

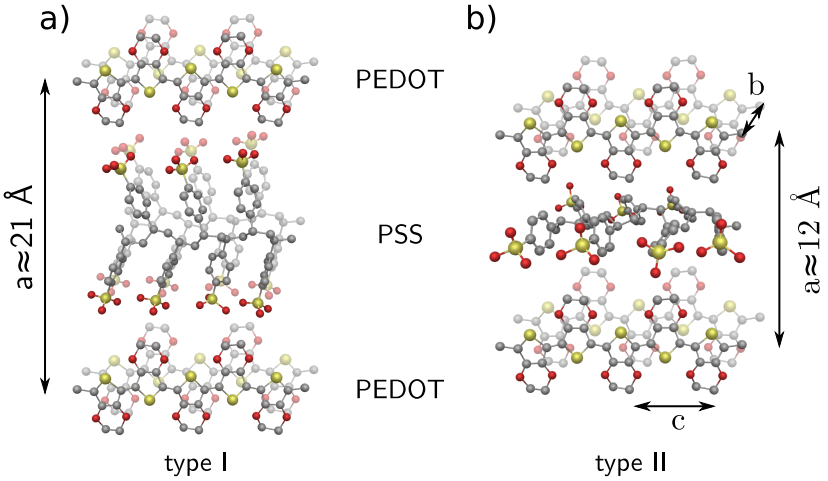

Figure 7.14
Two different types of lamellar stacking of alternating PEDOT and PSS chains that differ in the lattice spacing a in $[100]$ direction. The lattice spacing b and c correspond to the $[010]$ and $[001]$ crystal direction, respectively.[196] Adapted with permission from John Wiley & Sons, Copyright 2019.[30]

conductivity upon washing for HNO_3- and H_2SO_4-treated samples is related to a randomization of the lamellar stacking orientation of PEDOT:PSS accompanied by a lost degree of order. By contrast, HCl- and HCOOH-treated samples seem to be resistant upon subsequent H_2O-washing, due to the constant peak shape and intensity. However, the Bragg peak intensity is decreased from pristine, EG, HCl, HCOOH, HNO_3 to H_2SO_4 treatment, which goes along with the conductivity enhancement. Despite the relatively small conductivity for HCl- and HCOOH-treated PEDOT:PSS, their resilience against H_2O is remarkable, while the highly conductive samples obtained from HNO_3- and H_2SO_4-treatment suffer strongly from water induced degradation.

7.6.4 Vertical Lamellar Stacking

Figure 7.15 shows the sector integrals in face-on direction, giving information about the lamellar PEDOT:PSS stacking in q_z-direction. The applied treatments yield a very different scattering pattern in vertical direction. All samples show distinct peaks, which vary in q-spacing and intensity. The signals around $q \approx 1.3\,\text{Å}^{-1}$ and $1.8\,\text{Å}^{-1}$ are again attributed to the PSS and PEDOT π–π stacking, respectively. The scattering peaks around $q \approx 0.3\,\text{Å}^{-1}$ and $0.5\,\text{Å}^{-1}$, corresponding to a stacking distance of $d \approx 21\,\text{Å}$ and $12\,\text{Å}$, are assigned to two different lamellar stacking types of alternating PEDOT and PSS chains (types I and II in Figure 7.14).[202] An increase in lamellar stacking is attributed to an enhanced orientation and/or crystallization of the PEDOT and PSS chains. PSS-rich samples seem to prefer stacking type I (Figure 7.15b-d), which also show a tendency for non-oriented stacking (Figure 7.12b-d). Those treatments reveal a less efficient PSS removal, which gives on one hand an enhanced in-plane conductivity owed to the enhanced order. On the other hand, the high PSS content still limits the samples' conductivity.

Interestingly, HCl treatment, where the least efficient PSS removal is observed, show an enhanced stacking type II (Figure 7.15c). This stacking type is attributed to a more compact PEDOT:PSS stacking, which suggests an enhanced charge transport between the different PEDOT-rich domains owed to the reduced distance. However, in the case of HCl treatment, the advantage of ordered stacking regarding the conductivity is diminished by the high PSS content in the film. Both, HNO_3- and H_2SO_4-treatments (Figure 7.15e,f) show a different picture. These treatments provide very efficient PSS removal forcing the system to an efficient PEDOT:PSS packing, which is fulfilled with stacking type II. In this case, the H_2SO_4-treatment even shows a very intense second order of the lamellar stacking.[184,196] In combination with the reduced PSS content this leads to a remarkably enhanced conductivity. However, subsequent H_2O-washing yields a peak broadening and the appearance of a shoulder at smaller q-values. Especially the washed H_2SO_4 sample shows a reduced order as observed through the vanishing of the 2nd order Bragg peak in combination with a peak broadening and the appearance of an additional feature around $q \approx 0.44\,\text{Å}^{-1}$. This might be related to the aforementioned

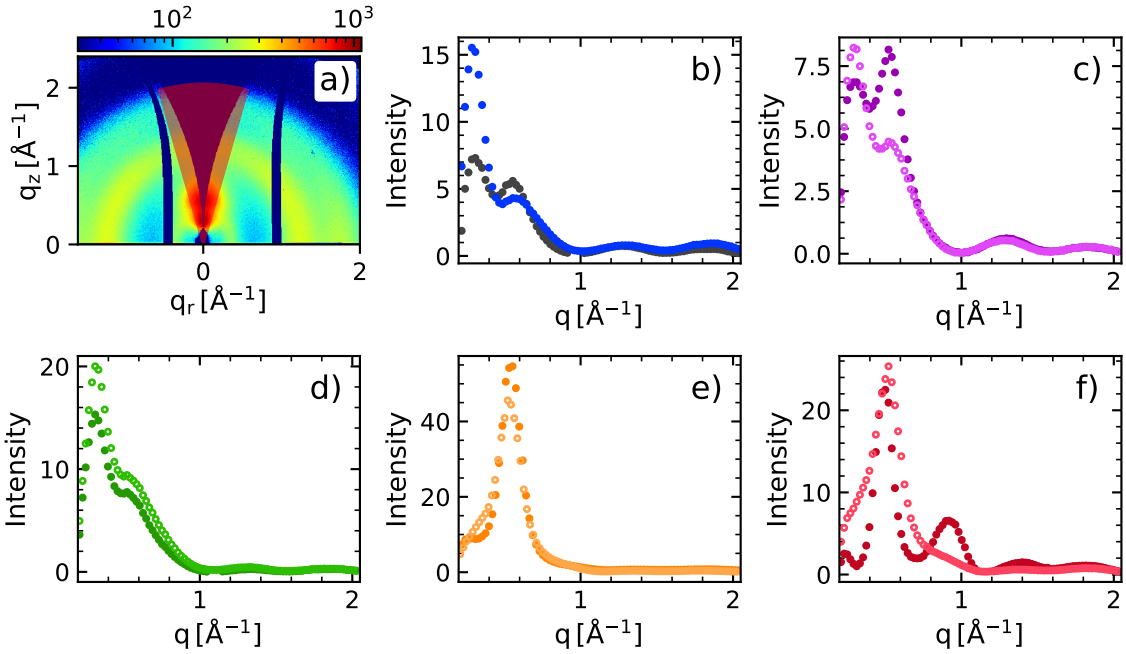

Figure 7.15
a) Exemplary face-on sector integration of $\chi = -16° - 16°$ on pristine PEDOT:PSS. The color scale represents the measured intensity in arbitrary units. b) Corresponding cuts for pristine (black) and EG treated (blue) sample. c-d) Face-on cuts for acid treated (filled dots) and subsequently H_2O-washed (hollow circles) samples for HCl, HCOOH, HNO_3, and H_2SO_4, respectively. Adapted with permission from John Wiley & Sons, Copyright 2019.[30]

high dielectric constant and acid strength. Since the pK_a values for weak acids and alcohols (EG, HCOOH) are typically larger than for PSS, they are not able to protonate the sulfonic groups on the PSS chains. However, they can interact with the already dissociated sulfonate groups to screen the negatively charged PSS and the positively charged PEDOT chains efficiently. Thus, they are causing a structural rearrangement, but an inefficient PSS extraction due to the weak acid characteristics. Strong acids on the other hand perform very well in protonating the PSS chains and therefore neutralizing their charged sulfonate groups, which is in agreement with the earlier discussed XPS study. In combination with a high dielectric constant, the separation of PSS and PEDOT is very efficient, which gives a high PSS extraction yield for HNO_3- and H_2SO_4-treated samples leading to an enhanced type II lamellar stacking. The obtained high order favors an in-plane charge transport. HCl seems to be a special case. On one hand it is a very strong acid, which is able to protonate PSS. On the other hand it shows a small dielectric constant, which gives an insufficient Coulomb screening of the charged PEDOT and PSS groups. Therefore, a preferred type II lamellar stacking seems possible, due to an easier structural rearrangement owed by

an increased chain mobility, but the screening is too weak to fully separate the PSS from the PEDOT and extract it efficiently. Furthermore, in contrast to HNO_3 and H_2SO_4, HCl is a weakly oxidizing acid which might also have an influence on the low PSS extraction yield.

Therefore, it can be concluded: A high dielectric constant is necessary for a successful screening of the charged groups of PEDOT and PSS chains, which enables a separation of both different chains.[183] However, a good dissociation constant is also favorable for protonation of the PSS' sulfonate groups, which enables a preferred type II lamellar stacking and thus an enhanced conductivity. A high dielectric constant and a low pK_a-value in combination seem to result in an effective separation and structural reorientation of PEDOT and PSS, followed by an efficient removal of insulating PSS.

For treatments that yield a low PSS content, a subsequent H_2O washing seems to be unfavorable for the morphology. The strongest impact is seen for the H_2SO_4-treated sample after washing, which shows a destroyed order of the lamellar stacking in combination with the reduced oriented PSS π–π stacking. In addition, the type II lamellar stacking is reduced and an additional shoulder appears at lower q-values, indicating an overall reduced crystallinity. However, XPS measurements indicate a residual amount of sulfuric acid in the non-washed H_2SO_4-treated films that vanishes after H_2O-washing. Therefore, an intercalation of HSO_4^--ions cannot be excluded, which might lead to a replacement of the PSS counter-ion and enables an enhanced Coulomb screening between PEDOT and PSS chains. Thus, the enhanced chain mobility could lead to an improved order of lamellar stacking and might lead to an enhanced conductivity. Subsequent H_2O-washing seems to destroy this order, which could be related to an extraction of residual H_2SO_4 content in this case.

7.6.5 Morphological Model

The obtained findings are summarized in a morphological model and depicted in Figure 7.16 to describe the underlying processes. It was found, the more efficient packed lamellar stacking type II for PEDOT:PSS (Figure 7.14b) is adjuvant for an enhanced conductivity. Furthermore, this type has a preferred order in the face-on direction, which increases the amount of edge-on oriented PEDOT π–π stacking. In addition, the applied treatments show a variation in the PSS extraction, which is favorable for an increased conductivity. The morphological model in Figure 7.16 depicts the overall enhanced number and edge-on orientation of PEDOT-rich domains (red rods) together with a reduced film thickness (height of each framed box), which originates from excess PSS removal (reduced saturation of excess PSS). The enhanced order of PEDOT-rich domains is reversed for HNO_3- and H_2SO_4-treatments after H_2O-washing, as depicted by the increasingly randomized orientation. The illustration of H_2O-washed HCOOH samples is in this case neglected as the obtained data suggest no structural change and therefore a high resistance against H_2O, comparable to the HCl treatment.

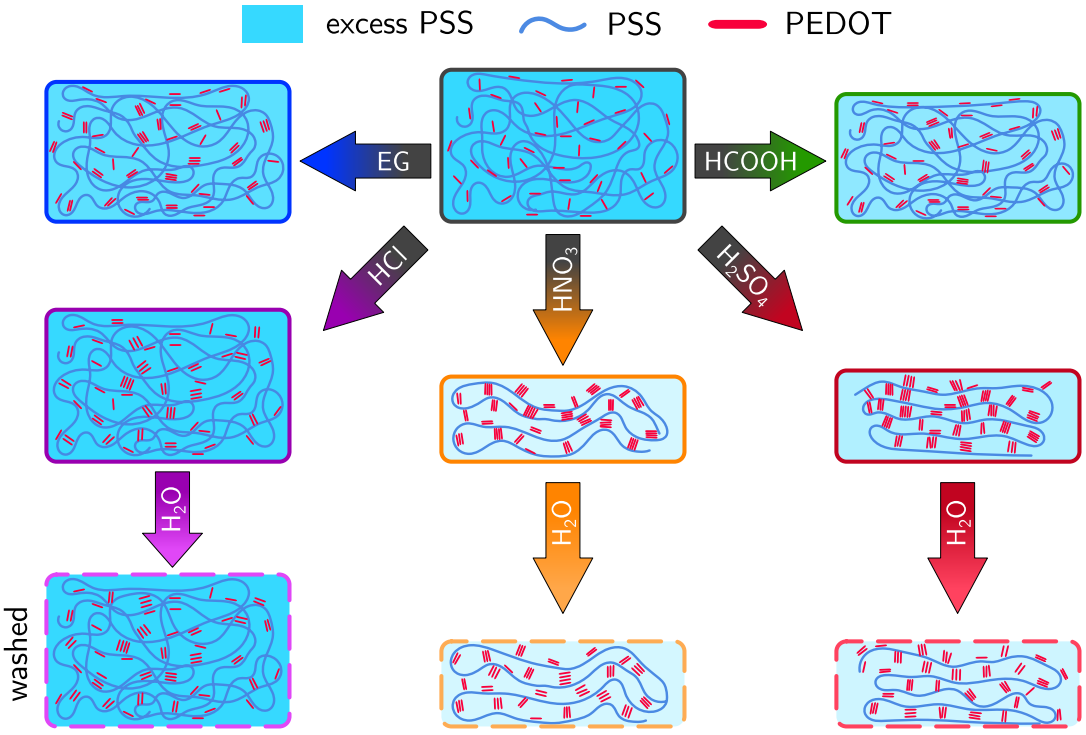

Figure 7.16
Structural model of PEDOT-rich domains in thin films. Thickness decrease and reduced excess PSS content is depicted in reduced height of framed boxes and fading of the light blue colored excess PSS matrix. Enhanced PEDOT π–π stacking is taken into account by an increased size and order of PEDOT-rich domains, while the improved lamellar stacking is depicted with an increased order along the PSS chains. Adapted with permission from John Wiley & Sons, Copyright 2019.[30]

7.7 Device Integration

The previous investigations have shown that a highly conducting polymeric electrode can be achieved by applying an acid treatment on PEDOT:PSS thin films. In order to examine the electrode performance in real devices, two representative treatments were selected to proof their application in a working ITO-free OLED. Namely, H_2SO_4 and HCOOH treatment were chosen as they achieved the highest conductivity values and the best H_2O resistance, respectively and were compared to a standard device using ITO electrodes. OLED test devices were fabricated and investigated in the frame of the Bachelor's thesis of Lina Maria Todenhagen.[177] The devices were fabricated according to Section 3.5 with two layers of subsequently spin coated PEDOT:PSS PH1000. Before deposition of the HTL and the emitting layer the corresponding treatment was performed and the electrodes were patterned. In Figure 7.17, some fabricated ITO-free OLED devices are exemplarily depicted together with a PEDOT:PSS electrode. Figure 7.17d shows an OLED in operation with the typical yellow-greenish color of

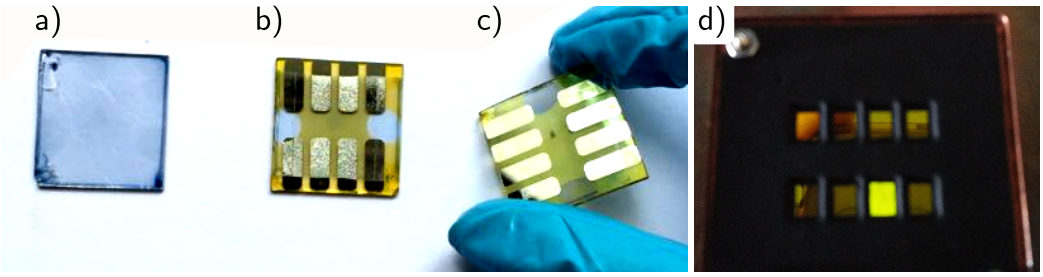

Figure 7.17
Images of a) acid post-treated PEDOT:PSS electrode and ITO-free OLEDs b) with and c) without degradation effects on the evaporated contacts.[177] d) OLED device under operation with one of eight active pixel.

the SUPER YELLOW® emitter, proving the successful implementation of the electrode. The obtained OLEDs were investigated regarding their current-voltage as well as their emission characteristics and power conversion efficiency employing a custom made measurement setup introduced in Section 4.5. The used setup is capable to characterize the angular dependent and total light emission as well as determining the electrical characteristics of OLEDs.

In Figure 7.18a, exemplary IV-curves of the fabricated OLEDs are depicted. The typical diode-like behavior already indicates a proper working device. However, the most obvious difference is the decreased slope for the OLEDs using PEDOT:PSS electrodes. This reduced slope is typically explained with the higher sheet resistance and the smaller conductivity of the polymeric electrodes compared to the ITO electrode of the reference device.[16,203] Therefore, an increased ohmic contribution in the device, e.g., a serial resistance, is concluded for OLEDs with H_2SO_4 and HCOOH treated electrodes. Furthermore, a slight shift of the onset voltage U_{bi} towards smaller values is visible, indicating a reduced work function for the electrodes. This is in agreement with the often reported modification of the PEDOT:PSS work function via various (post-)treatments that lead to a reduced PSS content.[15,131,172,204] The shift in the onset voltage becomes more evident by determining and averaging U_{bi} for several devices. For this purpose, the linear region of the current-voltage characteristics was fitted and extrapolated to $J = 0\,\mathrm{mA\,cm^{-2}}$. The intersection with the voltage axis yields U_{bi}, which are depicted in Figure 7.18c and showing a clear decrease in the onset voltage for devices powered with polymeric electrodes. Therefore, the acid treatment of the PEDOT:PSS electrodes and the resulting PSS extraction yields a modified work function for the anode, which becomes apparent in a reduced work function difference of the anode to the aluminum cathode and therefore a reduced built-in voltage U_{bi}.[166,204,205] The downside of this decrease is the increased energy barrier from the electrode to the hole transport and electron blocking layer, which is in this case PEDOT:PSS Al4083. Therefore, the charge carrier injection into the emission layer (PDY-132) is limited which reduces the overall diode current and leads to a decreased slope in the IV-curve as seen in Figure 7.18a.

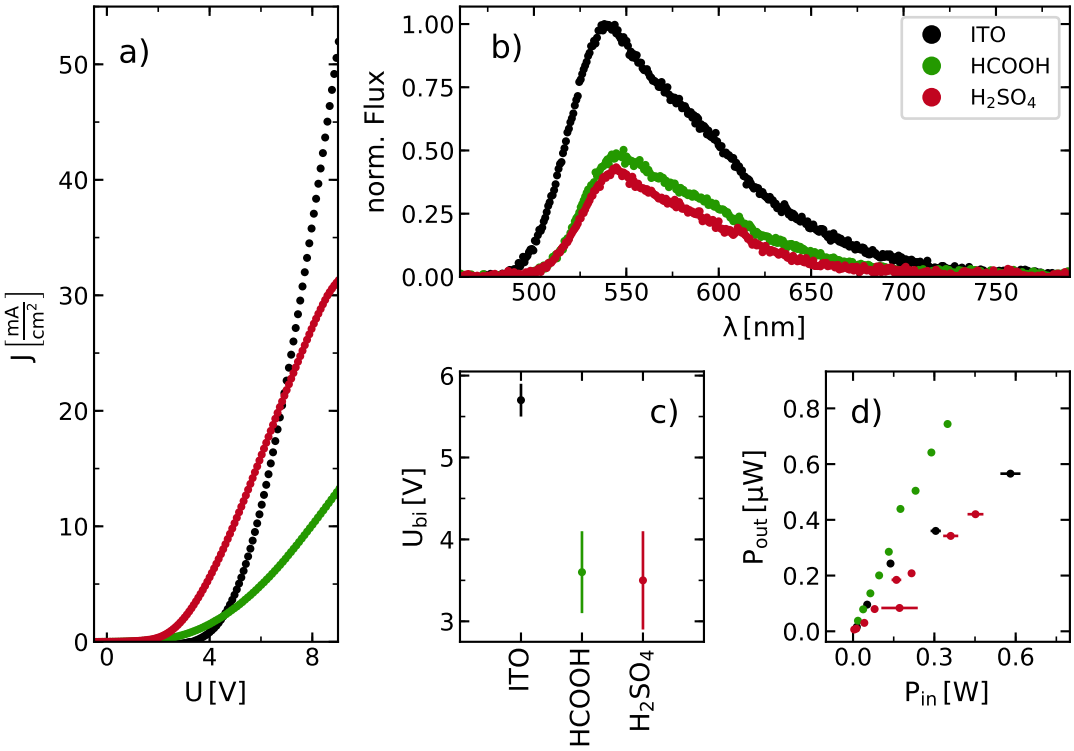

Figure 7.18
Characterization of OLED devices with selected high conducting PEDOT:PSS electrodes fabricated with HCOOH- (green) and H_2SO_4-treatment (red). a) Exemplary IV-curves of OLEDs, showing typical diode-like behavior. b) Emission spectra of corresponding OLEDs at 12 V; values are normalized to peak emission of reference OLED (black). c) From diode curves extracted built-in voltage U_{bi} of OLEDs with different electrodes. d) Integrated light emission power P_{out} versus electrical power consumption P_{in} of OLEDs with ITO reference electrode (black), HCOOH-treated (green) and H_2SO_4-treated (red) PEDOT:PSS electrodes.

This becomes visible in the light emission characteristics of the selected OLEDs, which are plotted in Figure 7.18b for an identical operating voltage of 12 V. The wavelength dependent light emission is normalized to the peak emission of the reference ITO device (black). As already indicated by the IV-curves, the light emission for the polymeric electrode devices is smaller than for the reference one. However, the shape of the emission spectra is maintained, indicating no acidic treatment induced modification of the emitter material by potential acid residuals in the film. For all samples the peak emission is maintained at $\lambda \approx 540$ nm corresponding $E_g \approx 2.3$ eV, which matches well the band gap of the used emitter. Furthermore, the integrated total emission of the OLEDs using HCOOH- and H_2SO_4-treated electrodes still reaches 52.7 % and 42.3 % of the reference device, respectively. This is especially impressive as the devices only serve as proof of principle and have not been optimized. Kim et al. showed the efficiency of ITO-free OLEDs, based on PEDOT:PSS electrodes

with a lower conductivity than examined here, can reach the performance of reference ITO devices via proper layer thickness optimization.[206] The above mentioned opposed effects of the lowered work function and increased injection barrier in combination with the lower conductivity might lead to the reduced but similar emission for both treatments. Therefore, the higher PSS content for HCOOH treated electrodes leads to a lower conductivity compared to H_2SO_4 treated ones. In combination with the presumed smaller injection barrier to the HTL for HCOOH treatment (due to the higher PSS content), those effects might cancel out and lead to a very similar emission for HCOOH and H_2SO_4 treated electrodes.

Furthermore, taking a look to the devices' power consumption and emission, both PEDOT:PSS devices perform quite well compared to the reference one. In Figure 7.18d the total power of light emission P_{out} is compared to the consumed electrical power P_{in}. The consumed electrical power is calculated from the applied voltage and the measured current density through the device. The total light emission is obtained by measuring the emission spectra with an integrating sphere according to Section 4.5. The obtained wavelength dependent radiant flux $\Phi_{e,\lambda}$ is then integrated in the range of 450 nm – 770 nm in order to get the total radiant flux Φ_e. Interestingly, the H_2SO_4 treated sample shows a very similar behavior as the reference device. This is probably related to the higher contribution of an ohmic resistor for the H_2SO_4 device, which is visible in the decreased slope in Figure 7.18a. Therefore, the current flow and thus the power consumption is reduced, but a presumed enhanced charge carrier injection might overcome this limitation and lead to a similar light emission as for the reference device. This becomes more evident for the HCOOH treated sample. Despite the strongly reduced slope in the diode curve, revealing a less ideal diode behavior compared to the reference, the light emission is still comparable high. This can be explained with the reduced conductivity of the HCOOH treated electrode, which gives a stronger ohmic contribution and reduces the current flow through the device. In combination with the presumably enhanced charge carrier injection, caused by the lower energy barrier due to the higher PSS content compared to the H_2SO_4 treated device, the power consumption is reduced. Thus, despite the lower current flow through the diode, the charge carrier injection and therefore the light emitting recombination in the emitter is more efficient. Hence, the HCOOH treated sample might not reach the brightness of comparable electrodes such as the reference ITO device, but allows a more efficient device operation.

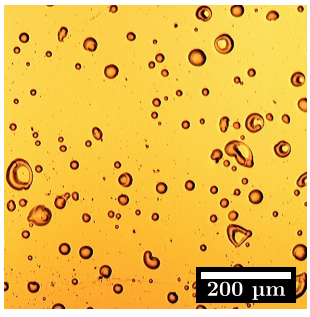

Figure 7.19
Defects on aluminum contacts of H_2SO_4 treated OLED (optical microscope).

Furthermore, it is noteworthy to mention that for long storage times the fabricated OLEDs revealed typical indications for device degradation. As depicted in Figure 7.17b and Figure 7.19, the evaporated aluminum

electrodes show defects most probably caused by aluminum oxidation that reduces the device performance.[207,208] This effect is enhanced during device operation, especially for the H_2SO_4 treated device and leads together with degradation of the functional layers eventually to device failure.[209] However, encapsulation could eliminate most of these degradation processes.

Overall, the obtained device efficiency stays behind its potential. Comparable ITO-free OLED devices achieved up to 90 % of the reference device efficiency.[203] In combination with additional functional layers such as silver nano-wires[14,16] or scattering layers,[203] even higher efficiencies were achieved. In any case, the obtained results clearly show the potential application of the here examined PEDOT:PSS electrodes in ITO-free devices. By implementing a full device stack, including ETL and HBL between the emitter and the evaporated electrode and further layer thickness optimization, efficiencies comparable to ITO-based OLEDs are expected. Taking into account suitable scattering layers, such as discussed in Chapter 5, the EQE of ITO-free devices could even exceed the performance of commonly ITO-based OLEDs.

7.8 Summary

In this chapter, the origin of the conductivity improvement of PEDOT:PSS thin films upon treatments with different weak and strong acids (organic and inorganic) was investigated. The impact of ethylene glycol, hydrochloric acid, formic acid, nitric acid, and sulfuric acid post-treatment on PEDOT:PSS thin films was studied, including their stability against subsequent H_2O-washing. The morphology and compositional changes of PEDOT and PSS were linked to the DC conductivity of probed thin films and were summarized in a morphological model in Figure 7.16. A significantly enhanced conductivity of $(1128 \pm 91)\,\mathrm{S\,cm^{-1}}$ for EG, $(392 \pm 29)\,\mathrm{S\,cm^{-1}}$ for HCl, $(1289 \pm 73)\,\mathrm{S\,cm^{-1}}$ for HCOOH, $(2099 \pm 143)\,\mathrm{S\,cm^{-1}}$ for HNO_3, and $(2938 \pm 325)\,\mathrm{S\,cm^{-1}}$ for H_2SO_4 treated samples was found. Furthermore, the AC response of selected electrodes was examined with impedance spectroscopy, revealing a promising potential for the high conducting samples fabricated with EG, HCOOH and H_2SO_4 treatment. The pristine PEDOT:PSS reference sample showed a capacitive behavior due to the high PSS content. The other investigated samples revealed low inductance combined with the already determined DC resistance. Overall, no phase shift and therefore no increased impedance was observed for frequencies <100 kHz, which allows in principle the application for AC powered devices such as OFETs in the given frequency range. The increased conductivity goes along with an increased absorbance in the near infrared region, indicating an increased charge carrier concentration. The FoM, which serves as a measure for the performance of a transparent electrode, was greatly enhanced for the different treatments. Over the whole range of visible light, the FoM was continuously above FoM > 40 with a peak value of $\mathrm{FoM}(\lambda = 425\,\mathrm{nm}) = 150$ for H_2SO_4-treatment. Therefore, the H_2SO_4-treated sample is considered to perform best as transparent elec-

trode, especially for blue emitting devices. The improved conductivity for the different treatments was attributed to several mechanisms in the thin films. Compositional XPS measurements showed a strongly reduced PSS content for HNO_3- and H_2SO_4-treatments, which goes along with their enhanced conductivity. Furthermore, a shift towards smaller binding energies of the PSS' sulfone group was observed, indicating an increased protonation of the SO_3^--group. Thus, a facilitated phase separation of PEDOT and PSS domains leads to efficient extraction of excess PSS due to diminished Coulomb screening. The interplay of reduced PSS content in combination with a structural rearrangement of the PEDOT-rich domains, which yields a high degree of order, was found to be beneficial for enhanced conductivity. Additionally, the lamellar stacking of alternating PEDOT and PSS chains was identified to be a crucial parameter for an enhanced in-plane conductivity, preferring the more efficient and more densely packed lamellar stacking type II (Figure 7.14). This stacking type provides a high content of edge-on oriented PEDOT π–π stacking due to the preferentially oriented lamellar stacking in q_z-direction, which is favorable for in-plane conductivity. The enhanced conductivity caused by a morphological and compositional change was linked to the electric screening behavior and the dissociation constant of the used acids. High dielectric constants enable efficient Coulomb screening and structural optimization of PEDOT-rich domains, which strong acids can support by protonation of charged sulfonate groups in PSS. In combination, a high PSS extraction yield can be achieved for the HNO_3- and H_2SO_4-treatments. However, in this case, a high water sensitivity is present, while treatments with less efficient PSS removal exhibit a good stability against H_2O, e.g., for HCl- and HCOOH-treatments. Concerning applications the sensitivity against water is causing several problems, which makes treatments that result in more stable and well conducting PEDOT:PSS films very appealing.

In order to test the highly conducting polymeric electrodes obtained by the different treatments under working conditions, the most promising ones were implemented into an ITO-free reference device OLED stack. Overall, the performance of the obtained devices powered by a HCOOH- and H_2SO_4-treated PEDOT:PSS electrode performed similar to the ITO equipped reference device. Despite the reduced light emission, mainly caused by the non-optimized layer stack and the lower conductivity, the HCOOH-treated electrode device revealed a lower energy consumption compared to the H_2SO_4 device. In summary, the proof of principle of a working ITO-free device with the investigated PEDOT:PSS electrodes was confirmed.

CHAPTER 8

Conclusion & Outlook

An essential factor for the limitation of the external quantum efficiency in OLED devices is originated in substrate and organic modes. Those are related to the refractive indices of the used materials and the thin film geometry of the devices, causing a 2D wave guiding effect for photons. The main task addressed in the present work was the development of functional layers that can be implemented into ITO-free OLED devices in order to reduce the internal total reflection and thus increase the photon outcoupling efficiency. A further requirement was a potentially large scale application, which was realized via the use of the spray deposition technique. Therefore, in the first place, an instrument was constructed in order to determine the angular and wavelength dependent scattering of ZnO thin films and the emission characteristics of OLED devices, respectively. Consequently, the constructed instrument was used in the frame of this work to evaluate the performance of fabricated devices. In the course of this work it turned out to be reasonable to replace the commonly used ITO electrode in OLED devices with PEDOT:PSS polymeric electrodes. By this, both investigated functional layers, the ZnO scattering layer and the PEDOT:PSS polymeric electrode, can be cast from solution via spray deposition, which was successfully tested. The two required functional layers were investigated regarding their optical and electronic response which was linked to their thin film morphology.

Nanostructured ZnO thin films were successfully fabricated via spray deposition. Structuring of the scattering layer was realized by diblock copolymer assisted sol-gel synthesis based on PS-*b*-PEO and the ZnO precursor ZAD. The obtained layers showed a strong diffuse scattering in the visible region of light, which was mainly addressed to the high surface roughness caused by the used deposition and calcination techniques. Hierarchically structured films were obtained by the implementation of additional PS

microspheres during the sol-gel process. The presence of large microspheres (⌀ 500 nm) resulted in an additional templating effect during film formation. The PS microspheres were embedded into the nanoporous network formed by the sol-gel process and were combusted together with the templating diblock copolymer via subsequent calcination. Consequently, a hierarchically structured thin film was obtained, consisting of a nanoporous ZnO network with embedded large sized pores. Moreover, addition of an excess homopolymer supply to the diblock copolymer in the form of PS microspheres resulted in selective swelling of the PS block. As a consequence, the nanoporous ZnO network revealed a slightly enhanced pore size caused by the swelling of the inner micellar core during the sol-gel process. The scattering ability of visible light was slightly enhanced with increasing microsphere concentration, while the surface roughness was not altered significantly. Even though the high roughness of the scattering layer was found to strongly contribute to the scattering, the implementation of additional scattering centers had obviously a beneficial effect on the diffuse scattering. Furthermore, no color shift was observable, which suggest such layers as suitable for enhancing the light extraction of white OLEDs. Towards the fabrication of an OLED with such a scattering layer implemented, the polymeric electrode PEDOT:PSS was chosen and deposited via spray coating on the rough ZnO layer. The scattering layer was homogeneously coated with the polymer whereas the macroscopic surface roughness was preserved. Even though a conductive ZnO/PEDOT:PSS scattering bilayer was obtained, the conductivity stayed behind its potential and had to be further enhanced.

Organic layer typically suffer under device degradation which is related to their sensitivity towards water and oxygen. Thus, before assembling a full OLED, it is reasonable to examine the PEDOT:PSS electrode in more detail to identify potential failure mechanisms. The influence of high humidity was tested in situ on pristine films and commonly treatments based on Zonyl or EG that both influence the morphology and the PSS content in the final films. It was found that the polymeric electrodes were highly sensitive towards water vapor. Their sensitivity is based on the hygroscopic PSS component which led to absorption of water molecules from the atmosphere. As a consequence, film swelling of more than the doubled thickness of the initial film was observed and enrichment layers of PEDOT and PSS at the substrate/air and film/air interface, respectively were clearly identified. The swelling was expected to be detrimental for device failure and therefore should be reduced. In addition, it was suggest that the absorption of water increases the sheet resistance in the films by increasing the inter-domain distances of highly conducting PEDOT crystallites, which is expected to be the most limiting factor for the electrodes conductivity. An irreversible effect of the reduced conductivity was assumed to be related to a morphological rearrangement of those PEDOT-rich domains that were embedded in the insulating PSS matrix. As a consequence, a reduced excess PSS content in the final film has two advantageous effects. Firstly, by extracting the insulating PSS component, the inter-domain distances of PEDOT-rich domains was reduced and thus the charge carrier transport between

those domains was facilitated. Secondly, the extraction of the hygroscopic PSS further reduced the water sensitivity significantly, as less hydrohpilic groups are present in the film. Thus, the overall water sorption was reduced and the diffusion of water molecules into the film was hindered, which is both beneficial for the device operation and lifetime.

Since the excess PSS amount in PEDOT:PSS was identified as limiting factor for the thin films conductivity, more efficient extraction methods were investigated. Hence, several weak and strong acids (organic and inorganic) were tested upon their PSS extraction capabilities, which was linked to the acid's strength (dissipation constant) and dielectric constant. The reduced PSS content in turn led to a compact lamellar stacking of alternating PEDOT and PSS chains that resulted in increased crystallinity and enhanced order of the conducting PEDOT-rich domains. As a consequence, enlarged PEDOT crystallites were highly oriented with reduced inter-domain distance in a drained PSS matrix, which in total facilitates charge transport between those domains. Among the investigated treatments, H_2SO_4 performed best regarding an enhanced order and the resulting increased conductivity. However, subsequently washing in water led to partly reversal of the beneficial structure and destroyed the high order of PEDOT crystallites which proofed the strong effect of morphology to a high conductivity. Contrary, weaker acids showed a tremendous resilience against water. For example, HCOOH treated PEDOT:PSS showed almost no change after excessive washing in water, neither in the morphology, nor in conductivity. As a consequence, a high stability of the polymeric electrode can be achieved for the sake of a limited maximum conductivity. The best performing treatments regarding high conductivity and high stability were used to successfully fabricate ITO-free OLEDs on the base of PEDOT:PSS polymeric electrodes. The H_2SO_4 treated PEDOT:PSS showed a comparable behavior to the ITO based reference cell, as the polymer electrode reached a similar conductivity as ITO. However, among the different devices, the very stable HCOOH treated films revealed the best stability of the fabricated OLEDs.

The present work shall serve as a guidance towards the full implementation of rough metal oxide scattering layers into OLED devices. The necessary requirements and characterizations were discussed in the different chapters of this thesis. Based on the results obtained in the present work, the combination of a hierarchically structured ZnO layer with a PEDOT:PSS polymeric electrode is considered as very suitable for enhancing the photon extraction yield of common OLED devices. Furthermore, large scaled fabrication techniques allow the fabrication of such bilayers from solution. While spray coating was used in the present work, roll-to-roll printing is as well considered as suitable. In order to achieve competitive device efficiencies, the layer stack has to be further optimized and improved. Since in the present work a standard device stack based on a singlet emitter is applied, it is reasonable to further examine the investigated layers in a triplet emitter system to elaborate the full potential of the scattering/electrode bilayer in an OLED device. In general, encapsulation is consid-

ered as highly recommended to avoid degradation effects of the organic layers. This might reduce the water sensitivity of the used polymeric electrodes and provide higher device stability. Furthermore, it might enable the usage of PEDOT:PSS electrodes obtained from the highly conducting but less stable treatments, such as H_2SO_4. However, measurements indicate, the residual acidity of such electrodes caused by the respective treatment might lead to oxidation effects in adjacent layers, which might reduce the lifetime in the full device stack and should be further investigated. Considering PEDOT:PSS electrodes, very high conductivities can be achieved for the sake of a reduced stability against H_2O. Overall, the fundamental findings of this thesis regarding ZnO/PEDOT:PSS bilayers and the role of PSS towards the conductivity in PEDOT:PSS electrodes together with the discussed characterization methods and data evaluation can help in future research activities.

Bibliography

[1] J. Bardeen and W. H. Brattain. "The Transistor, A Semi-Conductor Triode". In: *Physical Review* 74 (2 July 1948), pp. 230–231. DOI: 10.1103/PhysRev.74.230.

[2] C. K. Chiang, C. R. Fincher, Y. W. Park, A. J. Heeger, H. Shirakawa, E. J. Louis, S. C. Gau, and Alan G. MacDiarmid. "Electrical Conductivity in Doped Polyacetylene". In: *Physical Review Letters* 39 (17 Oct. 1977), pp. 1098–1101. DOI: 10.1103/PhysRevLett.39.1098.

[3] M. Pope, H. P. Kallmann, and P. Magnante. "Electroluminescence in Organic Crystals". In: *The Journal of Chemical Physics* 38.8 (1963), pp. 2042–2043. DOI: 10.1063/1.1733929.

[4] W. Helfrich and W. G. Schneider. "Recombination Radiation in Anthracene Crystals". In: *Physical Review Letters* 14 (7 Feb. 1965), pp. 229–231. DOI: 10.1103/PhysRevLett.14.229.

[5] C. W. Tang and S. A. VanSlyke. "Organic electroluminescent diodes". In: *Applied Physics Letters* 51.12 (1987), pp. 913–915. DOI: 10.1063/1.98799.

[6] Yoo-Yong Lee, Ho-Young Kang, Seok Hyeon Gwon, Gwang Mook Choi, Seung-Min Lim, Jeong-Yun Sun, and Young-Chang Joo. "A Strain-Insensitive Stretchable Electronic Conductor: PEDOT:PSS/Acrylamide Organogels". In: *Advanced Materials* 28.8 (2016), pp. 1636–1643. DOI: 10.1002/adma.201504606.

[7] David McCoul, Weili Hu, Mengmeng Gao, Vishrut Mehta, and Qibing Pei. "Recent Advances in Stretchable and Transparent Electronic Materials". In: *Advanced Electronic Materials* 2.5 (2016). 1500407, p. 1500407. DOI: 10.1002/aelm.201500407.

[8] Jianyong Ouyang. "Solution-Processed PEDOT:PSS Films with Conductivities as Indium Tin Oxide through a Treatment with Mild and Weak Organic Acids". In: *ACS Applied Materials & Interfaces* 5.24 (2013), pp. 13082–13088. DOI: 10.1021/am404113n.

[9] Michael Vosgueritchian, Darren J. Lipomi, and Zhenan Bao. "Highly Conductive and Transparent PEDOT:PSS Films with a Fluorosurfactant for Stretchable and Flexible Transparent Electrodes". In: *Advanced Functional Materials* 22.2 (2012), pp. 421–428. DOI: 10.1002/adfm.201101775.

[10] Jin Young Oh, Minkwan Shin, Jae Bok Lee, Jong-Hyun Ahn, Hong Koo Baik, and Unyong Jeong. "Effect of PEDOT Nanofibril Networks on the Conductivity, Flexibility, and Coatability of PEDOT:PSS Films". In: *ACS Applied Materials & Interfaces* 6.9 (2014). PMID: 24713072, pp. 6954–6961. DOI: 10.1021/am500769k.

[11] Xu Huang, Kai Wang, Chao Yi, Tianyu Meng, and Xiong Gong. "Efficient Perovskite Hybrid Solar Cells by Highly Electrical Conductive PEDOT:PSS Hole Transport Layer". In: *Advanced Energy Materials* 6.3 (2016). 1501773, p. 1501773. DOI: 10.1002/aenm.201501773.

[12] Jennifer R. Moore, Sebastian Albert-Seifried, Akshay Rao, Sylvain Massip, Benjamin Watts, David J. Morgan, Richard H. Friend, Christopher R. McNeill, and Henning Sirringhaus. "Polymer Blend Solar Cells Based on a High-Mobility Naphthalenediimide-Based Polymer Acceptor: Device Physics, Photophysics and Morphology". In: *Advanced Energy Materials* 1.2 (Feb. 15, 2011), pp. 230–240. DOI: 10.1002/aenm.201000035.

[13] Katherine A. Mazzio and Christine K. Luscombe. "The future of organic photovoltaics". In: *Chemical Society Reviews* 44 (1 2015), pp. 78–90. DOI: 10.1039/C4CS00227J.

[14] Whitney Gaynor, Simone Hofmann, M. Greyson Christoforo, Christoph Sachse, Saahil Mehra, Alberto Salleo, Michael D. McGehee, Malte C. Gather, Björn Lüssem, Lars Müller-Meskamp, Peter Peumans, and Karl Leo. "Color in the Corners: ITO-Free White OLEDs with Angular Color Stability". In: *Advanced Materials* 25.29 (May 2013), pp. 4006–4013. DOI: 10.1002/adma.201300923.

[15] F. L. E. Jakobsson, X. Crispin, L. Lindell, A. Kanciurzewska, M. Fahlman, W. R. Salaneck, and M. Berggren. "Towards all-plastic flexible light emitting diodes". In: *Chemical Physics Letters* 433.1 (2006), pp. 110–114. DOI: 10.1016/j.cplett.2006.11.007.

[16] Yilin Xu, Xiang Wei, Cong Wang, Jin Cao, Yigang Chen, Zhongquan Ma, Ying You, Jixiang Wan, Xiaohong Fang, and Xiaoyuan Chen. "Silver Nanowires Modified with PEDOT:PSS and Graphene for Organic Light-Emitting Diodes Anode". In: *Scientific Reports* 7 (Mar. 28, 2017), p. 45392. DOI: 10.1038/srep45392.

[17] Tae-Hee Han, Youngbin Lee, Mi-Ri Choi, Seong-Hoon Woo, Sang-Hoon Bae, Byung Hee Hong, Jong-Hyun Ahn, and Tae-Woo Lee. "Extremely efficient flexible organic light-emitting diodes with modified graphene anode". In: *Nature Photonics* 6 (Jan. 2012), p. 105. DOI: 10.1038/nphoton.2011.318.

[18] Zhaoyang Liu, Khaled Parvez, Rongjin Li, Renhao Dong, Xinliang Feng, and Klaus Müllen. "Transparent Conductive Electrodes from Graphene/PEDOT:PSS Hybrid Inks for Ultrathin Organic Photodetectors". In: *Advanced Materials* 27.4 (2015), pp. 669–675. DOI: 10.1002/adma.201403826.

[19] Jean-Pierre Veder, Roland De Marco, Graeme Clarke, San Ping Jiang, Kathryn Prince, Erno Pretsch, and Eric Bakker. "Water uptake in the hydrophilic poly(3,4-ethylenedioxythiophene):poly(styrene sulfonate) solid-contact of all-solid-state polymeric ion-selective electrodes". In: *Analyst* 136 (16 2011), pp. 3252–3258. DOI: 10.1039/C1AN15267J.

[20] Nitin Saxena, Josef Keilhofer, Anjani K. Maurya, Giuseppino Fortunato, Jan Overbeck, and Peter Müller-Buschbaum. "Facile Optimization of Thermoelectric Properties in PEDOT:PSS Thin Films through Acido-Base and Redox Dedoping Using Readily Available Salts". In: *ACS Applied Energy Materials* 1.2 (2018), pp. 336–342. DOI: 10.1021/acsaem.7b00334.

[21] Eun Jin Bae, Young Hun Kang, Kwang-Suk Jang, and Song Yun Cho. "Enhancement of Thermoelectric Properties of PEDOT:PSS and Tellurium-PEDOT:PSS Hybrid Composites by Simple Chemical Treatment". In: *Scientific Reports* 6 (Jan. 2016), p. 18805. DOI: 10.1038/srep18805.

[22] Seung Hwan Lee, Hongkwan Park, Soyeon Kim, Woohyun Son, In Woo Cheong, and Jung Hyun Kim. "Transparent and flexible organic semiconductor nanofilms with enhanced thermoelectric efficiency". In: *Journal of Materials Chemistry A* 2 (20 2014), pp. 7288–7294. DOI: 10.1039/C4TA00700J.

[23] Olga Bubnova and Xavier Crispin. "Towards polymer-based organic thermoelectric generators". In: *Energy & Environmental Science* 5 (11 2012), pp. 9345–9362. DOI: 10.1039/C2EE22777K.

[24] M. A. Baldo, D. F. O'Brien, Y. You, A. Shoustikov, S. Sibley, M. E. Thompson, and S. R. Forrest. "Highly efficient phosphorescent emission from organic electroluminescent devices". In: *Nature* 395.6698 (Sept. 1998), pp. 151–154. DOI: 10.1038/25954.

[25] Hong-Wei Chang, Jonghee Lee, Simone Hofmann, Yong Hyun Kim, Lars Müller-Meskamp, Björn Lüssem, Chung-Chih Wu, Karl Leo, and Malte C. Gather. "Nano-particle based scattering layers for optical efficiency enhancement of organic light-emitting diodes and organic solar cells". In: *Journal of Applied Physics* 113.20, 204502 (2013), p. 204502. DOI: 10.1063/1.4807000.

[26] S. Möller and S. R. Forrest. "Improved light out-coupling in organic light emitting diodes employing ordered microlens arrays". In: *Journal of Applied Physics* 91.5 (2002), pp. 3324–3327. DOI: 10.1063/1.1435422.

[27] Yiru Sun and Stephen R. Forrest. "Organic light emitting devices with enhanced outcoupling via microlenses fabricated by imprint lithography". In: *Journal of Applied Physics* 100.7, 073106 (2006), p. 073106. DOI: 10.1063/1.2356904.

[28] Yiru Sun and Stephen R. Forrest. "Enhanced light out-coupling of organic light-emitting devices using embedded low-index grids". In: *Nature Photonics* 2.8 (Aug. 2008), pp. 483–487. DOI: 10.1038/nphoton.2008.132.

[29] Lorenz Bießmann, Lucas Philipp Kreuzer, Tobias Widmann, Nuri Hohn, Jean-François Moulin, and Peter Müller-Buschbaum. "Monitoring the Swelling Behavior of PEDOT:PSS Electrodes under High Humidity Conditions". In: *ACS Applied Materials & Interfaces* 10.11 (2018). PMID: 29484879, pp. 9865–9872. DOI: 10.1021/acsami.8b00446.

[30] Lorenz Bießmann, Nitin Saxena, Nuri Hohn, Md Asjad Hossain, Jonathan G. C. Veinot, and Peter Müller-Buschbaum. "Highly Conducting, Transparent PEDOT:PSS Polymer Electrodes from Post-Treatment with Weak and Strong Acids". In: *Advanced Electronic Materials* 5.2 (Jan. 3, 2019), p. 1800654. DOI: 10.1002/aelm.201800654.

[31] Gert R. Strobl. *The Physics of Polymers: Concepts for Understanding Their Structures and Behavior*. Springer, 2007.

[32] Paul J. Flory. "Thermodynamics of High Polymer Solutions". In: *The Journal of Chemical Physics* 10.1 (1942), pp. 51–61. DOI: 10.1063/1.1723621.

[33] Maurice L. Huggins. "Thermodynamic Properties of Solutions of Long-Chain Compounds". In: *Annals of the New York Academy of Sciences* 43.1 (1942), pp. 1–32. DOI: 10.1111/j.1749-6632.1942.tb47940.x.

[34] Ludwik Leibler. "Theory of Microphase Separation in Block Copolymers". In: *Macromolecules* 13.6 (1980), pp. 1602–1617. DOI: 10.1021/ma60078a047.

[35] Frank S. Bates and Glenn H. Fredrickson. "Block Copolymer Thermodynamics: Theory and Experiment". In: *Annual Review of Physical Chemistry* 41.1 (1990). PMID: 20462355, pp. 525–557. DOI: 10.1146/annurev.pc.41.100190.002521.

[36] K. Binder. "Phase Transitions of Polymer Blends and Block Copolymer Melts in Thin Films". In: *Polymers in Confined Environments*. Ed. by S. Granick, K. Binder, P.-G. de Gennes, E. P. Giannelis, G. S. Grest, H. Hervet, R. Krishnamoorti, L. Léger, E. Manias, E. Raphaël, and S.-Q. Wang. Berlin, Heidelberg: Springer Berlin Heidelberg, 1999, pp. 1–89. DOI: 10.1007/3-540-69711-X_1.

[37] M. Christopher Orilall and Ulrich Wiesner. "Block copolymer based composition and morphology control in nanostructured hybrid materials for energy conversion and storage: solar cells, batteries, and fuel cells". In: *Chemical Society Reviews* 40 (2 2011), pp. 520–535. DOI: 10.1039/C0CS00034E.

[38] Y.-J. Cheng and J. S. Gutmann. “Morphology phase diagram of ultrathin anatase TiO2 films templated by a single PS-b-PEO block copolymer”. English. In: *Journal of the American Chemical Society* 128.14 (2006), pp. 4658–4674. DOI: 10.1021/ja0562853.

[39] Kuhu Sarkar, Monika Rawolle, Eva M. Herzig, Weijia Wang, Adeline Buffet, Stephan V. Roth, and Peter Müller-Buschbaum. “Custom-Made Morphologies of ZnO Nanostructured Films Templated by a Poly(styrene-block-ethylene oxide) Diblock Copolymer Obtained by a Sol–Gel Technique”. In: *ChemSusChem* 6.8 (2013), pp. 1414–1424. DOI: 10.1002/cssc.201300291.

[40] Monika Rawolle. “Structuring and Filling of Titania Films for Applications in Photovoltaics”. PhD thesis. Technische Universität München, 2013.

[41] Martin A. Niedermeier. “Novel structuring routines of titania films for application in photovoltaics”. PhD thesis. München: Technische Universität München, 2013.

[42] Patrick Lim Soo and Adi Eisenberg. “Preparation of block copolymer vesicles in solution”. In: *Journal of Polymer Science Part B: Polymer Physics* 42.6 (2004), pp. 923–938. DOI: 10.1002/polb.10739.

[43] M. Rivallin, M. Benmami, A. Gaunand, and A. Kanaev. “Temperature dependence of the titanium oxide sols precipitation kinetics in the sol–gel process”. In: *Chemical Physics Letters* 398.1 (2004), pp. 157–162. DOI: 10.1016/j.cplett.2004.09.046.

[44] Lin Song. “Tailoring titania photoanodes for application in solid-state dye-sensitized solar cells and hybrid solar cells”. PhD thesis. München: TU München, June 29, 2017.

[45] Larry L. Hench and Jon K. West. “The sol-gel process”. In: *Chemical Reviews* 90.1 (1990), pp. 33–72. DOI: 10.1021/cr00099a003.

[46] C. Jeffrey Brinker and George W. Scherer. *Sol-Gel Science*. 1st ed. Elsevier Science, Oct. 22, 2013.

[47] Kuhu Sarkar. “Nanostructured zinc oxide films for application in photovoltaics”. PhD thesis. Technische Universität München, 2014.

[48] Monika Rawolle, Erik V. Braden, Martin A. Niedermeier, David Magerl, Kuhu Sarkar, Thomas Fröschl, Nicola Hüsing, Jan Perlich, and Peter Müller-Buschbaum. “Low-Temperature Route to Crystalline Titania Network Structures in Thin Films”. In: *ChemPhysChem* 13.9 (2012), pp. 2412–2417. DOI: 10.1002/cphc.201200056.

[49] Lin Song, Volker Körstgens, David Magerl, Bo Su, Thomas Fröschl, Nicola Hüsing, Sigrid Bernstorff, and Peter Müller-Buschbaum. “Low-Temperature Fabrication of Mesoporous Titania Thin Films”. In: *MRS Advances* 2.43 (2017), pp. 2315–2325. DOI: 10.1557/adv.2017.406.

[50] Sung Yeun Choi, Marc Mamak, Scott Speakman, Naveen Chopra, and Geoffrey A. Ozin. "Evolution of Nanocrystallinity in Periodic Mesoporous Anatase Thin Films". In: *Small* 1.2 (2005), pp. 226–232. DOI: 10.1002/smll.200400038.

[51] David Magerl, Martine Philipp, Xing-Ping Qiu, Françoise M. Winnik, and Peter Müller-Buschbaum. "Swelling and Thermoresponsive Behavior of Linear versus Cyclic Poly(N-isopropylacrylamide) Thin Films". In: *Macromolecules* 48.9 (Apr. 2015), pp. 3104–3111. DOI: 10.1021/acs.macromol.5b00436.

[52] Yong Li and Toyoichi Tanaka. "Kinetics of swelling and shrinking of gels". In: *Journal of Chemical Physics* 92.2 (1990), pp. 1365–1371. DOI: 10.1063/1.458148.

[53] J. Jaczewska, I. Raptis, A. Budkowski, D. Goustouridis, J. Raczkowska, M. Sanopoulou, E. Pamuła, A. Bernasik, and J. Rysz. "Swelling of poly(3-alkylthiophene) films exposed to solvent vapors and humidity: Evaluation of solubility parameters". English. In: *Synthetic Metals* 157.18-20 (2007), pp. 726–732. DOI: 10.1016/j.synthmet.2007.07.015.

[54] Christoph J. Schaffer. "Morphological Degradation in Polymer-Fullerene Solar Cells". PhD thesis. München: Technische Universität München, July 2016.

[55] W. P. Su, J. R. Schrieffer, and A. J. Heeger. "Solitons in Polyacetylene". In: *Phys. Rev. Lett.* 42 (25 June 1979), pp. 1698–1701. DOI: 10.1103/PhysRevLett.42.1698.

[56] Claudia Maria Palumbiny. "Polymeric PEDOT:PSS electrodes for organic electronics: Understanding the conductivity-structure relation". PhD thesis. München: Technische Universität München, Nov. 2015.

[57] H. Bässler. "Localized states and electronic transport in single component organic solids with diagonal disorder". In: *Physica Status Solidi B* 107.1 (1981), pp. 9–54. DOI: 10.1002/pssb.2221070102.

[58] H. Bässler. "Charge Transport in Disordered Organic Photoconductors a Monte Carlo Simulation Study". In: *physica status solidi (b)* 175.1 (1993), pp. 15–56. DOI: 10.1002/pssb.2221750102.

[59] Rudolph A. Marcus. "On the Theory of Oxidation-Reduction Reactions Involving Electron Transfer. I". In: *The Journal of Chemical Physics* 24.5 (1956), pp. 966–978. DOI: 10.1063/1.1742723.

[60] Rudolph A. Marcus. "Electron transfer at electrodes and in solution: Comparison of theory and experiment". In: *Electrochimica Acta* 13.5 (1968), pp. 995–1004. DOI: 10.1016/0013-4686(68)80031-3.

[61] Allen Miller and Elihu Abrahams. "Impurity Conduction at Low Concentrations". In: *Physical Review* 120 (3 Nov. 1960), pp. 745–755. DOI: 10.1103/PhysRev.120.745.

[62] Carsten Deibel and Vladimir Dyakonov. "Polymer-fullerene bulk heterojunction solar cells". In: *Reports on Progress in Physics* 73.9 (2010), p. 096401. DOI: 10.1088/0034-4885/73/9/096401.

[63] Hagen Klauk. "Organic thin-film transistors". In: *Chemical Society Reviews* 39 (7 2010), pp. 2643–2666. DOI: 10.1039/B909902F.

[64] I. D. W. Samuel and G. A. Turnbull. "Organic Semiconductor Lasers". In: *Chemical Reviews* 107.4 (2007). PMID: 17385928, pp. 1272–1295. DOI: 10.1021/cr050152i.

[65] Michael S. Arnold, Jeramy D. Zimmerman, Christopher K. Renshaw, Xin Xu, Richard R. Lunt, Christine M. Austin, and Stephen R. Forrest. "Broad Spectral Response Using Carbon Nanotube/Organic Semiconductor/C60 Photodetectors". In: *Nano Letters* 9.9 (2009). PMID: 19637853, pp. 3354–3358. DOI: 10.1021/nl901637u.

[66] Harald Hoppe and Niyazi Serdar Sariciftci. "Organic solar cells: An overview". In: *Journal of Materials Research* 19.7 (2004), pp. 1924–1945. DOI: 10.1557/JMR.2004.0252.

[67] R. H. Friend, R. W. Gymer, A. B. Holmes, J. H. Burroughes, R. N. Marks, C. Taliani, D. D. C. Bradley, D. A. Dos Santos, J. L. Brédas, M. Lögdlund, and W. R. Salaneck. "Electroluminescence in conjugated polymers". In: *Nature* 397.6715 (Jan. 1999), pp. 121–128.

[68] Sebastian Reineke, Frank Lindner, Gregor Schwartz, Nico Seidler, Karsten Walzer, Bjorn Lussem, and Karl Leo. "White organic light-emitting diodes with fluorescent tube efficiency". In: *Nature* 459.7244 (May 2009), pp. 234–238. DOI: 10.1038/nature08003.

[69] Franky So, Junji Kido, and Paul Burrows. "Organic Light-Emitting Devices for Solid-State Lighting". In: *MRS Bulletin* 33.7 (2008), pp. 663–669. DOI: 10.1557/mrs2008.137.

[70] M. Pope and C. E. Swenberg. *Electronic Processes in Organic Crystals and Polymers*. Monographs on the physics and chemistry of materials. Oxford University Press, 1999.

[71] Stefan Höfle, Alexander Schienle, Christoph Bernhard, Michael Bruns, Uli Lemmer, and Alexander Colsmann. "Solution Processed, White Emitting Tandem Organic Light-Emitting Diodes with Inverted Device Architecture". In: *Advanced Materials* 26.30 (2014), pp. 5155–5159. DOI: 10.1002/adma.201400332.

[72] J.-H. Jou, M.-C. Sun, H.-H. Chou, and C.-H. Li. "White organic light-emitting devices with a solution-processed and molecular host-employed emission layer". English. In: *Applied Physics Letters* 87.4 (2005). DOI: 10.1063/1.1991997.

[73] Boris Riedel. "Effizienzsteigerung in organischen Leuchtdioden". PhD thesis. Karlsruher Institut für Technologie, 2011. DOI: 10.5445/KSP/1000023575.

[74] Heinz Bässler and Anna Köhler. "Charge Transport in Organic Semiconductors". In: *Unimolecular and Supramolecular Electronics I: Chemistry and Physics Meet at Metal-Molecule Interfaces*. Ed. by M. Robert Metzger. Berlin, Heidelberg: Springer Berlin Heidelberg, 2012, pp. 1–65. DOI: 10.1007/128_2011_218.

[75] Anna Köhler and Heinz Bässler. *Electronic Processes in Organic Semiconductors*. Wiley-VCH Verlag GmbH & Co. KGaA, May 2015. DOI: 10.1002/9783527685172.

[76] Vicki Cleave, Goghan Yahioglu, Pierre Le Barny, Richard H. Friend, and Nir Tessler. "Harvesting Singlet and Triplet Energy in Polymer LEDs". In: *Advanced Materials* 11.4 (1999), pp. 285–288. DOI: 10.1002/(SICI)1521-4095(199903)11:4<285::AID-ADMA285>3.0.CO;2-N.

[77] Yuichiro Kawamura, Kenichi Goushi, Jason Brooks, Julie J. Brown, Hiroyuki Sasabe, and Chihaya Adachi. "100% phosphorescence quantum efficiency of Ir(III) complexes in organic semiconductor films". In: *Applied Physics Letters* 86.7 (2005), p. 071104. DOI: 10.1063/1.1862777.

[78] W. L. Barnes. "Electromagnetic Crystals for Surface Plasmon Polaritons and the Extraction of Light from Emissive Devices". In: *Journal of Lightwave Technology* 17.11 (Nov. 1999), p. 2170.

[79] H. Greiner. "Light extraction from organic light emitting diode substrates: Simulation and experiment". English. In: *Japanese Journal of Applied Physics* 46.7 A (2007), pp. 4125–4137. DOI: 10.1143/JJAP.46.4125.

[80] Metin Tolan. *X-Ray Scattering from Soft-Matter Thin Films*. 1999. DOI: 10.1007/BFB0112834.

[81] B. L. Henke, E. M. Gullikson, and J. C. Davis. "X-Ray Interactions: Photoabsorption, Scattering, Transmission, and Reflection at E = 50-30,000 eV, Z = 1-92". In: *Atomic Data and Nuclear Data Tables* 54.2 (1993), pp. 181–342. DOI: 10.1006/adnd.1993.1013.

[82] John Lekner. "Reflection theory and the analysis of neutron reflection data". In: *Physica B: Condensed Matter* 173.1 (1991), pp. 99–111. DOI: 10.1016/0921-4526(91)90040-L.

[83] Peter Müller-Buschbaum. "GISAXS and GISANS as metrology technique for understanding the 3D morphology of block copolymer thin films". In: *European Polymer Journal* 81 (2016), pp. 470–493. DOI: 10.1016/j.eurpolymj.2016.04.007.

[84] Varley F. Sears. "Neutron scattering lengths and cross sections". In: *Neutron News* 3.3 (1992), pp. 26–37. DOI: 10.1080/10448639208218770.

[85] Alexander Hexemer and Peter Müller-Buschbaum. "Advanced grazing-incidence techniques for modern soft-matter materials analysis". In: *IUCrJ* 2.1 (Jan. 2015), pp. 106–125. DOI: 10.1107/S2052252514024178.

[86] P. Müller-Buschbaum, J. S. Gutmann, R. Cubitt, and M. Stamm. "Probing the in-plane composition of thin polymer films with grazing-incidence small-angle neutron scattering and atomic force microscopy". In: *Colloid and Polymer Science* 277.12 (Dec. 1999), pp. 1193–1199. DOI: 10.1007/s003960050509.

[87] B. Jacrot. "The study of biological structures by neutron scattering from solution". In: *Reports on Progress in Physics* 39.10 (Oct. 1976), pp. 911–953. DOI: 10.1088/0034-4885/39/10/001.

[88] Rémi Lazzari. "IsGISAXS: a program for grazing-incidence small-angle X-ray scattering analysis of supported islands". In: *Journal of Applied Crystallography* 35.4 (Aug. 2002), pp. 406–421. DOI: 10.1107/S0021889802006088.

[89] George H. Vineyard. "Grazing-incidence diffraction and the distorted-wave approximation for the study of surfaces". In: *Physical Review B* 26 (8 Oct. 1982), pp. 4146–4159. DOI: 10.1103/PhysRevB.26.4146.

[90] S. Dietrich and H. Wagner. "Critical surface scattering of x-rays at grazing angles". In: *Zeitschrift für Physik B Condensed Matter* 56.3 (Sept. 1984), pp. 207–215. DOI: 10.1007/BF01304174.

[91] S. Dietrich and H. Wagner. "Critical magnetic surface scattering of neutrons at grazing angles". In: *Zeitschrift für Physik B Condensed Matter* 59.1 (Mar. 1985), pp. 35–42. DOI: 10.1007/BF01325380.

[92] Slim T. Chourou, Abhinav Sarje, Xiaoye S. Li, Elaine R. Chan, and Alexander Hexemer. "HipGISAXS: a high-performance computing code for simulating grazing-incidence X-ray scattering data". In: *Journal of Applied Crystallography* 46.6 (Dec. 2013), pp. 1781–1795. DOI: 10.1107/S0021889813025843.

[93] David Babonneau. "FitGISAXS: software package for modelling and analysis of GISAXS data using IGOR Pro". In: *Journal of Applied Crystallography* 43.4 (Aug. 2010), pp. 929–936. DOI: 10.1107/S0021889810020352.

[94] J. Burle, C. Durniak, J. M. Fisher, M. Ganeva, G. Pospelov, W. Van Herck, J. Wuttke, and D. Yurov. *BornAgain - Software for simulating and fitting X-ray and neutron small-angle scattering at grazing incidece*. Ed. by MLZ Garching. 2018. URL: http://www.bornagainproject.org/ (visited on 04/01/2019).

[95] Yasuharu Yoneda. "Anomalous Surface Reflection of X Rays". In: *Physical Review* 131 (5 Sept. 1963), pp. 2010–2013. DOI: 10.1103/PhysRev.131.2010.

[96] T. Salditt, T. H. Metzger, J. Peisl, and G. Goerigk. "Non-specular X-ray scattering from thin films and multilayers with small-angle scattering equipment". In: *Journal of Physics D: Applied Physics* 28.4A (Apr. 1995), A236–A240. DOI: 10.1088/0022-3727/28/4a/046.

[97] P. Müller-Buschbaum. "Grazing incidence small-angle X-ray scattering: An advanced scattering technique for the investigation of nanostructured polymer films". English. In: *Analytical and Bioanalytical Chemistry* 376.1 (2003), pp. 3–10. DOI: 10.1007/s00216-003-1869-2.

[98] Peter Müller-Buschbaum. "The Active Layer Morphology of Organic Solar Cells Probed with Grazing Incidence Scattering Techniques". In: *Advanced Materials* 26.46 (2014), pp. 7692–7709. DOI: 10.1002/adma.201304187.

[99] S. K. Sinha, E. B. Sirota, S. Garoff, and H. B. Stanley. "X-ray and neutron scattering from rough surfaces". In: *Physical Review B* 38 (4 Aug. 1988), pp. 2297–2311. DOI: 10.1103/PhysRevB.38.2297.

[100] G. Renaud, R. Lazzari, and F. Leroy. "Probing surface and interface morphology with Grazing Incidence Small Angle X-Ray Scattering". English. In: *Surface Science Reports* 64.8 (2009), pp. 255–380. DOI: 10.1016/j.surfrep.2009.07.002.

[101] Johannes Schlipf. "The Morphology of Hybrid Perovskite Thin Films for Photovoltaic Application. Formation & Disintegration". PhD thesis. München: Fakultät für Physik, Dec. 11, 2018.

[102] Peter Müller-Buschbaum. "A Basic Introduction to Grazing Incidence Small-Angle X-Ray Scattering". In: *Applications of Synchrotron Light to Scattering and Diffraction in Materials and Life Sciences*. Ed. by Marian Gomez, Aurora Nogales, Cruz Mari Garcia-Gutierrez, and T. A. Ezquerra. Berlin, Heidelberg: Springer Berlin Heidelberg, 2009, pp. 61–89. DOI: 10.1007/978-3-540-95968-7_3.

[103] R. Hosemann, W. Vogel, D. Weick, and F. J. Baltá-Calleja. "Novel aspects of the real paracrystal". In: *Acta Crystallographica Section A* 37.1 (Jan. 1981), pp. 85–91. DOI: 10.1107/S0567739481000156.

[104] Christoph J. Schaffer, Claudia M. Palumbiny, Martin A. Niedermeier, Christian Jendrzejewski, Gonzalo Santoro, Stephan V. Roth, and Peter Müller-Buschbaum. "A Direct Evidence of Morphological Degradation on a Nanometer Scale in Polymer Solar Cells". In: *Advanced Materials* 25.46 (Sept. 12, 2013), pp. 6760–6764. DOI: 10.1002/adma.201302854.

[105] Zhang Jiang. "GIXSGUI: a MATLAB toolbox for grazing-incidence X-ray scattering data visualization and reduction, and indexing of buried three-dimensional periodic nanostructured films". In: *Journal of Applied Crystallography* 48.3 (June 2015), pp. 917–926. DOI: 10.1107/S1600576715004434.

[106] Paul Scherrer. "Bestimmung der Grösse und der inneren Struktur von Kolloidteilchen mittels Röntgenstrahlen". ger. In: *Nachrichten von der Gesellschaft der Wissenschaften zu Göttingen* (July 26, 1918), pp. 98–100.

[107] D. G. Bucknall, S. A. Butler, and J. S. Higgins. “Neutron reflectivity of polymer interfaces”. In: *Journal of Physics and Chemistry of Solids* 60.8 (1999), pp. 1273–1277. DOI: 10.1016/S0022-3697(99)00101-8.

[108] T. Gutberlet, R. Steitz, G. Fragneto, and B. Klösgen. “Phospholipid bilayer formation at a bare Si surface: a time-resolved neutron reflectivity study”. In: *Journal of Physics: Condensed Matter* 16.26 (June 2004), S2469–S2476. DOI: 10.1088/0953-8984/16/26/020.

[109] P. Müller-Buschbaum, E. Bauer, E. Maurer, A. Nelson, and R. Cubitt. “In-situ neutron reflectometry probing competitive swelling and de-swelling of thin polystyrene films”. In: *Physica Status Solidi RRL: Rapid Research Letters* 1.2 (2007), R68–R70. DOI: 10.1002/pssr.200600066.

[110] P. Müller-Buschbaum, E. Metwalli, J.-F. Moulin, V. Kudryashov, M. Haese-Seiller, and R. Kampmann. “Time of flight grazing incidence small angle neutron scattering”. In: *The European Physical Journal Special Topics* 167.1 (Feb. 2009), pp. 107–112. DOI: 10.1140/epjst/e2009-00944-5.

[111] W. Kreuzpaintner, J.-F. Moulin, D. Lott, R. Kampmann, M. Haese-Seiller, M. Störmer, and A. Schreyer. “Time-of-flight grazing incidence small angle neutron scattering on Gd nanowires”. In: *The European Physical Journal Special Topics* 167.1 (Feb. 2009), pp. 73–79. DOI: 10.1140/epjst/e2009-00939-2.

[112] Robert Cubitt and Giovanna Fragneto. “Neutron Reflection: Principles and Examples of Applications”. In: *SCATTERING: Scattering and Inverse Scattering in Pure and Applied Science*. Ed. by Roy Pike and Pierre Sabatier. 1st ed. Academic Press, Oct. 9, 2001. Chap. 2.8.3, pp. 1198–1208.

[113] Peter Müller-Buschbaum. “Influence of surface cleaning on dewetting of thin polystyrene films”. In: *European Physical Journal E: Soft Matter* 12.3 (2003), pp. 443–448. DOI: 10.1140/epje/e2004-00014-7.

[114] J. N. van Niekerk, F. R. L. Schoening, and J. H. Talbot. “The crystal structure of zinc acetate dihydrate, $Zn(CH_3COO)_2.2H_2O$”. In: *Acta Crystallographica* 6.8-9 (Sept. 1953), pp. 720–723. DOI: 10.1107/S0365110X53002015.

[115] V. Srikant and D. R. Clarke. “On the optical band gap of zinc oxide”. In: *Journal of Applied Physics* 83.10 (1998), pp. 5447–5451. DOI: 10.1063/1.367375.

[116] Ü. Özgür, Ya. I. Alivov, C. Liu, A. Teke, M. A. Reshchikov, S. Doğan, V. Avrutin, S.-J. Cho, and H. Morkoç. “A comprehensive review of ZnO materials and devices”. English. In: *Journal of Applied Physics* 98.4 (2005), pp. 1–103. DOI: 10.1063/1.1992666.

[117] Andreas Elschner, Stephan Kirchmeyer, Wilfried Lövenich, Udo Merker, and Knud Reuter. *PEDOT: Principles and Applications of an Intrinsically Conductive Polymer*. eng. Boca Raton, Florida, USA: CRC Press, Nov. 2, 2010.

[118] S. R. Tseng, Y. S. Chen, H. F. Meng, H. C. Lai, C. H. Yeh, S. F. Horng, H. H. Liao, and C. S. Hsu. "Electron transport and electroluminescent efficiency of conjugated polymers". In: *Synthetic Metals* 159.1 (2009), pp. 137–141. DOI: https://doi.org/10.1016/j.synthmet.2008.08.017.

[119] Merck KGaA. *Data Sheet*. Jan. 15, 2019. URL: https://www.merckgroup.com/content/dam/web/corporate/non-images/business-specifics/performance-materials/Optoelectronics/global/Datasheet-Livilux-PDY-132-Super-Yellow-EN.pdf.

[120] Achilleas Savva, Marios Neophytou, Charalambos Koutsides, Kyriacos Kalli, and Stelios A. Choulis. "Synergistic effects of buffer layer processing additives for enhanced hole carrier selectivity in inverted Organic Photovoltaics". In: *Organic Electronics* 14.11 (2013), pp. 3123–3130. DOI: 10.1016/j.orgel.2013.07.024.

[121] David B. Hall, Patrick Underhill, and John M. Torkelson. "Spin coating of thin and ultrathin polymer films". In: *Polymer Engineering & Science* 38.12 (1998), pp. 2039–2045. DOI: 10.1002/pen.10373.

[122] Dirk W. Schubert and Thomas Dunkel. "Spin coating from a molecular point of view: its concentration regimes, influence of molar mass and distribution". In: *Materials Research Innovations* 7.5 (2003), pp. 314–321. DOI: 10.1007/s10019-003-0270-2.

[123] Enrique J. Lavernia and Yue Wu. *Spray atomization and deposition*. Wiley, 1996.

[124] Dainius Perednis and Ludwig J. Gauckler. "Thin Film Deposition Using Spray Pyrolysis". In: *Journal of Electroceramics* 14.2 (Mar. 2005), pp. 103–111. DOI: 10.1007/s10832-005-0870-x.

[125] John B. Mooney and Shirley B. Radding. "Spray pyrolysis processing". In: *Annual review of materials science* 12.1 (1982), pp. 81–101.

[126] J. C. Viguié and J. Spitz. "Chemical Vapor Deposition at Low Temperatures". In: *Journal of the Electrochemical Society* 122.4 (1975), pp. 585–588.

[127] Youngkyoo Kim, Stelios A. Choulis, Jenny Nelson, Donal D. C. Bradley, Steffan Cook, and James R. Durrant. "Device annealing effect in organic solar cells with blends of regioregular poly(3-hexylthiophene) and soluble fullerene". In: *Applied Physics Letters* 86.6 (2005), p. 063502. DOI: 10.1063/1.1861123.

[128] Tracey M. Clarke, Amy M. Ballantyne, Jenny Nelson, Donal D. C. Bradley, and James R. Durrant. "Free Energy Control of Charge Photogeneration in Polythiophene/Fullerene Solar Cells: The Influence of Thermal Annealing on P3HT/PCBM Blends". In: *Advanced Functional Materials* 18.24 (2008), pp. 4029–4035. DOI: 10.1002/adfm.200800727.

[129] Tao Wang, Andrew J. Pearson, Alan D. F. Dunbar, Paul A. Staniec, Darren C. Watters, Hunan Yi, Anthony J. Ryan, Richard A. L. Jones, Ahmed Iraqi, and David G. Lidzey. "Correlating Structure with Function in Thermally Annealed PCDTBT:PC70BM Photovoltaic Blends". In: *Advanced Functional Materials* 22.7 (2012), pp. 1399–1408. DOI: 10.1002/adfm.201102510.

[130] Robert P. Meier. "Novel Structuring Routines for Organic Photovoltaics". PhD thesis. München: Fakultät für Physik, Feb. 16, 2012.

[131] Claudia M. Palumbiny, Johannes Schlipf, Alexander Hexemer, Cheng Wang, and Peter Müller-Buschbaum. "The Morphological Power of Soap: How Surfactants Lower the Sheet Resistance of PEDOT:PSS by Strong Impact on Inner Film Structure and Molecular Interface Orientation". In: *Advanced Electronic Materials* 2.4 (2016). 1500377, p. 1500377. DOI: 10.1002/aelm.201500377.

[132] *NIST X-ray Photoelectron Spectroscopy Database. NIST Standard Reference Database Number 20*. National Institute of Standards and Technology. URL: https://srdata.nist.gov/xps/.

[133] I. Miccoli, F. Edler, H. Pfnür, and C. Tegenkamp. "The 100th anniversary of the four-point probe technique: the role of probe geometries in isotropic and anisotropic systems". In: *Journal of Physics: Condensed Matter* 27.22 (2015), p. 223201. DOI: 10.1088/0953-8984/27/22/223201.

[134] Vittorio Scardaci, Richard Coull, and Jonathan N. Coleman. "Very thin transparent, conductive carbon nanotube films on flexible substrates". In: *Applied Physics Letters* 97.2 (2010), p. 023114. DOI: 10.1063/1.3462317.

[135] Martin Dressel and George Grüner. "Electrodynamics of Solids: Optical Properties of Electrons in Matter". In: *American Journal of Physics* 70.12 (2002), pp. 1269–1270. DOI: 10.1119/1.1516200.

[136] L. Hu, D. S. Hecht, and G. Grüner. "Percolation in Transparent and Conducting Carbon Nanotube Networks". In: *Nano Letters* 4.12 (2004), pp. 2513–2517. DOI: 10.1021/nl048435y.

[137] Evgenij Barsoukov and J. Ross Macdonald. *Impedance Spectroscopy: Theory, Experiment, and Applications*. 2nd ed. Wiley-Interscience, 2005.

[138] Thomas Stöcker, Anna Köhler, and Ralf Moos. "Why does the electrical conductivity in PEDOT:PSS decrease with PSS content? A study combining thermoelectric measurements with impedance spectroscopy". In: *Journal of Polymer Science Part B: Polymer Physics* 50.14 (2012), pp. 976–983. DOI: 10.1002/polb.23089.

[139] Caroline A. Schneider, Wayne S. Rasband, and Kevin W. Eliceiri. "NIH Image to ImageJ: 25 years of image analysis". In: *Nature Methods* 9 (June 2012), p. 671. DOI: 10.1038/nmeth.2089.

[140] David Nečas and Petr Klapetek. “Gwyddion: an open-source software for SPM data analysis”. In: *Central European Journal of Physics* 10.1 (Feb. 2012), pp. 181–188. DOI: 10.2478/s11534-011-0096-2.

[141] L. G. Parratt. “Surface Studies of Solids by Total Reflection of X-Rays”. In: *Physical Review* 95 (2 July 1954), pp. 359–369. DOI: 10.1103/PhysRev.95.359.

[142] Andrew Nelson. “Co-refinement of multiple-contrast neutron/X-ray reflectivity data using MOTOFIT”. In: *Journal of Applied Crystallography* 39.2 (Apr. 2006), pp. 273–276. DOI: 10.1107/S0021889806005073.

[143] Heinz Maier-Leibnitz Zentrum. “REFSANS: Reflectometer and evanescent wave small angle neutron spectrometer”. In: *Journal of large-scale research facilities* 1.A9 (2015). DOI: 10.17815/jlsrf-1-31.

[144] Jan Ilavsky. “NIKA: software for two-dimensional data reduction”. In: *Journal of Applied Crystallography* 45.2 (Apr. 2012), pp. 324–328. DOI: 10.1107/S0021889812004037.

[145] Gunthard Benecke, Wolfgang Wagermaier, Chenghao Li, Matthias Schwartzkopf, Gero Flucke, Rebecca Hoerth, Ivo Zizak, Manfred Burghammer, Ezzeldin Metwalli, Peter Müller-Buschbaum, Martin Trebbin, Stephan Förster, Oskar Paris, Stephan V. Roth, and Peter Fratzl. “A customizable software for fast reduction and analysis of large X-ray scattering data sets: applications of the new DPDAK package to small-angle X-ray scattering and grazing-incidence small-angle X-ray scattering”. In: *Journal of Applied Crystallography* 47.5 (Oct. 2014), pp. 1797–1803. DOI: 10.1107/S1600576714019773.

[146] Irina Ilicheva. “Investigations on ZnO Scattering Layers for OLED Applications”. Bachelors Thesis. Fakultät für Physik, Sept. 4, 2017.

[147] Y. Luo, L. Wang, Y. Ding, L. Li, and J. Shi. “High light-extracting efficiency for OLED directly fabricated on double-side nanotextured silica substrate”. English. In: *Optics Letters* 38.14 (2013), pp. 2394–2396. DOI: 10.1364/OL.38.002394.

[148] Gunar Kaune, Mine Memesa, Robert Meier, Matthias A. Ruderer, Alexander Diethert, Stephan V. Roth, Maria Dâ€™Acunzi, Jochen S. Gutmann, and Peter Müller-Buschbaum. “Hierarchically Structured Titania Films Prepared by Polymer/Colloidal Templating”. In: *ACS Applied Materials & Interfaces* 1.12 (2009). PMID: 20356168, pp. 2862–2869. DOI: 10.1021/am900592u.

[149] Gunar Kaune. “Strukturierung von anorganisch-organischen Hybridsystemen für Anwendungen in der Photovoltaik”. PhD thesis. München: Technische Universität München, Mar. 2010.

[150] Aswin Hongsingthong, Taweewat Krajangsang, Ihsanul Afdi Yunaz, Shinsuke Miyajima, and Makoto Konagai. "ZnO Films with Very High Haze Value for Use as Front Transparent Conductive Oxide Films in Thin-Film Silicon Solar Cells". In: *Applied Physics Express* 3.5 (May 2010), p. 051102. DOI: 10.1143/apex.3.051102.

[151] Nobuyuki Sekine, Cheng-Hsuan Chou, Wei Lek Kwan, and Yang Yang. "ZnO nano-ridge structure and its application in inverted polymer solar cell". In: *Organic Electronics* 10.8 (2009), pp. 1473–1477. DOI: 10.1016/j.orgel.2009.08.011.

[152] Rui Wang. "Hybrid Solar Cells based on ZnO Nanostructures". MA thesis. München: Technische Universität München, 2013.

[153] Robert D. Deegan, Olgica Bakajin, Todd F. Dupont, Greb Huber, Sidney R. Nagel, and Thomas A. Witten. "Capillary flow as the cause of ring stains from dried liquid drops". In: *Nature* 389.6653 (Oct. 1997), pp. 827–829. DOI: 10.1038/39827.

[154] Eran Rabani, David R. Reichman, Phillip L. Geissler, and Louis E. Brus. "Drying-mediated self-assembly of nanoparticles". In: *Nature* 426.6964 (Nov. 2003), pp. 271–274. DOI: 10.1038/nature02087.

[155] Anirudh Sharma, Maria Untch, Jamie S. Quinton, Rüdiger Berger, Gunther Andersson, and David A. Lewis. "Nanoscale heterogeniety and workfunction variations in ZnO thin films". In: *Applied Surface Science* 363 (2016), pp. 516–521. DOI: 10.1016/j.apsusc.2015.11.190.

[156] Tingting Xu, Swaminathan Venkatesan, David Galipeau, and Qiquan Qiao. "Study of polymer/ZnO nanostructure interfaces by Kelvin probe force microscopy". In: *Solar Energy Materials and Solar Cells* 108 (2013), pp. 246–251. DOI: 10.1016/j.solmat.2012.08.013.

[157] Babita Kumari, Shailja Sharma, Nirupama Singh, Vibha R. Satsangi, Sahab Dass, and Rohit Shrivastav. "Chemically etched ZnO thin films, with surface-evolved nano-ridges, for efficient photoelectrochemical splitting of water". In: *Journal of Solid State Electrochemistry* 19.5 (May 2015), pp. 1311–1320. DOI: 10.1007/s10008-015-2745-7.

[158] Masashi Ohyama, Hiromitsu Kouzuka, and Toshinobu Yoko. "Sol-gel preparation of ZnO films with extremely preferred orientation along (002) plane from zinc acetate solution". In: *Thin Solid Films* 306.1 (1997), pp. 78–85. DOI: 10.1016/S0040-6090(97)00231-9.

[159] Philipp Kraft. "Pilatus 2M - a detector for small angle X-ray scattering". Diss., Eidgenössische Technische Hochschule ETH Zürich, Nr. 18466, 2010. PhD thesis. ETH Zürich: ETH Zürich, 2010. DOI: 10.3929/ethz-a-006023165.

[160] G. Inzelt. *Conducting Polymers: A New Era in Electrochemistry*. Monographs in Electrochemistry. Springer, 2008.

[161] Soyeon Kim, Bernardi Sanyoto, Won-Tae Park, Seyul Kim, Saumen Mandal, Jong-Choo Lim, Yong-Young Noh, and Jung-Hyun Kim. "Purification of PEDOT:PSS by Ultrafiltration for Highly Conductive Transparent Electrode of All-Printed Organic Devices". In: *Advanced Materials* 28.46 (2016), pp. 10149–10154. DOI: 10.1002/adma.201603313.

[162] Timothy M. Swager. "50th Anniversary Perspective: Conducting/Semiconducting Conjugated Polymers. A Personal Perspective on the Past and the Future". In: *Macromolecules* 50.13 (2017), pp. 4867–4886. DOI: 10.1021/acs.macromol.7b00582.

[163] Rachel R. Smith, Adam P. Smith, Jeffery T. Stricker, Barney E. Taylor, and Michael F. Durstock. "Layer-by-Layer Assembly of Poly(3,4-ethylenedioxythiophene):Poly(styrenesulfonate)". In: *Macromolecules* 39.18 (2006), pp. 6071–6074. DOI: 10.1021/ma060775d.

[164] Seok-In Na, Seok-Soon Kim, Jang Jo, and Dong-Yu Kim. "Efficient and Flexible ITO-Free Organic Solar Cells Using Highly Conductive Polymer Anodes". In: *Advanced Materials* 20.21 (2008), pp. 4061–4067. DOI: 10.1002/adma.200800338.

[165] Jun-Seok Yeo, Jin-Mun Yun, Dong-Yu Kim, Sungjun Park, Seok-Soon Kim, Myung-Han Yoon, Tae-Wook Kim, and Seok-In Na. "Significant Vertical Phase Separation in Solvent-Vapor-Annealed Poly(3,4-ethylenedioxythiophene):Poly(styrene sulfonate) Composite Films Leading to Better Conductivity and Work Function for High-Performance Indium Tin Oxide-Free Optoelectronics". In: *ACS Applied Materials & Interfaces* 4.5 (2012). PMID: 22489686, pp. 2551–2560. DOI: 10.1021/am300231v.

[166] F. Zhang, A. Petr, H. Peisert, M. Knupfer, and L. Dunsch. "Electrochemical Variation of the Energy Level of Poly(3,4-ethylenedioxythiophene):Poly(styrenesulfonate)". In: *Journal of Physical Chemistry B* 108.45 (2004), pp. 17301–17305. DOI: 10.1021/jp0372439.

[167] S. K. M. Jönsson, J. Birgerson, X. Crispin, G. Greczynski, W. Osikowicz, A. W. Denier van der Gon, W. R. Salaneck, and M. Fahlman. "The effects of solvents on the morphology and sheet resistance in poly(3,4-ethylenedioxythiophene)-polystyrenesulfonic acid (PEDOT-PSS) films". In: *Synthetic Metals* 139.1 (2003), pp. 1–10. DOI: 10.1016/S0379-6779(02)01259-6.

[168] X. Crispin, F. L. E. Jakobsson, A. Crispin, P. C. M. Grim, P. Andersson, A. Volodin, C. van Haesendonck, M. Van der Auweraer, W. R. Salaneck, and M. Berggren. "The Origin of the High Conductivity of Poly(3,4-ethylenedioxythio-

phene)-Poly(styrenesulfonate) (PEDOT-PSS) Plastic Electrodes". In: *Chemistry of Materials* 18.18 (2006), pp. 4354–4360. DOI: 10.1021/cm061032+.

[169] Yong Hyun Kim, Christoph Sachse, Michael L. Machala, Christian May, Lars Müller-Meskamp, and Karl Leo. "Highly Conductive PEDOT:PSS Electrode with Optimized Solvent and Thermal Post-Treatment for ITO-Free Organic Solar Cells". In: *Advanced Functional Materials* 21.6 (2011), pp. 1076–1081. DOI: 10.1002/adfm.201002290.

[170] Jianyong Ouyang, Qianfei Xu, Chi-Wei Chu, Yang Yang, Gang Li, and Joseph Shinar. "On the mechanism of conductivity enhancement in poly(3,4-ethylenedioxythiophene):poly(styrene sulfonate) film through solvent treatment". In: *Polymer* 45.25 (2004), pp. 8443–8450. DOI: 10.1016/j.polymer.2004.10.001.

[171] Hui Shi, Congcong Liu, Qinglin Jiang, and Jingkun Xu. "Effective Approaches to Improve the Electrical Conductivity of PEDOT:PSS: A Review". In: *Advanced Electronic Materials* 1.4 (2015). 1500017, p. 1500017. DOI: 10.1002/aelm.201500017.

[172] Tae-Woo Lee and Youngsu Chung. "Control of the Surface Composition of a Conducting-Polymer Complex Film to Tune the Work Function". In: *Advanced Functional Materials* 18.15 (2008), pp. 2246–2252. DOI: 10.1002/adfm.200700766.

[173] Kenji Kawano, Roberto Pacios, Dmitry Poplavskyy, Jenny Nelson, Donal D. C. Bradley, and James R. Durrant. "Degradation of organic solar cells due to air exposure". In: *Solar Energy Materials and Solar Cells* 90.20 (2006), pp. 3520–3530. DOI: 10.1016/j.solmat.2006.06.041.

[174] Claudia M. Palumbiny, Christoph Heller, Christoph J. Schaffer, Volker Körstgens, Gonzalo Santoro, Stephan V. Roth, and Peter Müller-Buschbaum. "Molecular Reorientation and Structural Changes in Cosolvent-Treated Highly Conductive PEDOT:PSS Electrodes for Flexible Indium Tin Oxide-Free Organic Electronics". In: *Journal of Physical Chemistry C* 118.25 (2014), pp. 13598–13606. DOI: 10.1021/jp501540y.

[175] D. S. Sivia, W. A. Hamilton, and G. S. Smith. "Analysis of neutron reflectivity data: maximum entropy, Bayesian spectral analysis and speckle holography". In: *Physica B: Condensed Matter* 173.1 (1991), pp. 121–138. DOI: 10.1016/0921-4526(91)90042-D.

[176] Raphael Maier. "Investigations on Polymer Electrodes". Bachelors Thesis. Fakultät für Physik, Aug. 6, 2018.

[177] Lina Maria Todenhagen. "A Comparative Investigation on PEDOT:PSS-based Anodes in ITO-free Organic Light-Emitting Diodes". Bachelors Thesis. Fakultät für Physik, Aug. 28, 2018.

[178] Richard D. McCullough. "The Chemistry of Conducting Polythiophenes". In: *Advanced Materials* 10.2 (Jan. 26, 1999), pp. 93–116. DOI: 10.1002/(SICI)1521-4095(199801)10:2<93::AID-ADMA93>3.0.CO;2-F.

[179] Tatsuhiro Horii, Hanae Hikawa, Masato Katsunuma, and Hidenori Okuzaki. "Synthesis of highly conductive PEDOT:PSS and correlation with hierarchical structure". In: *Polymer* 140 (2018), pp. 33–38. DOI: 10.1016/j.polymer.2018.02.034.

[180] J. Y. Kim, J. H. Jung, D. E. Lee, and J. Joo. "Enhancement of electrical conductivity of poly(3,4-ethylenedioxythiophene)/poly(4-styrenesulfonate) by a change of solvents". In: *Synthetic Metals* 126.2 (2002), pp. 311–316. DOI: 10.1016/S0379-6779(01)00576-8.

[181] Tiejun Wang, Yingqun Qi, Jingkun Xu, Xiujie Hu, and Ping Chen. "Effects of poly(ethylene glycol) on electrical conductivity of poly(3,4-ethylenedioxythiophene)–poly(styrenesulfonic acid) film". In: *Applied Surface Science* 250.1 (2005), pp. 188–194. DOI: 10.1016/j.apsusc.2004.12.051.

[182] Changbong Yeon, Sun Jin Yun, Jumi Kim, and Jung Wook Lim. "PEDOT:PSS Films with Greatly Enhanced Conductivity via Nitric Acid Treatment at Room Temperature and Their Application as Pt/TCO-Free Counter Electrodes in Dye-Sensitized Solar Cells". In: *Advanced Electronic Materials* 1.10 (2015). 1500121, p. 1500121. DOI: 10.1002/aelm.201500121.

[183] Desalegn A. Mengistie, Mohammed A. Ibrahem, Pen-Cheng Wang, and Chih-Wei Chu. "Highly Conductive PEDOT:PSS Treated with Formic Acid for ITO-Free Polymer Solar Cells". In: *ACS Applied Materials & Interfaces* 6.4 (2014). PMID: 24460075, pp. 2292–2299. DOI: 10.1021/am405024d.

[184] Nara Kim, Seyoung Kee, Seoung Ho Lee, Byoung Hoon Lee, Yung Ho Kahng, Yong-Ryun Jo, Bong-Joong Kim, and Kwanghee Lee. "Highly Conductive PEDOT:PSS Nanofibrils Induced by Solution-Processed Crystallization". In: *Advanced Materials* 26.14 (2014), pp. 2268–2272. DOI: 10.1002/adma.201304611.

[185] Zeng Fan, Pengcheng Li, Donghe Du, and Jianyong Ouyang. "Significantly Enhanced Thermoelectric Properties of PEDOT:PSS Films through Sequential Post-Treatments with Common Acids and Bases". In: *Advanced Energy Materials* 7.8 (2017). 1602116, p. 1602116. DOI: 10.1002/aenm.201602116.

[186] Isidro Cruz-Cruz, Marisol Reyes-Reyes, and Román López-Sandoval. "Formation of polystyrene sulfonic acid surface structures on poly(3,4-ethylenedioxythiophene): Poly(styrenesulfonate) thin films and the enhancement of its conductivity by using sulfuric acid". In: *Thin Solid Films* 531 (2013), pp. 385–390. DOI: 10.1016/j.tsf.2012.12.050.

[187] Claudia M. Palumbiny, Feng Liu, Thomas P. Russell, Alexander Hexemer, Cheng Wang, and Peter Müller-Buschbaum. "The Crystallization of PEDOT:PSS Polymeric Electrodes Probed In Situ during Printing". In: *Advanced Materials* 27.22 (2015), pp. 3391–3397. DOI: 10.1002/adma.201500315.

[188] David R. Lide. *CRC Handbook of Chemistry and Physics, Internet Version 2005*. Ed. by John R. Rumble. 85th ed. Boca Raton, Florida, USA, 2005.

[189] Arnold F. Hollemann and Nils Wiberg. *Lehrbuch der Anorganischen Chemie*. ger. 102nd ed. Berlin, Boston: De Gryter, 2008.

[190] www.clippercontrols.com. *Dielectric Constant Values*. Ed. by Clipper Controls Inc. Aug. 13, 2018. URL: http://www.clippercontrols.com/pages/Dielectric-Constant-Values.html (visited on 08/13/2018).

[191] R. J. Gillespie and R. H. Cole. "The dielectric constant of sulphuric acid". In: *Transactions of the Faraday Society* 52 (0 1956), pp. 1325–1331. DOI: 10.1039/TF9565201325.

[192] Nicolas Massonnet, Alexandre Carella, Olivier Jaudouin, Patrice Rannou, Gautier Laval, Caroline Celle, and Jean-Pierre Simonato. "Improvement of the Seebeck coefficient of PEDOT:PSS by chemical reduction combined with a novel method for its transfer using free-standing thin films". In: *Journal of Materials Chemistry C* 2 (7 2014), pp. 1278–1283. DOI: 10.1039/C3TC31674B.

[193] G. Greczynski, Th. Kugler, and W. R. Salaneck. "Characterization of the PEDOT-PSS system by means of X-ray and ultraviolet photoelectron spectroscopy". In: *Thin Solid Films* 354.1 (1999), pp. 129–135. DOI: 10.1016/S0040-6090(99)00422-8.

[194] Anthony G. Wren, Roger W. Phillips, and Lucio U. Tolentino. "Surface reactions of chlorine molecules and atoms with water and sulfuric acid at low temperatures". In: *Journal of Colloid and Interface Science* 70.3 (1979), pp. 544–557. DOI: 10.1016/0021-9797(79)90062-6.

[195] Jiao Wang, Kefeng Cai, and Shirley Shen. "Enhanced thermoelectric properties of poly(3,4-ethylenedioxythiophene) thin films treated with H2SO4". In: *Organic Electronics* 15.11 (2014), pp. 3087–3095. DOI: 10.1016/j.orgel.2014.09.012.

[196] K. E. Aasmundtveit, E. J. Samuelsen, L. A. A. Pettersson, O. Inganäs, T. Johansson, and R. Feidenhans'l. "Structure of thin films of poly(3,4-ethylenedioxythiophene)". In: *Synthetic Metals* 101.1 (1999). International Conference on Science and Technology of Synthetic, pp. 561–564. DOI: 10.1016/S0379-6779(98)00315-4.

[197] Nara Kim, Byoung Hoon Lee, Doowhan Choi, Geunjin Kim, Heejoo Kim, Jae-Ryoung Kim, Jongjin Lee, Yung Ho Kahng, and Kwanghee Lee. "Role of Interchain Coupling in the Metallic State of Conducting Polymers". In: *Physical Review Letters* 109 (10 Sept. 2012), p. 106405. DOI: 10.1103/PhysRevLett.109.106405.

[198] Seong-Min Kim, Chang-Hyun Kim, Youngseok Kim, Nara Kim, Won-June Lee, Eun-Hak Lee, Dokyun Kim, Sungjun Park, Kwanghee Lee, Jonathan Rivnay, and Myung-Han Yoon. "Influence of PEDOT:PSS crystallinity and composition on electrochemical transistor performance and long-term stability". In: *Nature Communications* 9.1 (Sept. 21, 2018), p. 3858. DOI: 10.1038/s41467-018-06084-6.

[199] Yijie Xia and Jianyong Ouyang. "Salt-Induced Charge Screening and Significant Conductivity Enhancement of Conducting Poly(3,4-ethylenedioxythiophene):Poly(styrenesulfonate)". In: *Macromolecules* 42.12 (2009), pp. 4141–4147. DOI: 10.1021/ma900327d.

[200] N. S. Murthy and H. Minor. "General procedure for evaluating amorphous scattering and crystallinity from X-ray diffraction scans of semicrystalline polymers". In: *Polymer* 31.6 (1990), pp. 996–1002. DOI: 10.1016/0032-3861(90)90243-R.

[201] Kevin van de Ruit, Ilias Katsouras, Dirk Bollen, Ton van Mol, René A. J. Janssen, Dago M. de Leeuw, and Martijn Kemerink. "The Curious Out-of-Plane Conductivity of PEDOT:PSS". In: *Advanced Functional Materials* 23.46 (2013), pp. 5787–5793. DOI: 10.1002/adfm.201301175.

[202] Seyoung Kee, Nara Kim, Bong Seong Kim, Seongjin Park, Yun Hee Jang, Seoung Ho Lee, Jehan Kim, Junghwan Kim, Sooncheol Kwon, and Kwanghee Lee. "Controlling Molecular Ordering in Aqueous Conducting Polymers Using Ionic Liquids". In: *Advanced Materials* 28.39 (2016), pp. 8625–8631. DOI: 10.1002/adma.201505473.

[203] H.-W. Chang, Y. H. Kim, J. Lee, S. Hofmann, B. Lüssem, L. Müller-Meskamp, M. C. Gather, K. Leo, and C.-C. Wu. "Color-stable, ITO-free white organic light-emitting diodes with enhanced efficiency using solution-processed transparent electrodes and optical outcoupling layers". English. In: *Organic Electronics* 15.5 (2014), pp. 1028–1034. DOI: 10.1016/j.orgel.2014.02.017.

[204] A. M. Nardes, M. Kemerink, M. M. de Kok, E. Vinken, K. Maturova, and R. A. J. Janssen. "Conductivity, work function, and environmental stability of PEDOT:PSS thin films treated with sorbitol". In: *Organic Electronics* 9.5 (2008), pp. 727–734. DOI: 10.1016/j.orgel.2008.05.006.

[205] Stefan Höfle. "Flüssigprozessierte organische Tandem-Leuchtdioden". PhD thesis. Karlsruher Institut für Technologie, 2015. DOI: 10.5445/KSP/1000045067.

[206] Yong Hyun Kim, Jonghee Lee, Simone Hofmann, Malte C. Gather, Lars Müller-Meskamp, and Karl Leo. "Achieving High Efficiency and Improved Stability in ITO-Free Transparent Organic Light-Emitting Diodes with Conductive Polymer Electrodes". In: *Advanced Functional Materials* 23.30 (2013), pp. 3763–3769. DOI: 10.1002/adfm.201203449.

[207] Wook Song and Jun Yeob Lee. "Degradation Mechanism and Lifetime Improvement Strategy for Blue Phosphorescent Organic Light-Emitting Diodes". In: *Advanced Optical Materials* 5.9 (2017), p. 1600901. DOI: 10.1002/adom.201600901.

[208] Hany Aziz and Zoran D. Popovic. "Degradation Phenomena in Small-Molecule Organic Light-Emitting Devices". In: *Chemistry of Materials* 16.23 (2004), pp. 4522–4532. DOI: 10.1021/cm040081o.

[209] Sebastian Scholz, Denis Kondakov, Björn Lüssem, and Karl Leo. "Degradation Mechanisms and Reactions in Organic Light-Emitting Devices". In: *Chemical Reviews* 115.16 (2015). PMID: 26230864, pp. 8449–8503. DOI: 10.1021/cr400704v.

[210] Johannes Schlipf, Pablo Docampo, Christoph J. Schaffer, Volker Körstgens, Lorenz Bießmann, Fabian Hanusch, Nadja Giesbrecht, Sigrid Bernstorff, Thomas Bein, and Peter Müller-Buschbaum. "A Closer Look into Two-Step Perovskite Conversion with X-ray Scattering". In: *Journal of Physical Chemistry Letters* 6.7 (2015), pp. 1265–1269. DOI: 10.1021/acs.jpclett.5b00329.

[211] Nuri Hohn, Steffen J. Schlosser, Lorenz Bießmann, Sebastian Grott, Senlin Xia, Kun Wang, Matthias Schwartzkopf, Stephan V. Roth, and Peter Müller-Buschbaum. "Readily available titania nanostructuring routines based on mobility and polarity controlled phase separation of an amphiphilic diblock copolymer". In: *Nanoscale* 10.11 (2018), pp. 5325–5334. DOI: 10.1039/C7NR09519H.

[212] Johannes Schlipf, Lorenz Bießmann, Lukas Oesinghaus, Edith Berger, Ezzeldin Metwalli, Johannes A. Lercher, Lionel Porcar, and Peter Müller-Buschbaum. "In Situ Monitoring the Uptake of Moisture into Hybrid Perovskite Thin Films". In: *Journal of Physical Chemistry Letters* 9.8 (2018). PMID: 29613793, pp. 2015–2021. DOI: 10.1021/acs.jpclett.8b00687.

[213] Kun Wang, Lorenz Bießmann, Matthias Schwartzkopf, Stephan V. Roth, and Peter Müller-Buschbaum. "Tuning of the Morphology and Optoelectronic Properties of ZnO/P3HT/P3HT-b-PEO Hybrid Films via Spray Deposition Method". In: *ACS Applied Materials & Interfaces* 10.24 (2018). PMID: 29808684, pp. 20569–20577. DOI: 10.1021/acsami.8b05459.

[214] Nuri Hohn, Steffen J. Schlosser, Lorenz Bießmann, Lin Song, Sebastian Grott, Senlin Xia, Kun Wang, Matthias Schwartzkopf, Stephan V. Roth, and Peter Müller-Buschbaum. "Impact of Catalytic Additive on Spray Deposited and Nanoporous Titania Thin Films Observed via in Situ X-ray Scattering: Implications for Enhanced Photovoltaics". In: *ACS Applied Nano Materials* 1.8 (July 20, 2018), pp. 4227–4235. DOI: 10.1021/acsanm.8b00985.

[215] Qi Zhong, Lei Mi, Ezzeldin Metwalli, Lorenz Bießmann, Martine Philipp, Anna Miasnikova, Andre Laschewsky, Christine M. Papadakis, Robert Cubitt, Matthias Schwartzkopf, Stephan V. Roth, Jiping Wang, and Peter Müller-Buschbaum. "Effect of chain architecture on the swelling and thermal response of star-shaped thermo-responsive (poly(methoxy diethylene glycol acrylate)-block-polystyrene)3 block copolymer films". In: *Soft Matter* 14.31 (2018), pp. 6582–6594. DOI: 10.1039/C8SM00965A.

[216] Nuri Hohn, Andreas E. Hetzenecker, Michael A. Giebel, Sebastian Geier, Lorenz Bießmann, Volker Körstgens, Nitin Saxena, Johannes Schlipf, Wiebke Ohm, Peter S. Deimel, Francesco Allegretti, Johannes V. Barth, Stephan V. Roth, Thomas F. Fässler, and Peter Müller-Buschbaum. "Amphiphilic diblock copolymer-mediated structure control in nanoporous germanium-based thin films". In: *Nanoscale* 11 (4 2019), pp. 2048–2055. DOI: 10.1039/C8NR09427F.

[217] Johannes Schlipf, Yinghong Hu, Shambhavi Pratap, Lorenz Bießmann, Nuri Hohn, Lionel Porcar, Thomas Bein, Pablo Docampo, and Peter Müller-Buschbaum. "Shedding Light on the Moisture Stability of 3D/2D Hybrid Perovskite Heterojunction Thin Films". In: *ACS Applied Energy Materials* 2.2 (2019), pp. 1011–1018. DOI: 10.1021/acsaem.9b00005.

[218] Nitin Saxena, Benjamin Pretzl, Xaver Lamprecht, Lorenz Bießmann, Dan Yang, Nian Li, Christoph Bilko, Sigrid Bernstorff, and Peter Müller-Buschbaum. "Ionic Liquids as Post-Treatment Agents for Simultaneous Improvement of Seebeck Coefficient and Electrical Conductivity in PEDOT:PSS Films". In: *ACS Applied Materials & Interfaces* 11.8 (2019), pp. 8060–8071. DOI: 10.1021/acsami.8b21709.

[219] Lucas P. Kreuzer, Tobias Widmann, Nuri Hohn, Kun Wang, Lorenz Bießmann, Leander Peis, Jean-Francois Moulin, Viet Hildebrand, André Laschewsky, Christine M. Papadakis, and Peter Müller-Buschbaum. "Swelling and Exchange Behavior of Poly(sulfobetaine)-Based Block Copolymer Thin Films". In: *Macromolecules* 52.9 (2019), pp. 3486–3498. DOI: 10.1021/acs.macromol.9b00443.

[220] Sophie Nieuwenhuis, Qi Zhong, Ezzeldin Metwalli, Lorenz Bießmann, Martine Philipp, Anna Miasnikova, André Laschewsky, Christine M. Papadakis, Robert Cubitt, Jiping Wang, and Peter Müller-Buschbaum. "Hydration and Dehydration Kinetics: Comparison between Poly(N-isopropyl methacrylamide) and

Poly(methoxy diethylene glycol acrylate) Films". In: *Langmuir* 35.24 (2019). PMID: 31117727, pp. 7691–7702. DOI: 10.1021/acs.langmuir.9b00535.

[221] Nian Li, Lin Song, Lorenz Bießmann, Senlin Xia, Wiebke Ohm, Calvin J. Brett, Efi Hadjixenophontos, Guido Schmitz, Stephan V. Roth, and Peter Müller-Buschbaum. "Morphology Phase Diagram of Slot-Die Printed TiO2 Films Based on Sol–Gel Synthesis". In: *Advanced Materials Interfaces* 6.12 (2019), p. 1900558. DOI: 10.1002/admi.201900558.

List of Figures

List of Publications

Publications related to the present work

- L. Bießmann, L. P. Kreuzer, T. Widmann, N. Hohn, J.-F. Moulin, P. Müller-Buschbaum: "Monitoring the Swelling Behavior of PEDOT:PSS Electrodes under High Humidity Conditions"; *ACS Appl. Mater. Interfaces 2018*, **10**.11, 9865–9872; DOI: 10.1021/acsami.8b00446.[29]
  Content and figures adapted with permission. Copyright 2018 American Chemical Society.
- L. Bießmann, N. Saxena, N. Hohn, Md A. Hossain, J. G. C. Veinot, P. Müller-Buschbaum: "Highly Conducting, Transparent PEDOT:PSS Polymer Electrodes from Post-Treatment with Weak and Strong Acids"; *Adv. Electron. Mater. 2019*, **5**.2, 1800654; DOI: 10.1002/aelm.201800654.[30]
  Content and figures adapted with permission. Copyright 2019 John Wiley & Sons.

Further publications

- J. Schlipf, P. Docampo, C. J. Schaffer, V. Körstgens, L. Bießmann, F. Hanusch, N. Giesbrecht, S. Bernstorff, T. Bein, P. Müller-Buschbaum: "A Closer Look into Two-Step Perovskite Conversion with X-ray Scattering"; *J. Phys. Chem. Lett. 2015*, **6**.7, 1265–1269; DOI: 10.1021/acs.jpclett.5b00329.[210]
- N. Hohn, S. J. Schlosser, L. Bießmann, S. Grott, S. Xia, K. Wang, M. Schwartzkopf, S. V. Roth, P. Müller-Buschbaum: "Readily available titania nanostructuring routines based on mobility and polarity controlled phase separation of an amphiphilic diblock copolymer"; *Nanoscale 2018*, **10**.11, 5325–5334; DOI: 10.1039/C7NR09519H.[211]
- J. Schlipf, L. Bießmann, L. Oesinghaus, E. Berger, E. Metwalli, J. A. Lercher, L. Porcar, P. Müller-Buschbaum: "In Situ Monitoring the Uptake of Moisture into Hybrid Perovskite Thin Films"; *J. Phys. Chem. Lett. 2018*, **9**.8, 2015–2021; DOI: 10.1021/acs.jpclett.8b00687.[212]

- K. Wang, L. Bießmann, M. Schwartzkopf, S. V. Roth, P. Müller-Buschbaum: "Tuning of the Morphology and Optoelectronic Properties of ZnO/P3HT/P3HT-b-PEO Hybrid Films via Spray Deposition Method"; *ACS Appl. Mater. Interfaces 2018*, **10**.24, 20569–20557; DOI: 10.1021/acsami.8b05459.[213]
- N. Hohn, S. J. Schlosser, L. Bießmann, L. Song, S. Grott, S. Xia, K. Wang, M. Schwartzkopf, S. V. Roth, P. Müller-Buschbaum: "Impact of Catalytic Additive on Spray Deposited and Nanoporous Titania Thin Films Observed via in Situ X-ray Scattering: Implications for Enhanced Photovoltaics"; *ACS Appl. Nano Mater. 2018*, **1**.8, 4227–4235; DOI: 10.1021/acsanm.8b00985.[214]
- Q. Zhong, L. Mi, E. Metwalli, L. Bießmann, M. Philipp, A. Miasnikova, A. Laschewsky, C. M. Papadakis, R. Cubitt, M. Schwartzkopf, S. V. Roth, J. Wang, P. Müller-Buschbaum: "Effect of chain architecture on the swelling and thermal response of star-shaped thermo-responsive (poly(methoxy diethylene glycol acrylate)-block-polystyrene)$_3$ block copolymer films"; *Soft Matter 2018*, **14**.31, 6582–6594; DOI: 10.1039/C8SM00965A.[215]
- N. Hohn, A. E. Hetzenecker, M. A. Giebel, S. Geier, L. Bießmann, V. Körstgens, N. Saxena, J. Schlipf, W. Ohm, P. S. Deimel, F. Allegretti, J. V. Barth, S. V. Roth, T. F. Fässler, P. Müller-Buschbaum: "Amphiphilic diblock copolymer-mediated structure control in nanoporous germanium-based thin films"; *Nanoscale 2019*, **11**.4, 2048–2055; DOI: 10.1039/C8NR09427F.[216]
- J. Schlipf, Y. Hu, S. Pratap, L. Bießmann, N. Hohn, L. Porcar, T. Bein, P. Docampo, P. Müller-Buschbaum: "Shedding Light on the Moisture Stability of 3D/2D Hybrid Perovskite Heterojunction Thin Films"; *ACS Appl. Energy Mater. 2019*, **2**.2, 1011–1018; DOI: 10.1021/acsaem.9b00005.[217]
- N. Saxena, B. Pretzl, X. Lamprecht, L. Bießmann, D. Yang, N. Li, C. Bilko, S. Bernstorff, P. Müller-Buschbaum: "Ionic Liquids as Post-Treatment Agents for Simultaneous Improvement of Seebeck Coefficient and Electrical Conductivity in PEDOT:PSS Films"; *ACS Appl. Mater. Interfaces 2019*, **11**.8, 8060–8071; DOI: 10.1021/acsami.8b21709.[218]
- L. P. Kreuzer, T. Widmann, N. Hohn, K. Wang, L. Bießmann, L. Peis, J.-F. Moulin, V. Hildebrand, A. Laschewsky, C. M. Papadakis, P. Müller-Buschbaum: "Swelling and Exchange Behavior of Poly(sulfobetaine)-based Block Copolymer Thin Films"; *Macromolecules 2019*, **52**.9, 3486–3498; DOI: 10.1021/acs.macromol.9b00443[219]
- S. Nieuwenhuis, Q. Zhong, E. Metwalli, L. Bießmann, M. Philipp, A. Miasnikova, A. Laschewsky, C. M. Papadakis, R. Cubitt, J. Wang, P. Müller-Buschbaum: "Hydration and Dehydration Kinetics: Comparison between Poly(N-isopropyl methacrylamide) and Poly(methoxy diethylene glycol acrylate)"; *Langmuir 2019*, **35**.24, 7691–7702; DOI: 10.1021/acs.langmuir.9b00535[220]

- N. Li, L. Song, L. Bießmann, S. Xia, W. Ohm, C. J. Brett, E. Hadjixenophontos, G. Schmitz, S. V. Roth, P. Müller-Buschbaum: "Morphology Phase Diagram of Slot-Die Printed TiO_2 Films Based on Sol–Gel Synthesis"; *Adv. Mater. Interfaces 2019*, **6**.12, 1900558; DOI: 10.1002/admi.201900558[221]

Scientific reports

- L. Bießmann, C. J. Schaffer, J. Schlipf, V. Körstgens, S. Bernstorff, P. Müller-Buschbaum: "ZnO scattering layers for OLED applications"; *Lehrstuhl für Funktionelle Materialien, Annual Report 2014*.
- L. Bießmann, P. Müller-Buschbaum: "Mesostructured ZnO scattering layer"; *Lehrstuhl für Funktionelle Materialien, Annual Report 2015*.
- L. Bießmann, P. A. Staniec, P. Müller-Buschbaum: "Investigations on hierarchically structured ZnO for enhanced light scattering in OLED applications"; *Lehrstuhl für Funktionelle Materialien, Annual Report 2016*.
- L. Bießmann, J.-F. Moulin, P. Müller-Buschbaum: "Following the thickness evolution and water uptake of PEDOT:PSS thin films under high humidity conditions by in-situ time-of-flight neutron reflectometry"; *Lehrstuhl für Funktionelle Materialien, Annual Report 2017*.
- L. Bießmann, N. Saxena, N. Hohn, Md A. Hossain, J. G. C. Veinot, P. Müller-Buschbaum: "Impact of weak and strong acids on structure and composition of PEDOT:PSS polymer electrodes"; *Lehrstuhl für Funktionelle Materialien, Annual Report 2018*.

Conference Talks

- L. Bießmann, M. Dyakonova: "Polyelectrolytes";
  Lehrstuhl für Funktionelle Materialien, Summer School,
  Bergheim (Obertauern, Austria), 24 – 27 Jun 2014.
- K. Wang, L. Bießmann, N. Saxena: "Conducting Polymers";
  Lehrstuhl für Funktionelle Materialien, Summer School,
  Bergheim (Obertauern, Austria), 21 – 24 Jun 2016.
- L. Bießmann, M. Trunk, B. Su, H. Xu, S. Bernstorff, P. Müller-Buschbaum: "Structural in-operando investigations on PEDOT:PSS electrodes under high humidity conditions";
  DPG Frühjahrstagung,
  Dresden (Germany), 19 – 24 Mar 2017.

- L. Bießmann, L. P. Kreuzer, T. Widmann, N. Nuri, J.-F. Moulin, P. Müller-Buschbaum: "Monitoring the swelling behavior of PEDOT:PSS thin films under high humidity conditions";
  3rd International Biennial Science Meeting of the MLZ,
  Grainau (Germany), 19 – 22 Jun 2017.
- L. Bießmann, L. P. Kreuzer, T. Widmann, N. Hohn, J.-F. Moulin, P. Müller-Buschbaum: "Monitoring the thickness evolution and water uptake of PEDOT:PSS thin films under high humidity conditions by in-situ neutron reflectometry";
  International Conference on Neutron Scattering,
  Daejeon (Republic of Korea), 9 – 13 Jul 2017.
- L. Bießmann, L. P. Kreuzer, T. Widmann, N. Hohn, J.-F. Moulin, P. Müller-Buschbaum: "Monitoring the Swelling Behavior of PEDOT:PSS Electrodes under High Humidity Conditions";
  DPG Frühjahrstagung,
  Berlin (Germany), 11 – 16 Mar 2018.
- W. Cao, F. Jung, L. Bießmann: "AFM & SEM";
  Lehrstuhl für Funktionelle Materialien, Summer School,
  Bergheim (Obertauern, Austria), 12 – 15 Jun 2018.

Conference poster presentations

- L. Bießmann, C. J. Schaffer, J. Schlipf, V. Körstgens, S. Bernstorff, P. Müller-Buschbaum: "Investigations on ZnO scattering layers for OLED applications";
  DPG Frühjahrstagung, Berlin (Germany), 15 – 20 Mar 2015.
- L. Bießmann, C. J. Schaffer, J. Schlipf, V. Körstgens, S. Bernstorff, P. Müller-Buschbaum: "Spray deposited ZnO scattering layers for OLED applications";
  2nd International Biennial Science Meeting of the MLZ, Grainau (Germany), 15 – 18 Jun 2015.
- L. Bießmann, P. Müller-Buschbaum: "Investigations on ZnO scattering layers for OLED applications";
  5th Colloquium of the Munich School of Engineering, Garching b. München (Germany), 9 Jul 2015.
- L. Bießmann, C. J. Schaffer, J. Schlipf, V. Körstgens, S. Bernstorff, P. Müller-Buschbaum: "Mesostructured ZnO scattering layers for OLED applications";
  DPG Frühjahrstagung, Regensburg (Germany), 6 – 11 Mar 2016.
- L. Bießmann, P. Müller-Buschbaum: "Designing nanostructured scattering layers for OLED applications";
  6th Colloquium of the Munich School of Engineering, Garching b. München (Germany), 7 Jul 2016.

- L. Bießmann, P. A. Staniec, P. Müller-Buschbaum: “Investigations on Hierarchically Structured ZnO for Enhanced Light Scattering in OLED Applications”; *GISAXS*, Hamburg (Germany), 16 – 18 Nov 2016.
- L. Bießmann, P. A. Staniec, P. Müller-Buschbaum: “Enhanced Light Scattering in OLED Applications by Hierarchically Structured ZnO”; *1st BornAgain School and User Meeting*, Garching b. München (Germany), 21 – 22 Nov 2016.
- L. Bießmann, N. Saxena, P. Müller-Buschbaum: “Investigations on PEDOT:PSS polymeric electrodes for OLED applications”; *8th Colloquium of the Munich School of Engineering*, Garching b. München (Germany), 19 Jul 2018.
- L. Bießmann, N. Saxena, K. Wang, D. Yang, C. Bilko, S. Bernstorff, P. Müller-Buschbaum: “Structural investigations on PEDOT:PSS polymeric electrodes by means of GISAXS and GIWAXS”; *4th German SNI Conference*, Garching b. München (Germany), 17 – 19 Sep 2018.

Acknowledgments

This thesis is more than just a documentation of my PhD project at the Chair of Functional Materials, commonly known as E13. The considerable amount of work I had to cope with would not have been possible to tackle without the overwhelming help, support and good advices from many sides. For this, I am very grateful and want to thank those people in the following lines.

First of all, I would like to thank Peter Müller-Buschbaum for the opportunity to work on this inspiring and challenging topic. This came along with his guidance, his support and his believing me capable of accomplishing this task. The challenging problems I had to overcome during the seemingly countless and sometimes very surprising beamtimes, together with managing of several projects and with guiding students, forced me to stay focused and helped me to work more effective. At the same time, he was giving me the freedom to develop own ideas and also following own (off-topic) projects. By this, I was able to improve both, my professional and personal skills, and gained plenty of personal experiences and impressions. Thanks for that!

I want to thank all of my current and former colleagues of E13, where I not only found help but also very good friends. By the great team spirit during various of beamtimes, the travel and the night shifts with my fellow colleagues made much more fun. I want to thank my meanwhile former colleagues Daniel Moseguí González, Claudia M. Palumbiny and Christoph J. Schaffer for their serenity and patience during all these questions and discussions we had in Café Schaffer and elsewhere. Especially, I want to thank Nitin Saxena and Johannes Schlipf, keeping me company from my start to the end in the best way I can imagine and for your devotional contribution in the escalation force. The Herzig-Group with Stephan H. Pröller, Jenny M. Lebert, Mihael Čorić, and Oliver Filonik, for their accompany during so many late-evening discussions, surprise meetings and their very special humor. Franziska Löhrer, Nuri Hohn, Lucas P. Kreuzer, Sebastian Grott, Shambhavi Pratap, Tobias Widmann, Simon J. Schaper, Volker Körstgens, Markus Trunk for the great after-lunch and after-work discussions. Lin Song, Weijia Wang, Senlin Xia for the amazing insights into the Chinese culture. I also want to thank our "new" generation, Julian Heger, Christina Geiger, Lennart Reb, Anna-Lena Oechsle, Dominik Schwaiger, Roy Schaffrinna, Kerstin Wienhold, and Manuel Scheel for their fresh ideas and unimpaired view. Thanks to Christine M. Papadakis and her group, especially to Bart-Jan Niebuur and Florian Jung, for listening so patient to all of the solar cell and sol-gel related talks in our group seminar. Further, I want to thank all of the former group members that were always happy to

answer questions, among them Konstantinos N. Raftopoulos, Martine Philipp, and Ezzeldin Metwalli, as well as Kuhu Sarkar for your time and effort to introduce me into this interesting topic. Thank you for making my time here so unforgettable!

A large part of this work is based on many successful beamtimes. Obviously, this would not have been possible without the help of my collaboration partners at synchrotrons and neutron facilities. I want to thank all the people that provided their beamlines and shared their experience and thus made it possible to probe all these samples in whichever environment we could think of. Thank you, Stephan V. Roth, Matthias Schwartzkopf, Wiebke Ohm, André Rothkirch, Calvin Brett, Marc Gensch from DESY, Sigrid Bernstorff from Elettra, Paul Staniec from the Diamond Light Source, Jean-François Moulin from the MLZ, and Robert Cubitt and Lionel Porcar from the ILL. Particularly, I want to thank the P03 staff for the great time during beamtimes and for the accompany during our joint conferences.

Furthermore, I would like to thank the people in the background. Among them, the E13 workshop crew with Reinhold Funer, Nick Schröder and Sebastian Fink for fixing our beamtime equipment in the very last seconds and realizing our crazy ideas for our setups. Additionally, I want to thank Michael Böhmer from the electronics workshop who helped me a lot during the construction of the *goniometer setup* and Dieter Müller who always provided us with any kind of IT equipment. Not to forget, our good souls in the secretaries' office, Carola Kappauf, Marion Waletzki and Susanna (Susi) Fink, for keeping everything silently running in the background. A special thanks to you for your patience with all my questions and your help in mastering the bureaucracy monster of the TUM.

It is always helpful to delegate upcoming work when a lot of stuff has to be done. For this, I want to thank my students that helped a lot with their work and also contributed to this thesis. I highly appreciate your helping hands in the lab and your strong motivation and effort in coping your projects and at the same time helping me to manage all this work. Felix Sievers, Irina Ilicheva, Lina M. Todenhagen, Raphael Maier and Dominik Schullerer, thank you.

Of course, such a paperwork cannot be proofed by one alone. A big thank you to all the proof readers who helped to correct this thesis and who sacrificed their precious time to ferret out these typos and mistakes hiding in the deep of all of these words. Thank you, Sebastian Grott, Julian Heger, Nuri Hohn, Lucas P. Kreuzer, Stephan H. Pröller, Lennart Reb, Johannes Schlipf, and Tobias Widmann.

Last but not least, the biggest thanks goes to my family. Especially my parents, Rolf and Roswitha, who inspired me and encouraged me to stay curious throughout my whole life. I am very thankful for your never-ending support and believing in me which was always a source of endurance to me. Thank you! Finally, my dear Marina, who went with me through all the ups and downs of my time as PhD candidate. I thank you for your patience and endorsement during all the time and I am very grateful having you in my life!